Development of Finite Element Analysis of Magnetic Resonance Elastography to Investigate its Potential Use in Abdominal Aortic Aneurysms

Lyam Hollis

A thesis submitted for the degree of Doctor of Philosophy.

University of Edinburgh.

February 16, 2016

Abstract

Abdominal aortic aneurysm (AAA) is a form of cardiovascular disease whereby a change in the material properties of the vessel wall results in a localised dilation of the abdominal aorta. The primary risk of AAAs is rupture with mortality rates close to 90%. Whilst surgical intervention can be performed to repair AAAs, such procedures are considered high risk. As a result, surgery is only performed upon AAAs that are considered likely to rupture. The current method of prediction is the diameter criterion, with surgical intervention performed if the diameter of the AAA exceeds 5.5cm. Research has demonstrated that this is a weak method of predicting rupture and as such other methodologies are sought. One promising method is patient specific modelling (PSM) which involves the reconstruction of individual patient AAA geometries from imaging datasets, and finite element analysis (FEA) to calculate the stresses acting on the AAA wall, with the peak stress typically used as the predictor. A weakness of this methodology is the lack of patient specific material property values defined in the simulation. A potential technique to address this limitation is magnetic resonance elastography (MRE), an MR-based technique which utilises a phase-contrast sequence to characterise displacements caused by shear waves induced into the tissue by an external mechanical driver. An inversion algorithm is used to calculate local material property values of the tissue from these displacements. The aim of this thesis was to investigate the capability of utilising MRE to obtain material property measurements from AAAs that could be incorporated into PSM.

To achieve this an FE method of modelling MRE was developed. The influence of modelling parameters upon the material property measurements made using the direct inversion (DI) algorithm was investigated, with element type and boundary conditions shown to have an effect. The modelling technique was then utilised to demonstrate the influence that the size of an insert had upon shear modulus measurements of that insert using DI in both 2- and 3-dimensions, and the multi-frequency dual elasto-visco algorithm (MDEV), an extension of DI combining information from multiple frequencies. Meanwhile a comparison of the modelling technique against an MRE scan of a phantom showed that whilst measurements made from the two techniques were different at low frequencies, they became similar as the frequency increased. This suggested that such differences were attributable to increased noise in the scanned data.

FEA of MRE performed on idealised AAA geometries demonstrated that AAA size, shear viscosity of the thrombus and shear modulus of the AAA wall all influenced the accuracy of MRE measurements in the thrombus. Meanwhile MRE scanning of a small cohort of AAA patients had been undertaken and phase images investigated for signs of wave propagation to investigate the capabilities of the current MRE setup. Phase images were dominated by noise and there was no wave propagation visualised in any of the AAAs.

This thesis demonstrates that the current MRE setup is not capable of achieving accurate measurements of material properties of AAA for PSM. Visualisation of wave propagation in AAAs is technically demanding and requires further development. A more fundamental concern however is the size dependence of the inversion algorithm used and the inability to consistently make accurate measurements from AAA geometries.

Lay Summary

Abdominal aortic aneurysms (AAAs) are a form of cardiovascular disease affecting 2% of men over 65. The disease is represented by a dilation of the aorta, the main artery transporting blood away from the heart, in the lower region of the abdomen. Rupture of AAAs has a high mortality rate, but whilst surgery can be performed to treat the condition, it is invasive and risky. Additionally, many AAAs will not rupture during the natural lifetime of the patient. For these reasons, surgical intervention is only performed if it is deemed likely that the AAA will rupture. The current method of predicting rupture is the diameter criterion, whereby surgery is performed if the AAA diameter exceeds 5.5 cm. This is typically seen as a weak method of predicting rupture however, and alternatives are sought. One such alternative is patient specific modelling (PSM). This utilises computational modelling to calculate the stress placed on the AAA wall by the internal blood pressure. It is the highest value of this stress which is used as the predictor of rupture. A weakness with this technique is that it requires material property (stiffness) data from each individual patient to accurately calculate the stresses. The aim of this thesis was to investigate whether magnetic resonance elastography (MRE), an MRI-based technique previously utilised in other tissues to measure material properties, could be used to acquire material property data that could be used in PSM of AAAs. Through MRE scanning of a small cohort of patients, and by performing computational simulations of MRE, this thesis has demonstrated that the current setup of MRE is not capable of achieving such measurements. The primary concern highlighted by this thesis was that MRE measurements of AAA material properties are not simply dependent upon the material properties of the AAA itself, but also on the size of the AAA. Since AAAs vary greatly in size from one patient to another, this represents a significant limitation.

Declaration of Originality

I hereby declare that the research in this thesis, and the thesis itself, was composed and originated entirely by myself, except where specifically stated otherwise, in the Centre for Cardiovascular Science at the University of Edinburgh and has not been submitted for any degree or professional qualification.

Lyam Hollis

Acknowledgements

First and foremost, I would like to thank my supervisors, Pete, Pankaj, Neil and David. Their support, encouragement and advice has been invaluable to my completion of this thesis.

Throughout the course of my PhD I have become indebted to a number of people for their help and guidance. The modelling in this thesis would not have been possible without the FEA tuition I received from Lauren Thomas-Seale and Noel Conlisk. The patience of Noel and David Kenwright in helping with all my coding problems should also not be understated. In terms of the MRI work, an enormous thanks must go to Scott Semple for all his advice; to Lucy Hiscox for providing the scans in chapter 4; to Eric Barnhill and Paul Kennedy for their patience in explaining all the basic concepts and for their help with the software; and to all the radiographers who put up with me wheeling the apparatus in and out the scan room and collected data. Thanks also to Irene for helping out with all my paperwork and sorting out any money related issues. I am also hugely grateful to all the volunteers and patients who gave up their free time to be scanned for my project and to the BHF for their funding.

There are numerous people who have helped me take my mind off work when things have been difficult. All the BHF students in the QMRI, particularly those with whom I began the PhD programme, have made this a wonderful place to work. Special mention should go to the ‘hockey lads and wags’: your unwavering friendship has kept me going.

Finally I would like to thank my Mum, Dad, Jemma and Neall. Without your love and support this thesis would not have been possible. This thesis is dedicated to you.

Contents

Appendix

List of Figures

List of Tables

List of Abbreviations

AAA	Abdominal aortic aneurysm
BMI	Body mass index
CAD	Computer aided design
CFD	Computational fluid dynamics
CT	Computerised tomography
EVAR	Endovascular aneurysm repair
FEA	Finite element analysis
FSI	Fluid structure interaction
ILT	Intraluminal thrombus
LFE	Local frequency estimation
MDEV	Multi-frequency dual elasto-visco
MMP	Matrix metalloproteinase
MRE	Magnetic resonance elastography
MRI	Magnetic resonance imaging
PE	Phase encoding
PSM	Patient specific modelling
PWV	Pulse wave velocity
RPI	Rupture potential index
SNR	Signal-to-noise ratio
SPD	Spatio-temporal directional
TR	Repetition time
TE	Echo time
USPIO	Ultrasmall paramagnetic iron oxide particles
VPH	Virtual physiological human
VSMC	Vascular smooth muscle cell

List of Symbols

a_i	Inner diameter of vessel wall
B	Magnetic field strength
$\mathbf{C}$	Damping matrix
C_{ijkl}	Complex stiffness tensor
$\mathbf{F}$	Force vector
f	Frequency
G	Shear modulus
G^*	Complex shear modulus
G'	Storage modulus
G''	Loss modulus
$\mathbf{G}_r$	Magnetic field vector
$\mathbf{K}$	Stiffness matrix
$\mathbf{M}$	Lumped mass matrix
m	Mass
$\mathbf{p}$	Load vector
$\mathbf{r}$	Position vector
T	Vessel wall thickness
t	Time
$\mathbf{u}$	Displacement vector
γ	Gyromagnetic ratio
δ_{ij}	Kronecker delta function
ϵ_{ij}	Strain matrix
Λ	Lamé parameters
ν	Spatial frequency
ρ	Density
σ_{ij}	Stress matrix
Φ	Phase shift
ω	Angular frequency

Chapter 1

Introduction

This chapter begins by outlining the key concepts behind this thesis and reviewing the relevant literature. It then states the aims of the thesis and provides a brief outline of the structure.

1.1 Abdominal Aortic Aneurysms

The cardiovascular system plays a critical role in human life, circulating blood around the body. Just some of the crucial roles it performs are the provision of nutrients and oxygen for the cells to metabolise, transportation of hormones from one organ to another to regulate vital functions and the facilitation of the removal of waste products from the body. Consequently disease of this system is often extremely serious with cardiovascular diseases accounting for 28% of all deaths in the United Kingdom in 2012 [1]. The main artery in the human body is the aorta which transports blood directly out of the heart. Initially ascending, it curves back on itself at the aortic arch before descending into the abdomen and bifurcating into the iliac arteries. Abdominal aortic aneurysms (AAAs), a form of cardiovascular disease affecting 2% of men over 65 [2] occur just above this bifurcation. In such cases a change in the material properties of the vessel wall results in a dilation of the artery with an AAA typically defined as having a diameter exceeding 3 cm [3] or 1.5 times the size of the suprarenal aorta [4]. The primary threat of AAAs is that of rupture with mortality close to 90% if such an event occurs outside a hospital [5]. This section of the introduction aims to provide a background summary of the diagnosis, risk factors, development, treatment and prediction of the likelihood of rupture of AAAs.

1.1.1 Diagnosis

Diagnosis of AAA is crucial for the survival prospects of the patient. AAAs are typically asymptomatic with only around 5% of AAAs being inflammatory (presenting with symptoms) [6]. This has meant that in the past the majority of AAAs have been diagnosed through incidental findings from scans performed for other purposes, meaning that the first presentation of many AAA patients was following rupture. Since the mortality rate following rupture is approximately 80-90% [7] this clearly presented a significant problem.

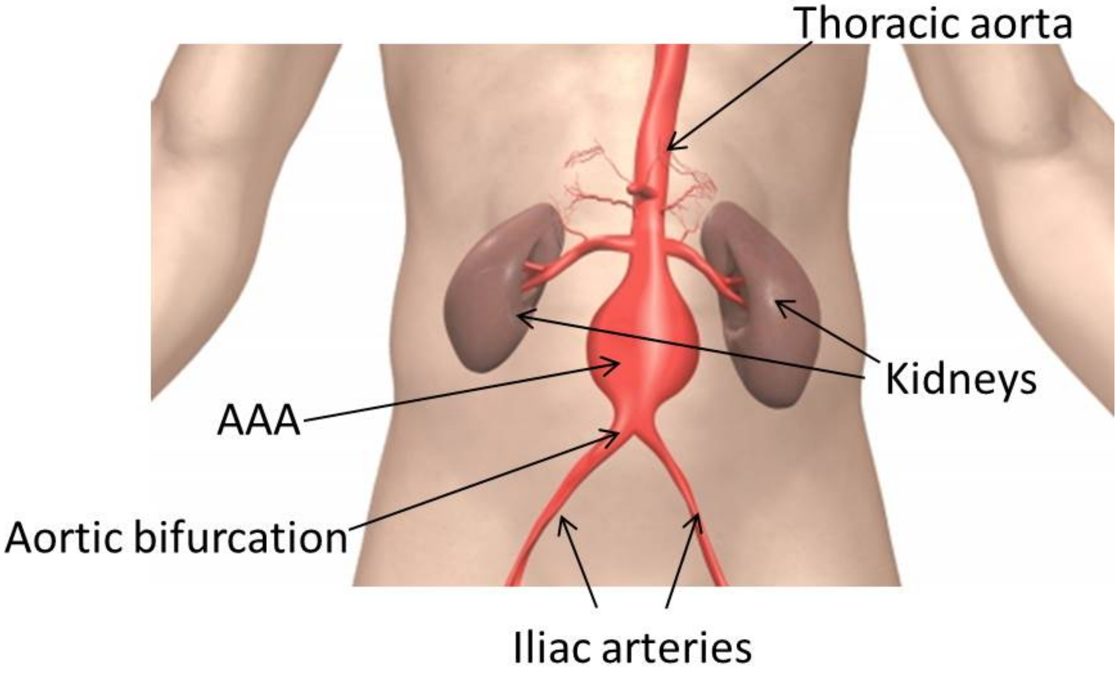

Figure 1.1: Diagram of the human abdomen with an abdominal aortic aneurysm. Adapted from NHS Abdominal Aortic Screening Programme: http://aaa.screening.nhs.uk/public

More recently attention has focused on screening patients in high risk groups. Since the prevalence of AAA is fairly low even within high risk groups, emphasis here must be placed on both accuracy of the diagnostic technique and its cost. The cheapest method of diagnosis is via manual palpation however the sensitivity of this technique is poor with only 29% of AAAs with a diameter less than 4 cm detected [8]. In contrast, computerised tomography (CT) scans offer excellent resolution with good accuracy of diameter measurements but are typically considered as too expensive for such purposes [9]. As such ultrasound is the technique of choice offering a sensitivity greater than 94% [10].

The first screening trial was conducted in the United Kingdom from 1988-1994 and out of a total of 15,775 people AAAs were found in 4% [11]. Studies since then have typically had similar findings: the Multicentre Aneurysm Screening Study (MASS) conducted in the UK found a prevalence of 4.9% [12]; the Western Australia trial for screening AAAs, a prevalence of 7.2% [13]; and the Viborg study conducted in Denmark, a prevalence of 4.0% [14]. In contrast to this, a more recent study by Conway et al. (2012) [15] again conducted in the UK reported a much lower prevalence of just 1.6%. It was concluded that the reason for this reduced rate was the inclusion of younger subjects than in previous studies and a lack of ethnic diversity in the population studied. Importantly the MASS trial found a reduction in mortality of 53% through AAA related incidents in the screened population. Also of significance was a cost-analysis study by Søgaard et al. (2012) [16] which demonstrated that screening patients routinely for AAAs was cost-effective in comparison to not screening.

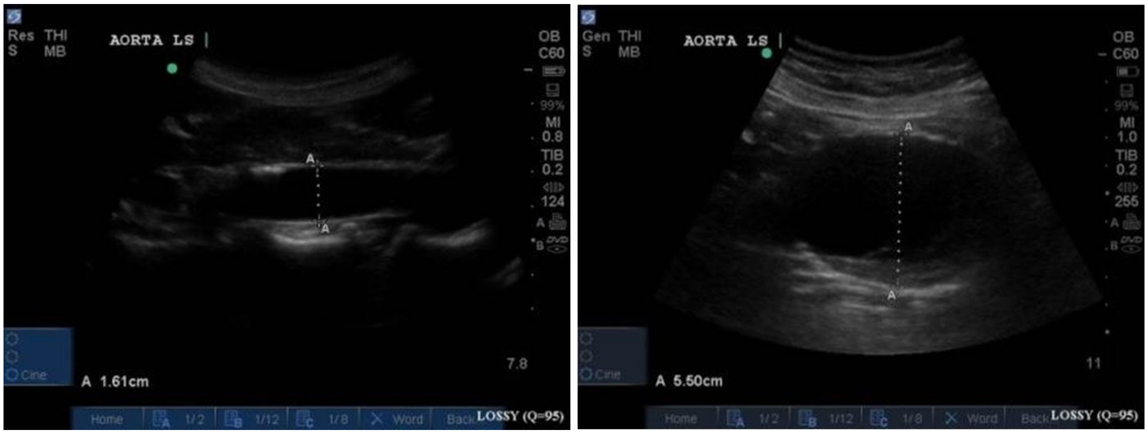

Figure 1.2: Ultrasound images of a healthy aorta (left) and an AAA (right). Images from the NHS screening programme: http://www.dbh.nhs.uk/our_services/medical_imaging/AAA_Screening_programme.aspx

1.1.2 Risk Factors

Smoking

Smoking has long been recognised as the primary risk factor for AAAs [17,18] and responsible for increased growth rate [19]. Indeed a study by Brady et al. (2004) [20] showed AAA growth rate in smokers to be increased by up to 20% in comparison to non-smokers. A screening programme of 447 men (210 with AAAs and 237 without) aged 50 and over in the Huntingdon area of the UK in 1999 concluded that AAAs were significantly more prevalent in smokers than non-smokers; echoed in a subsequent study a year later showing AAAs were four times as prevalent in smokers as they were in lifelong non-smokers [21]. The Huntingdon study also noted the importance of the duration of the habit; a longer habit leading to increased risk. For previous smokers the cessation period was significant in decreasing the risk of AAA [22]. These findings were reinforced by the Tromsø study in 2001 [10]. This took a population of 2962 men (263 with AAAs) and 3424 women (74 with AAAs) and showed that the risk of AAA increased by 6-7 times for smokers. Again they also showed a strong association between length of habit and risk, and that a longer cessation period for non-smokers was beneficial; though they attributed this to a decreased period over which they had smoked. The increased risk of AAA as a result of smoking is largely cited as being a result of nicotine [23, 24].

Serum HDL Cholesterol

A second risk factor identified by the Tromsø study was serum HDL cholesterol [10] echoing the results of an earlier population based study subjects in Rotterdam [25]. These results showed that subjects with a serum HDL cholesterol level less than 1.20 $\text{mmol}\cdot\text{l}^{-1}$ were 70% more likely to develop AAAs than those with levels greater than 1.79 $\text{mmol}\cdot\text{l}^{-1}$. This increased risk was attributed to an atherogenic process.

Hypertension

The role of hypertension as a risk factor for AAAs is debated. Several studies have found no significant relationship at all [26, 27]. Meanwhile a study as early as 1950 showed that women were more susceptible to AAAs if hypertensive than men [28]; a finding which was later replicated in the Tromsø study [10]. A study by Vardulaki et al. (2000) [21] found that whilst there was no relationship between systolic blood pressure and the risk of AAAs, raised diastolic pressure led to an increase in risk of between 30-40%. This study alongside the Tromsø study also showed a significant relationship between anti-hypertensive medication and AAA risk. One possible reason for the ambiguity in the literature as to the role of hypertension as a risk factor for AAA is the variation in its definition: the range for systolic hypertension in the literature quoted here is 140 mmHg to 199 mmHg.

Age

AAA prevalence has been consistently shown to increase strongly with age. The study by Vardulaki et al. (2000) showed the percentage of the population with AAAs increased from 2.7% for 65-69 year olds to 4.4% for 75-79 year olds [21]. Again the findings of the Tromsø study supported this [10]. The influence of age as a risk factor for AAA is well recognised in the literature with the majority of studies focusing solely on the over 65's. As a result of the increased risk screening programmes for this age group are also becoming more prevalent [17, 29, 30].

Gender

Gender is also a recognised risk factor for AAAs. Men are around five times more likely to develop an AAA than women [31]. Despite this the mortality rate for men and women is similar, with AAAs being the fifteenth largest killer of men in the United States in 2003 and the 20th largest for women [32] with the risk of AAA rupture 4 times greater for women than men [33]. Possible reasons for this statistical anomaly are different treatment in clinical practice or biological factors. Whilst there is little literature on this, in support of the latter, increased growth rate of AAAs has been observed in women compared to men and typically women present with AAAs at an older age [34,35]. Procedures for AAA repair have also been shown to be less successful for women [36, 37].

Genetics

A study in 1986 showed that 19.2% of people whose first-degree relative had suffered from an AAA also suffered themselves, compared to just 2.4% of those who had no family history [38]. A more recent study by Kuivaniemi et al. (2003) again showed this increased risk for first degree relatives of an AAA sufferer [39]. A 2005 review paper by Sandford et al. (2007) concluded that although there was strong evidence for a genetic risk factor, the process was complex, little understood and probably the result of multiple gene polymorphism [40] with a similar conclusion drawn by Nordon et al. (2011) [41]. In contrast to this, several studies have argued against genetic risk factors or concluded that their role is exaggerated as a result of maternal smoking increasing the vulnerability of their offspring to later life cardiovascular disease whilst simultaneously increasing their own risk of AAA [42,43].

1.1.3 Development and Progression

Structure of the Vessel Wall

Physically the development of AAAs is associated with a change in the material properties of the vessel wall resulting from alterations in the physiological structure [44]. The vessel wall is constructed of three layers. The intima is the innermost and thinnest layer consisting of a single layer of endothelial cells and a subendothelial layer of vascular smooth muscle cells (VSMCs) and collagen fibres. Outside the intima is the media. This is the thickest layer, where the majority of elastin in the vessel walls is found. Again VSMCs and collagen are also found, with the circumferential structural arrangement of VSMCs adding largely to the strength of the layer. The outer layer of the vessel is the adventitia consisting of collagen, fibroblasts and fibrocytes [45]. The media and adventitia contribute most to the mechanical properties of the vessel wall [46]. Meanwhile it should be noted that the stress-strain curves for elastin and collagen are different: at low stresses the contribution of elastin is large, however as the stress increases, collagen fibres are recruited. This leads to a subsequent stiffening of the vessel wall [45, 47].

Wall Stress, Inflammation and Material Property Changes of the Vessel Wall

Strong association has been found between the presence of atherosclerosis - a build-up of plaque inside arteries - in the abdominal aorta and AAA formation [48]. Whilst traditionally it has been believed that AAA formation occurs as a result of an arterial remodelling response to atherosclerosis, more recent studies have questioned whether the two conditions are related to one another or if they simply share the same common risk factors [49]. In reality the mechanisms by which AAAs form remains relatively poorly understood.

Despite this there is typically agreement in the field that inflammation plays a significant role. In this regard it is believed that a change in local wall stress values causes an increase in the activity of inflammatory cells. This in turn promotes the synthesis of matrix metalloproteinase 2 and 9 (MMP-2 and MMP-9) which cause degradation to elastin and collagen and thus a breakdown of the extracellular matrix. The result of this is a local reduction of the elastic modulus of the vessel wall and a subsequent expansion in response to the local stresses induced by blood pressure. Since this expansion also tends to increase the local wall stress the process is cyclic and the AAA grows as a result [50–52].

Hemodynamic Changes and the Devlopement of the Intraluminal Thrombus

Intraluminal thrombus (ILT) is extremely common in AAA's existing in over 90% of patients with an AAA greater than 5 cm and the volume of ILT is typically larger for ruptured than non-ruptured AAAs [53]. The formation of ILT is largely believed to be the result of a change in the hemodynamics that occurs as a result of the dilation of the vessel. The majority of research into this phenomenon has been performed using computational fluid dynamics (CFD), a technique which typically uses a large amount of computational resources in order to obtain fluid flow characteristics under pre-defined geometries and fluid properties. Such studies have shown the development of vortices in the growing sac region of the AAA [54]. This ultimately results in a decrease in shear stress at the vessel wall whilst simultaneously creating a high fluid shear stress in the lumen at the outer regions of the vortices [55]. As such platelet activation is encouraged within the lumen, whilst deposition is promoted at the AAA wall [56] thus thrombus formation is instigated.

In more developed AAAs the thrombus consists of three layers: a luminal layer, a medial layer and an abluminal layer [57]. The appearance and properties of the thrombus vary depending on the layer. According to Wang et al. (2001) [58] the innermost layer, the luminal, appeared red and contained thick fibrin bundles. Following mechanical testing the Young's modulus of this layer was calculated at 0.54 MPa. Moving outwards the medial layer appeared white with the fibres appearing degraded, whilst the material was less stiff with a Young's modulus of 0.28 MPa. The outermost layer, the abluminal, appeared dark brown and had suffered from a large amount of fibre degradation, to the extent that mechanical testing was no longer possible. More recent research has further identified differences in the constituent materials in each of these layers significantly showing that proteases with the potential to cause degradation to the vessel wall were largely inactive in the abluminal region [59].

Modelling AAA Growth

In an attempt to understand the pathogenesis of AAAs, several authors have attempted to model AAA growth and remodelling (changes in the AAA structure). Such models tend to assume that AAA development results from evolution of the constituent materials in response to stress. Notably Watten et al. (2004) [60] assumed a parallel arrangement of elastin and collagen fibres, with collagen recruited only when a the arrangement was stretched by a specified factor, known as the recruitment stretch. Degradation and deposition of collagen allows remodelling of the recruitment stretch, thus allowing the collagen stretch to reach an equilibrium value. AAA growth is therefore assumed to be driven by elastin degradation, which causes increased stretch of the AAA forcing collagen to adapt

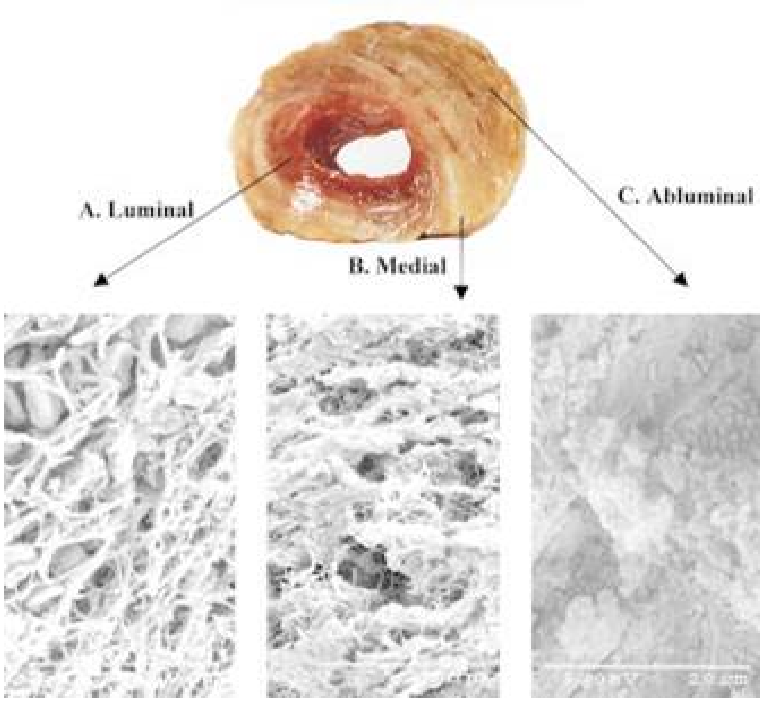

Figure 1.3: Cross-section of an AAA showing the luminal, medial and abluminal layers along with a scanning electron micrograph from each region. Image taken from Wang et al.(2001) [58] with permission.

in order to achieve a new equilibrium stretch value. Stress distributions in the model were shown to closely represent those seen in reality, whilst a subsequent paper demonstrated close agreement with physiological observations of AAA maximum diameter increase and ratios of AAA diameter from systole to diastole throughout development [61]. Whilst such models offer promise, a review by Humphrey and Holzapfel (2012) [62] identified that a current lack of longitudinal data on AAA growth prevents validation.

1.1.4 Treatment

AAA's are repaired by surgical intervention. There are two surgical procedures performed to achieve this: open repair and endovascular aneurysm repair (EVAR).

Open Repair

The first successful AAA open repair was performed Dubost, Allary and Oeconomos [63] with large improvements having been made in both graft design and surgical techniques since then. To perform the procedure the patient is placed under general anaesthetic and a large midline or flank incision is made into the abdomen to access the AAA. The AAA is then opened and the thrombotic tissue is removed from within the aorta before a graft is sutured in place. Depending on the individual AAA the graft can extend down to the bifurcation or into the iliac arteries.

EVAR

An alternative to open repair was introduced by Parodi et al. in 1991 [64]. This surgery is non-invasive, does not involve the removal of the AAA tissue and the procedure can be performed under general or local anaesthetic. A small incision is made in the groin and a stent-graft is inserted into the AAA through the femoral or iliac arteries. Once in place the stent-graft is expanded in order to anchor it in place. The graft prevents blood from flowing into the AAA sac, shielding the vessel wall from the stresses associated with AAA.

Open Repair Versus EVAR

A significant amount of research has been conducted to compare open surgery and EVAR. EVAR has become progressively more popular since its inception and accounted for 74% of elective repairs in the United States in 2010 in comparison to just 5.2% in 2000 [65]. The non-invasive nature of EVAR is typically cited as its main advantage. The experience is less traumatic for the patient and the cost, at least at the point of the initial surgery, is lower [66]. Perhaps more importantly the highly invasive open repair procedure is also seen as a high risk for AAA patients who are typically elderly and frail and often suffering from other conditions besides the aneurysm. This is reflected in the 30 day mortality statistics which show survival rates of 98.4% from EVAR in comparison to 95.2% from open repair.

Whilst the short-term statistics show clear support for EVAR the longer term outcomes are more complex. Later complications are much more common following EVAR than open repair with up to 25% of patients suffering from endoleaks, where blood begins to flow back into the AAA sac [67]. Such endoleaks are typically associated with longer AAAs [68] and mean that EVAR patients are often forced to have follow up procedures. These effectively add to the expense of the procedure and result in the total cost of EVAR being greater than open repair [69]. In addition to this, whilst the 30 day survival rates for EVAR are better than open repair, intermediate and long term survival rates for both procedures are not significantly different [70].

1.1.5 AAA Rupture

If AAA rupture is not treated urgently it is fatal. Approximately 50% of patients with AAA rupture never reach the hospital and even in the instances that they do there remains a 30-50% mortality rate [71]. Upon rupture the patient typically experiences pain in the back or abdomen, suffers from a pulsatile mass in the abdomen and becomes hypotensive [5]. Maintaining a state of permissive hypotension has been shown to improve survival prospects [72]. Additionally, survival prospects are dependent on the hospital to which the patient is admitted. Hospitals that deal with a large number of AAA patients have a significantly lower mortality rate than those hospitals that deal with relatively few AAAs [65]. This is largely thought to be as a result of surgeons in such hospitals having received greater training and having had more practice to deal with such cases. Additionally such hospitals are typically in regions with large populations, therefore transfer time to the hospital is often reduced [73].

1.1.6 Rupture Prediction

Since AAA has such high mortality it is preferable to perform surgical intervention where possible. However because intervention itself is relatively risky and since in many patients the AAA may never rupture within their lifetime, the decision to surgically intervene is based upon a prediction as to whether it is likely that the AAA will rupture [74]. The current method of prediction is the diameter criterion: if the AAA reaches a diameter greater than 5.5 cm then surgical intervention is performed. The diameter criterion has, however, long been criticised as unreliable [75]; Darling et al. (1977) demonstrated that rupture occurred in 12.8% of AAAs smaller than 5 cm, whilst 40% of AAAs greater than 5 cm never ruptured [76]. As a result a lot of research has focused on achieving an improved method of prediction. Several studies have demonstrated that AAA growth rate is related to rupture [77, 78] however separating this effect from the diameter criterion has been difficult since rapidly growing AAAs tend to be larger [79]. More recently a pilot study by Richards et al. (2011) [80] utilised ultrasmall paramagnetic iron oxide particle (USPIO) uptake in AAAs to characterise inflammation. This technique aims to identify AAAs that are likely to expand rapidly and thus identify likelihood of rupture. Another technique known as patient specific modelling (PSM) has also been researched extensively. This utilises finite element analysis (FEA) to calculate stresses acting on the AAA wall. FEA and PSM will be discussed in more depth in this introduction.

1.1.7 Summary

Improvements in surgical procedures and the increased use of screening programmes has led to an improvement in the prognosis of AAA patients in recent years [81]. Despite this the decision as to whether surgical intervention should be performed is still dependent on the diameter criterion, a weak method of predicting the likelihood of AAA rupture. A better predictive model would therefore result in a lower mortality rate of the disease.

1.2 Rheology

Rheology is defined as the study of the flow of matter: in essence, recognition of the inability of Hooke's law of elasticity or Newton's law of viscosity to truly describe realistic solids and fluids due to the complex structure of matter. Rheology tends to characterise materials as a combination of these two properties in order to achieve a better description of their behaviour. This section outlines the basic principles of rheology relevant to this thesis.

1.2.1 Linear Elasticity

Traditionally solids have been described by Hooke's law. In 1-dimension this states that the strain, σ, undergone by a material is proportional to the stress, ϵ, that is placed upon it:

$$\sigma = E\epsilon \tag{1.1}$$

where E is a constant dependent on the material under investigation known as Young's modulus. This implies that the material will always return to its initial shape when a load is removed. It also implies that the final deformation has no dependence upon the rate at which the load is applied. Whilst both these conditions can be approximated for some materials under certain conditions, they do not hold true in general [82].

The concept of stress and strain can be extended to 3-dimensions. Here the stress, ϵ_{kl}, and strain, σ, matrices are related to one another by the stiffness matrix, C_{ijkl}, a rank-4 tensor consiting of up to 36 independent variables [83]:

$$\sigma_{ij} = C_{ijkl}\epsilon_{kl} \tag{1.2}$$

The indices represent the three spatial directions. The summation convention has been applied here such that repeated indices should be summed over. Since the stress and strain matrices and the stiffness tensor contain symmetries, they are often written as vectors and a matrix respectively. As a result the simplest form of Hooke's law, for an isotropic 3-D body, is often written as:

$$\begin{pmatrix} \sigma_{xx} \\ \sigma_{yy} \\ \sigma_{zz} \\ \sigma_{yz} \\ \sigma_{xz} \\ \sigma_{xy} \end{pmatrix} = \frac{E}{(1+v)(1-2v)} \cdot \begin{pmatrix} 1-v & v & v & 0 & 0 & 0 \\ v & 1-v & v & 0 & 0 & 0 \\ v & v & 1-v & 0 & 0 & 0 \\ 0 & 0 & 0 & \frac{(1-2v)}{2} & 0 & 0 \\ 0 & 0 & 0 & 0 & \frac{(1-2v)}{2} & 0 \\ 0 & 0 & 0 & 0 & 0 & \frac{(1-2v)}{2} \end{pmatrix} \begin{pmatrix} \epsilon_{xx} \\ \epsilon_{yy} \\ \epsilon_{zz} \\ 2\epsilon_{yz} \\ 2\epsilon_{xz} \\ 2\epsilon_{xy} \end{pmatrix} \tag{1.3}$$

where v is Poisson's ratio.

1.2.2 Viscosity

Viscosity is a material property relating to fluids and describes the extent to which fluids are resistant to flow. This resistance results from interactions between particles travelling at different velocities. At a solid interface the no-slip boundary condition is assumed. This is based upon the frictional interaction between the solid and the fluid and implies that the velocity of the fluid at the surface is equal to zero. For a Newtonian fluid the shear rate,

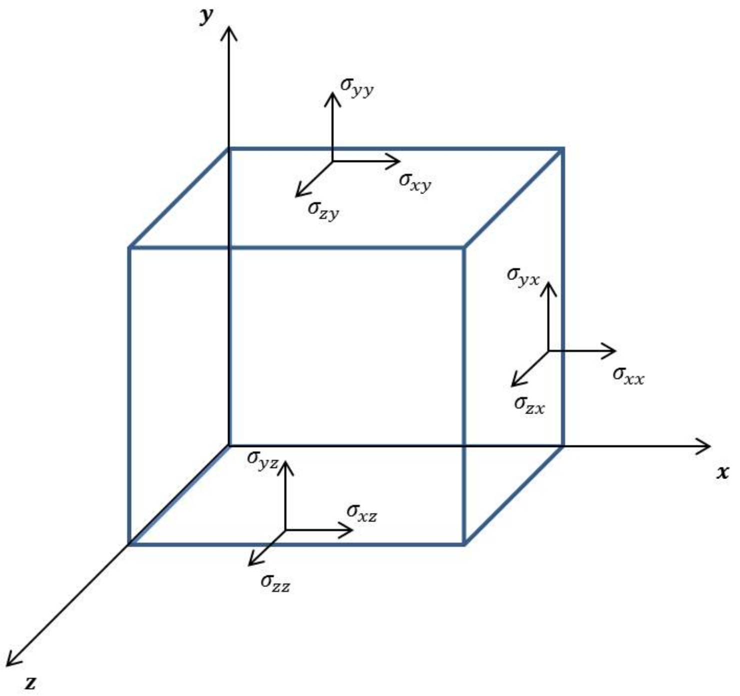

Figure 1.4: Illustration to show the components of the strain matrix acting upon an element. The diagonal components are the normal strains whilst the non-diagonal components represent the shear strains.

$\dot{\gamma}$, defined as the gradient of the velocity across the fluid layers, is directly proportional to the shear stress acting upon the solid over which the fluid is flowing:

$$\tau = -\eta\dot{\gamma} \tag{1.4}$$

Here the viscosity of the fluid, η is defined as the constant of proportionality. In human arteries the velocity profile tends to be parabolic and the wall shear stress plays an important role in endothelial function [84].

1.2.3 Viscoelasticity

Linear elasticity and viscosity offer descriptions in highly idealised situations that are often not representative of reality. Viscoelasticity aims to bridge this gap between theory and reality by combining these two concepts to provide a more complete description. Materials are typically modelled in terms of springs, providing the elastic component, and dashpots, providing the viscous component. Springs and dashpots can be connected to one another in series or in parallel meaning that a range of different models exist [85].

The most significant difference between viscoelastic and linear elastic models is that the strain the material is undergoing is not simply dependent upon the instantaneous stress placed upon it but additionally upon the history of the stress placed upon it. As such viscoelastic materials have several properties not seen in linear elastic properties. Firstly if a constant stress is applied to the material the strain continues to increase. This phenomenon is termed creep. Secondly if a constant strain is maintained, the stress decreases (known as relaxation). Thirdly there is a lag between the application of stress to the material and the strain response (known as hysteresis) [86].

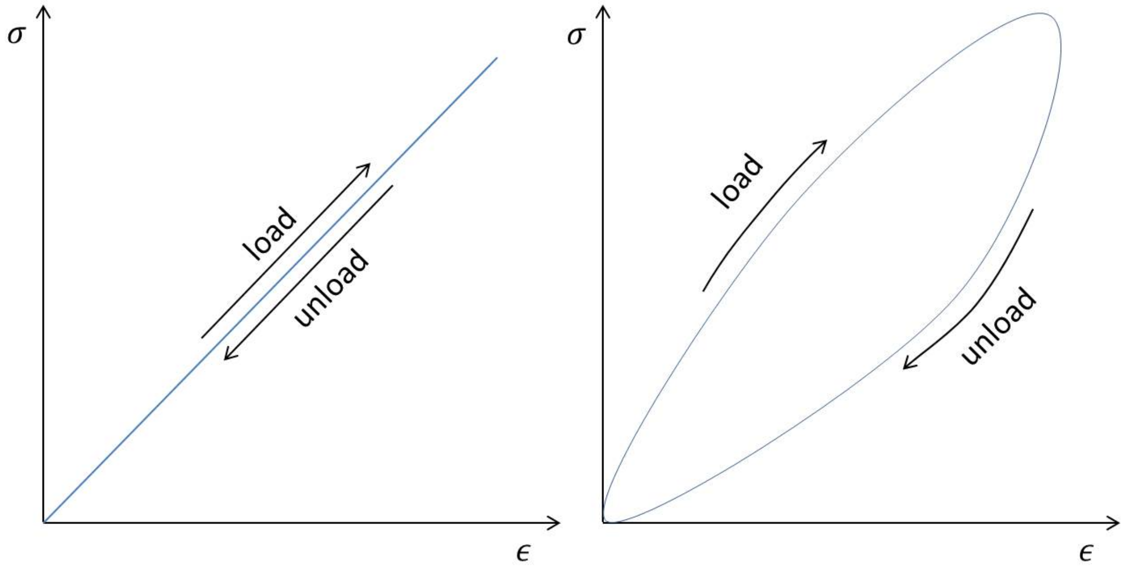

Figure 1.5: The stress-strain curves for a linear elastic material (left) and a viscoelastic material (right).

For an oscillating load this phase lag results in a dissipation of energy within the material and attenuation of the propagating wave [87] such that stress and the strain can be written as time-dependent sine functions:

$$\sigma = \sigma_0 \sin(\omega t - \delta) \tag{1.5}$$

$$\epsilon = \epsilon_0 \sin(\omega t) \tag{1.6}$$

where t is time, ω is the angular frequency, σ_0 and ϵ_0 represent the amplitudes of the strain and stress respectively, and δ is defined as the phase lag between the oscillating stress and the strain response.

Equation (1.5) can be redefined using the addition rule for trigonometric addition:

$$\sigma = \sigma_0 \left(\sin(\omega t)\cos(\delta) + \cos(\omega t)\sin(\delta)\right) \tag{1.7}$$

This implies that two new identities can be defined:

$$\sigma_0' = \sigma_0 \cos(\delta) \tag{1.8}$$

$$\sigma_0'' = \sigma_0 \sin(\delta) \tag{1.9}$$

Simple trigonometric relations therefore imply that:

$$|\sigma_0| = \left((\sigma_0')^2 + (\sigma_0'')^2\right)^{1/2} \tag{1.10}$$

$$\delta = \tan^{-1}\left(\frac{\sigma_0'}{\sigma_0''}\right) \tag{1.11}$$

The elastic element of material is the storage modulus defined as:

$$G' = \frac{\sigma_0'}{\epsilon_0} \tag{1.12}$$

whilst the viscous element of the material, known as the loss modulus is:

$$G'' = \frac{\sigma_0''}{\epsilon_0} \tag{1.13}$$

This implies that the phase lag between the stress and the strain can also be defined in terms of the storage and loss moduli:

$$\delta = \tan^{-1}\left(\frac{G'}{G''}\right) \tag{1.14}$$

From this it can be seen that there is no phase lag in an elastic material, whereas in purely viscous material the phase lag is equal to $\pi/2$ radians. As a result of equation (1.14) a new identity known as the complex shear modulus is defined where G' represents the real component and G'' represents the imaginary component:

$$G^* = G' + iG'' \tag{1.15}$$

where i is the imaginary number equal to $\sqrt{-1}$.

By inserting equations (1.8) and (1.9) into equations (1.12) and (1.13) the magnitude of the complex shear modulus is the ratio of the amplitudes of the stress to strain waves:

$$\begin{aligned} G^* &= \frac{\sigma_0}{\epsilon_0}\left(\cos(\delta) + i\sin(\delta)\right) \\ &= \frac{\sigma_0}{\epsilon_0} e^{i\delta} \\ \Rightarrow |G^*| &= \frac{\sigma_0}{\epsilon_0} \end{aligned} \tag{1.16}$$

The viscoelastic model used throughout this thesis is the Kelvin-Voigt model, a linear viscoelastic model. This consists of a spring and dashpot connected in parallel (figure 1.6). As a result of this parallel connectivity the total stress acting on the system is the sum of the stress acting in the spring and dashpot, whilst the strain must be equivalent in both. The complex shear modulus for the Kelvin-Voigt model is [88]:

$$G^* = G + i\omega\eta \tag{1.17}$$

where G is the shear modulus. Unlike other models of viscoelasticity this implies that the storage modulus is independent of the frequency of vibrations. The same is not true of the loss modulus, where high frequency waves suffer from greater attenuation than those of low frequency.

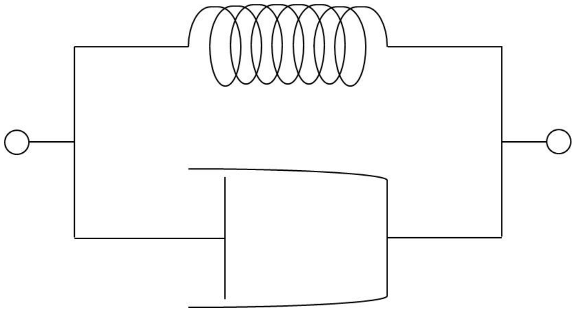

Figure 1.6: The Kelvin-Voigt model consists of a spring and dashpot in parallel.

1.3 Finite Element Analysis

Finite element analysis (FEA) is a numerical method of achieving approximate solutions to a wide variety of physical problems using partial differential equations. The technique was first developed in the 1950's and was initially used in the aerospace industry. Expansion out from this field began in the 1960's when the technique began to be utilised in civil engineering [89]. Today FEA is used in a wide range of fields such as structural, thermal and electrical analysis. The basic premise is to break down an initially complex system into a collection of simpler sub-regions such that solutions in each of these sub-regions can be calculated and thus an approximation of the overall system attained. This section of the introduction outlines the various stages of solving a problem using FEA and the basic theory behind the technique. Post-processing of FEA data is largely dependent on the problem in question and will therefore not be covered in this section.

1.3.1 Model Creation

Geometry

Once the real world problem has been identified it must be recreated *in silico*. The first stage of this is to create the geometry. This is often achieved using a computer aided design (CAD) package, or for medical purposes, via segmentation of CT or MRI scans. Approximations to the geometry are often made using symmetry relationships or by removing parts of the model far from the region of interest for simplification or to reduce computational time.

Discretisation

Once the geometry has been created the model must be discretised or meshed. This is the process by which the model is divided into sub-regions in which approximate solutions can be obtained. Each individual sub-region is known as an element and there are a variety of element types available. Points within each element at which equilibrium is satisfied are called nodes. These represent coordinate locations with typically 3 degrees of freedom for solids. Equilibrium conditions are forced upon the nodes and solutions for

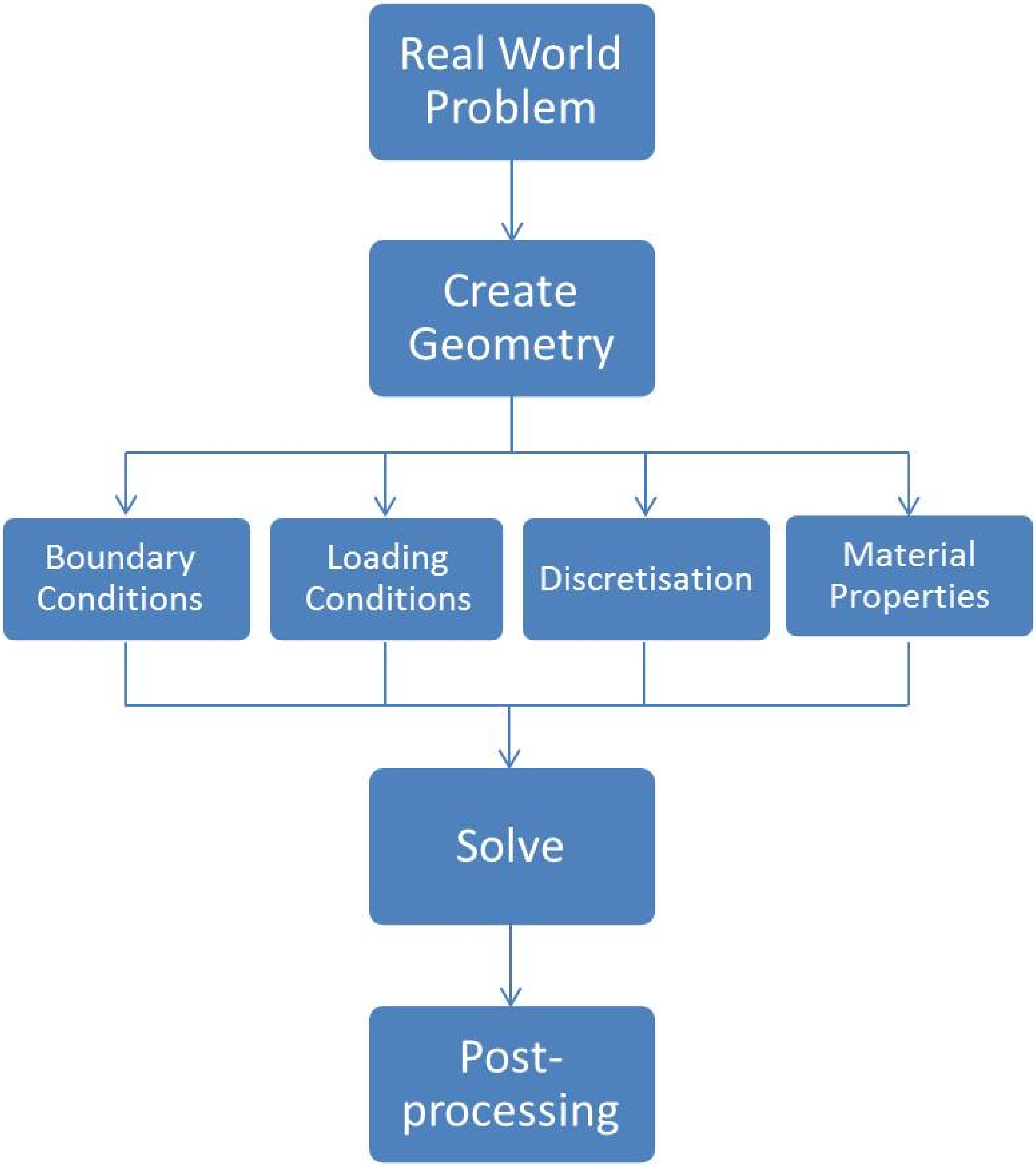

Figure 1.7: Diagram of the workflow involved in FEA

the displacements are found here. The order of an element relates to how many nodes that element has: first order elements have nodes only at the vertices whilst higher order elements have nodes typically along their edges as well.

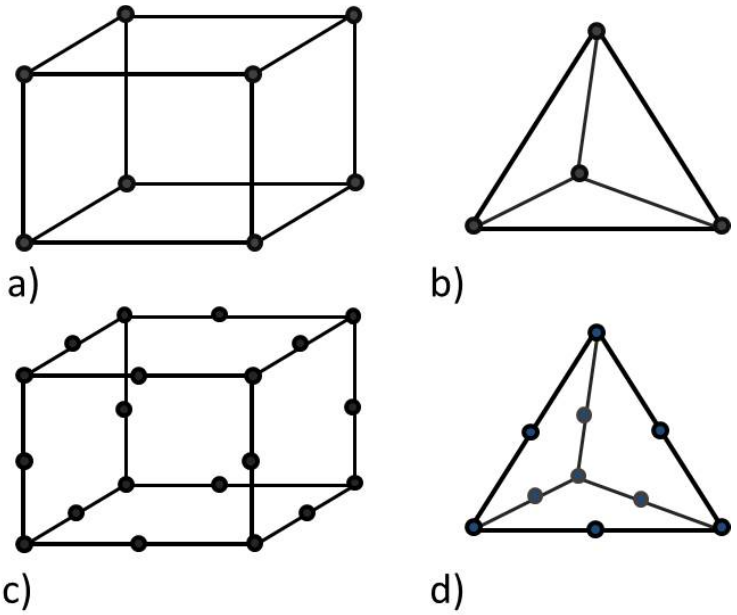

Figure 1.8: a) A first order 8-noded hexahedral element, b) a first order 4-noded tetrahedral element, c) a second order 20-noded hexahedral element, d) a second order 10-noded tetrahedral element.

Loading Conditions

The loading conditions represent the external forces that are acting upon the system being modelled. These must be identified and quantified in the real world and defined in terms of their magnitude, direction and the region over which they are to be applied in the model. Applied loads can be static or dynamic.

Boundary Conditions

Since FE simulations are performed on a confined system constraints must be placed on that system to approximate the real world environment. These are known as boundary conditions and typically define motion at one or more degrees of freedom.

Material Properties

The response of a system to a load is dependent upon the material properties of the parts within that system and as a result FEA requires the definition of such properties to perform simulations. Such definitions can vary greatly in terms of complexity from a simple linear elastic model to more complex viscoelastic, hyperelastic or viscoplastic models defined by the user. Typically these definitions are based upon results from mechanical testing performed in the laboratory.

1.3.2 FEA Theory

Aside from a relatively small number of steady-state simulations in chapter 2 the majority of the simulations performed in this thesis have been transient and as such this will be the focus of the theory in this section. There are two approaches to solving transient simulations; implicit and explicit. This thesis has used the explicit approach, which is common in problems concerned with wave propagation and is advantageous because it does not require inversion of the stiffness matrix at each iteration, thus making it less computationally expensive and more time efficient than the implicit approach [90].

Explicit Approach

The explicit approach in *Abaqus* is based around approximation of the displacement, $\mathbf{u}$, and its first, $\dot{\mathbf{u}}$, and second, $\ddot{\mathbf{u}}$, temporal derivatives at each time increment. Using the central difference integration rule, the displacement at time step $i+1$ is [90]:

$$\mathbf{u}^{(i+1)} = \mathbf{u}^{(i)} + \Delta t^{(i+1)} \cdot \dot{\mathbf{u}}^{(i+1/2)} \tag{1.18}$$

where Δt is the size of the time increment, whilst the mid-increment first derivative of the displacement is given by:

$$\dot{\mathbf{u}}^{(i+1/2)} = \dot{\mathbf{u}}^{(i-1/2)} + \frac{\Delta t^{(i+1)} + \Delta t^{(i)})}{2} \cdot \ddot{\mathbf{u}}^{(i)} \tag{1.19}$$

To begin the simulation this implies that $\dot{\mathbf{u}}^{(-1/2)}$, the derivative of the displacement at $t = 0$, must be calculated. Assuming the second derivative of the displacement remains constant from $t = 0$ to the first increment, then from the equations of motion for constant acceleration:

$$\dot{\mathbf{u}}^{(1/2)} = \dot{\mathbf{u}}^{(0)} + \frac{\Delta t^{(1)} + \Delta t^{(0)}}{2} \cdot \ddot{\mathbf{u}}^{(0)} \tag{1.20}$$

Inserting this into equation (1.19) and rearranging gives:

$$\dot{\mathbf{u}}^{(-1/2)} = \dot{\mathbf{u}}^{(0)} - \frac{\Delta t^{(0)}}{2} \cdot \ddot{\mathbf{u}}^{(0)} \tag{1.21}$$

where $\dot{\mathbf{u}}^{(0)}$ and $\ddot{\mathbf{u}}^{(0)}$ are the initial velocities and accelerations placed on the system by the user through boundary and loading conditions.

Calculation of $\dot{\mathbf{u}}^{(i+1/2)}$ in equation (1.19) requires knowledge of $\ddot{\mathbf{u}}^{(i)}$. To this end the equation of motion for a system with multiple degrees of freedom is [91]:

$$\mathbf{M}\ddot{\mathbf{u}} + \mathbf{C}\dot{\mathbf{u}} + \mathbf{K}\mathbf{u} = \mathbf{F}_{ext} \tag{1.22}$$

Here $\mathbf{C}$ and $\mathbf{K}$ are the damping and stiffness matrices; $\mathbf{F}_{ext}$ is the vector corresponding to the external loads acting upon the system; and $\mathbf{M}$ is the mass matrix. The explicit approach in *Abaqus* assumes that the mass matrix is lumped and thus a diagonal matrix of the constituent masses of the system:

$$\mathbf{M} = \begin{pmatrix} m_1 & 0 & \dots & 0 \\ 0 & m_2 & \dots & 0 \\ \vdots & \vdots & \ddots & \vdots \\ 0 & 0 & \dots & m_n \end{pmatrix} \tag{1.23}$$

In equation (1.22), $\mathbf{M}\ddot{\mathbf{u}}$ represents Newton's 2$^{\text{nd}}$ law corresponding to the inertial forces, $\mathbf{F}$ [92]:

$$\mathbf{F} = \mathbf{M}\ddot{\mathbf{u}} \tag{1.24}$$

whilst the other terms on the left hand side represent the internal forces, $\mathbf{F}_{int}$, consisting of the damping forces, $\mathbf{F}_{damp}$, and the elastic forces, $\mathbf{F}_{elas}$ [92]:

$$\mathbf{F}_{int} = \mathbf{F}_{damp} + \mathbf{F}_{elas} = \mathbf{C}\dot{\mathbf{u}} + \mathbf{K}\mathbf{u} \tag{1.25}$$

From equations (1.22) and (1.24) this implies that [93]:

$$\mathbf{F}_{ext} - \mathbf{F}_{int} = \mathbf{F} = \mathbf{M}\ddot{\mathbf{u}} \tag{1.26}$$

Thus for each increment, i [90]:

$$\ddot{\mathbf{u}}^{(i)} = \mathbf{M}^{-1} \cdot (\mathbf{F}_{ext}^{(i)} - \mathbf{F}_{int}^{(i)}) \tag{1.27}$$

Substituting this into equation (1.19) gives:

$$\dot{\mathbf{u}}^{(i+1/2)} = \dot{\mathbf{u}}^{(i-1/2)} + \frac{\Delta t^{(i+1)} + \Delta t^{(i)})}{2} \cdot \mathbf{M}^{-1} \cdot (\mathbf{F}_{ext}^{(i)} - \mathbf{F}_{int}^{(i)}) \tag{1.28}$$

Inversion of the lumped mass matrix is straightforward and the system of partial differential equations decouples such that it can be solved independently for each degree of freedom [94]. The process is then repeated for each subsequent time increment using the information obtained in the previous increment [95].

1.4 Patient Specific Modelling

Although the anatomy of most humans comprises of the same organs, the size and structure of these organs vary dramatically. Additionally processes within the human anatomy such as cognitive processing or the immune system's response to disease are hugely variable. Whilst such variations can be seen to have some dependence on such things as age or gender there is still a large amount of variability within each of these sub-groups to the extent that differences even exist between identical twins who share the same genetic structure. This implies that individual response to disease states are highly dependent on that individual. In contrast treatments are typically based on average measurements made across a wide range of patients in clinical trials.

Patient specific modelling (PSM) aims to address this by using individual patient data to create computational models of a specific disease state in order to make calculations that aid in diagnosis, prognosis or the planning of clinical treatment or surgical intervention. The technique utilises numerical methods such as FEA, CFD or fluid structure interaction (FSI) modelling, a combination of FEA and CFD, to achieve these aims.

Initially developed throughout the 1990's, research into PSM now covers a range of anatomical structures. These studies have investigated such scenarios as bones such as the femur to research the effectiveness of osteoporosis treatment [96] and fracture risk [97]; blood flow in the coronary arteries to aid in the fitting of medical devices [98]; and respiratory motion in treatment of lung cancer [99]. Of particular note in the field is the Virtual Physiological Human (VPH) Institute for Integrative Biomedical Research. The VPH aims to use computational simulations to model physical systems and processes with the ultimate goal of creating an *in silico* human body. The project is funded by the European Commission and currently consists of over 20 institutions across Europe [100].

1.4.1 PSM of AAAs

PSM represents a potential replacement for the diameter criterion in predicting the risk of AAA rupture. Segmentation software is used to reconstruct the geometry of the AAA from either CT or magnetic resonance imaging (MRI) images which is then exported in the FEA software. Here an internal pressure is placed upon the modelled AAA and the peak stress acting on the vessel wall is calculated (figure 1.9). It is this stress, or often an index based upon this stress and other critical values [101], that is typically used as the predictor of AAA rupture since in engineering terms, rupture will occur when the stress exceeds the failure strength of the vessel wall [102].

Relative success has been achieved through this method and has typically shown that the stress placed upon the wall had a large dependency upon the geometry of the AAA [103–105]. Of particular note in this regard, Fillinger et al. (2003) used receiver operating characteristic (ROC) curves to show that peak wall stresses calculated with FEA using geometries obtained from CT scans are more effective predictors of rupture than the diameter of the AAA [106].

Despite these successes, PSM of AAAs is currently not in clinical practice. The next section aims to explain the reasons behind this, outlining the current limitations of PSM with regard to AAA and where applicable, describe the steps that are being taken to address these shortfalls.

1.4.2 Limitations in PSM of AAAs Resulting from FEA

Currently PSM in general suffers from limitations with regard to the time that simulations take to perform and the expertise required by the individual carrying out the simulations. Whilst these issues must be addressed before the technique can become widely accessible, it should also be recognised that technical insufficiencies with respect to FEA also place

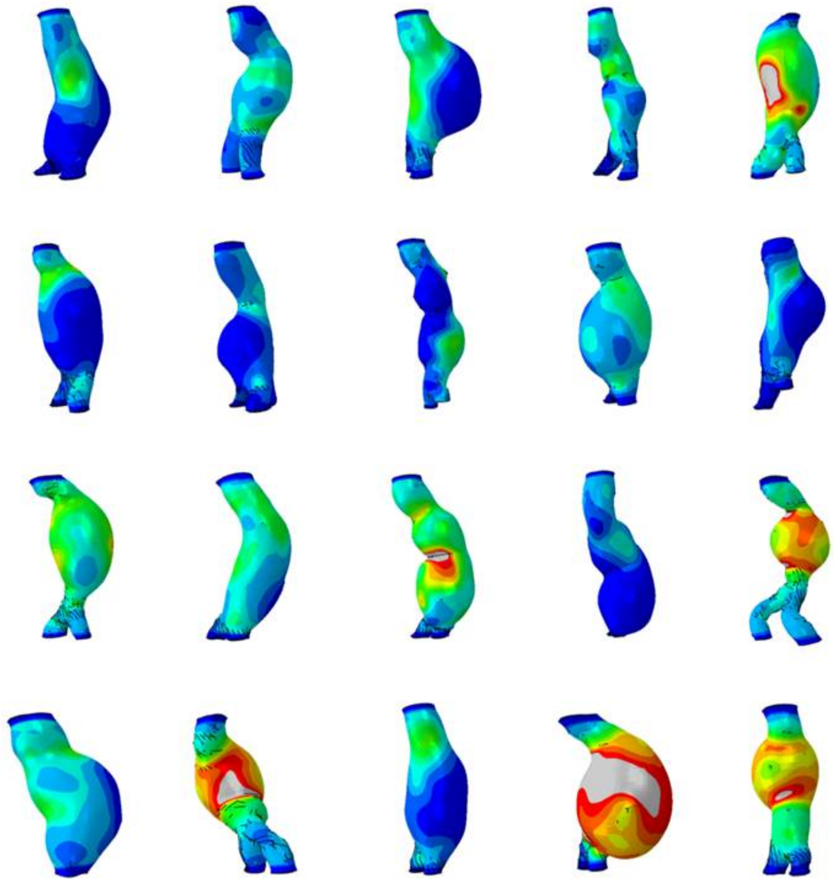

Figure 1.9: Patient specific models of AAAs. Blue indicates regions of low stress, whilst red indicates regions of high stress. The variation in geometry of these AAAs and the stresses acting on the wall can be clearly seen here. Image author: Noel Conlisk (unpublished)

limitations upon PSM in AAA. If methods could be developed to address these limitations PSM's ability to predict the risk of rupture would be further improved.

Boundary Conditions

Despite boundary conditions being investigated extensively in other similar fields [107] there is little research upon this in the field of AAAs. Whilst Gasbarro et al. (2007) [108] defined interactions between the AAA and surrounding tissue, the vast majority of AAA research is performed with fixed displacement boundary conditions only applied at the vessel ends.

Pre-Stress

AAAs are subjected to long-term strains and stresses which contrasts greatly to the PSM approach which neglects this. According to Gee et al. (2009) this causes an overestimation of deformation and stresses in PSM [109]. Despite this, the majority of research continues to neglect pre-stressing largely because characterising it is a complex process, whilst its inclusion would also result in longer simulation times.

Exclusion of FSI

In order to remove complexity from the modelling thus making the process less computationally expensive and more time efficient fluids are typically not included in the model. Several studies have justified this by showing that FSI has little effect on the peak wall stress. Leung et al. (2006) showed that inclusion of FSI in PSM simulations resulted in a difference in peak stress of less than 1% in comparison to FEA [110]. This was supported by Fraser et al. (2009) who showed that whilst fluid interaction played an important role in the development of AAA, it had little effect on the peak wall stress [111].

Exclusion of Calcium Deposits

Calcification of both the mural layer and thrombus has been associated with AAAs for some time [112]. The exact role of these deposits in the prognosis of AAAs is unclear, largely because there is relatively little research in the field. As a result studies using PSM have rarely included them in their analysis. Despite this however, several studies have typically shown that the influence of calcification is to increase the peak wall stress placed on the AAA wall to as much as three times that of the value when the calcifications are not taken into account [113–116].

Vessel Wall Thickness

PSM studies have typically assumed the thickness of the vessel wall to remain constant throughout the entirety of the aneurysm and from one subject to another. This results from the inability of CT scans to accurately dissociate the vessel wall from the thrombus [117]. Whilst MRI scans can dissociate these tissues, they are also liable to suffer from motion artefacts as a result of the relatively lengthy imaging time and the position of the AAA [118, 119].

This assumption is however inaccurate. Raghavan et al.(2006) [120] showed relatively large variations in vessel wall thickness between both subjects, and at different regions within individual aneurysms. Additionally they showed that typically rupture occurred at points where the wall was thin. This is in agreement with a study by Venkatasubramaniam et al. (2004) [104] who showed via finite element analysis that the strength of the vessel wall is inversely proportional to its thickness.

Recent publications have begun to address this issue. Martufi et al. (2009) developed a methodology of estimating the wall thickness based upon variations in the texture of the CT image used for segmentation [121]. Whilst this work has not been replicated elsewhere, similar methodologies have been adopted by other groups [122].

Exclusion of ILT

Intraluminal thrombus (ILT) is extremely common in AAAs existing in over 90% of patients with an AAA greater than 5 cm and that the volume of ILT is typically larger for ruptured than non-ruptured AAAs [53]. Despite this, ILT has often not been included in PSM studies of AAA's. This occurs largely because of the previously mentioned inability of CT scans to differentiate between the vessel wall and the ILT [117].

The function of the ILT in AAAs is the subject of debate. The vast majority of research has suggested that it provides a cushioning effect for the vessel wall, reducing the peak wall stress placed upon it [44, 116, 117, 123, 124]. Further complexity is added however with the hypothesis that the presence of thrombus gives rise to hypoxia in the aneurysm wall which leads to a breakdown in the extracellular matrix reducing the strength of the vessel wall [125, 126]. Additionally it has been shown that the existence of ILT causes changes in the blood flow patterns through the AAA, thus resulting in changes in the stresses placed on the wall [123]. In some instances the ILT can fissure or crack which also results in a redistribution of stress in the wall. To this end Polzer et al. (2011) [127] demonstrated that large cracks and cracks that come into contact with the wall increase the risk of AAA rupture.

As the significance of ILT upon AAAs has become increasingly evident, fewer studies are failing to include the ILT in their simulations.

Material Properties

The application of material properties is a general weakness for PSM. Whilst the premise of PSM is to treat the patient as an individual, measurement of properties is extremely difficult *in vivo*. As such the majority of studies use properties measured from *ex vivo* mechanical testing of samples and thus are not patient specific in this respect.

With regard to AAAs, the vast majority of studies base their material properties for the vessel wall on measurements made by Raghavan and Vorp in 2000 [128], whilst material properties for the ILT are based on measurements made by Wang et al. in 2002 [129]. It has however been shown that throughout AAA development, inflammatory responses in the AAA wall cause it to weaken [125, 130] . This would imply that the risk of rupture in more developed AAAs, which are generally larger, would be increased in comparison to smaller less developed AAAs.

Several other studies have directly investigated the impact of material property variations in stresses calculated on the vessel wall. In 1997 Mower et al. [131] utilised highly idealised symmetrical AAAs to show a strong dependence of stress on both the material properties of the AAA wall and the ILT. More recently Doyle et al. (2012) [132] measured material properties from a ruptured AAA using mechanical testing and performed PSM on that patient's AAA using CT data acquired shortly before rupture occurred. Comparing these results against those acquired using the standard non-specific properties, Doyle showed increases of 67% in wall stress and 320% in wall strain for the patient specific material properties.

In 2006 Vande Geeste et al. attempted to address this issue by introducing the Rupture Potential Index (RPI) [133]. This hypothesised that wall strength was dependent on parameters such as age, gender and smoking. As such they coupled these parameters alongside the peak wall stress to create a new index to predict rupture. Whilst this technique has been shown to be relatively successful [134], it still fails to make a direct measurement of wall strength and does not take into account the material properties of the ILT.

1.4.3 Summary

FEA is often a balancing act between achieving high accuracy and expense in relation to computational time and efficiency. In this regard it is likely that the development of technology will allow more complex and accurate models of AAAs that address many of the issues described here. This will not however account for the lack of specificity in material properties. In order for this to be achieved, a method of measuring such properties *in vivo* must be developed.

1.5 Magnetic Resonance Elastography

This section introduces magnetic resonance elastography (MRE), an MRI-based technique that utilises shear wave propagation to measure mechanical properties of tissue *in vivo*. This section will provide a brief introduction to MRI before discussing the theory, applications and development of MRE.

1.5.1 Magnetic Resonance Imaging

MRI was initially proposed as an imaging technique in the early 1970's [135] with the first scan taking place in 1980 at the University of Aberdeen [136]. It was not until the 1990's that the presence of MRI scanners in hospitals became commonplace across the UK. MRI offers good contrast to soft tissue whilst not exposing the patient to any form of radiation. Whilst in the clinic it is typically used to examine anatomical structure, the nature of MRI acquisition allows a wide range of applications such as functional MRI, that detects brain activity; diffusion MRI, that maps diffusion processes of molecules; and, of particular relevance to this thesis, MRE. The following describes the fundamental concepts behind MRI and the acquisition process [137–139].

Nuclear Magnetic Resonance

In the classical description of MRI a uniform magnetic field is applied in the z-direction (figure 1.10) across the sample, thus aligning the spins and causing the average magnetic moment to also be in the z-direction. An electromagnetic field is then applied perpendicular to the direction of the original magnetic field. This is chosen at a precise frequency so as to excite the nuclei to a higher energy state. Again in a classical sense the net magnetisation is flipped such that is now perpendicular to the magnetic field. This frequency is dependent upon the gyromagnetic ratio of the nuclei in question and the magnetic field that has been applied, such that to excite a nuclei with a gyromagnetic ratio of γ in a magnetic field strength B, an angular frequency of:

$$\omega = -\gamma \cdot B \tag{1.29}$$

is required. This is known as the larmor frequency. This equation can also be utilised in order to achieve slice selection for the image in question. By applying a second magnetic field in the same direction as the original field, but on this occasion giving it a gradient rather than making it uniform, the larmor frequency of the nuclei in the sample is given spatial dependence along the axis of the magnetic fields. To this end, by using a single frequency or small ranges of frequencies a slice of the sample can be imaged.

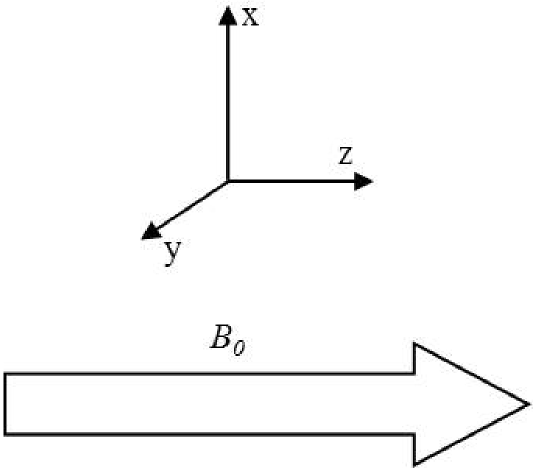

Figure 1.10: Coordinate system and direction of magnetic field in MRI.

Phase and Frequency Encoding

In order that the NMR signal is dependent upon its x- and y- coordinates, phase and frequency encoding gradients are employed. The frequency gradient is a static magnetic field that is applied in the y-direction with the purpose of enhancing the larmor frequency at each x-coordinate. As such the frequency at which spins precess becomes dependent on

x-coordinate. The next stage is to apply a phase encoding gradient. This is a short burst that modifies the spins precession so that its frequency remains the same but its phase is shifted. The signal is again applied in such a way that the phase shift is dependent upon the y-coordinate.

T_1, T_2 and T_2* Decay

Following excitation the nuclear spins return to their equilibrium. It is variations in this process that can be used to characterise different tissues. There are however several different elements in this relaxation process that can be observed.

The first of these is T_1 relaxation which observes the magnetisation of the sample returning to thermal equilibrium with its surroundings. The T_2 signal meanwhile, represents the exponential decay of the transverse component of the magnetisation in the xy-plane.

Following the application of the electromagnetic field, the magnetic moments precess around the x-axis initially at the same frequency as the larmor frequency. Local inhomogeneities in the magnetic field of the sample however, cause a dephasing of the spins, such that signal (loss of phase) decays very quickly. The dephasing of the spins as a result of these local inhomogeneities is known as T_2* relaxation. In order to remove this effect, a spin echo sequence can be applied. This is achieved by a second pulse that flips the angle of the magnetic moments by 180°. This causes rephasing to take place: the slower spins are now placed ahead of the faster spins which therefore catch up. When this occurs, an echo signal is produced. This is then followed by another rapid dephasing. The time between the echo signal and the initial electromagnetic pulse is twice the time between that pulse and the second pulse. The intensity of the second signal is however lower than the first signal. This is because of the dephasing due to T_2 effects and therefore the T_2 signal can be calculated by assuming exponential decay, thus the T_2* local inhomogeneities of the magnetic field have been removed.

In contrast an efficient method of obtaining T_2* weighted images is to use a gradient echo sequence. Again a radiofrequency is applied across the sample though in this case, it is usually at an angle between 20-80° rather than at right angles. Immediately following the radiofrequency a negative gradient for frequency encoding is applied. After a short period, this gradient is replaced by a positive gradient. As a result rephasing occurs, similar to the rephasing in spin echo: those spins precessing at a higher frequency will now fall behind those which were precessing at a lower frequency and will therefore catch up. This creates an echo. On this occasion the rephasing does not take account of the inhomogeneities in the main magnetic field or the spin-spin relaxation, but the dephasing that is caused by the negative gradient. As such the decay is dependent upon local field inhomogeneties: the T_2* signal. Because the angle of the initial radiofrequency is lower and because of the speed of the decay of the T_2* signal compared to the T_2 signal, the acquisition time for gradient echo is less than that of spin echo.

K-Space

The signal received by the coils is translated to data and exists in k-space. Each point in k-space contains information regarding all points in Euclidean space. Each line in the y-direction represents phase whilst those in the x-direction represent frequency. Points proximal to the origin in k-space provide contrast, whilst those further out provide detail. As such removing either greatly detracts from the quality of the image. In order to obtain a meaningful image from the data in k-space a Fourier transform is performed. This transformation breaks a signal down into the sum of its component simple waves of various single frequencies. The phase and frequency of these waves allow the spatial mapping of the signal because the signal was encoded through these, whilst the amplitude of the signal gives the intensity of the signal at each point.

1.5.2 MRE Theory

MRE was first developed by Muthupillai et al. (1995) using a phase-contrast MR sequence in order to visualise propagating shear waves induced into the tissue by an external driver [140,141]. In phase-contrast a bipolar gradient pulse is used to quantify velocity by applying successive gradients of equal magnitude in opposing directions. This implies that stationary nuclei will undergo no change in phase, but since nuclei in motion are moving through a gradient field, these will experience a resulting change in phase [142]. The net phase shift, Φ is related to the position of the spin, $\mathbf{r}(t)$, via:

$$\Phi = \gamma \int_0^{\tau} \mathbf{G}_r(t) \cdot \mathbf{r}(t)\ dt \tag{1.30}$$

where $\mathbf{G}_r(t)$ is the time-dependent magnetic field acting over a duration τ.

Assuming that the spin is travelling at a constant velocity, $\mathbf{v}(t)$ the displacement is related to its initial position, $\mathbf{r}_0$:

$$\mathbf{r}(t) = \mathbf{r}_0 + \mathbf{v}(t) \tag{1.31}$$

Using the summation rule of integration, this implies that the phase shift in equation (1.30) can be rewritten as [143]:

$$\Phi = \gamma \int_0^\tau \mathbf{G}_r(t) \cdot \mathbf{r}_0 \; dt + \gamma \int_0^\tau \mathbf{G}_r(t) \cdot \mathbf{v}(t) \; dt \tag{1.32}$$

Here the first integral relates to the phase shift of stationary spins, whilst the second integral relates to the phase shift of moving spins. In phase encoding, since two gradients are applied in opposite directions with equal magnitudes, this implies that the first integral is equal to zero.

In MRE a harmonic load is applied to the system meaning that the position of the spin can be described as a complex displacement, $\boldsymbol{\xi}$, around the mean position:

$$\boldsymbol{\xi}(\mathbf{r}, t) = \xi_0 \cdot \cos(k_r \mathbf{r} - \omega t + \theta) \tag{1.33}$$

where ξ_0 is the amplitude of the induced vibration and k_r is the wavenumber.

As such equation (1.32) can be written as:

$$\Phi = \gamma \int_0^\tau \xi_0 \cdot \mathbf{G}_r(t) \cdot \cos(k_r \mathbf{r} - \omega t + \theta) \; dt \tag{1.34}$$

The frequency with which the direction of the magnetic field $\mathbf{G}_r(t)$ is switched between positive and negative is matched to the frequency of the induced vibrations. This implies that integrating this function which respect to time will equal 0 assuming an integer number of cycles, $N \in \mathbf{N}$. This in turn places the upper limit over which the integral is to be performed as NT where T is the period of the induced frequency. Utilising this information and since $\omega = 2\pi/T$ the phase shift becomes:

$$\phi = \frac{\gamma N T (\mathbf{G}_0 \cdot \xi_0)}{2} \cdot \cos(k_r \mathbf{r} + \theta) \tag{1.35}$$

where $\mathbf{G}_0$ is the amplitude of the oscillating magnetic field.

This means that the phase shift from an externally induced harmonic oscillation can be determined. This information provides the foundation for MRE. There is however a dilemma here: high frequency waves provide greater resolution in MRE yet typically suffer from a large degree of attenuation in human tissue. As a result it would be beneficial to increase the amplitude of the wave in order to increase the depth of penetration. However large displacements are subject to 'phase wraps', where the phase of the wave shifts by a phase greater than 2π producing an artefact in the phase data. Phase unwrapping algorithms have been developed that remove this artefact but these remain ineffective if wrapping is too strong [144, 145]. This typically limits MRE in humans to frequencies lower than 200 Hz.

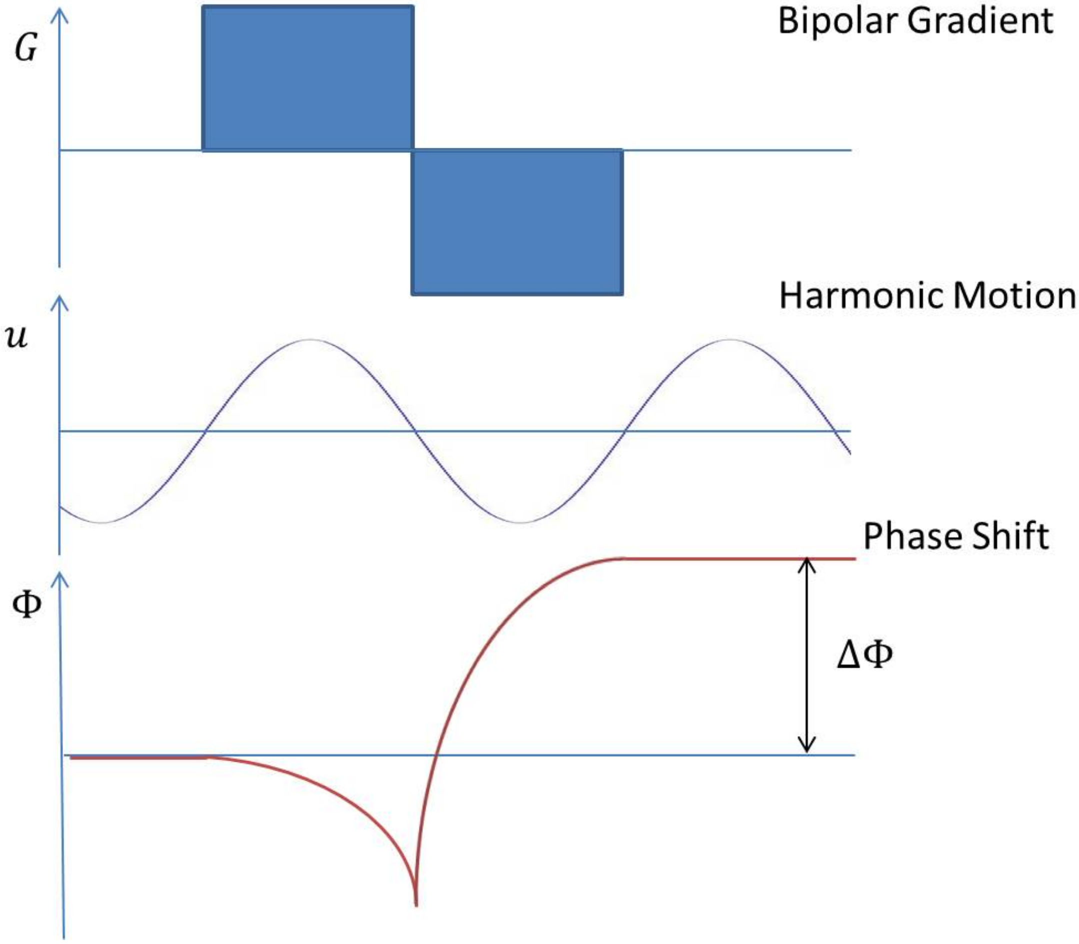

Figure 1.11: Diagram to show how the bipolar gradient is synchronised to the induced vibrations and the resulting phase shift from a moving spin in the system.

1.5.3 Inversion

The true goal of MRE is to convert MR acquired phase shifts resulting from an external harmonic driver into measurements of the material properties of the tissue through which the wave is propagating. Since these phase shifts are dependent on the material properties this is an inverse problem, and as such solutions are achieved through the use of an inversion algorithm. The resulting map of material properties created via inversion is known as an elastogram. It should be noted that in the previous section, the MR sequence utilised obtained the phase shift resulting from a harmonic vibration. Throughout this section inversion will largely be discussed as calculating material properties from displacements caused by the harmonic motion [146]. It is therefore important to stress that the displacements are directly proportional to the phase shifts and as such the input for the equations discussed is interchangeable between the two.

There are several different methods of performing inversion used in MRE. The least common of these is forward inversion [147]. This utilises FEA to iterate material properties until wave propagation in the model matches that seen in the real system. Whilst these offer good spatial resolution the iterative FEA process is time consuming, particularly for more complex geometries. Additionally a full 3-D dataset is required for accurate measurements [148].

A second method of inversion is known as the local frequency estimator (LFE). This was first introduced by Knutsson et al. (1994) [149] as a method of estimating the frequencies and bandwidth of local signals and was adapted for MRE by Manduca et al. (1996) [150]. The algorithm uses lognormal quadrature wavelet filters to sample the wave image at a range of frequencies in order to obtain an estimate for the local wavelength. Calculation of the shear modulus, G, is then based upon:

$$G = \rho f^2 \lambda^2 \tag{1.36}$$

where ρ is the density of the medium, f is the frequency of the induced waves and λ is the wavelength. This equation assumes that the material is locally homogeneous and incompressible [151]. Additionally the density of human tissue is assumed to be constant with a typical value of approximately 1000 kg·m^{-3} used for the majority of anatomical structures. Whilst the LFE algorithm performs relatively well in the presence of noise it has poor spatial resolution [152]. It should also be noted that the value calculated using the LFE is the shear modulus, not the complex shear modulus: the LFE makes the assumption of pure elasticity of the material.

The third common method of inversion is the direct inversion (DI). This is the method that has been used throughout this thesis and will therefore be discussed in more detail here. DI can be derived from the equations of motion. To begin with, recall equation 1.2, the relationship between the stress acting upon a material and the resultant strain is dependent upon the complex stiffness tensor:

$$\sigma_{ij} = C_{ijkl}\epsilon_{kl} \tag{1.2}$$

For DI, the material is assumed to be isotropic and as a result the number of independent variables reduces to two, known as the Lamé parameters, Λ, the first Lamé parameter and G^*, the shear modulus. These are complex variables with real components representing the elastic properties of the material and complex components representing the attenuation properties. This implies that our analysis is undertaken in the frequency domain using complex displacements: the real and imaginary components correspond to the amplitude and phase respectively. Assuming these conditions then the relationship between the stress and the strain becomes [153]:

$$\sigma_{ij} = 2G^*\epsilon_{ij} + \Lambda\delta_{ij}\epsilon_{kk} \tag{1.37}$$

where δ_{ij} is the Kronecker delta function which is equal to 1 if $i = j$ and 0 otherwise.

Redefining the strain tensor in terms of displacements, where the comma represents the first derivative:

$$\epsilon_{ij} = \frac{1}{2}(u_{i,j} + u_{j,i}) \tag{1.38}$$

then equation (1.2) can be rewritten:

$$\sigma_{ij} = G^*(u_{i,j} + u_{j,i}) + \Lambda\delta_{ij}u_{k,k} \tag{1.39}$$

In an isotropic linearly elastic material undergoing harmonic motion, the equation of motion is [154]:

$$\sigma_{ij,j} + f_i = -\rho\omega^2 u_i \tag{1.40}$$

where f_i equates to the body forces acting on the system. This implies that:

$$[G^*(u_{i,j} + u_{j,i}) + \Lambda\delta_{ij}u_{k,k}]_{,j} + f_i = -\rho\omega^2 u_i \tag{1.41}$$

Assuming that the density of the material remains constant under small deformations, this implies that the term relating to the body forces can be neglected [155]. Additionally by considering the i, j and k values that return non-zero values for the Kronecker delta function, equation (1.41) can be rewritten:

$$[G^*(u_{i,j} + u_{j,i})]_{,j} + [\Lambda u_{j,j}]_{,i} = -\rho\omega^2 u_i \tag{1.42}$$

In soft tissue and at the frequency range used in MRE the longitudinal wavelength is typically orders of magnitude larger than the shear wavelength. As such the spatial derivatives of the compressional wave are typically treated as negligible in comparison to the spatial derivatives of the shear wave. Since Λ is associated with bulk motion, this implies that the term $\Lambda u_{j,j}$ can be neglected. Additionally the majority of human tissue is incompressible meaning that the $u_{j,j}$ term can also be neglected [153]. Resultantly this allows inversion using a direct solution to the Helmholtz equation:

$$G^* = -\rho\omega^2 \frac{u_i}{u_{i,jj}} \tag{1.43}$$

where $u_{i,jj}$ is the Laplace operator and more commonly presented as $\nabla^2\ \mathbf{u}$.

In order for the derivation of this algorithm to have been performed, a number of assumptions were made. Whilst these have been stated at each stage of the derivation where applicable, their importance to the thesis is such that for clarification purposes they should be outlined more explicitly. Therefore, the medium through which the wave is propagating should be:

- linearly elastic
- isotropic

- infinite
- uniform density
- incompressible

Clearly it is impossible for an *in vivo* medium to correspond exactly to these assumptions, though in local regions away from tissue boundaries, approximations to such assumptions can be made [153,156]. Whilst the assumption of planar wave propagation is not explicitly made in the derivation of this algorithm, it should be noted that any wave propagating through such a medium, where the load is not considered to be applied within the medium, would comply with planarity. As such, wave planarity will be treated as an assumption from this point onwards.

Importantly for the purposes of this thesis, equation (1.43) decouples the shear waves into the component directions such that [152]:

$$G^* = -\rho\omega^2 \left(\frac{u_1}{u_{1,jj}} + \frac{u_2}{u_{2,jj}} + \frac{u_3}{u_{3,jj}} \right) \tag{1.44}$$

where the indices 1, 2, and 3 represent the spatial directions x, y and z respectively. Helpfully for MRE, where collecting information across multiple slices and in all three encoding directions is temporally expensive, this implies that inversion, even for a 3-D body, can be performed in 2-D:

$$G^* = -\rho\omega^2 \frac{u_1}{u_{1,11} + u_{1,22}} \tag{1.45}$$

Caution should be noted here, however, since inversion is based on an incomplete wavefield and accuracy of the measurement will suffer as a result. Though application of the 2-D inversion algorithm is common throughout the literature to achieve an approximate measurement, it is only in the purely theoretical circumstance where the wavefield has no dependence upon y and z, essentially a planar shear wave propagating in the yz-plane, that 2-D inversion achieves the same degree of accuracy as the 3-D inversion (though the 3-D inversion remains subject to the assumptions outlined previously). Indeed, this theoretical idea can be extended: aligning the direction of wave propagation along an axis, the problem can be thought of in 1-D alone such that:

$$G^* = -\rho\omega^2 \frac{u_1}{u_{1,11}} \tag{1.46}$$

In this instance, and recognising that the shear modulus for an elastic solid is given by [157]:

$$G = \frac{1}{4\pi^2}\rho\omega^2\lambda^2 \tag{1.47}$$

Comparing equations (1.46) and (1.47), it can be seen that the displacement term in the DI algorithm, with regards to the storage modulus at least, essentially equates to a local calculation of the wavelength of the shear wave at that point (figure 1.12). As mentioned previously, such analysis in 1 or 2-D can be utilised to approximate the shear modulus, particularly where the wave in that plane appears planar, or it can be used as a simplistic method to test algorithm ability [157, 158]. Both such methods have been utilised in this thesis.

Whereas the LFE is relatively robust to noise but suffers from poor spatial resolution, the opposite is true of DI. The Laplacian, often used in image processing as an edge detection tool, is extremely noise sensitive, however, it is also able to detect subtle changes in wavelength very effectively providing it with good resolution [159]. In order to remove noise, filters are often applied to the complex wave image. The most commonly applied are band-pass filters [153] which remove frequencies above and below certain thresholds. This however requires user expectations upon the range of shear moduli and is therefore subject to error in extreme cases. Recent work by Barnhill et al. (2013) [158] aims to address this by applying a range of convolution kernels in order to calculate the Laplacian and taking the geometric median of these.

Whilst DI allows calculation of both the real and imaginary components of the complex shear modulus this thesis has typically focused on the real part relating to the elastic properties for several reasons:

- Whilst viscoelastic parameters have often been investigated using MRE there has been little validation of the capabilities of the technique to achieve accurate measurements of these properties.
- Characterisation of viscoelastic parameters requires scans at multiple frequencies.

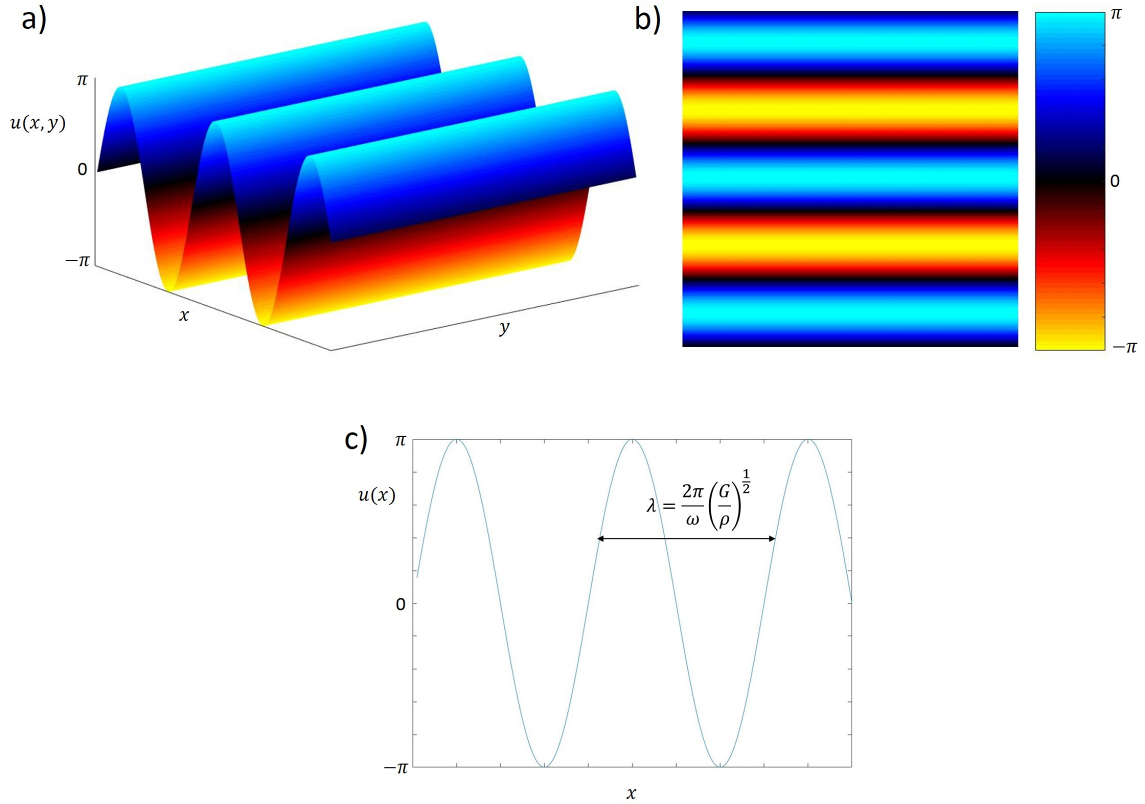

Figure 1.12: An idealised shear wave for inversion in 1 or 2-D. a) 3-D surface plot of the complex wave. b) A 2-D plot of the wave corresponding to the 3-D surface plot in a). Complex wave images will be presented in this format throughout the thesis. c) A representation of the 1-D problem corresponding to a). The wavelength can be related to the shear modulus if the input frequency is known and the density of the medium is assumed constant.

This project aimed to develop MRE with a view to investigating AAA's. From the outset of the project it was perceived that scanning at multiple frequencies would be impractical because of the length of time the patient would be in the scanner.

- The loss modulus is typically an order of magnitude lower than the storage modulus. This implies that numerical errors and the effects of modelling parameters such as boundary conditions would be greatly increased in measurements of the loss modulus. As such accurate modelling of the viscous properties would likely involve more complex models taking more time to run.

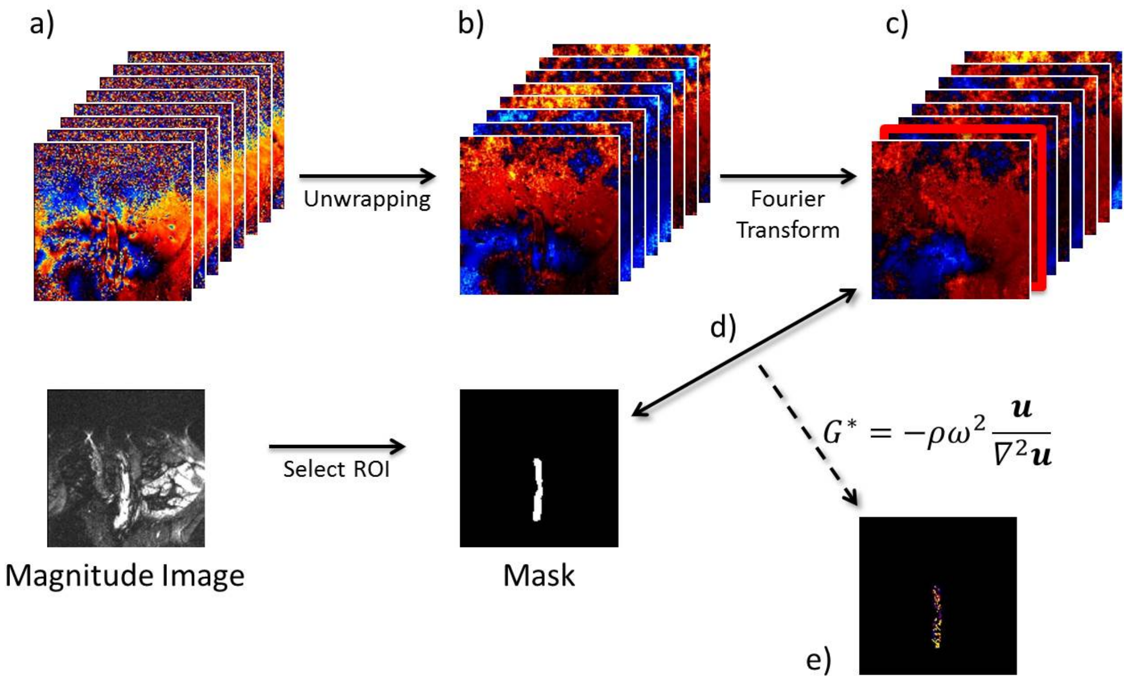

Figure 1.13: Typical protocol for analysing MRE data. The example seen here is for a healthy aorta. (a) Phase and magnitude images are acquired. (b) The phase data is unwrapped and a mask is created around the region of interest from the magnitude image. (c) The phase data is Fourier transformed and the image relating to the frequency of interest is selected (typically the second image). (d) The mask is applied to the complex wave image. (e) The inversion algorithm is applied to the data and the elastogram created.

1.5.4 Research in the Field

Current research using MRE focuses on a range of anatomical structures. This section focuses on several key areas of interest within MRE and those more specific to this thesis.

Brain

Several studies have shown that the material properties of the brain are sensitive to a number of disease states. Most notably Murphy et al. (2011) [160] showed reduced stiffness of cerebral tissue in Alzheimer's patients in comparison with control subjects whilst Wuerfel et al. (2010) [161] demonstrated degradation of cerebral tissue in multiple sclerosis patients. Significant differences between the properties of white and grey cerebral matter have also been demonstrated [162].

MRE of the brain has the potential to be significant for several other reasons. Firstly propagation of ultrasound waves through the skull is problematic since attenuation at such frequencies is very high [146]. Additionally ultrasonic elastography often investigates the strain of tissue under a manual compression [163]. Both of these factors make ultrasound elastography impractical in this region and thus makes *in vivo* material property measurements largely dependent upon MRE. Secondly, acquisition of MRE data from the brain is relatively straightforward. Vibrations are typically applied through a head pillow or a head cradle and are transmitted into the brain well through the skull [162]. There is also relatively little by way of body motion in the brain in comparison to other regions of the body allowing for long acquisition times and minimal artefacts in the data. As such developments in the field in both data acquisition and in terms of post-processing are often achieved using data acquired in the brain [164, 165].

Liver

Liver fibrosis is the only disease state for which MRE is currently used as a clinical diagnostic technique. Typically fibrosis has been diagnosed using a biopsy but this process is highly invasive. Studies using MRE have shown a significant increase in the stiffness of fibrotic liver tissue in comparison to normal liver tissue and were also able to identify the different stages of fibrosis progression [166, 167]. In terms of its diagnostic capability MRE was shown to be more effective than both ultrasound elastography and biopsy [168].

Heart

Cardiac MRE presents significant challenges since it attempts to utilise a phase-encoding gradient sequence to characterise small amplitude vibrations in a region of high natural motion. In this regard Rump et al. (2007) [169] utilised fractional encoding, whereby the duration of the bipolar gradient is reduced to less than the period of the induced wave in order to reduce the repetition time (TR) of the sequence (the time between successive radiofrequency pulses). By employing this technique they were able to acquire images of wave propagation in the human heart for the first time.

It was recognised by Kolipaka et al. (2009) that assumptions utilised in typical MRE inversion were not appropriate for the heart and a new inversion was derived based on wave propagation in a spherical shell [170]. Utilising this inversion a subsequent study by the same group demonstrated a strong relationship between pressure and stiffness in a porcine heart [171].

Aorta

Of particular relevance to this thesis are the studies that have been conducted looking at aortic stiffness. The first study in this field was performed by Woodrum et al. (2006) [172] and looked at an *ex vivo* porcine aorta and upon an *in vivo* human femoral artery. Since the resolution of MRE is not good enough to image directly into the vessel wall a principle known as the waveguide effect was utilised. Here the idea is to utilise the mechanically created wave to induce a pressure wave into the fluid within the vessel. The velocity of this wave is dependent on the thickness and the elastic modulus of the vessel wall in accordance with a form of the Moens-Koertweg equation:

$$ET = 2\rho a_i \lambda^2 f^2 \tag{1.48}$$

where E is the Young's modulus, T is the thickness of the vessel wall and a_i is the interior radius of the tube. This implies that a direct measurement of the shear wave within the vessel wall is not necessary to measure its stiffness but that this can be achieved by analysis of the wave propagating in the lumen.

Since this initial study interest within the field has developed. Woodrum et al. published another study in 2009 [151], again looking at *ex vivo* porcine aorta to show a significant difference increase in the product of the Young's modulus and wall thickness in hypertensive pigs in comparison to normotensive pigs. Xu et al. (2012) [173] also showed an increase in *ex vivo* porcine aorta stiffness after it had been fixed in formalin.

Several studies have now also looked into *in vivo* aortic stiffness utilising MRE in more detail. Kolipaka et al.(2012) [174] utilised an induced frequency of 60 Hz to demonstrate a significant difference in the stiffness of hypertensive and normotensive subjects. The stiffness calculated in this study is known as the effective stiffness since it makes use of DI algorithm and therefore is not a true measure of the stiffness of the aorta, where the conditions cannot be approximated to the assumptions of infinite homogeneity used in its derivation. Meanwhile a further study by Xu et al. (2013) [175] showed a correlation between the Young's modulus-wall thickness product and age, whilst a study by Damughatla et al. (2013) [176] showed similar correlation between age and MRE measured stiffness using the LFE inversion algorithm (as with Kolipaka et al. (2012) this was reported as effective stiffness). Indeed in this study MRE measured stiffness values were shown to have a better correlation with age than pulse wave velocity (PWV), the gold standard measurement of arterial stiffness. Most recently a study by Kenyhercz et al. (2015) [177] investigated variation of effective arterial stiffness over the course of the cardiac cycle. The paper defined eight phases of the cardiac cycle and showed cyclical variation over these. Additionally arterial stiffness was shown as increased in all volunteers at end-systole compared to end-diastole.

1.5.5 Summary

MRE allows non-invasive measurements of material properties *in vivo*. Previous work conducted upon the heart and aorta demonstrate that it is possible to obtain such measurements from regions subject to a large amount of motion aside from the induced shear waves used by the technique. This provides hope that the technique can be applied to AAAs such that the resulting measurements that can be incorporated into PSM.

1.6 Thesis Aims

A review of literature relating to AAAs demonstrates the potential for PSM to predict risk of rupture. One of the primary weaknesses of this technique is the application of material properties, whose values are prescribed from measurements made in *ex vivo* mechanical testing, and therefore not specific to the patient. MRE is a recently developed technique that makes non-invasive measurements of material properties *in vivo*. This therefore provides the potential for integration of MRE measurements into PSM of AAAs in order to improve prediction of rupture risk.

The aim of this thesis was to investigate the capability of utilising MRE to obtain material property measurements from AAAs that could be incorporated into PSM.

To achieve this, a method of simulating MRE using FEA was developed. This was then utilised to test several pieces of MRE post-processing software to identify those that would be appropriate for use in AAAs. The potential for achieving accurate measurements of material properties in AAAs was then tested using this technique in simplistic CAD designed AAA geometries. Concurrently the ability to induce and visualise shear waves using MRE into AAAs was tested on a small cohort of patients.

1.7 Thesis Structure

The structure of this thesis is as follows:

- Chapter 1 has introduced the relevant topics, providing an overview of the literature and outlining the aims of thesis.
- Chapter 2 outlines the development of the modelling process from simplistic 2-D models with uniform elastic material properties, to more complex 3-D models containing an insert and defined with viscoelastic material properties. The influence of modelling parameters such as boundary conditions, mesh type and constraints upon the measurements made through inversion have also been investigated.
- Chapter 3 investigates how the size of an insert, both with respect to size in and out of the plane of the image, affects the accuracy of the measurements made. The chapter also introduces the 3-D direct inversion algorithm and an extension of the direct inversion, the multi-frequency dual elasto-visco (MDEV) algorithm and compares these. Finally the ability of directional filtering to remove reflected waves and the resulting artefacts in the elastogram associated with these, along with its ability to obtain accurate measurements is investigated.
- Chapter 4 compares results from FEA with those from a commercially available phantom in order to assess the advantages and disadvantages of each technique.
- Chapter 5 utilises FEA of MRE in idealised CAD geometries of AAAs to assess the capability of the technique in such geometries.
- Chapter 6 investigates whether it is currently possible to induce waves into AAAs using MRE for potential measurement of the material properties. The results are compared against data from a healthy volunteer.

- Chapter 7 concludes the work performed in this thesis and discusses the further work that should be undertaken based on its findings.

Chapter 2

Modelling of MRE using FEA

2.1 Introduction

Testing and development of MRE post-processing software requires knowledge of the material properties of the test object, such that the resulting MRE measurements can be validated. To this end there are a number of commercial phantoms available with quoted stiffness values [178]. Such phantoms are however limited since they do not allow the user variations in geometry or material properties. To overcome this several studies have created their own phantoms using agar gel [148, 179], yet this process is also time consuming and generally requires mechanical testing of the material to attain its true properties, a process requiring its destruction.

FEA represents a solution to these problems. Material properties are defined within the pre-processing stage of the modelling, thus a direct comparison between these prescribed values and the values attained through analysis of the data using the MRE post-processing software can be drawn. Using FEA in this manner offers the potential to iterate over a large range of geometries and material properties allowing optimisation of the MRE methodology and the ability to obtain quantitative data on issues of clinical interest such as minimum lesion size which may be observed on the elastogram.

To date a small number of MRE simulation methodologies have been described. Notably Chen et al. (2005) [180] used a 2-dimensional model to show increased accuracy in simulated shear wavelengths at higher densities and lower shear moduli. Leclerc et al. (2013) [181] iteratively altered 3-dimensional FEA model parameters to match with wave propagation in a phantom. Meanwhile Kolipaka et al. (2009) [170] compared uniform beam, plate and shell phantoms with 3-D FEA models of the same structures, showing good agreement between MRE scans and FEA datasets. The purpose of FEA development here was to create a technique that could validate inversion algorithms.

Of relevance to this thesis was the work by Thomas-Seale et al. (2011) [182]. This utilised a steady-state FEA technique to investigate MRE in atherosclerotic plaques. Whilst this author has access to the steady-state technique used in this publication, a limitation is that the technique provides complex displacements output at a specified frequency (for the purposes of MRE simulations, the frequency of induced vibrations is selected). As a result simulated data using this technique is output is in the frequency domain whereas in MRE, data is acquired in the time domain. Although application of MRE inversion algorithms typically involves analysis in the frequency domain, and thus prior application of the Fourier transform to the temporal data, many of the existing MRE post-processing software packages are compatible only with data in the time domain, therefore rendering steady-state simulated data incompatible with much of that software. This implies that a transient method of simulation outputting in the time domain would be beneficial.

As such this chapter aims to demonstrate the development of a transient explicit method of simulating MRE and compare the results with the steady-state technique previously described by Thomas-Seale (2011) [182]. The chapter also aims to investigate how varying modelling parameters affects measurements of material properties through inversion.

2.2 Methods

This section outlines the modelling technique used to simulate the MRE process. This approach involves the simulation of MRE data by FEA and integration of this data with the MRE post-processing software. An illustration outlining the steps in this process is presented in figure 2.1. A more detailed description of the modelling process including the post-processing is presented in Appendix I. Whilst this description is for the 3-D analysis that is utilised in chapters 3, 4 and 5, the relevant procedures can easily be truncated to 2-D.

2.2.1 Simulation Type

Two simulation techniques have been utilised in this chapter: a transient explicit method and the steady-state technique outlined in Thomas-Seale (2011) [182]. All of the simulations were run using *Abaqus Version 6.10-1 (Dassault Système Simulia Corp., Providence, Rhode Island,USA)*. Since one of the aims of this thesis was to develop a transient method of simulating MRE, the steady-state technique was simply used for comparative purposes. Unless stated all simulations are performed using the transient method.

The transient simulations used fixed time increments of the order 10^{-6} s. Once the simulation was successfully completed displacement data was extracted from a pre-defined

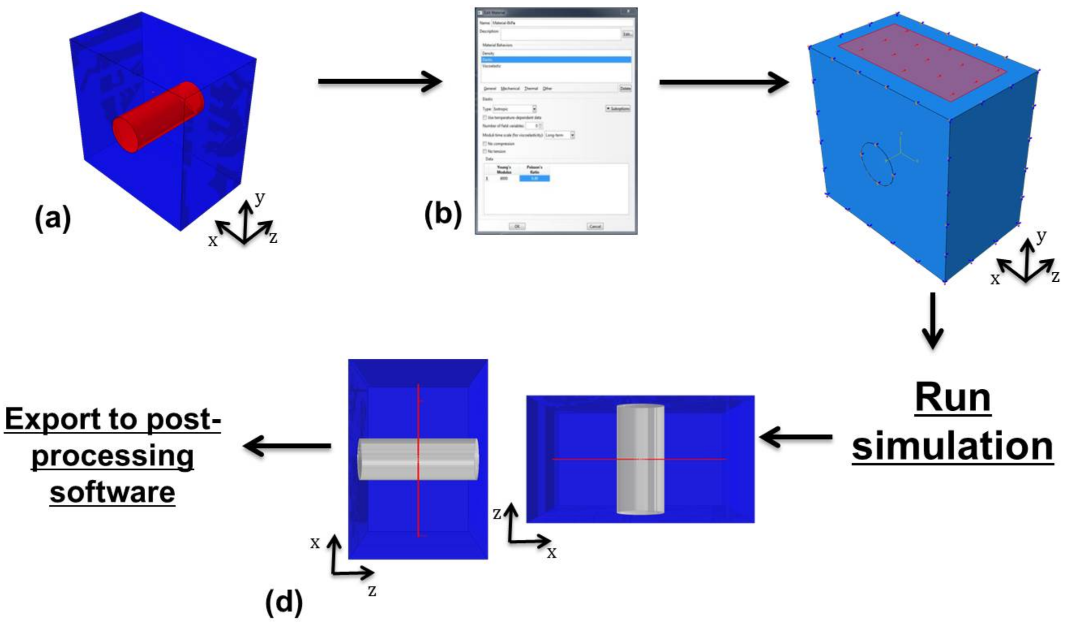

Figure 2.1: Modelling workflow. (a) Creation of the geometry. (b) Assignment of the material properties. (c) Application of the load and assignment of boundary conditions. (d) Extraction of data from 2-dimensional plane.

two-dimensional plane. Data was output at 8 pre-defined equally spaced time-points over the period of the wave at the frequency of interest. To allow the system to approach steady-state the wave was allowed to propagate for 8 wave cycles before the data was output. Data was imported into *Matlab R2013a (Mathworks, Natick, Massachusetts, USA)* series of wave images.

In the steady-state simulations displacement data is in the frequency domain and as such the real and imaginary values at the frequency of interest were extracted from *Abaqus* and imported into *Matlab* as the complex wave image. Figure 2.3 highlights the stages at which the steady-state and the transient techniques output in the MRE workflow.

2.2.2 Post-Processing

Once in *Matlab* a 1-dimensional Fourier transform was applied in the temporal direction upon each pixel for the wave images from the transient simulation. The second bin in the frequency domain corresponds to the complex wave image at the frequency of interest and was therefore selected for further analysis. This corresponds to the frequency domain image output from the steady-state simulation, with both sets of data at this point in the

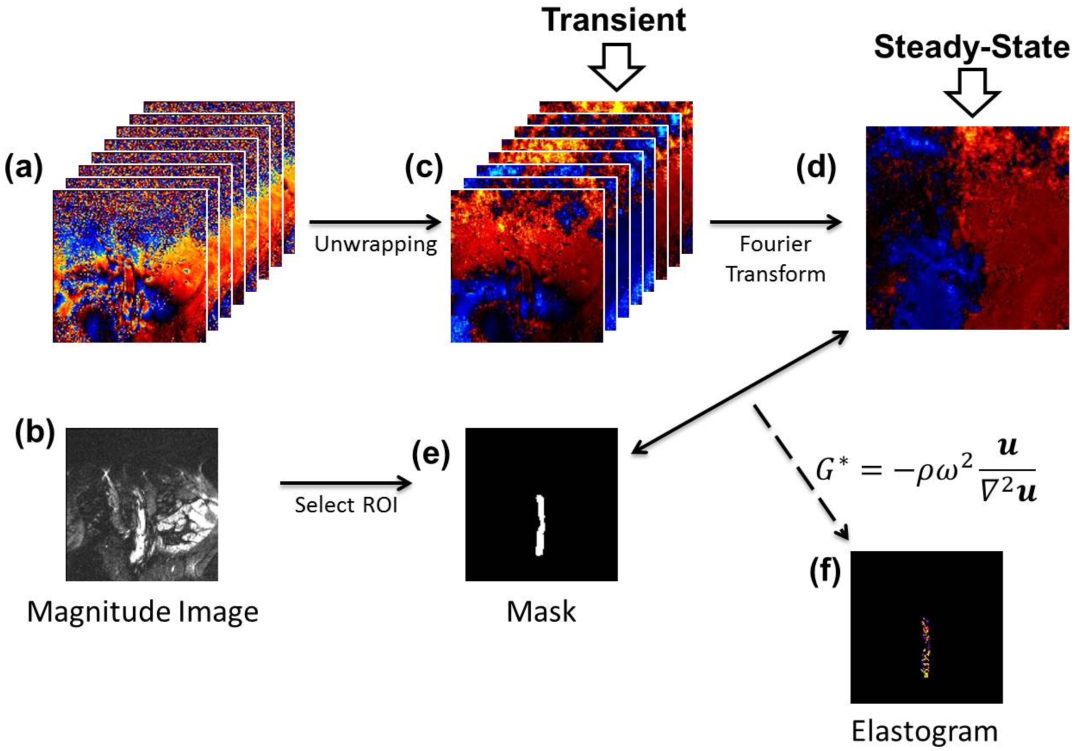

Figure 2.2: Recreation of figure 1.13 to demonstrate the points in the MRE workflow that the different methods of simulation aim to recreate.

correct format for application of the inversion algorithm to create the elastogram. The lack of noise in the modelling data in comparison to *in vivo* or phantom MRE meant that the application of band-pass filters was unnecessary. Regions of interest were then identified and masks created to isolate these. The areas of these masks were selected avoiding pixels that were within 2 mm of boundaries between the different regions within the model and pixels that were within 5 mm of the edge of the region over which the inversion was performed.

2.2.3 Outline of the Modelling Development

Development of the transient simulation method began in 2-dimensions, before being expanded to 3-D. Since the 2-D inversion algorithm involves direct inversion of the Helmholtz equation for planar waves, the development initially aimed to simulate planar wave propagation in the 2-D model. Once this had been achieved 3-D models were created again with the aim of achieving planar waves in the 2-D analysis. Finally 3-D models more analogous to true MRE where wave propagation only at best approximates planarity were created.

2.2.4 2-D Planar

Geometry

The model was a 50x200 mm^2 rectangle (figure 2.3). The region of interest was a 50x50 mm^2 region taken at a depth of 50 mm in the y-direction such that it is sufficiently away from the region where the load is applied. The overall depth of the model in this direction is chosen such that reflections travelling from the bottom of the model do not reach the region of interest and cause interference with the waves in this region. Data was extracted using a set of pathpoints with 1 mm spacing.

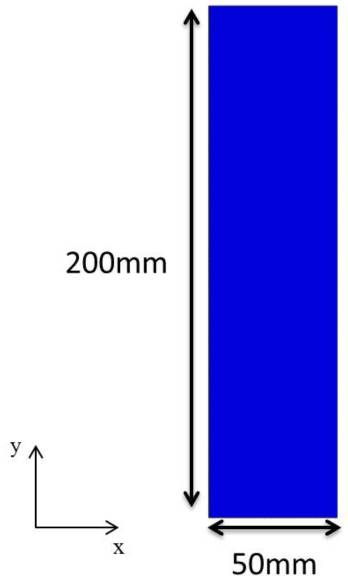

Figure 2.3: Dimensions and orientation of the 2-D planar wave model.

Material Properties

The density was defined as being 1047 kg·m^{-3} since this is representative of the typical density of the human anatomy. The material was defined as linear elastic with a shear modulus of 3 kPa and was assumed to be almost incompressible with a Poisson's ratio of 0.49.

Loading and Boundary Conditions

The vibrations were applied as a concentrated force across all the nodes on the upper surface of the model. The 'Amplitudes' module is used to define the frequency of the vibrations. The size of the vibrations was 0.001 N per node in the x-direction. Frequencies of 50, 60, 70, 80, 90 and 100Hz were applied to the model. These are in the typical range of *in vivo* MRE studies. Symmetric boundary conditions with displacements fixed in the y-direction were applied to all sides of the model.

Mesh

Linear quadrilateral elements (CPS4R) with reduced integration were used to mesh this model. Meshing was achieved using local seeds with an element length of 1 mm being derived for each edge in the model.

Manual Measurements

In order to investigate the accuracy of the models a one dimensional cut taken through the centre of the complex wave image was analysed. The wavelength in each region was measured manually and the shear modulus was calculated via the following formula [183]:

$$\mu = \rho f^2 \lambda^2 \tag{2.1}$$

Manual measurements are often associated with user bias and poor accuracy. In order to reduce this as much as possible the wavelength was always selected from the same plane in the centre of the model. The wave in this plane was then plotted in *Matlab* and a line drawn through the intersection of the wave with $x = 0$ to the x-axis (figure 2.4). Ticks were placed along the x-axis at 0.1 mm intervals. Where possible the length of more than one wavelength was measured so as to further decrease any errors.

Discretisation Errors

Data output from both *in vivo* and *in silico* MRE is discrete in form. This implies that application of the Laplacian is subject to a discretisation error. For planar waves whose velocity contribution is almost exclusively in one direction (i.e. the wave is travelling along

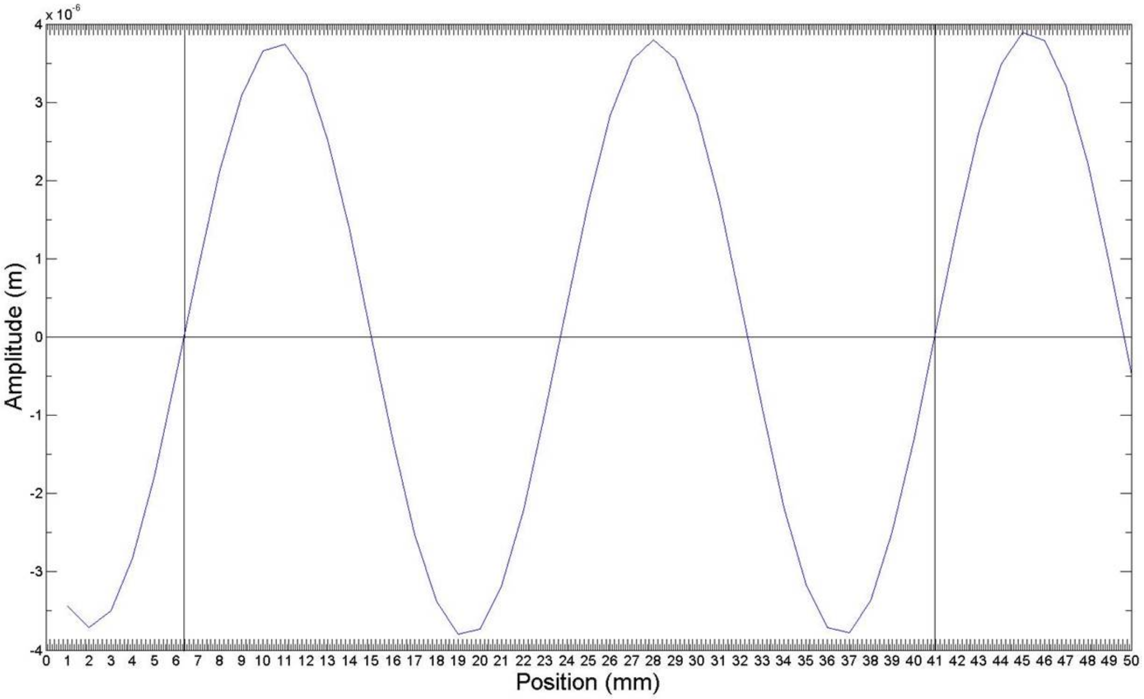

Figure 2.4: An example of how the manual measurements of the wavelength were made. The 1-D wave was plotted from a single plane in the 2-D complex wave image. The vertical lines aided accurate measurements in the position that the wave crossed the x-axis.

one of the directional axes) the Laplacian can be thought of as simply the second derivative of the function in that direction:

$$\nabla^2 \mathbf{u} = \frac{d^2 u_x}{dx^2} \quad \text{if} \quad v_y = 0 \tag{2.2}$$

Since the displacement in the y-direction is constant, this implies that the discretisation error in the 2-D Laplacian is equivalent to the discretisation error from the 1-D second derivative for which an estimate is easily calculable in *Matlab* (see Appendix II). Since the waves created here were designed to propagate exclusively in the y-direction a direct comparison with these discretisation errors has been performed.

2.2.5 3-D Planar Model

Geometry

A 3-D model with dimensions 50x50x50 mm^3 was created to investigate planar waves (figure 2.5). The region of interest was a 50x50 mm^2 slice running directly through the central z-plane of the model. Data was extracted using pathpoints as described in the methodology for the 2-D planar model.

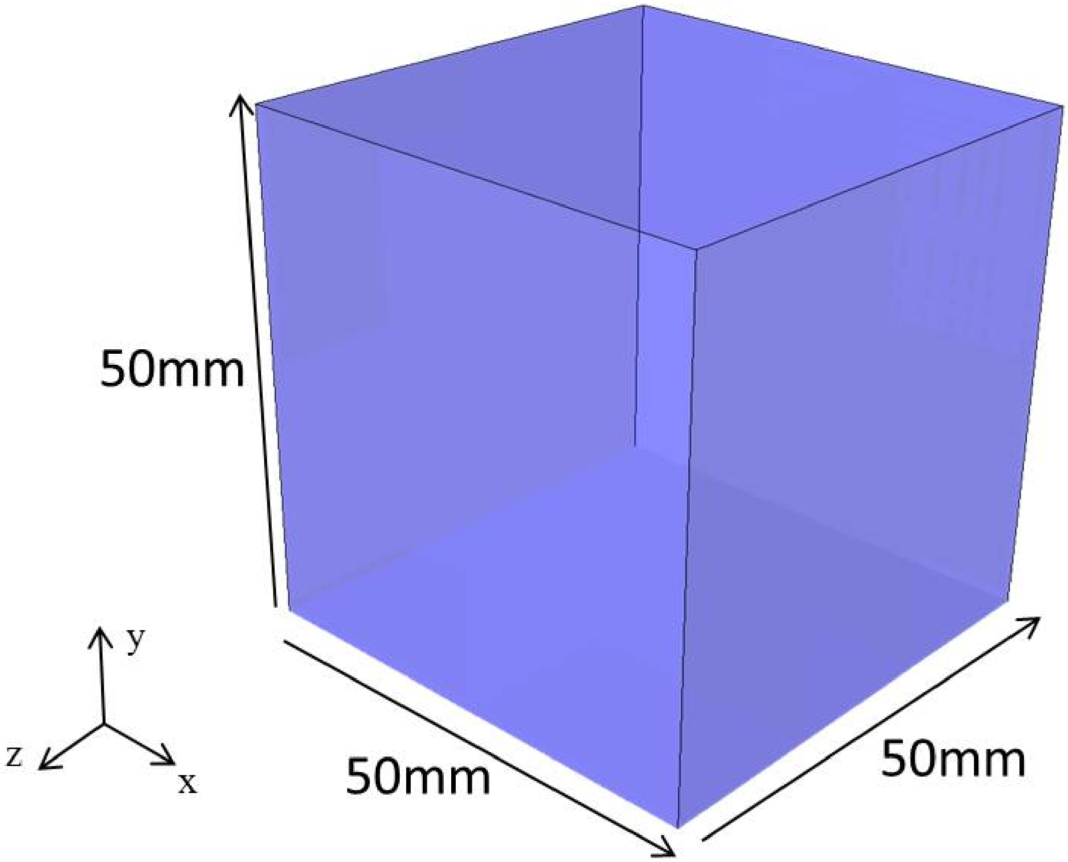

Figure 2.5: Geometry and orientation of the 3-D planar model.

Material Properties

The material is again defined as linear elastic. Since a higher frequency range was used in these models in comparison to the 2-D planar model the shear modulus of the material has been increased to 9 kPa in order to make the waves of comparable wavelengths to those in the 2-D planar model. The material density was defined as 1047 kg·m^{-3} and the Poisson's ratio was 0.49.

Loading and Boundary Conditions

As in the 2-D planar model the vibrations were applied via a concentrated force load upon all nodes in the upper surface. The force per node applied was 0.001 N in the z-direction. As such only displacement data in the z-direction were extracted from the completed model for the 2-D analysis. Whilst frequencies below 100 Hz are typically used *in vivo* these frequencies were incompatible with this geometry: the simulations failed to complete with an error message that the "the ratio of the deformation speed to wave speed exceeds 1.0000 in at least one element." As a result of this the frequencies used in this model were 100, 125, 150, 175 and 200 Hz.

Symmetric boundary conditions with displacements fixed in the y-direction were applied to all side surfaces of the model. No boundary conditions have been applied to the lower surface of the model because of the mesh in this region.

Mesh

Eight-noded hexahedral elements with reduced integration (C3D8R) were used to mesh the model. The element size was determined using local seeds with an element length of 1 mm defined for all edges in the model.

Whereas simulation time of MRE in 2-D was short (under ten minutes) thus allowing a deep model that allowed the wave to propagate away from the region of interest without the interference of reflections, this luxury is not afforded in 3-D modelling which is more temporally expensive (a model with the same depth as the 2-D model would take several days to run). As a result a layer of infinite elements (CIN3D8) has been applied to the bottom surface. These allow the wave to propagate away from the regions of interest in the model with no reflections. Application of infinite elements does not come as a standard option in *Abaqus/CAE* and therefore requires editing of the input file. More details upon how this has been achieved can be found in Appendix I.

Manual Measurements and Discretisation

Since the aim of this model was to utilise a 3-D model to create planar wave propagation in the 2-D analysis, the comparison with the manual measurements and the discretisation errors described in the methodology for the 2-D planar model remain valid and were also utilised here.

2.2.6 3-D Non-Planar Models

Geometry

Four cuboid geometries of dimensions 80x80x50 mm^3 were created. The first of these models was uniform in terms of the material properties throughout. The other three contained a cylindrical insert running through their centre. The radius of these inserts was different in each model with radii of 10 mm, 15 mm and 20 mm used (figure 2.6). The region of interest was a 64x64 mm^3 slice running directly through the central z-plane of the model. Again the pathpoints methodology described previously was used to extract data from the model. Table 2.1 shows the tests that the different models have been utilised for.

Model Name	**Uniform**	**Insert 1**	**Insert 2**	**Insert 3**
Shear Modulus	✓	✓	✓	✓
Frequency	✓	✓	✓	✓
Boundary Conditions		✓		
Constraints		✓		
Element Type		✓		
Simulation Type		✓		

Table 2.1: Experiments performed with each of the different models.

Material Properties

The density and Poisson's ratio were maintained as 1047 $\text{kg}\cdot\text{m}^{-3}$ and 0.49 respectively throughout all the simulations.

Whilst the planar models previously outlined were designed such that the waves would propagate away from the region of interest without reflections, this was not considered time efficient when undertaking a study with a large number of models. Furthermore

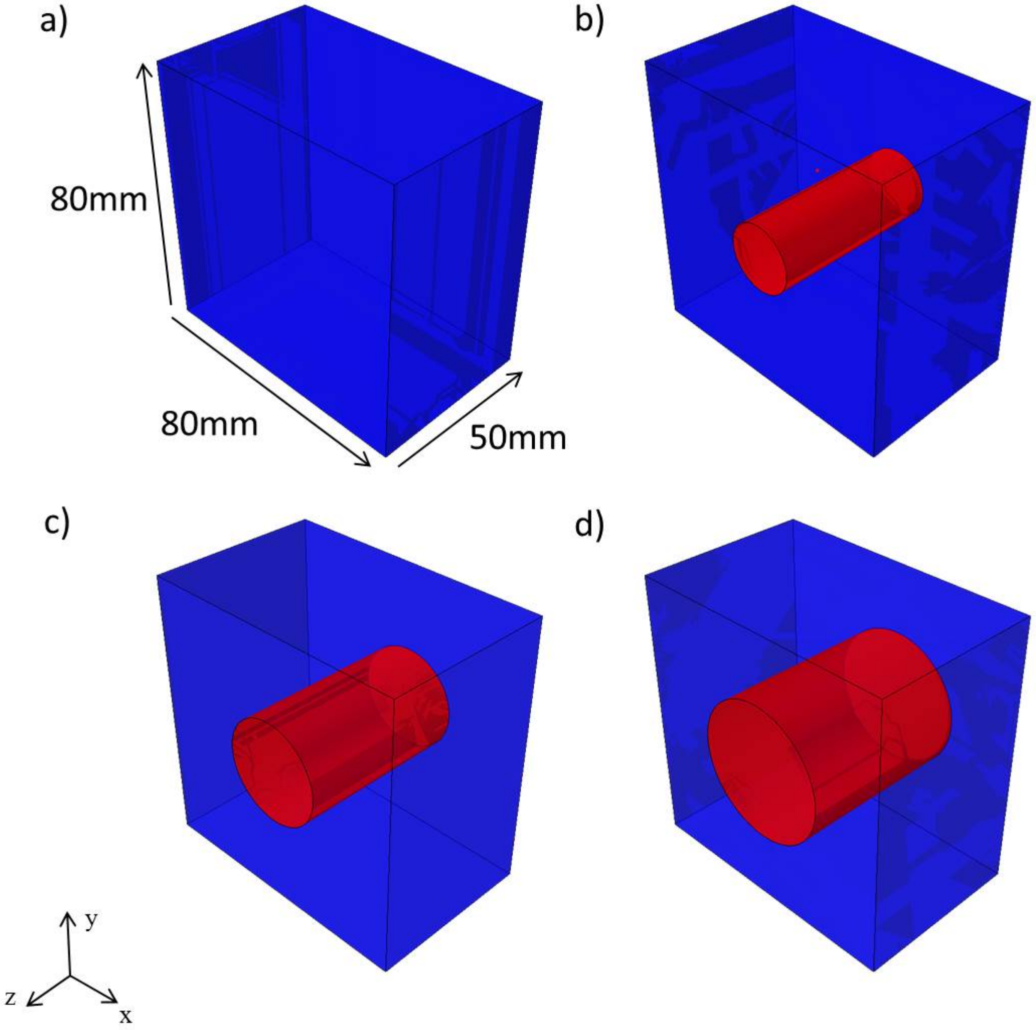

Figure 2.6: Geometry and orientation of the 3-D non-planar models: a) uniform model; b) insert 1; c) insert 3; and d) insert 4.

reflections are present in both *in vivo* anatomical scans and phantom scans [159], therefore their presence *in vitro* is a more accurate. As such viscoelastic properties were utilised to introduce damping. For simplicity the Kelvin-Voigt model of linear viscoelasticity with a shear viscosity of 1 Pas was utilised.

Variations of the prescribed shear modulus were utilised to investigate how this affects the measurements made through inversion. In the uniform model shear moduli of 2- 9 kPa were applied. In all three insert models the shear modulus of the insert was varied using values of 4-9 kPa whilst the background shear modulus was maintained at 3kPa. In the insert 1 model the effects of varying the background shear modulus whilst the shear modulus of the insert was maintained were studied. For this the insert shear modulus of 9 kPa was used whilst the background shear modulus was varied from 3-15 kPa.

All studies investigating the change in shear modulus were performed using vibrational frequencies of 100Hz. Loading conditions were applied as described in the next section whilst encastred boundary conditions were applied to all sides upon which the load was not being applied. C3D8R elements 1 mm^3 in size were used in all models.

Loading and Boundary Conditions

As with the 2-D and 3-D planar models the load is applied via a concentrated force acting upon nodes on the upper surface with a force per node of 0.001 N. The nodes selected do not however cover the entire surface with the load not applied to the outer 3 mm of the surface. Frequencies of 50, 60, 70, 80, 90 and 100 Hz were applied to all of the models. For this purpose the shear modulus of the uniform model was 3 kPa whilst in the insert models the shear moduli of the background and the insert were 3 kPa and 9 kPa respectively.

For all models boundary conditions were applied to all surfaces with the exception of that upon which the load was being applied. Insert model 1 was used to test how the boundary conditions affect the measurements acting on the model. The boundary conditions tested were encastred (fixes all displacements and rotations at the nodes on the defined surface), x-symmetry, y-symmetry and z-symmetry (each of these fixes the displacements in the specified direction whilst allowing displacements in the other two) (table 2.2).

For this study the background shear modulus was 3 kPa and the insert shear modulus was varied from 4-9 kPa. In all models investigating the loading and boundary conditions 1 mm^3 C3D8R elements were used.

Boundary Condition	x	y	z
x-symmetry	0	U	U
y-symmetry	U	0	U
z-symmetry	U	U	0
Encastred	0	0	0

Table 2.2: Summary of the allowed motion for each of the boundary conditions used in this chapter for displacements in the x, y and z-directions where 0 implies that the boundary is fixed and U implies the boundary is unconstrained in that direction.

Constraints

The definition of the boundary between the two regions of the model was investigated using the insert 1 model. Firstly the two regions were merged together in the assembly module with the intersecting boundaries retained. In this instance the intersection between the two regions is maintained with nodes at this intersection shared between the elements on both sides. Secondly the two regions were tied together using the constraints tool. For this purpose *Abaqus* defines a slave and a master surface for the connecting surfaces between the two parts. Each point on the slave surface is constrained to have the same motion as the nearest point to it on the master surface. Finally a frictional interaction was defined between the different regions of the model. Here the two materials are treated as separate parts which interact with one another based on user defined properties. Values of 0.5, 0.75, 1 and 1.25 were tested for the coefficient of friction (figure 2.7).

The background shear modulus for this study was 3 kPa whilst the insert shear modulus was varied from 4-9 kPa. A frequency of 100 Hz was applied as the load and the boundaries were fixed using encastred boundary conditions. The models were meshed using 1 mm^3 C3D8R elements.

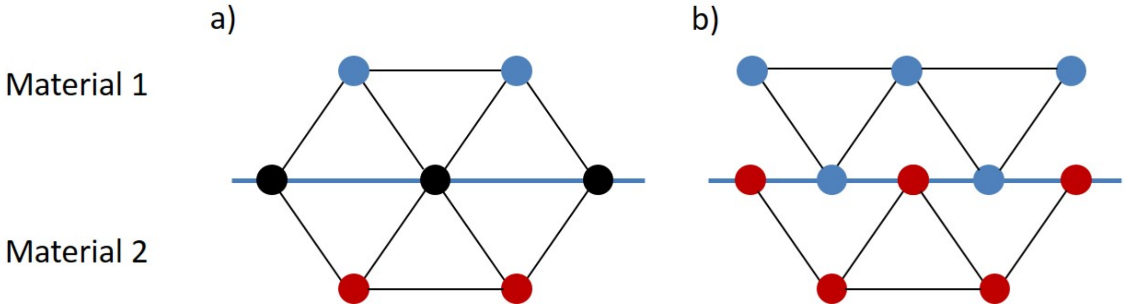

Figure 2.7: Diagram showing the mesh for the constraints used in this study. a) The two materials are merged as a single part with nodes at the interface (black) shared between the two materials. b) For the tie constraint and the fractional interaction the materials are meshed separately. For the tie constraint the red nodes at the interface represent the nodes on the slave surface whilst the blue nodes represent those on the master surface. These blue nodes are unconstrained whilst the red nodes are constrained to have the same motion as the master surface at that point.

Mesh

Eight-noded hexahedral (C3D8R), 4-noded linear tetrahedral (C3D4) and 10-noded quadratic tetrahedral elements (C3D10M) were compared using the insert 1 model. The C3D8R and C3D4 elements were meshed defining a 1 mm element length on all edges. Since the C3D10M elements are of higher order in comparison to the C3D8R and the C3D4 elements a lower mesh density was used with a 1.25 mm element length defined.

Element type was investigated under varying frequencies and shear moduli. The frequencies used were 50, 60, 70, 80, 90 and 100 Hz with background and insert shear moduli of 3 kPa and 9 kPa respectively. The insert shear modulus was varied from 4-9 kPa whilst the background shear modulus was maintained at 3 kPa and the frequency at 100 Hz.

Transient .v. Steady-State

The insert 1 model has again been used to compare the transient and steady-state methods of simulating MRE. Variations in frequency and shear modulus have been performed with both simulation techniques as outlined in the previous section. For both models C3D8R elements were utilised with the element length along each edge defined as 1 mm.

Manual Measurements and Discretisation

Since the waves are no longer designed to be planar the methods of comparing against shear modulus calculated from manual measurements of the wavelength and estimated errors for the discretisation are no longer applicable and therefore have not been used for these models.

Wave Decomposition

Displacements resulting from wave propagation can be represented in terms of displacements from the shear wave, u_i^S, and displacements from the compressional wave, u_i^C:

$$u_i = u_i^S + u_i^C \tag{2.3}$$

It is recognised within the MRE literature that the compressional component of the wave can have a small influence on the accuracy of the results. It would therefore be useful to investigate the relative influence of the shear and compressional waves on the inverted data. For this to be achieved, it was required that the shear and compressional components of the wave were reconstructed independently from the full displacement field. This can be achieved using Helmholtz decomposition which states that a vector field, in this case the displacement, can be decomposed such that [184, 185]:

$$u_i = \epsilon_{ijk}\Psi_{k,j} + \Phi_{,i} \tag{2.4}$$

Here Ψ_k and Φ represent vector and fields known as potentials corresponding to the shear and compressional waves respectively. ϵ_{ijk} is the Levi-Civita symbol defined as:

$$\epsilon_{ijk} = \begin{cases} +1 & \text{if } (i,j,k) \text{ is } (1,2,3),(2,3,1) \text{ or } (3,1,2) \\ -1 & \text{if } (i,j,k) \text{ is } (3,2,1),(1,3,2) \text{ or } (2,1,3) \\ 0 & \text{if } i=j \text{ or } j=k \text{ or } k=i \end{cases}$$

such that $\epsilon_{ijk}\Psi_{k,j}$ represents the curl of Ψ_k and $\Phi_{,i}$ represents the spatial derivative of Φ.

Since the curl of the gradient function is equal to 0, as is the divergence of curl, this implies that:

$$\epsilon_{ijk}u_{k,j} = \epsilon_{ijk}\epsilon_{klm,j}\Psi_{m,l} \tag{2.5}$$

$$u_{i,i} = \Phi_{,ii} \tag{2.6}$$

Whilst this process separates the shear and compressional components of the wave, the operators do not preserve the features of the wavefield. Not only are the potentials dimensionless, but they are subject to a phase shift of $pi/2$. This therefore implies that no direct comparison can be drawn either between these potentials and the initial wavefield, or between one another [186]. Sun et al. (2011) [187] addressed this by introducing a balancing factor, α:

$$\frac{\left|u_i^S\right|}{\left|u_i^C\right|} = \alpha\frac{\psi}{|\phi|} \tag{2.7}$$

where:

$$\alpha = \frac{v^S}{v^C} \tag{2.8}$$

Here v_s and v_c are the velocities of the compressional and shear waves respectively.

This, however, results in something of a paradox: in order to compare the relative contributions of the displacement field from the compressional and shear waves, the velocities of the waves must be known, yet the purpose of MRE is to measure the shear modulus, a value which, under the assumptions made in the derivation of the DI algorithm, is proportional to the shear velocity. This immediately implies that the calculation of α is an approximation, however, small variations in either the compressional and shear velocities will have a limited influence upon this velocity ratio, whilst research in other fields have typically associated such variations in this ratio with variations in porosity, something that is not a factor here [188, 189]. To this end, the speeds for waves travelling through a uniform, linear elastic material have been used to calculate an approximation for α:

$$v^C = \sqrt{\frac{1}{\rho}\left(\frac{G}{1-2\upsilon} + \frac{4}{3}G\right)} \tag{2.9}$$

$$v^S = \sqrt{\frac{G}{\rho}} \tag{2.10}$$

As such the magnitude of the displacement and the magnitude of the Laplacian of the displacement can be considered as follows:

$$u_i = k\left(\epsilon_{ijk}u_{k,j} + \alpha u_{i,i}\right) \tag{2.11}$$

$$u_{i,ll} = k\left(\epsilon_{ijk}u_{k,j} + \alpha u_{i,i}\right)_{,ll} \tag{2.12}$$

where k is a constant taking into account the change in amplitude following the application of the curl and divergence operators. Since it affects both the displacement and Laplacian of the displacement, it can be ignored from this point onwards. The Laplacian operator is linear therefore equation (2.12) can be rewritten:

$$u_{i,ll} = \left(\epsilon_{ijk}u_{k,j}\right)_{,ll} + \alpha\left(u_{i,i}\right)_{,ll} \tag{2.13}$$

From these relations, the fractional contribution of the compressional wave to the displacement can be defined as:

$$f_u = \frac{\alpha\left|u_{i,i}\right|}{\left|\epsilon_{ijk}u_{k,j}\right| + \alpha\left|u_{i,i}\right|} \tag{2.14}$$

whilst the fractional contribution of the compressional wave to the Laplacian of the displacement is:

$$f_{\nabla} = \frac{\alpha \left|(u_{i,i})_{,ll}\right|}{\left|(\epsilon_{ijk} u_{k,j})_{,ll}\right| + \alpha \left|(u_{i,i})_{,ll}\right|} \tag{2.15}$$

The fractional contribution of the compressional wave to the displacement term in the inversion algorithm (termed onwards as the fractional wave contribution) is given by:

$$f = \frac{1 + f_u}{1 + f_{\nabla}} - 1 \tag{2.16}$$

In this regard a perfect shear field would yield a value equal to 0, whilst a perfect compressional field would equal a value equal to 1. As such, there will be inaccuracies resulting from the compressional wave for all fractional wave contribution values that are not equal to 0, with errors increasing in size as the fractional wave contribution increases.

The fractional wave contribution was investigated for each boundary condition with a background shear modulus of 3 kPa and insert shear modulus values varied from 4-9 kPa. Vibrations induced at a frequency of 100 Hz. Whilst inversion was performed in 2-D throughout this chapter, it was recognised that in order that investigation of the fractional wave contribution the full wave field should be taken into account. As such data was extracted from all three spatial directions accross five xy-planes. Details of how this was achieved can be found in appendix I.

2.2.7 Convergence Studies

In FEA the accuracy of the model is typically dependent upon the number of elements used: the more elements the greater the accuracy of the model. Increasing the number of elements in the model however generally increases the time that the model takes to run. It is therefore the convention to perform a convergence study to determine the number of elements that are required for good accuracy in the model whilst maintaining a reasonable simulation time. The process involves iteratively running the model with a larger and larger mesh density until the change in the results (typically either displacements or stress are selected as outputs for which convergence is sought) from one mesh to the next drops below a certain percentage. In this instance the model is said to have converged.

A convergence study has been performed for each geometry used in this chapter. Convergence has been looked for in the shear modulus measurements since this is the relevant parameter for this thesis, and since it is a function of the displacement. Convergence has been assumed to have been achieved if the difference between the shear modulus measurements from one mesh density to the next is below 5%. An example of a convergence study for the insert model 1 is shown in Appendix III.

2.3 Results

2.3.1 2-D Planar Model

Visual inspection showed that propagation of the waves very closely approximated to planarity for all frequencies and the corresponding elastograms were very smooth (figure 2.8). The error (defined as the percentage difference calculated between the measured and predefined shear moduli) in the shear modulus measurements made from the inversion algorithm increased with increasing frequency. At a frequency of 50 Hz the measured shear modulus is 3047 Pa corresponding to an error of 1.6%, whilst at 100 Hz the measured shear modulus is 3129 Pa corresponding to an error of 4.3%. These errors closely match the calculated 1-D discretisation errors. The highest error for the manual measurements was 2.1% at 70 Hz with the errors for all other frequencies being less than 1%. Figure 2.9 shows a plot of the calculated error for each.

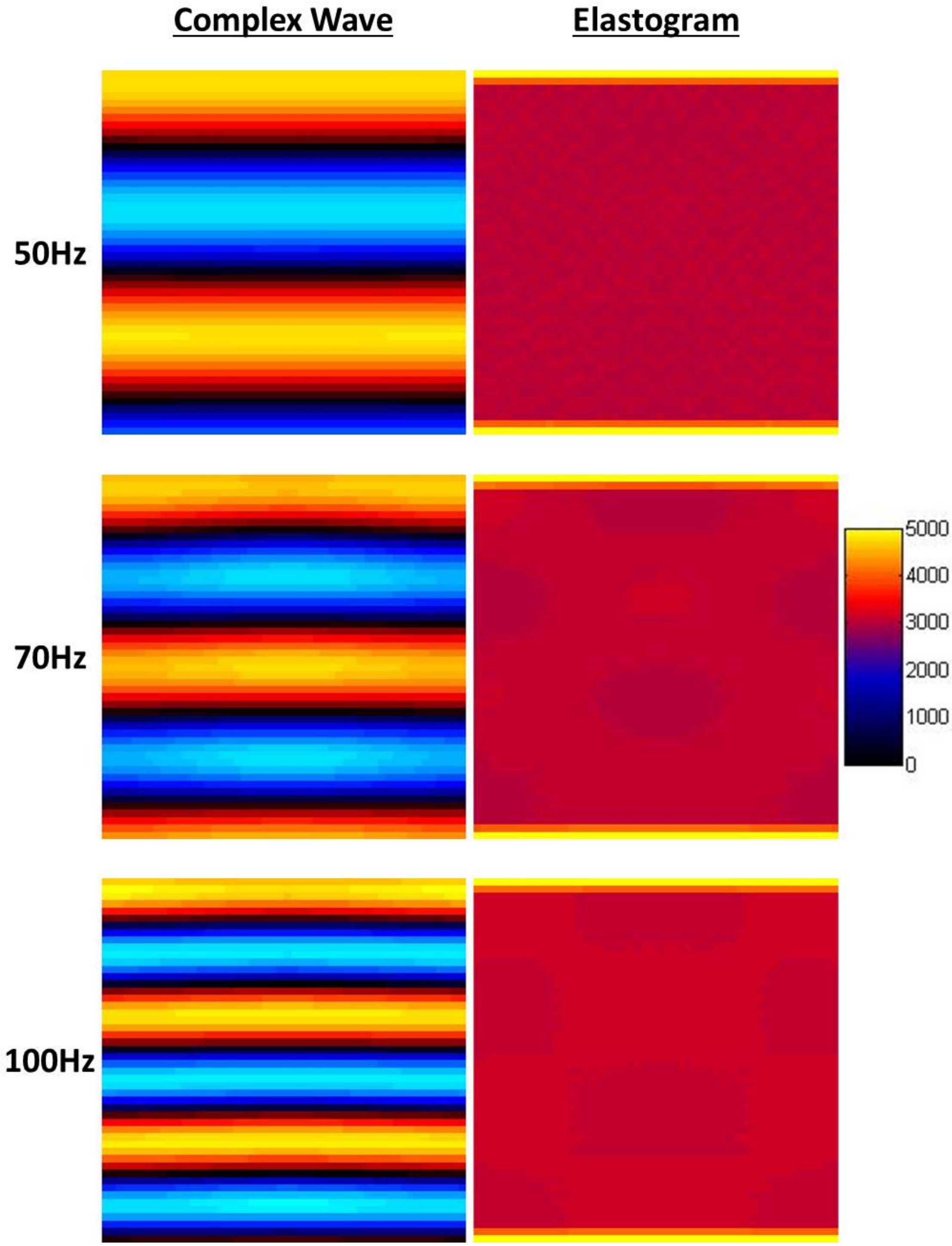

Figure 2.8: Examples of the complex wave images and elastograms for the 2-D planar model for vibrations of 50, 70 and 100 Hz. Wave propagation closely approximated planar and the resulting elastograms were smooth at all frequencies.

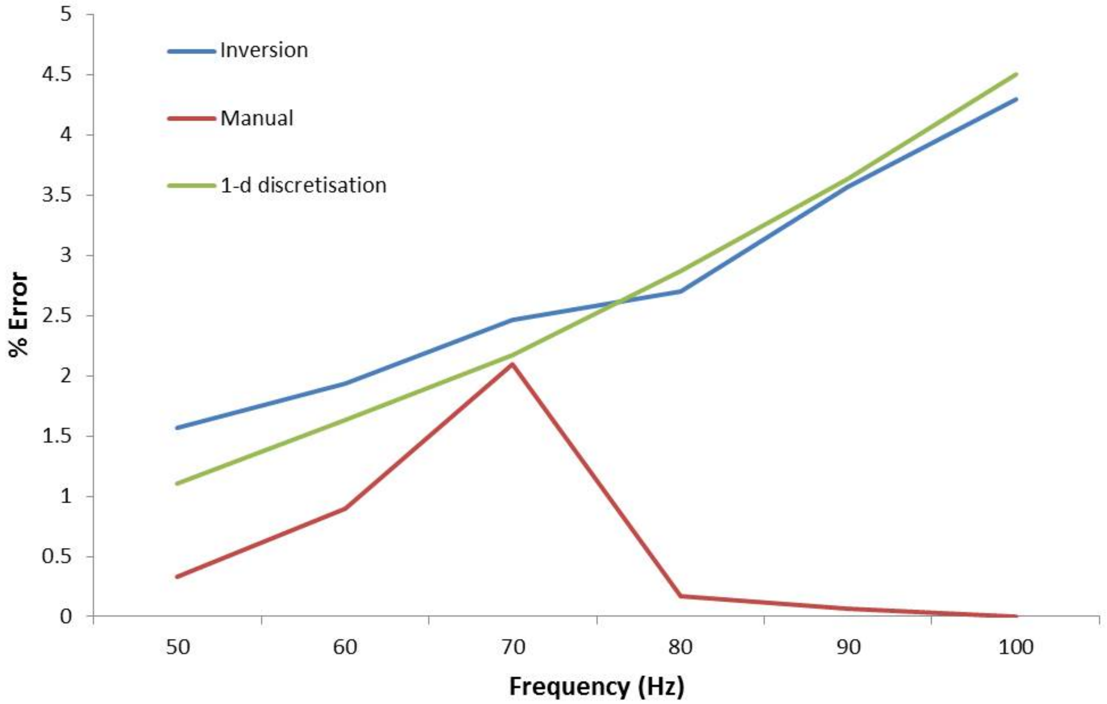

Figure 2.9: Error percentages calculated for the 2-D planar model. Manual measurements typically achieved a high level of accuracy, whilst the inverted errors correlated well with those estimated for discretisation.

2.3.2 3-D Planar Model

As in the 2-D planar models visual inspection showed that wave propagation closely approximated planarity and again the resulting elastograms were smooth (figure 2.10). Errors from the inversion increased with increasing frequency (2.4% at 100 Hz to 5.4% at 200 Hz) following the same trend seen in the errors calculated for 1-D discretisation errors (1.5% at 100 Hz and 6.1% at 200 Hz). Manual measurements of the shear modulus were underestimated with errors equal to or smaller than 2% for all frequencies. The percentage errors are demonstrated graphically in figure 2.11.

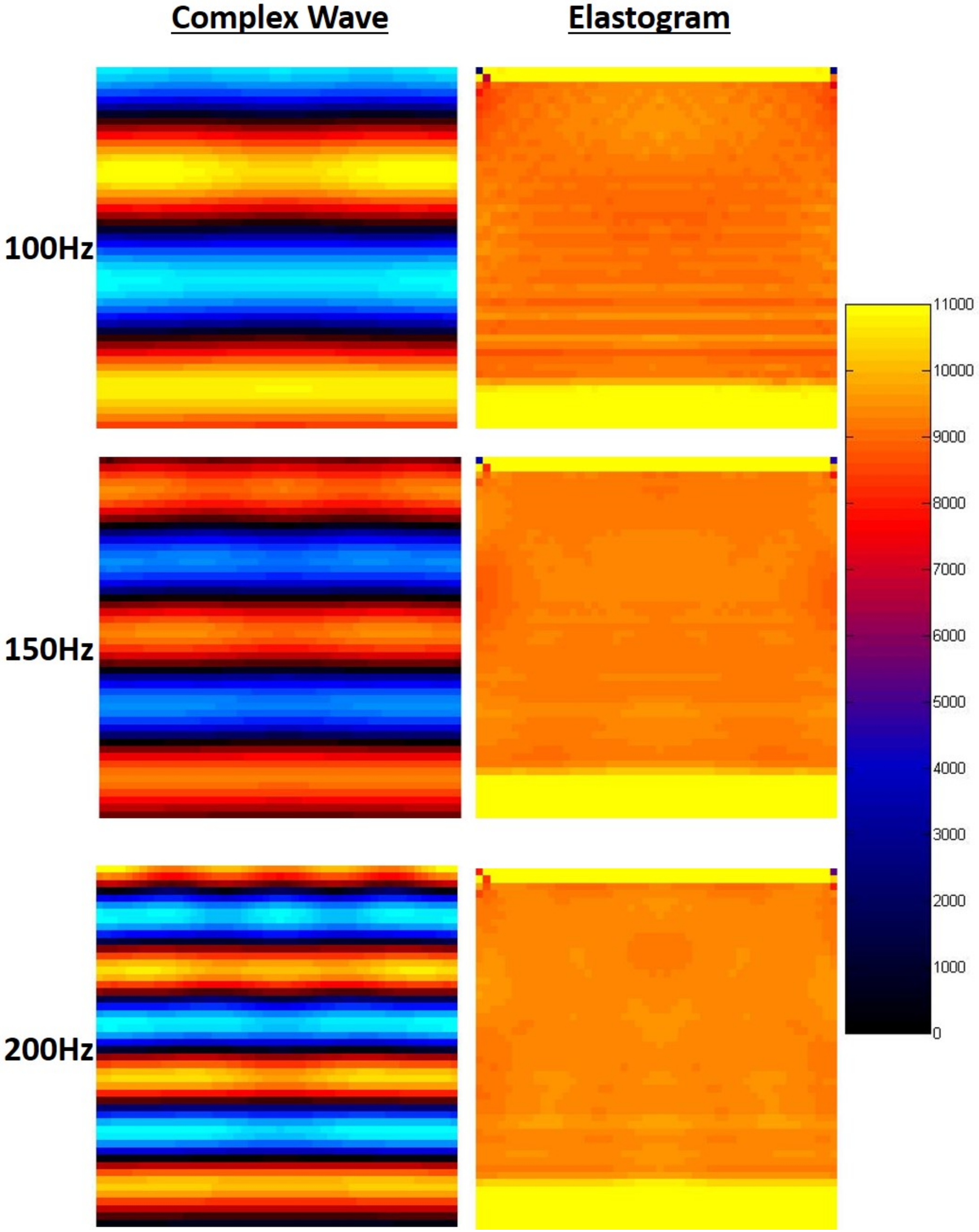

Figure 2.10: Complex wave images and elastograms for the 3-D planar model for vibrations of 100, 150 and 200 Hz. Wave propagation again closely approximated planar with the resulting elastograms smooth throughout the region of interest.

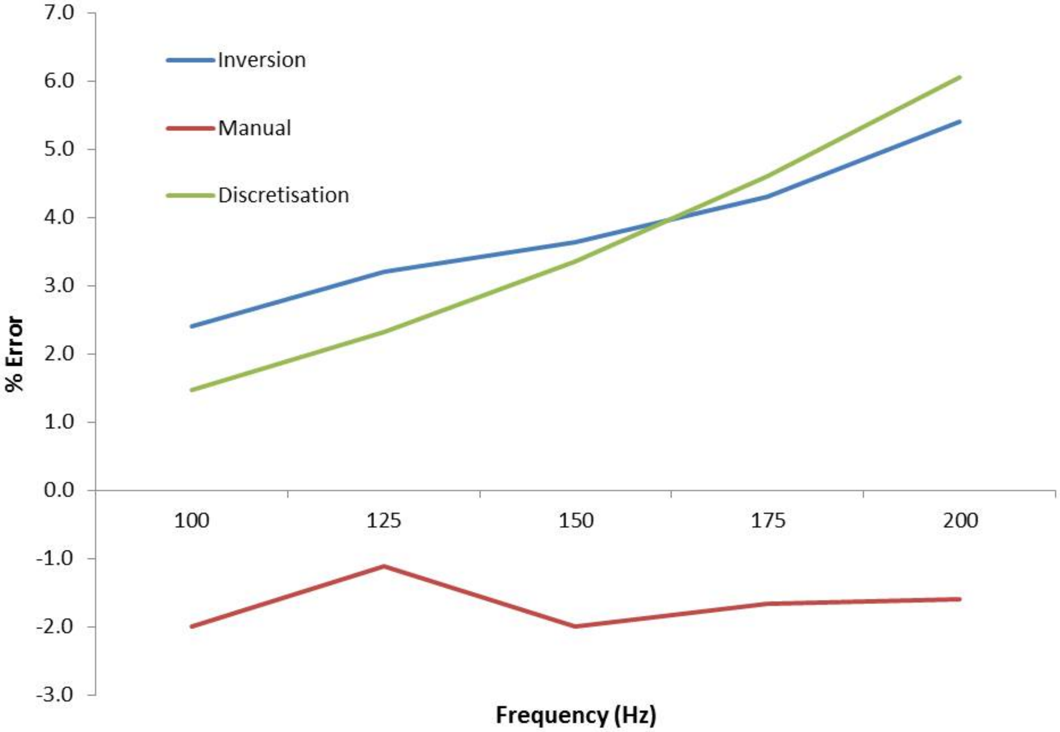

Figure 2.11: Error percentages calculated for the 3-D planar model. As with the 2-D planar models wave propagation closely approximated that of planar. Again relatively good accuracy was achieved with manual measurments whilst the inverted results correlated well with the estimated discretisation error.

2.3.3 3-D Non-Planar Models

Material Properties

Increasing the prescribed shear modulus of the uniform model resulted in an increase in the measured shear modulus through inversion (figure 2.12). In all cases the insert shear modulus was an overestimation. Whilst the size of the overestimation was 31% for the 2 kPa model, it was in the range of 3-5% for all prescribed other shear moduli. Artefacts appeared towards the bottom of the 2 kPa model where wave propagation appeared reduced (figure 2.13).

Increasing the prescribed insert shear modulus increased the measured insert value in all three insert models whilst the background measurement remained relatively constant throughout. In all cases the shear modulus was overestimated (figures 2.14-2.16). In the

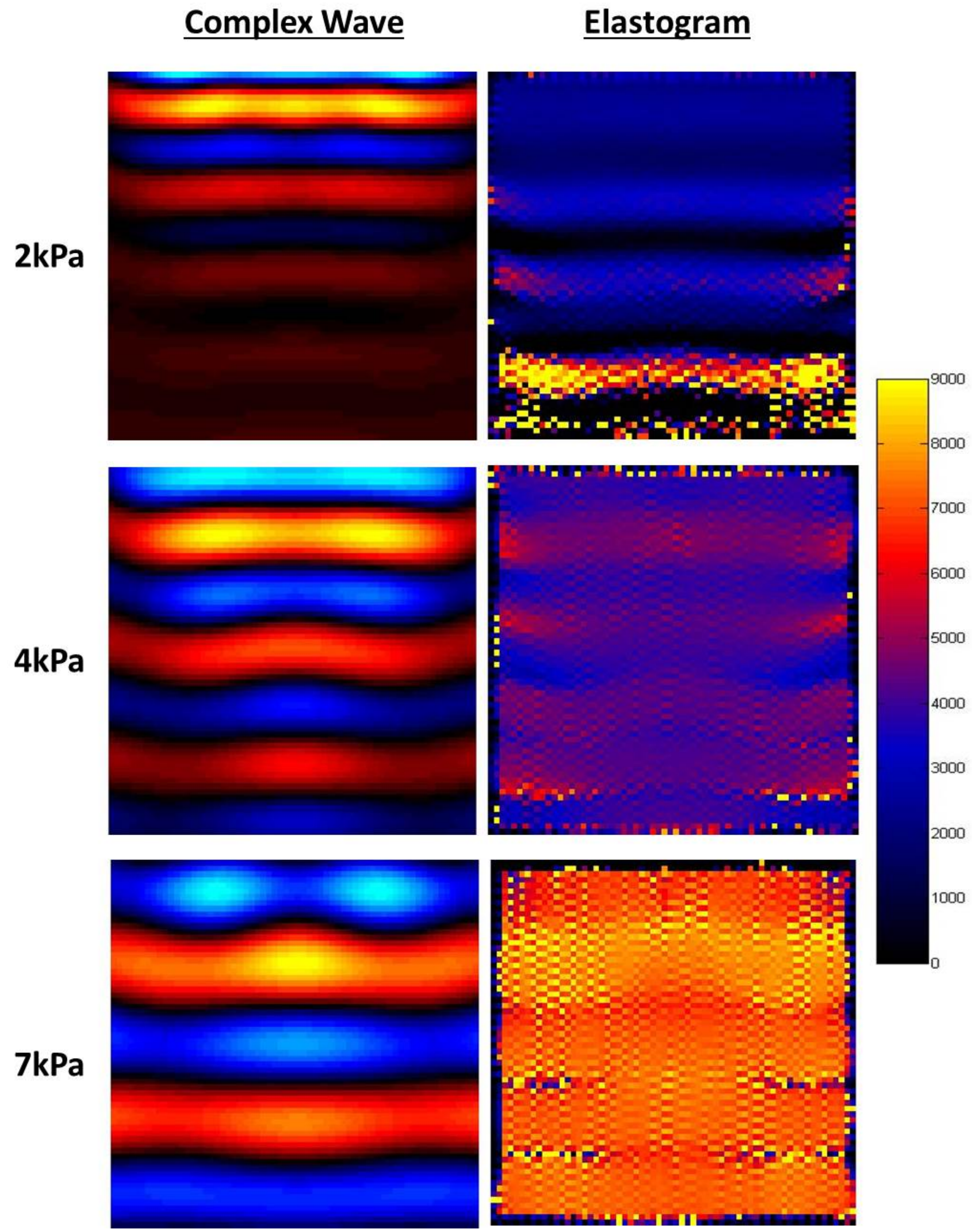

Figure 2.12: Examples of the complex waves and elastograms for the non-planar uniform model. Wave propagation less closely approximated planar wave propagation than in the 2- and 3-D planar models. The resulting elastograms were less smooth. Additionally the introduction of viscoelastic properties led to increased damping, particularly at low shear moduli. This was reflected by artefacts in the lower regions of these elastograms.

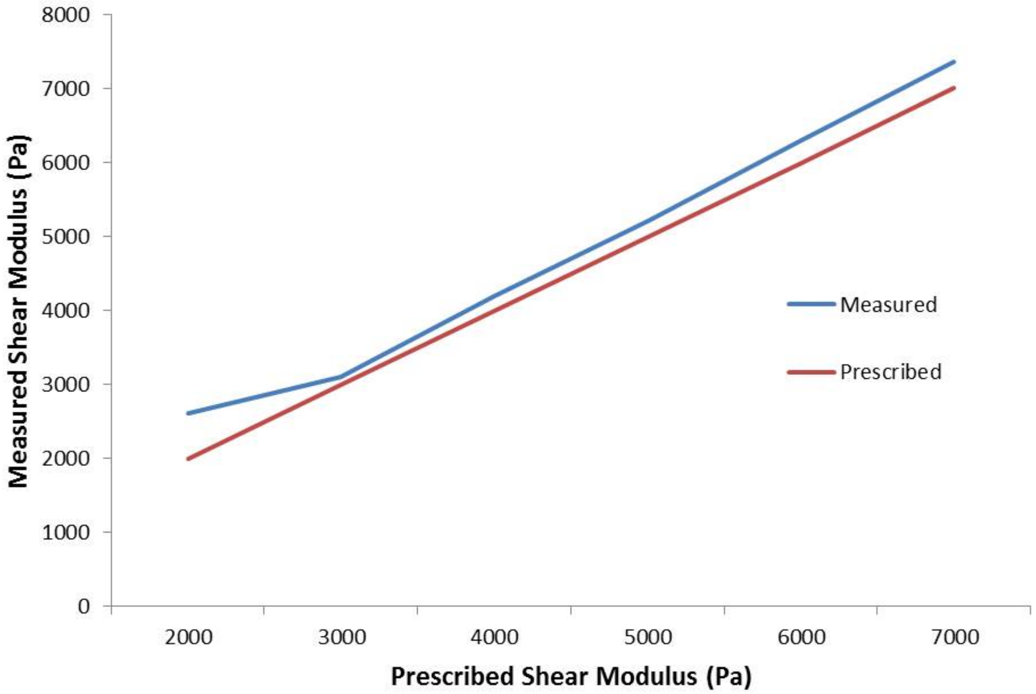

Figure 2.13: Measured shear modulus values against the prescribed values for the uniform model. With the exception of the 2 kPa model, errors in the measurements were consistently low.

case of the background measurements this overestimation was typically around 12%, whilst for the insert the size of the error was dependent upon the prescribed shear modulus: the overestimation tended to increase with increased prescribed shear modulus. The size of the error also seemed to show some dependency on the size of the insert with the errors in model 3 being lower than those in models 1 and 2 (figure 2.17).

Increasing the background shear modulus in insert model 1 resulted in an increase in the background measurements (figures 2.18 and 2.19). Again all measurements were overestimations whilst the size of the error increased with the prescribed shear modulus: 7% for a background shear modulus of 3 kPa in comparison to 30% for 15 kPa. There was a wide range of errors in the shear modulus measurements of the insert in this experiment (7-29%), however there did not seem to be a direct relationship between the size of the error and the prescribed background shear modulus.

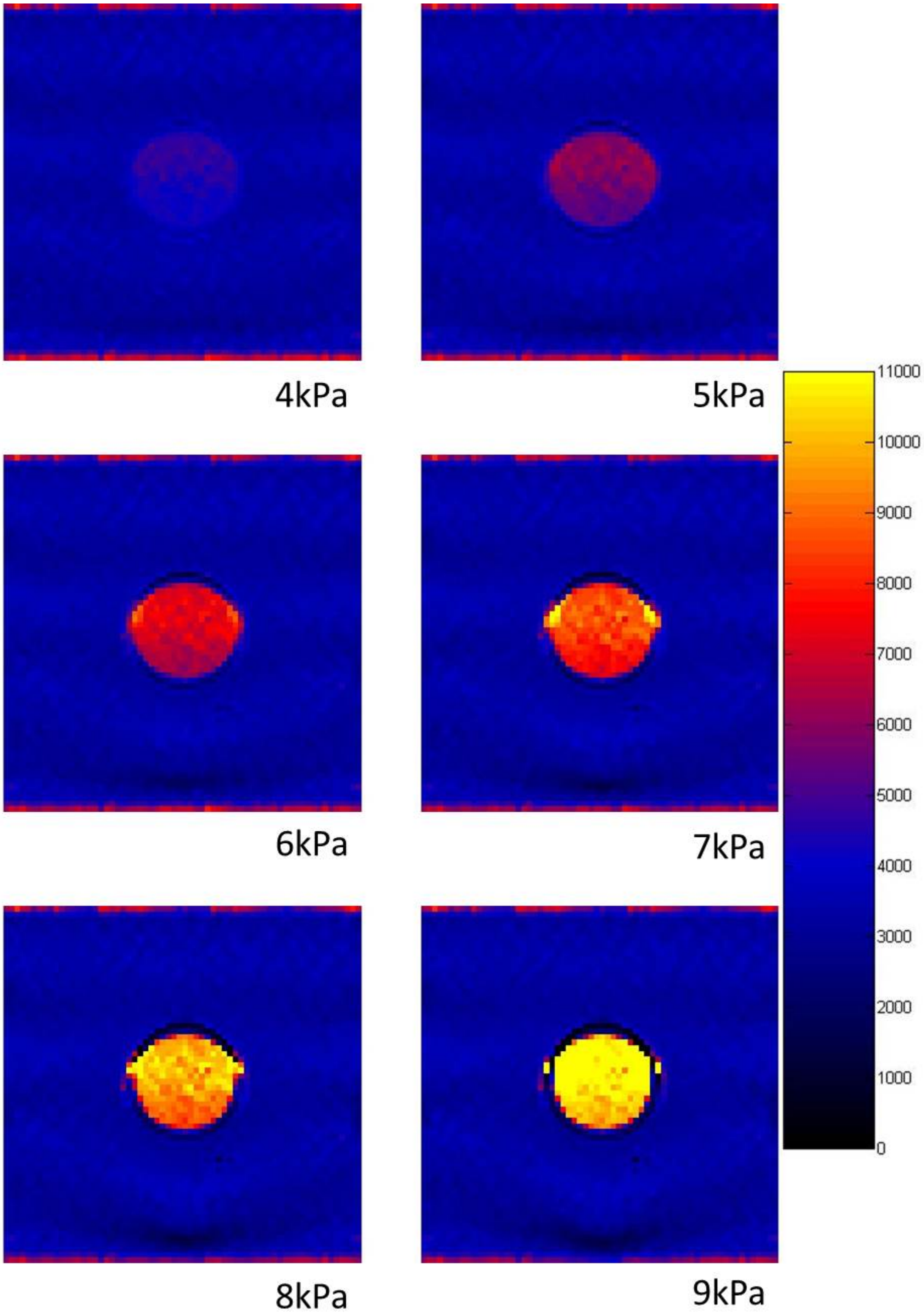

Figure 2.14: Elastograms for insert 1 model with a range of prescribed insert shear modulus values. Increasing the prescribed shear modulus of the insert had a notable effect on its stiffness in the elastogram.

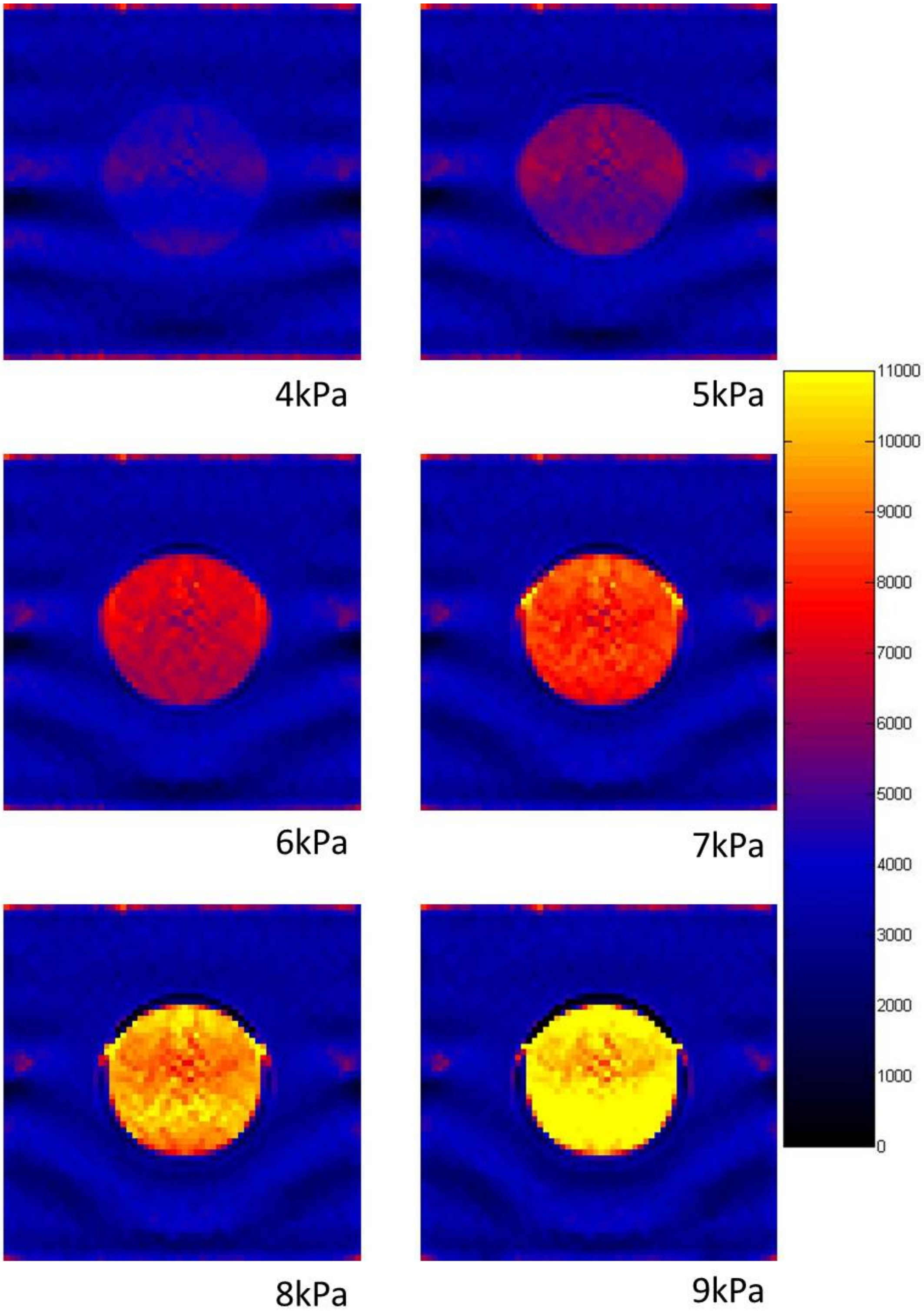

Figure 2.15: Elastograms for insert 2 model with a range of prescribed insert shear modulus values. Increasing the prescribed shear modulus of the insert had a notable effect on its stiffness in the elastogram.

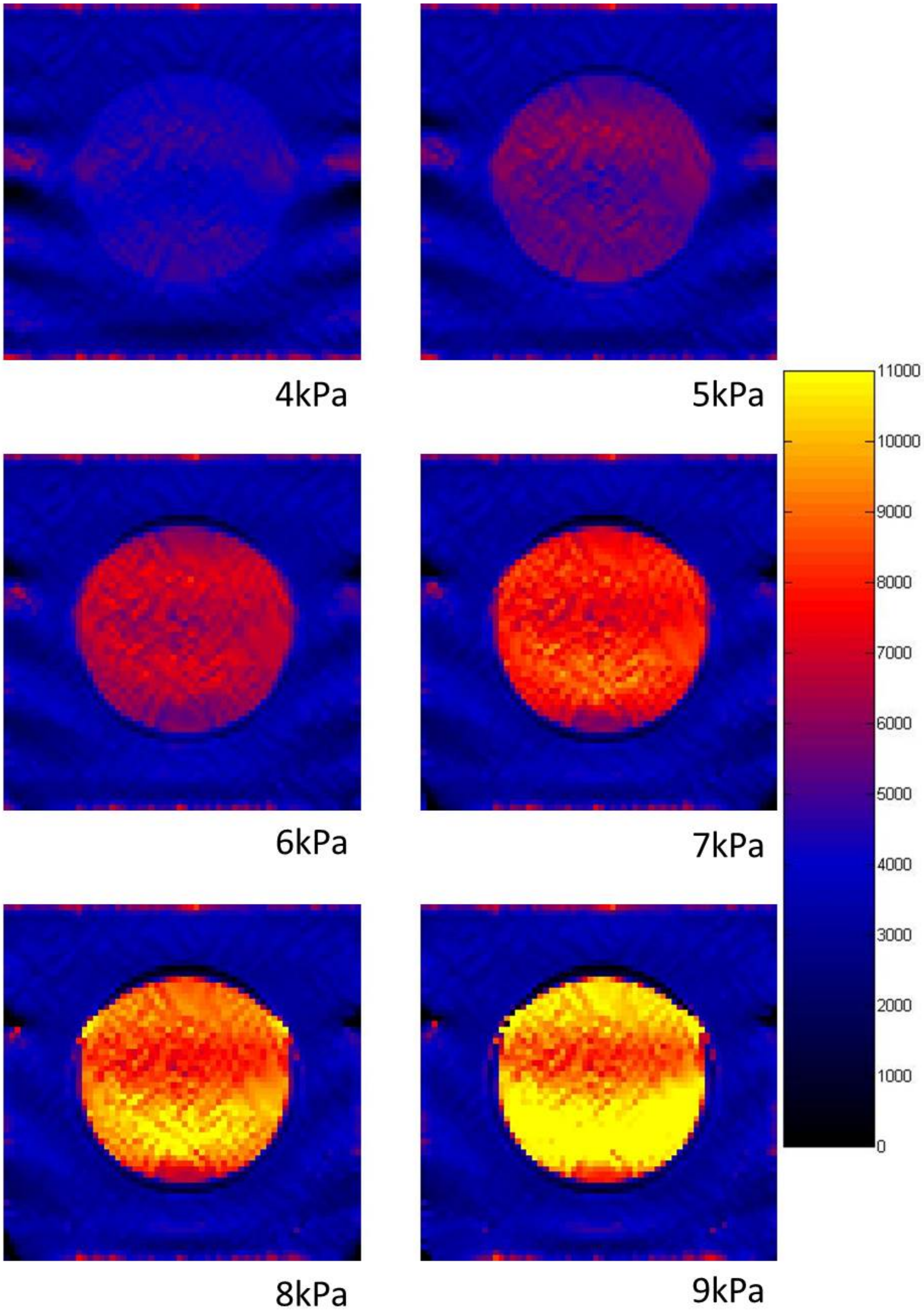

Figure 2.16: Elastograms for insert 3 model with a range of prescribed insert shear modulus values.Increasing the prescribed shear modulus of the insert had a notable effect on its stiffness in the elastogram.

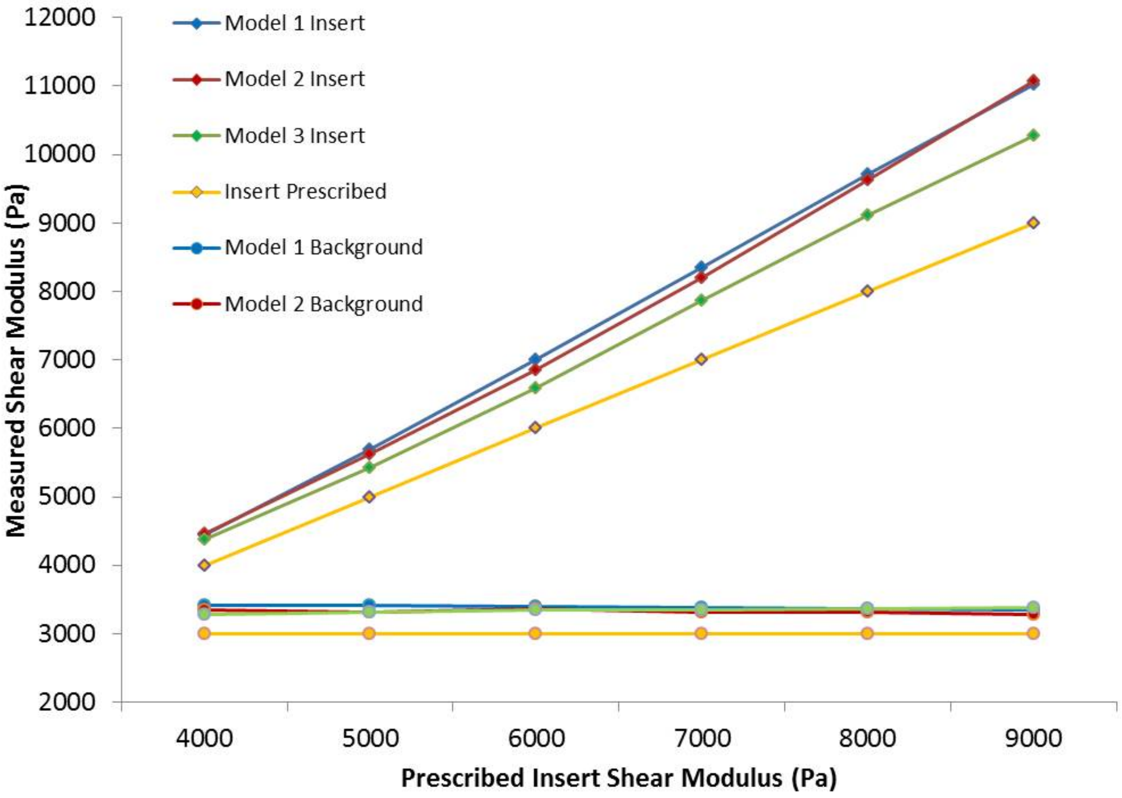

Figure 2.17: Measured shear modulus values against the prescribed values for the insert models. Values in the larger model 3 insert were more accurate than those measured in the model 1 and 2 inserts.

Frequency

Shear modulus measurements in the uniform model were again overestimated. This error seemed to show some slight dependency on the frequency of the measurements with errors of 8, 9 and 9% for frequencies of 50, 60 and 70 Hz respectively contrasting with errors of 5, 5 and 6% for frequencies of 80, 90 and 100%. Visual inspection of the complex wave image shows that the amplitude of the wave propagation towards the bottom of the model was reduced in the 100 Hz simulation more than at lower frequencies. Whereas the elastograms of these regions at lower frequencies were relatively smooth, the same regions from the 100 Hz simulations seemed to represent a wave structure. Examples of the complex wave images and the elastograms are shown in figure 2.20 whilst the data is graphically represented in figure 2.21.

For the insert models the errors in the measurement of the background shear modulus were relatively consistent and similar for all three models with errors typically in the range of

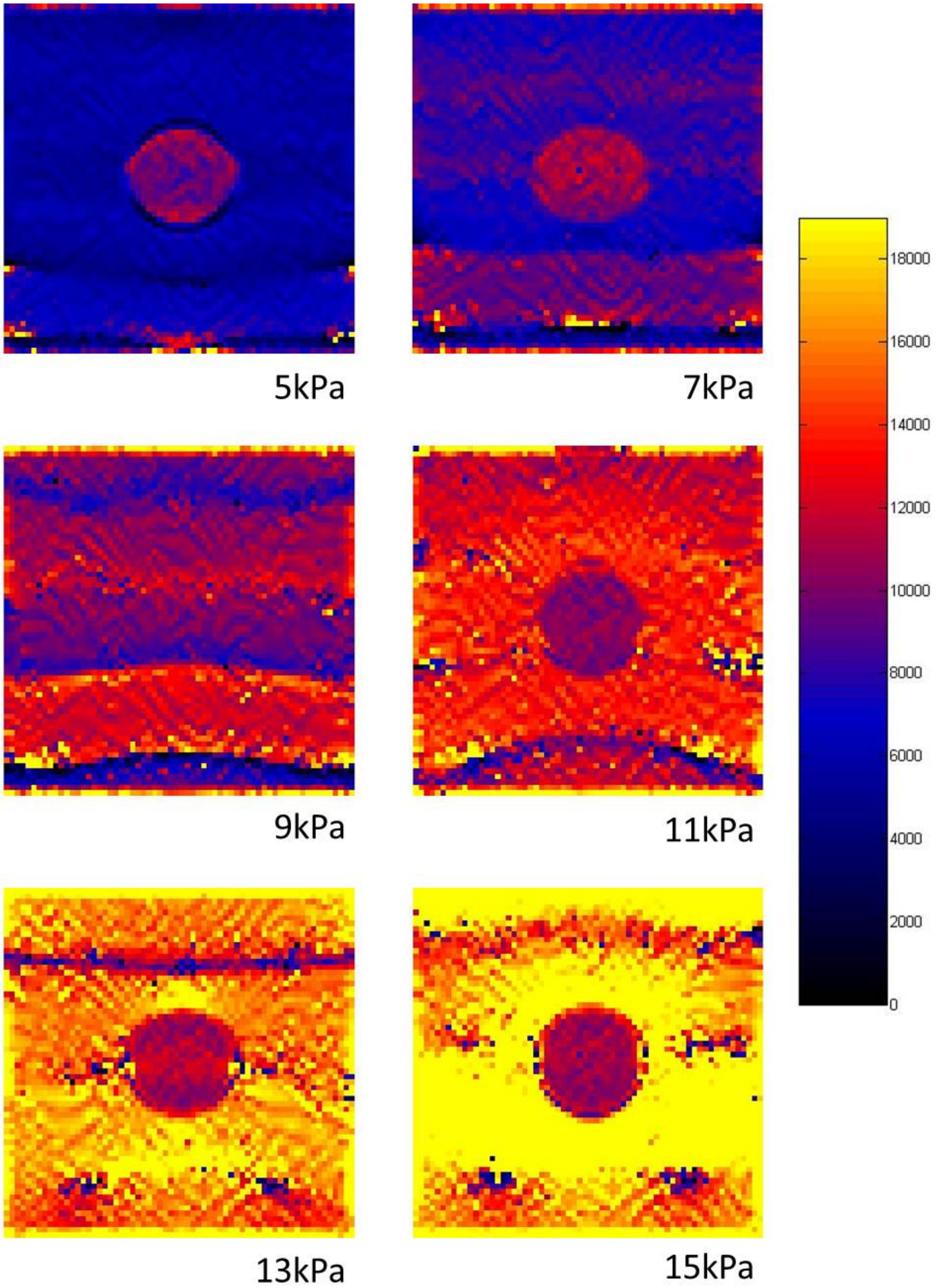

Figure 2.18: Elastograms for insert 1 model with a range of prescribed background shear modulus values. Increasing the prescribed shear modulus had a notable effect on its stiffness in the elastogram.

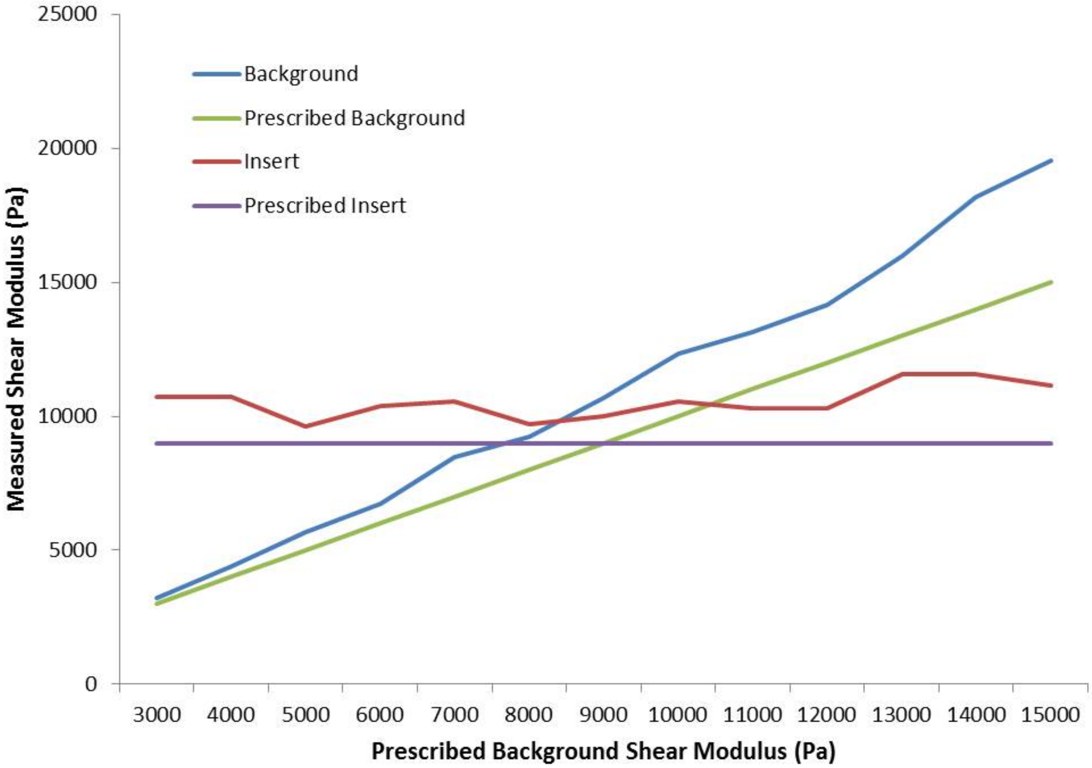

Figure 2.19: Measured shear modulus values against the prescribed values for the insert 1 model when the prescribed shear modulus for the background is varied. Errors in the insert measurement were variable but appeared to have no direct relationship with the prescribed shear modulus of the background.

10—13%. There seemed little obvious dependency on the size of these errors with respect to frequency. Errors in the measurements of the inserts were largely dependent on the frequency with large overestimations occurring at 50 (86% for model 1) and 60 Hz (40% for model 1). The extent of the overestimation was typically lower in the insert 3 model than in the insert 1 and 2 models (figures 2.22-2.25).

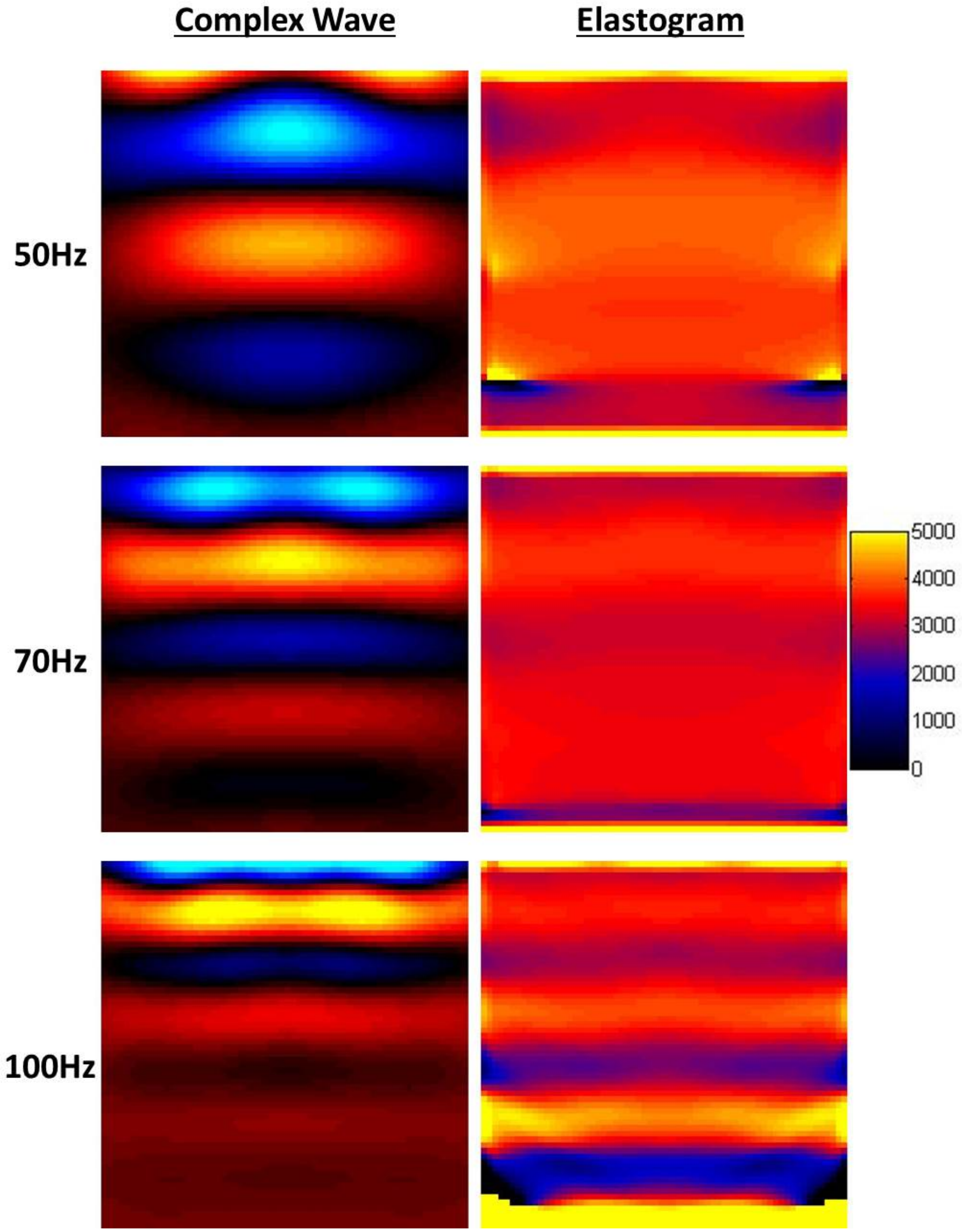

Figure 2.20: Elastograms and complex wave images for the uniform model for frequencies of 50, 70 and 100 Hz. Amplitudes in the lower regions of the models were significantly lower at high frequencies. This resulted in artefacts in the elastograms in these regions of the model.

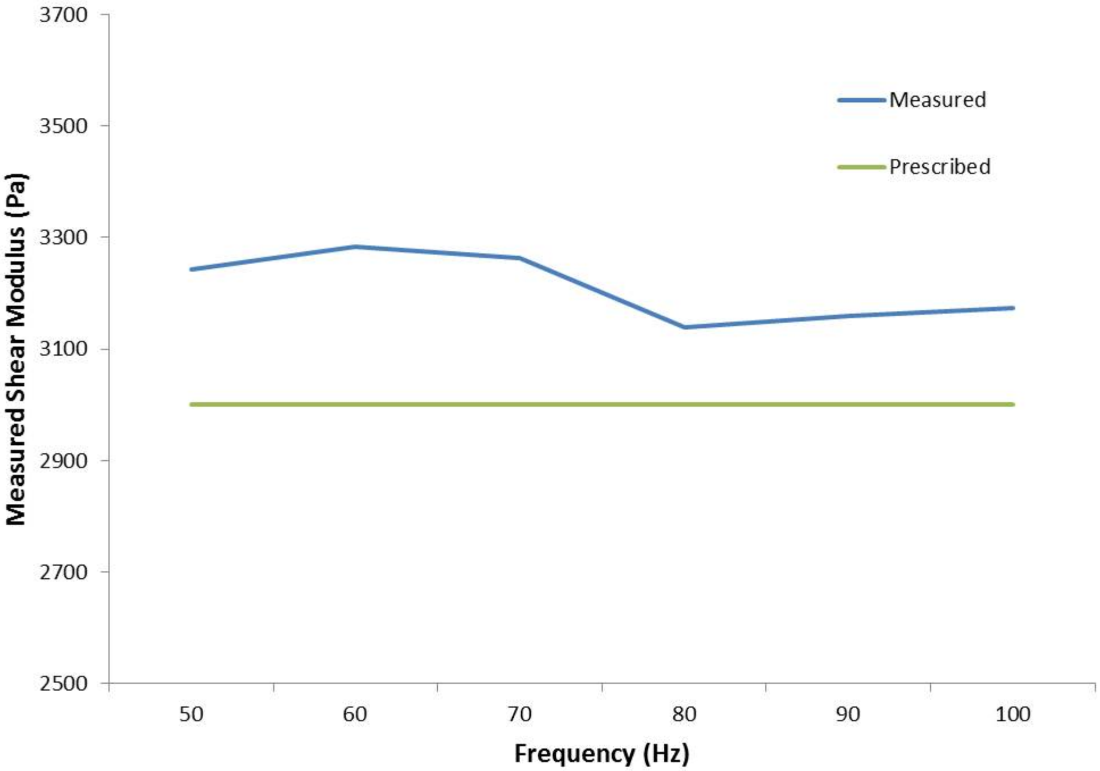

Figure 2.21: Measured shear modulus values against frequency for the uniform model. Errors seemed slightly higher at the lower frequencies.

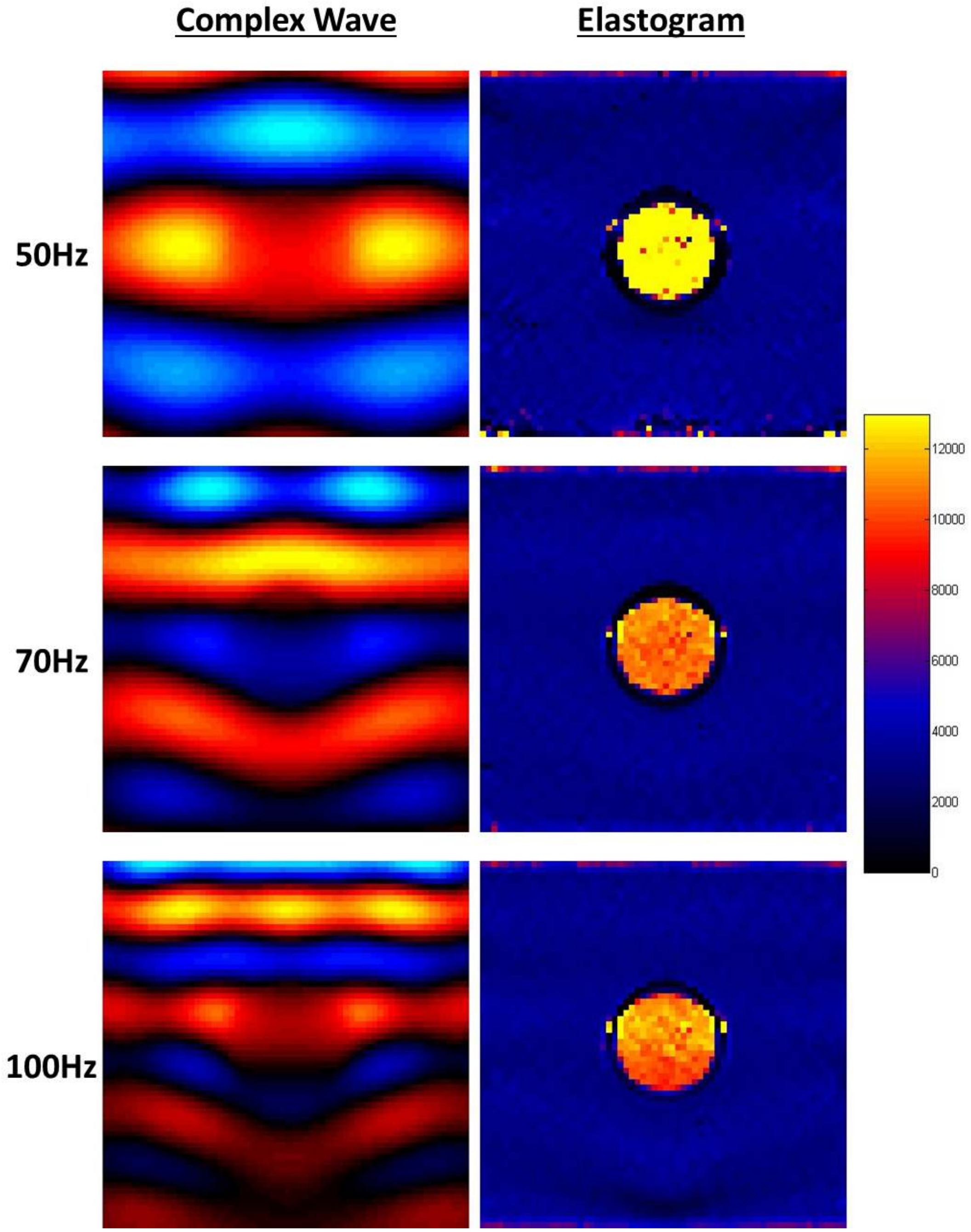

Figure 2.22: Elastograms and complex wave images for the insert 1 model for frequencies of 50, 70 and 100 Hz. The insert appeared noticeably stiffer in the elastogram at 50 Hz than at 70 or 100 Hz.

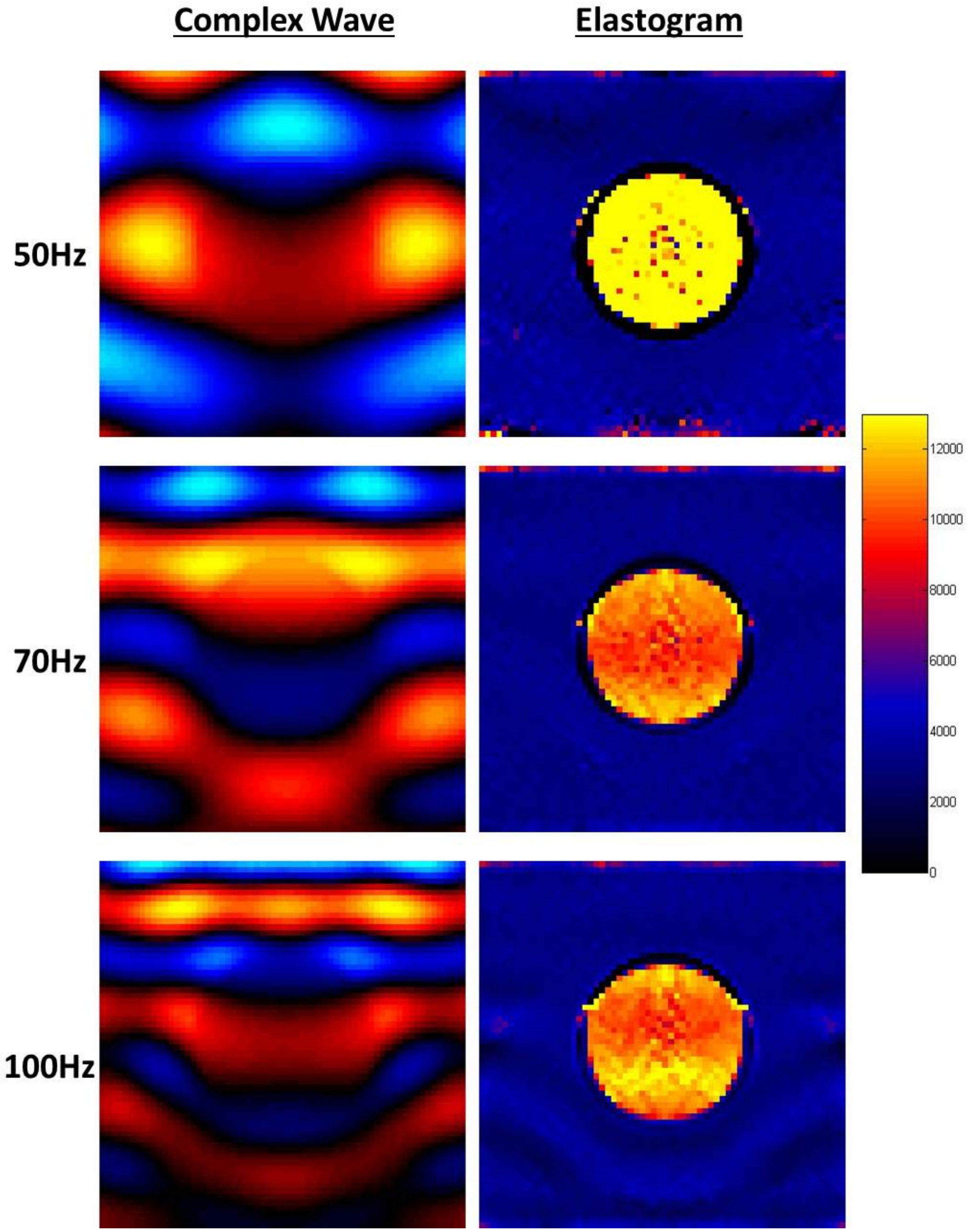

Figure 2.23: Elastograms and complex wave images for the insert 2 model for frequencies of 50, 70 and 100 Hz. The insert appeared noticeably stiffer in the elastogram at 50 Hz than at 70 or 100 Hz.

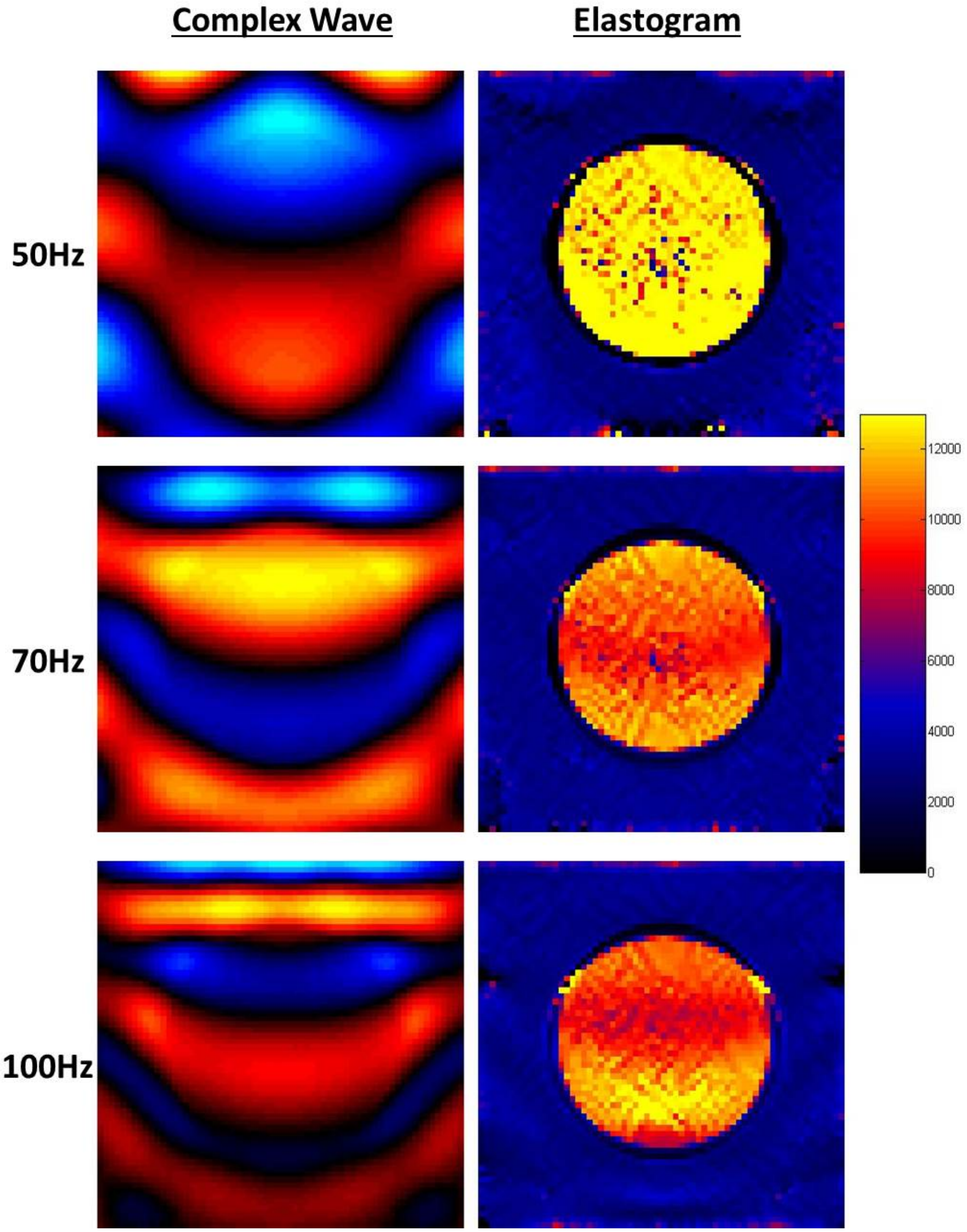

Figure 2.24: Elastograms and complex wave images for the insert 3 model for frequencies of 50, 70 and 100 Hz. The insert appeared noticeably stiffer in the elastogram at 50 Hz than at 70 or 100 Hz.

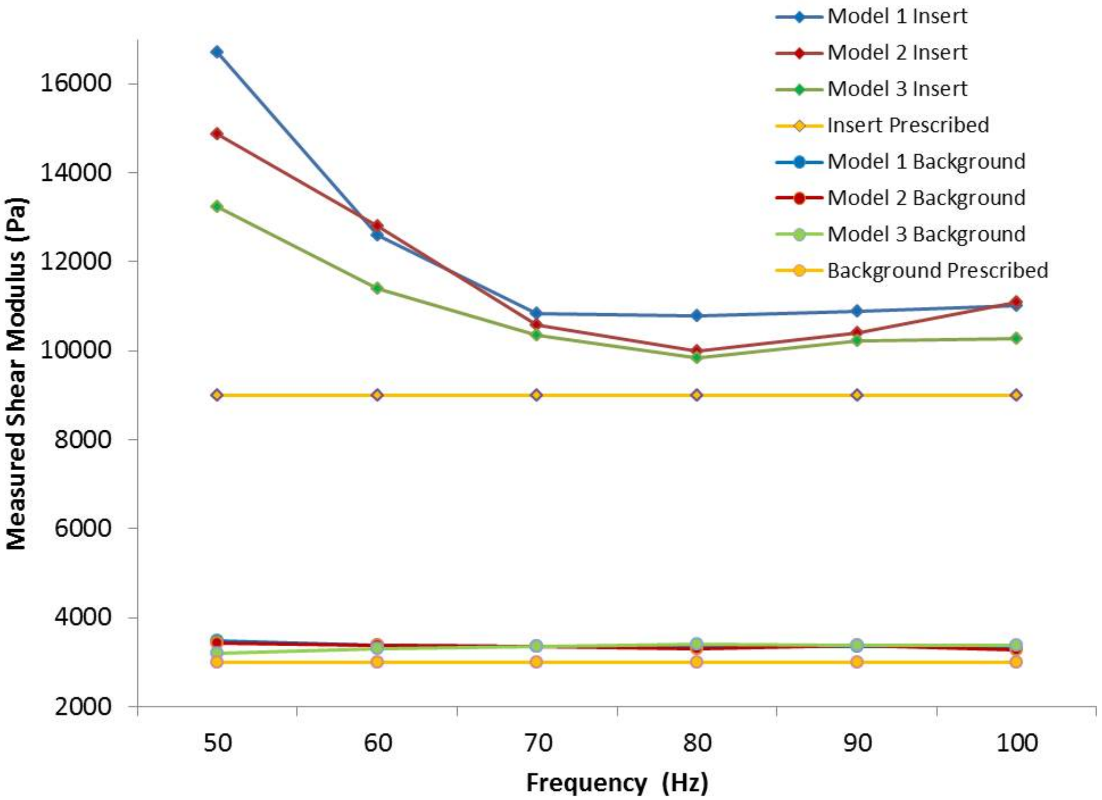

Figure 2.25: Measured shear modulus values against frequency for the insert models. In all three models the measured shear modulus of the insert was dramatically higher at lower frequencies. This effect decreased with increased insert size.

Boundary Conditions

Measurements in both the background and the insert were overestimated for all prescribed shear moduli with all the boundary conditions. In the inserts the greatest errors were obtained for the x-symmetry boundary conditions, with errors larger than 20% for all prescribed insert values. Similar overestimations were also achieved for the encastred boundary conditions. The size of the overestimations was greatly reduced using y-symmetry and z-symmetry boundary conditions with errors in the range of 7-13%.

The sizes of the overestimations were reduced in the background. The largest overestimation for the majority of the prescribed background values was obtained using encastred boundary conditions (7-13%). The range of error values was similar for all three of the symmetric boundary conditions in the range of 6-9% (figure 2.26).

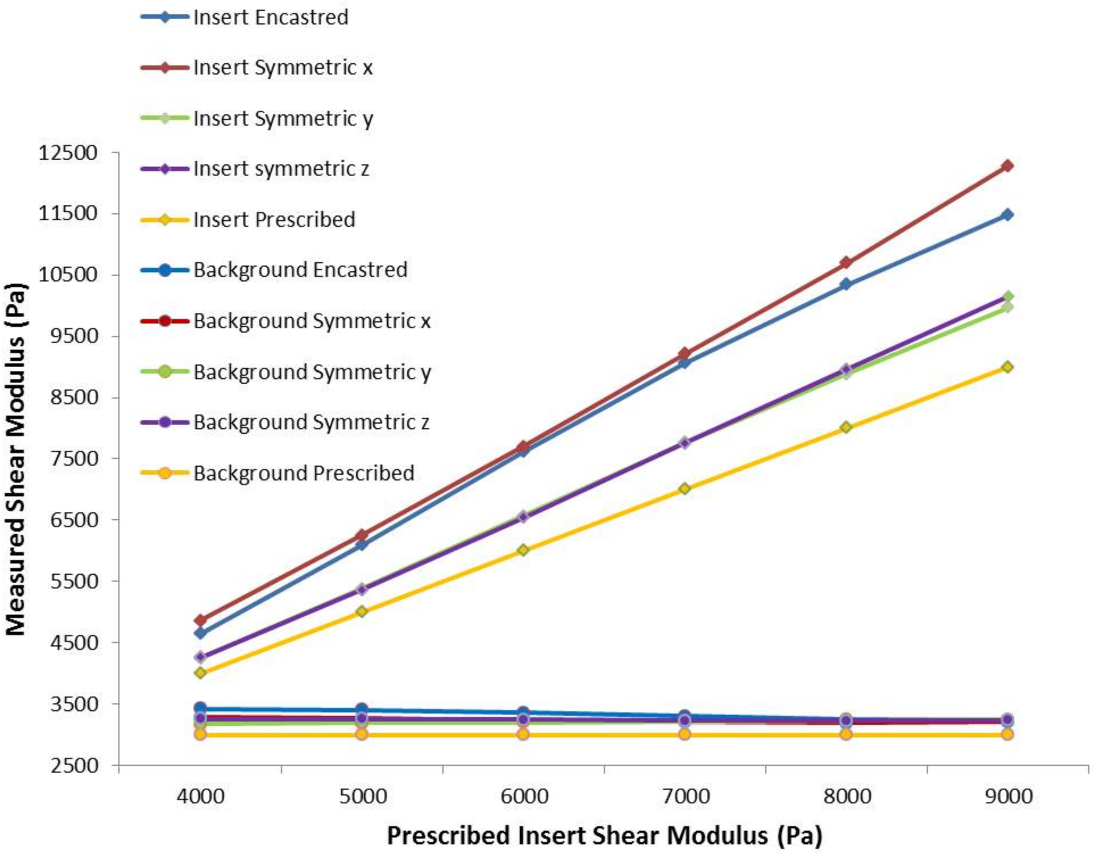

Figure 2.26: Measured shear modulus values for the different boundary conditions used in the insert 1 model. The type of boundary condition applied had a clear impact on the measurments. Encastred and x-symmetry boundary conditions caused large overestimations. These were reduced using y- and z-symmetry conditions.

Wave Decomposition

Fractional wave contribution values typically appeared independent of the shear modulus of the insert. There was little difference between the values for the x, y and z-symmetric boundary conditions (typically around $0.05 - 0.06$), however, the value for the encastred boundary condition was lower (between $0.025 - 0.03$) (figure 2.27). Inspection of the maps of the fractional wave contribution showed that the value for the y and z-symmetric boundaries was smaller in the lower regions of the model, whereas there appeared little spatial dependence for either the encastred or x-symmetric boundary conditions (figure 2.28).

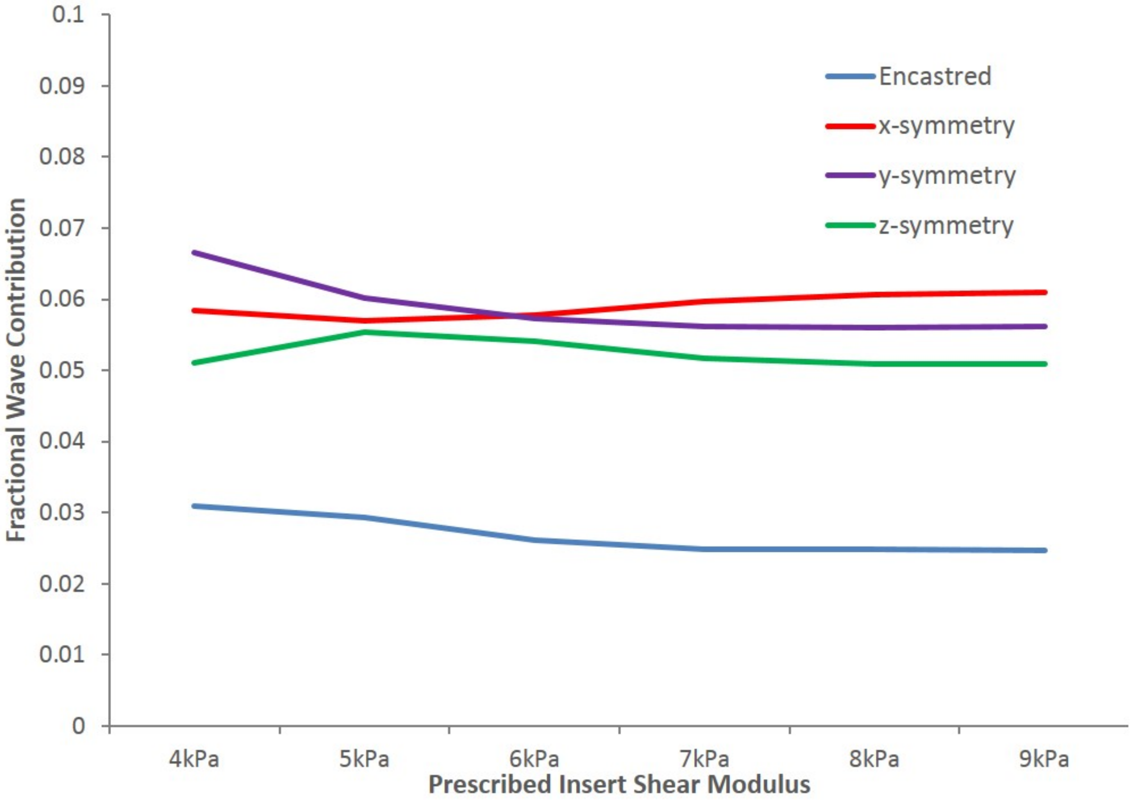

Figure 2.27: Graph showing the fractional wave contribution for the different boundary conditions. The contribution was smaller for the encastred boundary condition than the other three boundary conditions tested.

Constraints

The background and insert measurements from the tied constraints and the merged parts simulations matched each other almost exactly (figure 2.29). Visual inspection of complex wave images showed propagation of the wave in both sections of the model. In all

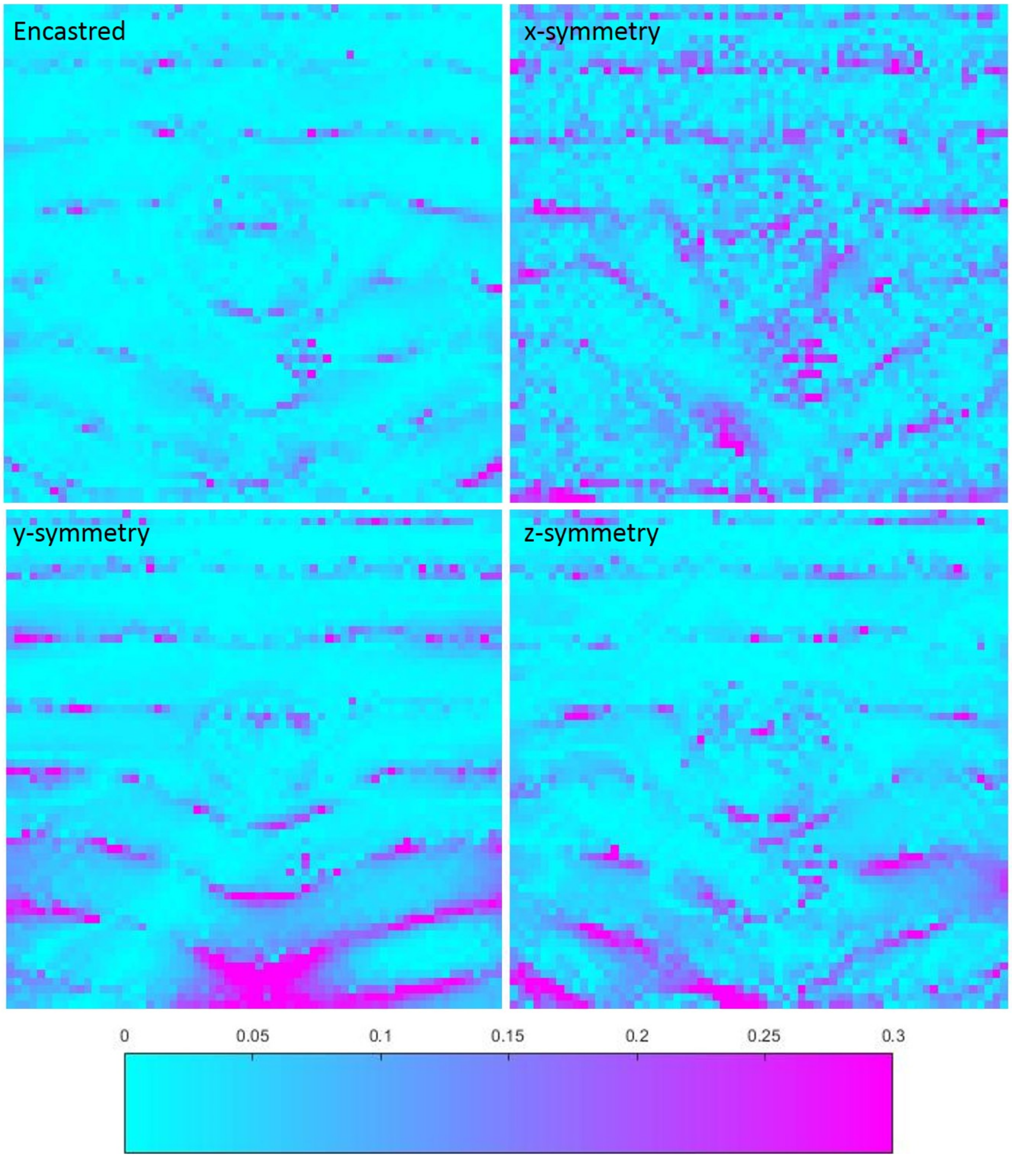

Figure 2.28: Maps of the fractional wave contribution for the different boundary conditions for the 9 kPa model. For the y and z-symmetric boundaries the values typically seemed to increase towards the lower regions of the model.

of the frictional interaction simulations the measurements in the background were slight underestimations of around 2.5%. Large errors were obtained in the inserts however, where overestimations were typically in excess of 300%. Inspection of the complex wave images showed that whilst wave propagation could be observed in the background, the amplitudes of the waves within the inserts was minimal (figure 2.30).

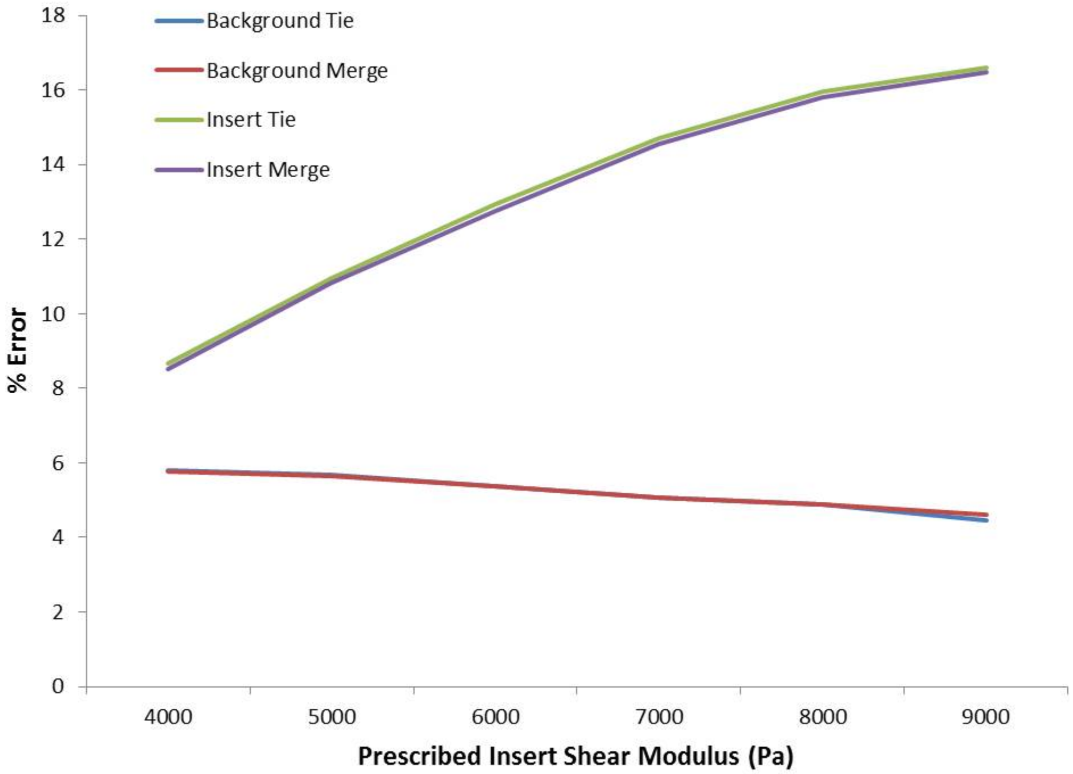

Figure 2.29: Errors in the shear modulus measurements for the tie constraints and merged parts used in the insert 1 model. The difference between the measurements following application of either condition was negligible.

Mesh

There was good consistency between the shear modulus measurements in the C3D8R and C3D10M elements. There were large overestimations for the C3D4 elements in both regions of the model (figure 2.31).

Simulation Type

Shear moduli calculated from the inversion algorithm and from manual measurements show good agreement between the transient and steady-state methods for variations in both frequency and shear modulus.

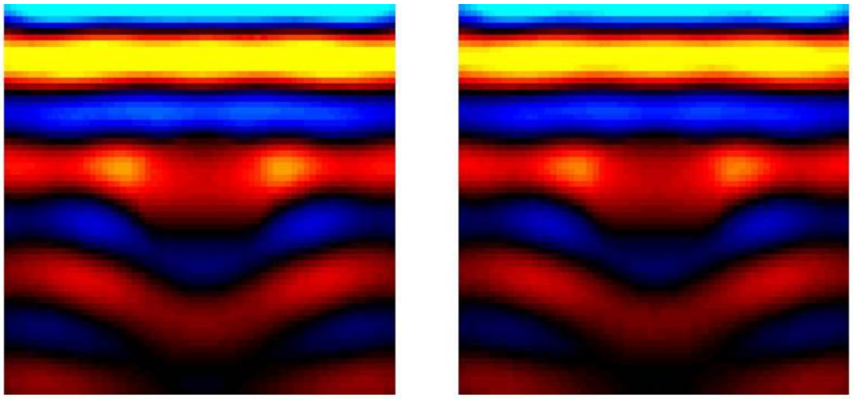

Tied

Merged

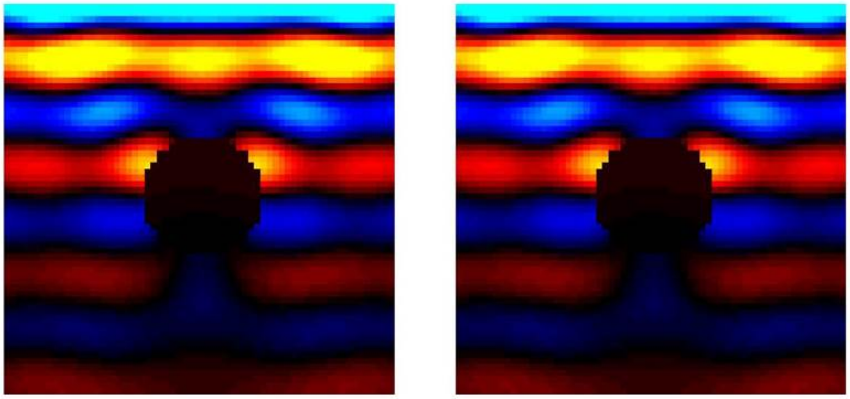

CoF 0.75

CoF 1.0

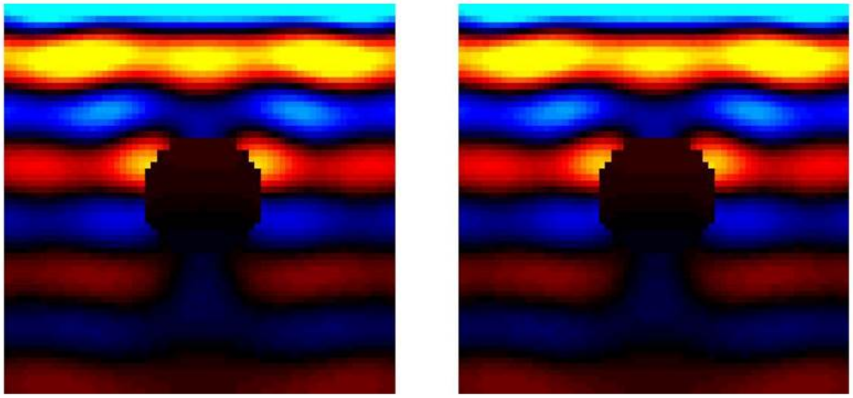

CoF 1.25

1.5kPa

Figure 2.30: Complex waves images for the tied constraints, merged parts and the four coefficients of friction tested. Wave propagation in the tied and merged models looked almost identical, whereas for all defined coefficients of friction amplitudes of the waves in the insert was minimal.

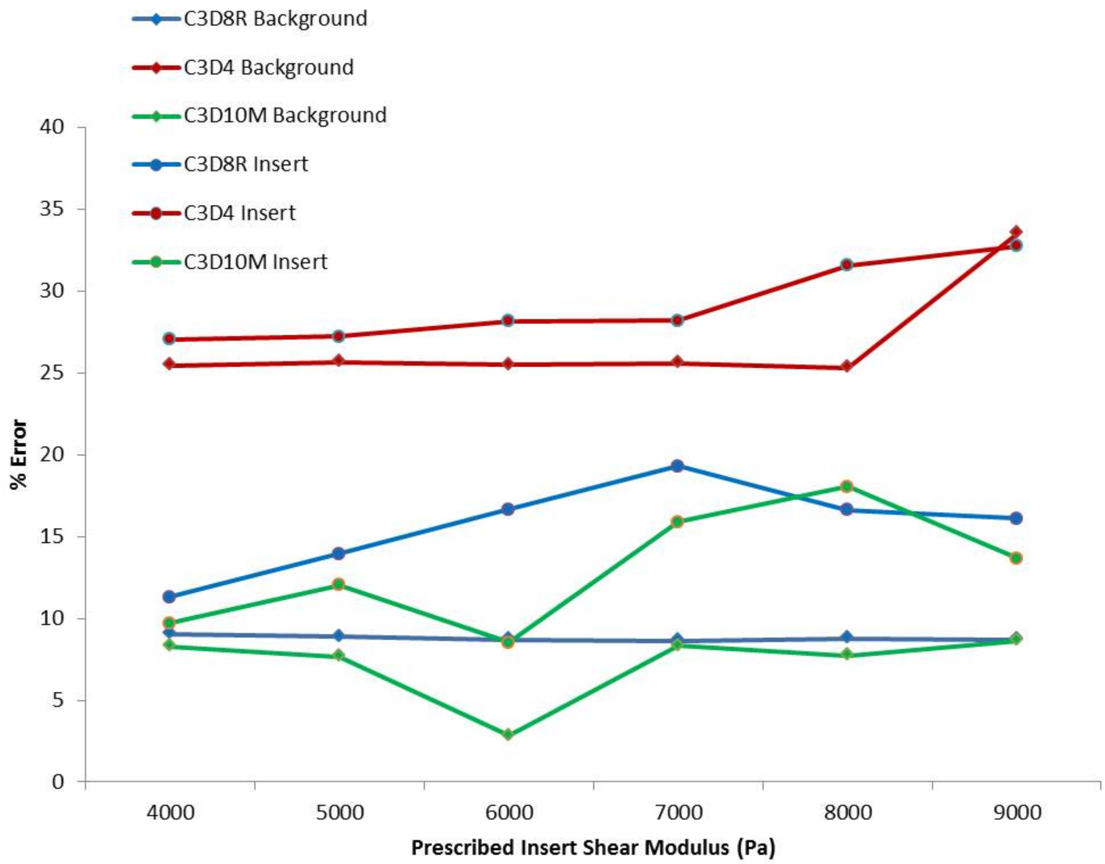

Figure 2.31: Errors in the shear modulus measurements for the different element types tested. The sizes of the errors using C3D8DR and C3D10M elements were relatively consistent with one another. Using C3D4 elements increased overestimations in both regions of the model.

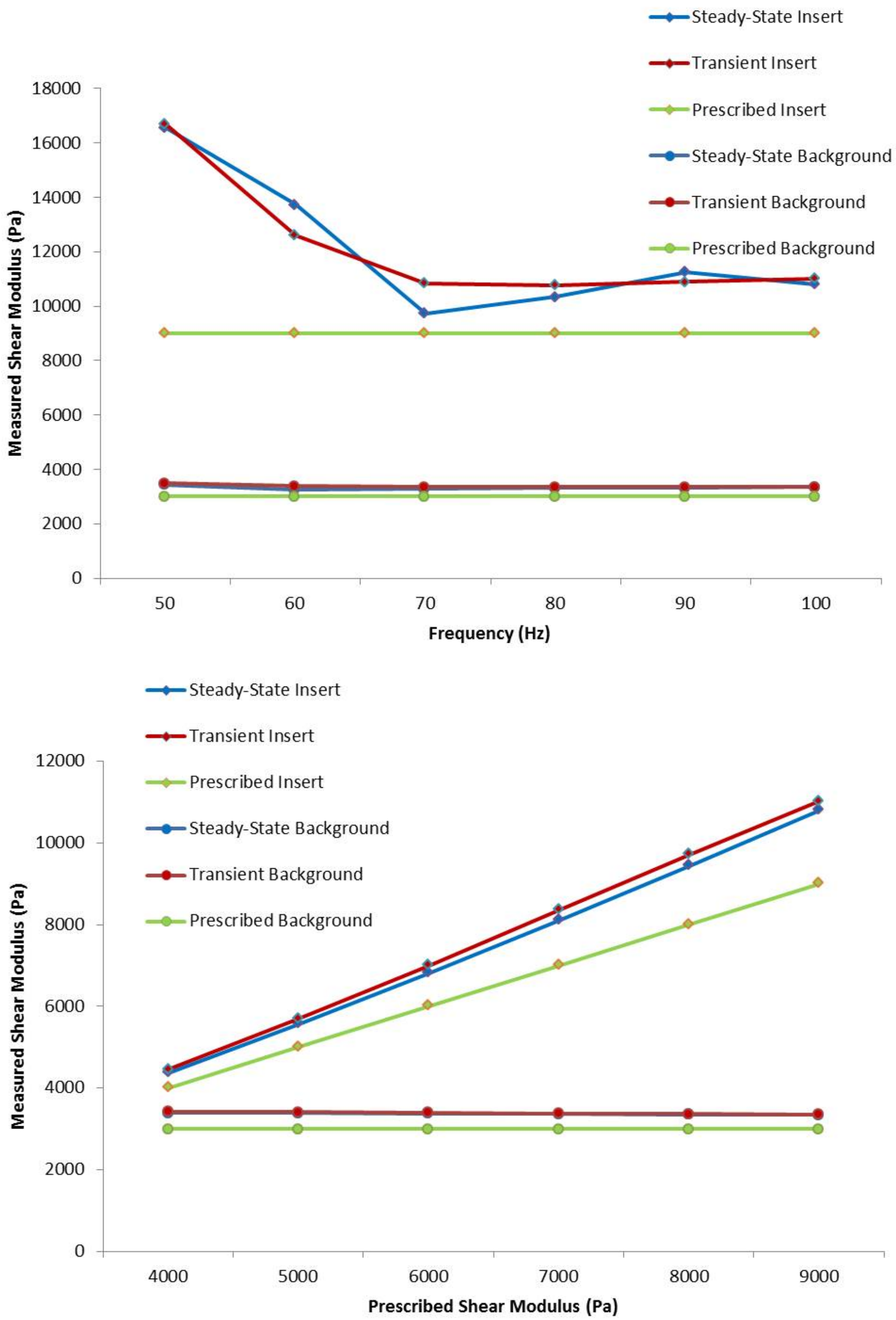

Figure 2.32: Measured shear modulus values for steady-state and transient simulations in the insert 1 model when frequency (top) and prescribed insert shear modulus (bottom) are varied. Results in both studies using the two techniques were in relatively good agreement with one another.

2.4 Discussion

This chapter aimed to demonstrate the development of a modelling technique that will be used throughout this thesis. The process began with the simplest scenario of planar wave propagation in a 2-D model with uniform properties, before extending this concept to 3-D. The planarity of the induced waves was then removed before finally an insert was placed into the geometry to investigate the effects it would have.

In the first stage of this development both the 2-D and 3-D models demonstrated good agreement with the theory of planar wave propagation underlying the 2-D MRE DI. Firstly these measurements were in good agreement with those that would be expected as a result of the discretisation error, whilst the manual measurements, which are void from discretisation errors, also showed close agreement with the prescribed values (figures 2.9 and 2.11). Although manual measurements could be seen as user dependent and inaccurate, often the user makes the measurement simply by drawing a line upon the complex wave image where they believe the peaks to be from visual inspection and then using the software they are using to measure the length of the line [183], the method of measurement outlined here removed the user dependence in choosing the peaks of the wave and offered a comparatively high degree of accuracy as a result. Indeed the slight underestimation achieved under the planar wave conditions in the 3-D planar model is consistent with literature in that the FEA wave velocity was lower than the theoretical wave velocity as a result of mesh discretisation [190].

Despite the clear wave propagation and good resolution of the elastograms in all models where non-planar waves were examined, the shear modulus measurements achieved by inversion typically suffered from an overestimation which was particularly prevalent in the inserts at low frequencies (figure 2.25). There are three potential sources for such an error: numerical errors from the modelling; an inappropriate choice of modelling parameters to represent the real-life situation being modelled; or an inability of the inversion to truly characterise the material properties of the material based upon the propagating wave. These three possible sources of error are discussed in the following paragraphs.

In the first regard it should be noted that numerical errors are always present in FEA. Their effect however can be limited by increasing the density of the mesh. For all the models described in this thesis convergence studies were performed, with the mesh density used in this chapter being well above the density at which convergence has been defined as being achieved (Appendix III). As such, whilst numerical errors undoubtedly have some effect on the results in this chapter, in all likelihood they are so small as to have little significant bearing on the results.

Conversely it is clear that modelling parameters can have a significant effect on the accuracy of the shear modulus measurements produced by the inversion algorithm. To this end the use of C3D4 elements dramatically increased the size of the overestimation (figure 2.31). This effect was due to tetrahedral elements being structurally stiffer than hexahedral elements and thus has important implications when meshing more complex structures that are incompatible with a hexahedral mesh [191, 192]. It was shown here that the problem can be resolved by using the quadratic tetrahedral C3D10M elements, though this increases computational time.

The definition of the constraint between two parts of the model also impacts upon the accuracy of the inversion algorithm. Whilst there was little difference in the shear modulus measurements when the two parts were tied together and when they were merged with one another to create a single part (figure 2.29), defining a frictional coefficient between the two parts greatly reduced the transfer of the wave from one region to another and in the context of the insert model here, caused large overestimations in the measured shear modulus of that insert (figure 2.30).

Inaccuracies resulting from the definition of boundary conditions are likely to be due to both the use of inappropriate modelling parameters and a failure of the inversion algorithm to truly characterise the material properties. The encastred boundary condition has often been used in FEA simulations of MRE [170, 181], though in reality the boundaries in MRE will not be totally fixed: waves will pass through a patient into the scan table and with respect to phantoms, the waves will also be transmitted into the phantom's case. Symmetric boundary conditions where motion is fixed in just one direction and uninterrupted in the other two is also not representative of reality. Unfortunately the range of boundary conditions offered by *Abaqus*, and indeed most other FEA software packages, is fairly limited and does not allow a better approximation to reality. The boundary conditions investigated in this chapter produced a wide range of results, with encastred boundary conditions seeming to result in large overestimations in the stiffness in both the background and insert of the model. To this end y-symmetric boundary conditions typically produced the most accurate results in both regions (figure 2.26). This was perhaps because motion of the wave in the shear planes was undisturbed when the boundary condition was applied in this direction.

For all the boundary conditions tested in this chapter, the contribution of the shear wave to the displacement term of the inversion algorithm was greater than the compressional wave, since the value was significantly lower than 0.5, though it was not inconsequential for any of the boundary conditions tested. The boundary condition with the lowest fractional wave contribution values, the encastred condition, suffered from large overestimations. Furthermore, whilst there were limited differences between the contribution of the compressional wave for all three symmetric boundary conditions, there were fairly large differences in the size of the overestimations between these conditions. This suggested that whilst compressional waves do influence the measurement and result in errors from the inversion algorithm, there were other more significant sources of errors in the models within this chapter. In this regard it should also be noted that for the y and z-symmetric boundary conditions, regions where the fractional wave contributions were high were often towards the edge of the model and outside the regions of interest used in this chapter (figure 2.28).

Whilst boundary conditions present a clear problem in the definition of the model and attempting to represent realistic conditions, they also present a problem in the MRE inversion. Firstly the existence of a boundary invalidates the assumption of an infinite homogenous medium upon which the algorithm is derived [156]. Additionally waves reflected off the boundary interfere with those induced and result in interference patterns appearing in the wave image. Whilst reflections and scattering are prevalent in the human body, they are typically more noticeable in phantoms and FEA simulations, where the boundaries between regions are clearly defined [152, 193]. Whilst the use of viscoelastic properties in the simulations presented in this chapter helped to reduce the impact of reflections, their effects can be seen in the elastograms for the insert models as a small black ring around the inserts (figure 2.22). The ability to use directional filters to remove the effects of reflections and to smooth the elastograms is investigated in more detail in chapter

3.

Although the viscoelastic properties reduce the impact of reflections on the model they can also have an adverse effect on the measurements of the shear modulus. This has the potential to occur either when the values for the prescribed shear modulus are low, or when the frequency of the vibrations applied to the model are high, resulting in increased damping of the wave. In the 3-D non-planar uniform model the wave appeared to be highly damped in the complex wave image for a prescribed stiffness of 2 kPa thus leading to a degraded elastogram and the large overestimation in the measurement when compared to the other higher prescribed values (figure 2.12).

Seemingly the major issue, and one of the main sources of error in stiffness estimation, is the assumption of planar waves made by the inversion algorithm. Planar waves may be generated in a uniform phantom, however, inclusion of an insert causes the waves to be non-planar. It is thought that this was the main reason for the overestimation of stiffness measurements seen in the results of this chapter. This hypothesis was supported by the manual measurements made in the 2-D and 3-D planar wave models which showed relatively accurate measurements of the shear moduli (figures 2.9 and 2.11).

Whilst the 2-D inversion algorithm is commonly used throughout the literature, and indeed in this chapter, it should be recognised that it does not take into account the full wavefield [153]. In the instances where good approximation to planar wave propagation in the 2-D plane was achieved, sufficient accuracy was reached using the 2-D algorithm. In instances where the wave propagation less resembled planarity however, accuracy was reduced. It was therefore deemed likely that a more complete description of the wavefield would achieve a more accurate result and that the 3-D DI would be better equipped to deal with the types of waves created in this chapter.

The non-planarity of the waves also helped to explain the frequency dependence in the accuracy of the measurements. A visual comparison of the complex wave images from various frequencies showed that the lower frequency waves were less planar than those of higher frequency (figure 2.20). Whilst this may contribute to the overestimation of the shear modulus through inversion at lower frequencies, it should also be noted that the wavelength of the induced wave was longer for these lower frequencies. As a result a smaller fraction of the wave was captured in the region of measurement and it was seen that this was likely to have contributed to the overestimations seen here.

The relatively good agreement between the steady-state and explicit technique and particularly the existence of the large overestimations in the insert shear modulus at low frequencies in both models implied that the errors were due to the inability of the inversion algorithm to properly obtain the material properties from the wave fields (figure 2.32). Whilst the two simulation types were looking at the same problem they were solving it in different ways and achieving similar results. Since the explicit simulation runs for a finite time it only approximates steady-state and therefore it would be expected that the results would be slightly different. There are also practical differences between the two techniques: largely in the context of this thesis, the motivation was to create a technique that would be applicable to all types of post-processing software. For instance since the steady-state technique outputs in the frequency domain it was not possible to apply directional filters to data from it. An additional attraction of the transient methodology was that it generally had a shorter computational time than the steady-state.

Although increasing the prescribed shear modulus in all cases resulted in an increase in the measured shear modulus, the largest concern from the data presented in this chapter in the context of this thesis was the seeming variation in the shear modulus measurements for different size inserts. This suggests that the measurements are geometrically dependent which has significant implications upon the potential use of the technique for AAAs which vary greatly in terms of their size and shape.

2.5 Conclusions

An explicit method of simulating MRE has been demonstrated and compared favourably with a previously defined steady-state technique. Modelling parameters such as boundary conditions and element type were shown to have an impact on the measurements made using the 2-D DI algorithm. Overestimations in this technique were commonplace where planar waves were not concerned. The reasons for this warranted further investigation particularly to investigate whether these effects were still present if the 3-D inversion algorithm was used. Additionally the size of the inserts appeared to have an effect on the measurements made. Given the nature of this thesis with relation to AAAs this presented as a significant issue and was identified as warranting further work.

Chapter 3

The Impact of Geometry upon MRE Measurements

3.1 Introduction

Chapter 2 introduced an explicit FEA methodology to simulate MRE and investigated how modelling parameters affect the measurements made through the inversion of displacement data extracted from these models. The chapter raised several key questions in relation to this thesis. Possibly the most important was how the insert size affected the measurements made through inversion. The work in this chapter intended to investigate this in more detail, both in terms of the size of the insert in the plane of the complex wave image (its diameter), and the size of the insert outside the plane of the image (its length).

It was hypothesised that the overestimations commonly seen in chapter 2 were likely to be due at least in part to the incomplete datasets being analysed. This chapter therefore introduces 3-D analysis which takes into account the full displacement field and therefore has the potential to obtain more accurate measurements. Chapter 2 also demonstrated that the compressional wave influences the displacement term in the inversion algorithm. As such, larger models have been used in this chapter in an attempt to move the boundaries further away from the region of interest and help reduce this effect. Additionally it should be noted that whilst the compressional contribution varied with different boundary conditions, there did not seem to be a direct relationship between the size of the contribution and the size of the error in measurement. This suggested that other factors had a greater influence upon the accuracy of the measurement. It was therefore expected in this chapter that size and vibrational frequency would be the largest factors influencing the accuracy of measurement, and that through use of the 3-D inversion algorithm, when the insert was sufficiently large (in terms of its size both inside and outside the plane of the image) and for higher frequency vibrations, good accuracy would be achieved.

A recent extension of the 3-D algorithm is the multi-frequency dual elasto-visco (MDEV) inversion [194]. This combines the data from multiple frequencies to attain frequency independent material property variables. By doing this the technique aims to reduce the impact of reflections and to improve the resolution of the technique [165]. The abilities of 2-D and 3-D direct inversions and MDEV have therefore been compared in this chapter. An alternative method to MDEV for reducing the effects of reflections is directional filtering. Two such methods of achieving this are also introduced and analysed in this chapter [195, 196].

3.2 Methods

This section outlines the methodologies used in this chapter. The setup was based largely on the results acquired in chapter 2 and therefore further details regarding these parameters can be found in the methods section there.

3.2.1 Geometries

The dimensions of all the models used in this chapter were 80x80x100 mm^3. Each geometry contained a cylindrical insert placed at its centre. In order to investigate the effects of out-of-plane insert size, the length of the insert was varied, with lengths of 2, 4, 6, 10, 20, 30, 40, 50, 60, 70, 80, 90 and 100 mm used (figure 3.1). These inserts had a radius of 10 mm. To investigate the effects of in-plane insert size, inserts of radii 5, 10, 15, 20 and 30 mm were used. The length of these inserts was 100 mm. In all models the insert and background regions of the model were merged together as a single part.

3.2.2 Material Properties

In each model the shear modulus of the background was maintained at 3 kPa whilst the insert shear modulus was varied from 4-9 kPa. The viscoelastic properties were defined using the Kelvin-Voigt model of elasticity using a shear viscosity of 1 Pas. The density was 1047 kg·m^{-3} whilst the material was assumed near incompressible with a Poisson's ratio of 0.49.

3.2.3 Modelling Setup

Load

The load was applied to a set of nodes on the upper surface as a concentrated force in the z-direction with a force per node of 0.001 N. The size of this region was consistent

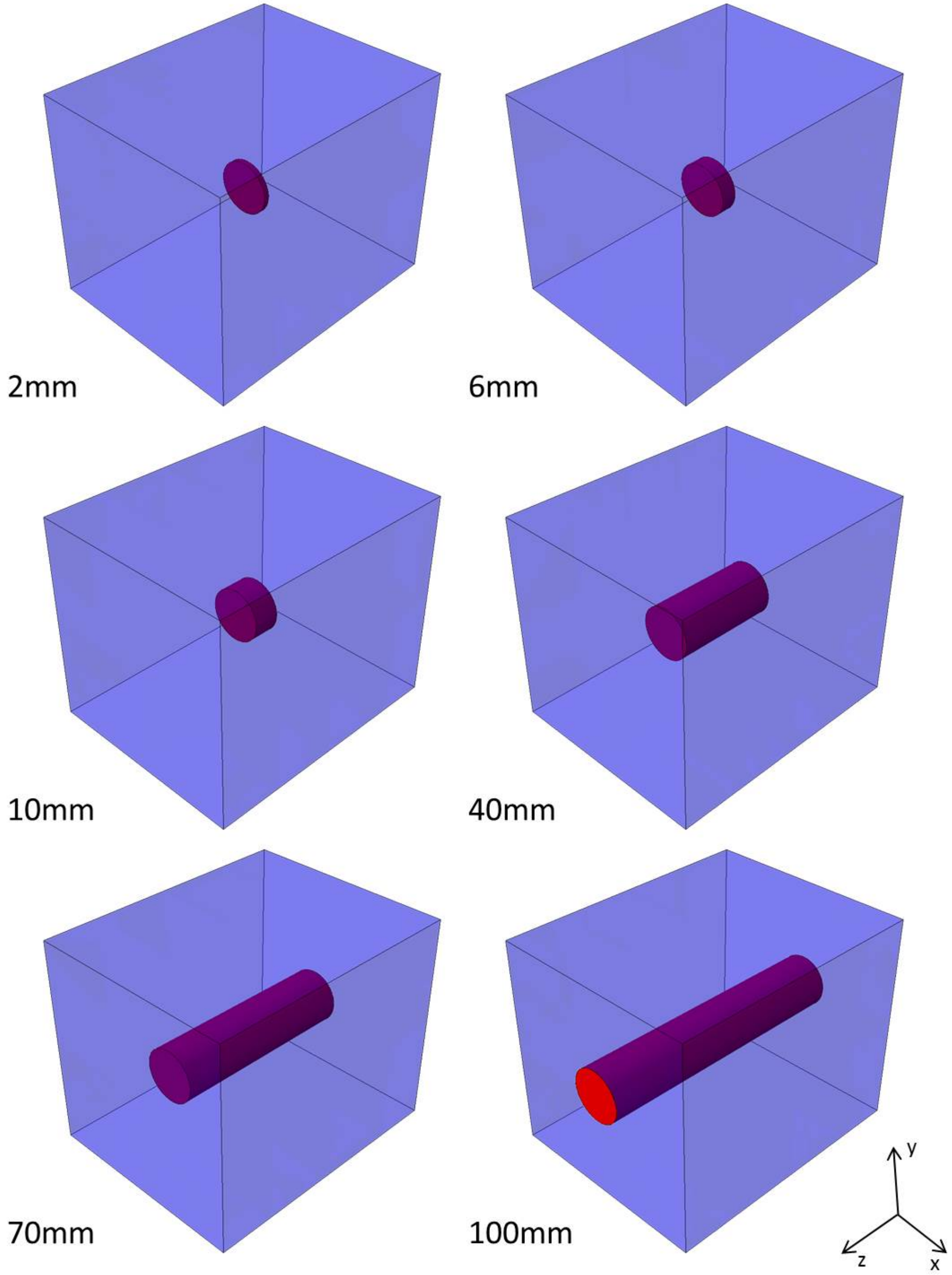

Figure 3.1: Examples of the out-of-plane insert geometries that were used in this chapter for an insert with a radius of 10 mm. The labels represent the length of the insert shown. Data for analysis 3-D analysis was extracted from the 5 central xy-planes in the model.

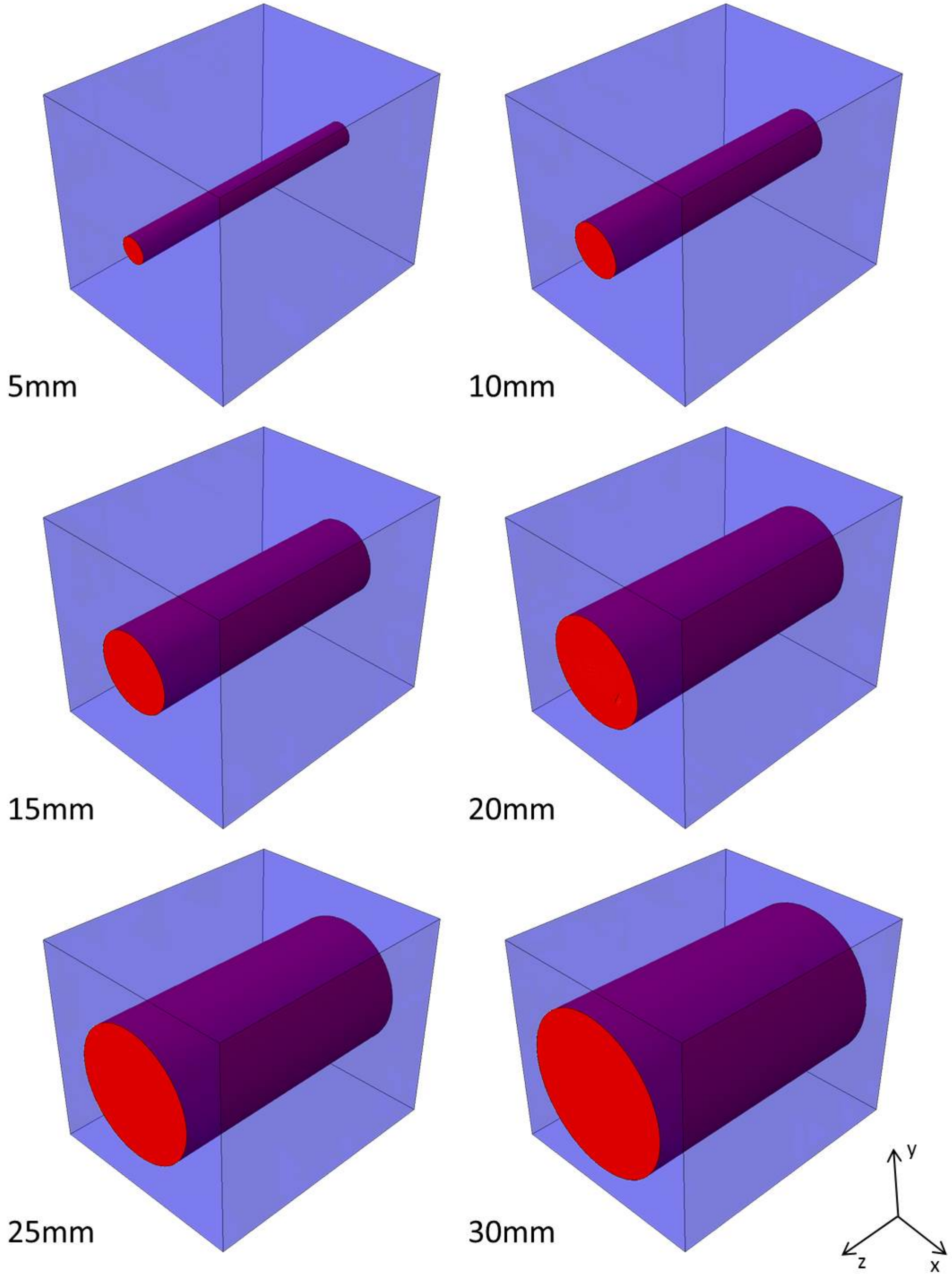

Figure 3.2: The in-plane insert geometries that were used in this chapter. The labels represent the radius of the insert shown. Data for analysis 3-D analysis was extracted from the 5 central xy-planes in the model.

throughout all of the models. Frequencies of 50, 70 and 100 Hz were applied to each of the models.

Boundary Conditions

As discussed in chapter 2, boundary conditions are known to affect the results of inversion both *in silico* and *in vivo*, however, little has been done to accurately replicate *in vivo* boundaries *in silico*. The boundary conditions used throughout the rest of this thesis have therefore been chosen to reduce the influence of the boundary as much as possible. Based on the findings of chapter 2, symmetric boundary conditions in the y-direction have been chosen, since this condition allows unconstrained motion in the shearing directions, therefore not forcing nodal points upon the shear wave at these boundaries. This decision was supported by the work in chapter 2 which demonstrated that such a boundary condition typically led to the lowest overestimation in the measured shear modulus of both the background and insert regions in comparison to all other tested boundary conditions.

Mesh

Whilst C3D8R elements allow short computational time, several of the model geometries used in this chapter were incompatible with these, and as such all models were meshed using C3D10M elements. The element length was defined as 1.25 mm along each edge within the model and convergence studies were performed on each geometry to demonstrate that this provided a high enough mesh density for accurate simulation.

3.2.4 Inversion

Inversion was performed using the 2-D and 3-D direct inversion algorithms and MDEV. Whilst the 2-D algorithm requires data from a single direction in one plane, the 3-D algorithm requires data from 5 planes and all three spatial directions with a voxel size of 1 mm^3. Directions as to how this was performed are included in Appendix I. MDEV also requires a full 3-D dataset but from multiple frequencies. A description of the MDEV algorithm along with the *Matlab* code to perform the algorithm are included in Appendix IV. It is important to note that DI utilises data at a single frequency whilst MDEV obtains a frequency independent variable from multiple frequencies referred to as $|G^*|$ where:

$$|G^*| = \left((G')^2 + (G'')^2\right)^{1/2} \tag{3.1}$$

As a result values obtained from DI and MDEV are not directly comparable. As such the fractional error of the measured $|G^*|$ value to the prescribed value has been used to compare 3-D DI and MDEV. The prescribed $|G^*|$ values for each independent frequency and MDEV are summarised in table 3.1. The standard deviations of the measurements were also calculated in both the background and insert regions. In this regard it is recognised that the material properties are defined in the model as uniform. A large variability in the shear modulus resulting from artefacts in the image is therefore likely to manifest itself as a large standard deviation.

	$|G^*|$ (Pa)			
Prescribed Shear Modulus	50 Hz	70 Hz	100 Hz	MDEV
3 kPa	3016	3032	3065	3035
4 kPa	4012	4024	4049	4026
5 kPa	5009	5019	5039	5021
6 kPa	6008	6016	6033	6018
7 kPa	7007	7014	7028	7015
8 kPa	8006	8012	8024	8013
9 kPa	9005	9011	9022	9012

Table 3.1: Expected $|G^*|$ values based on the assigned shear modulus and shear viscosity for each frequency and for MDEV.

3.2.5 Directional Filtering

Two separate directional filters were studied. These were first outlined in a paper by Manduca et al. (2003) [195]. The first was the spatio-temporal direction (SPD) filter. This performs a 2-D Fourier transform upon the data in the temporal direction and the spatial direction from which the reflected waves are to be removed. A mask is then applied to this data removing frequencies corresponding to negative wave velocities. The second filter was the cos-squared dependent (cos) filter. This performs a 2-D Fourier transform upon spatial images at each time point. A cos-squared dependent mask is then applied to these images again to remove the components relating to waves with negative velocities. For both filters an inverse Fourier transform is then applied to the filtered data and inversion performed in the same manner as before. More details on both filters can be found in Appendix V.

3.3 Results

3.3.1 Inversion

2-D .v. 3-D

Variations in the out-of-plane insert geometries showed that errors in the insert measurements were larger for smaller length inserts and for higher prescribed insert shear moduli for both the 2-D and the 3-D inversion. For both analyses the measurements remained constant above and beyond a certain insert length. This length was shorter for the 3-D inversion than the 2-D inversion and was dependent on the frequency (for the 9 kPa insert this length was 30 mm with the 3-D inversion and 50 mm with 2-D inversion) (figure 3.4). Whilst there was typically little difference between the accuracy of the 70 and 100 Hz measurements (for lengths above 30 mm following 3-D inversion of the 9 kPa insert errors were in the range of 1-2.5% and 0-1.5% respectively), the errors were larger at 50 Hz (1-9%). In the background the errors at 50 and 70 Hz were independent of the prescribed insert shear modulus and the insert length. High prescribed insert shear modulus caused large inaccuracies in the background measurements at 100 Hz and large variability of measurements with regards to insert length (figure 3.5). Inspection of the complex wave images showed decreased wave propagation in this lower regions of the background at 100 Hz resulting in heavy distortion of the elastograms here. Such distortions were present in elastograms from both the 2- and 3-D inversions (figure 3.6). Measurements in the background were more accurate following 3-D inversion than 2-D inversion for all three frequencies (for the 9 kPa insert at 100 Hz errors ranged from 1-4% for 3-D and 3-5% for 2-D). Standard deviations were variable with both the 2-D and 3-D inversion with no clear evidence to suggest that one method of inversion achieved lower values than the other (table 3.2).

With respect to variations in the in-plane insert geometries, errors generally decreased with increasing diameter (in the 3-D inversion at 100 Hz errors were 40% and 3% for the 5 and 30 mm inserts respectively) and increased for higher prescribed insert shear moduli (for

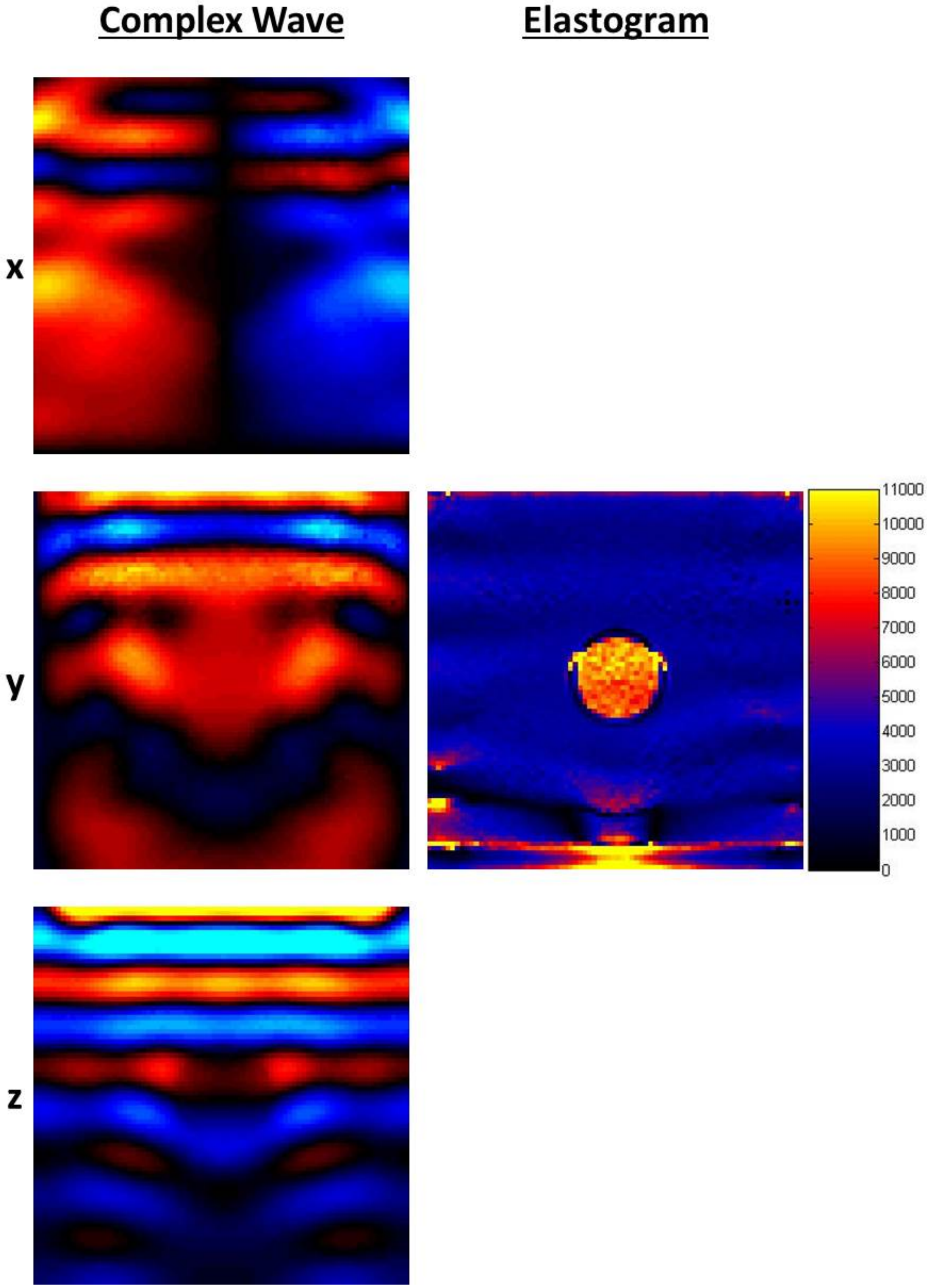

Figure 3.3: Complex waves from the central plane in the x-, y- and z-directions used in the 3-D inversion and the corresponding elastogram from the 9 kPa 100 mm length insert vibrated at 100 Hz.

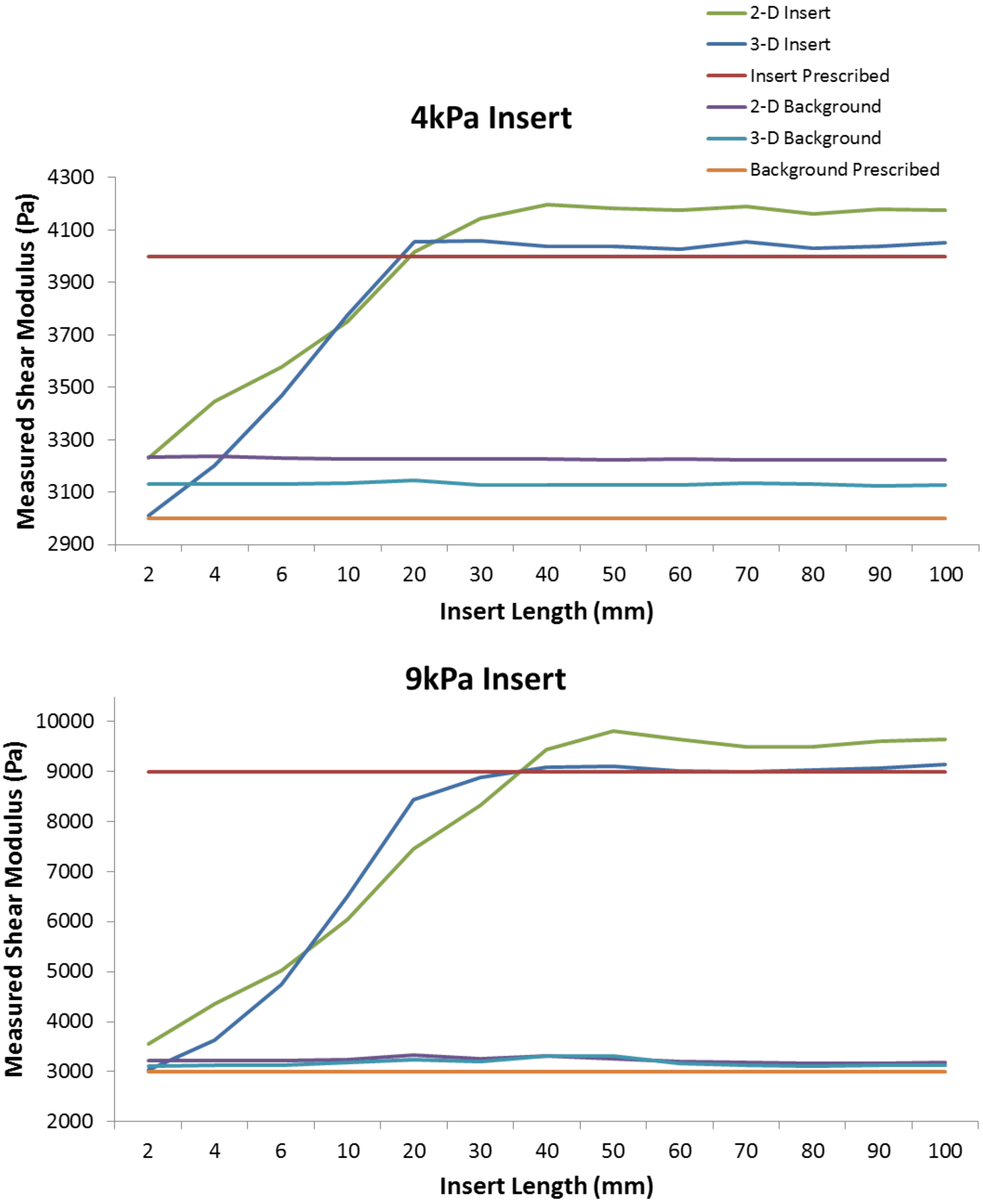

Figure 3.4: Graphs comparing the 2-D and 3-D shear modulus measurements from the background and inserts for the out-of-plane insert geometry variations for prescribed insert shear moduli of 4 and 9 kPa with 100 Hz vibrations. The 3-D measurements were more accurate in both the background and inserts. Additionally the length beyond which consistent measurements were made was shorter for the 3-D inversion than the 2-D.

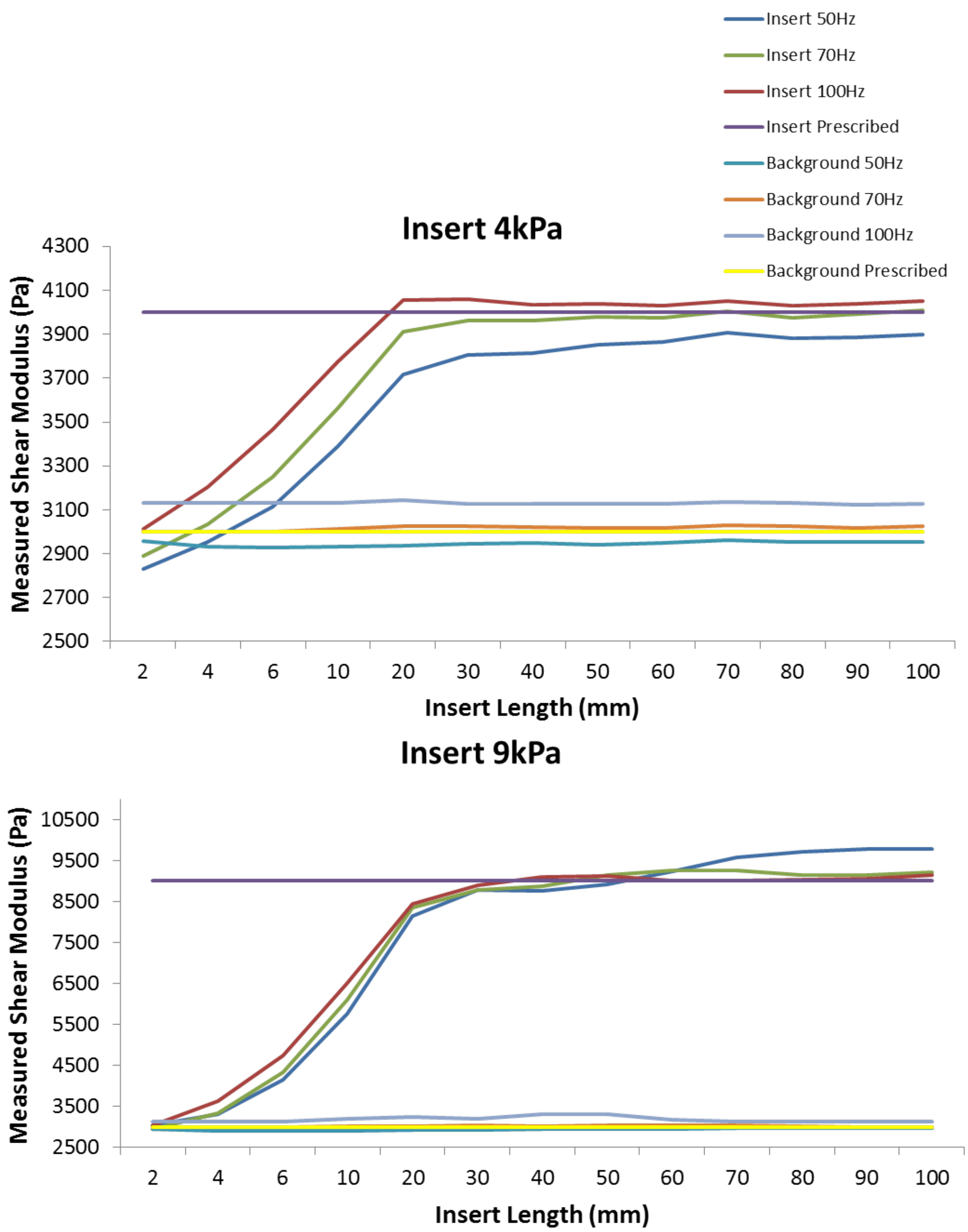

Figure 3.5: Graphs comparing shear modulus measurements following 3-D inversion at frequencies of 50, 70 and 100 Hz from the backgrounds and inserts for the out-of-plane insert geometry variations for prescribed insert shear moduli of 4 and 9 kPa. In the insert accuracy was poorest following 50 Hz vibrations, whilst in the background it was poorest following 100 Hz vibrations.

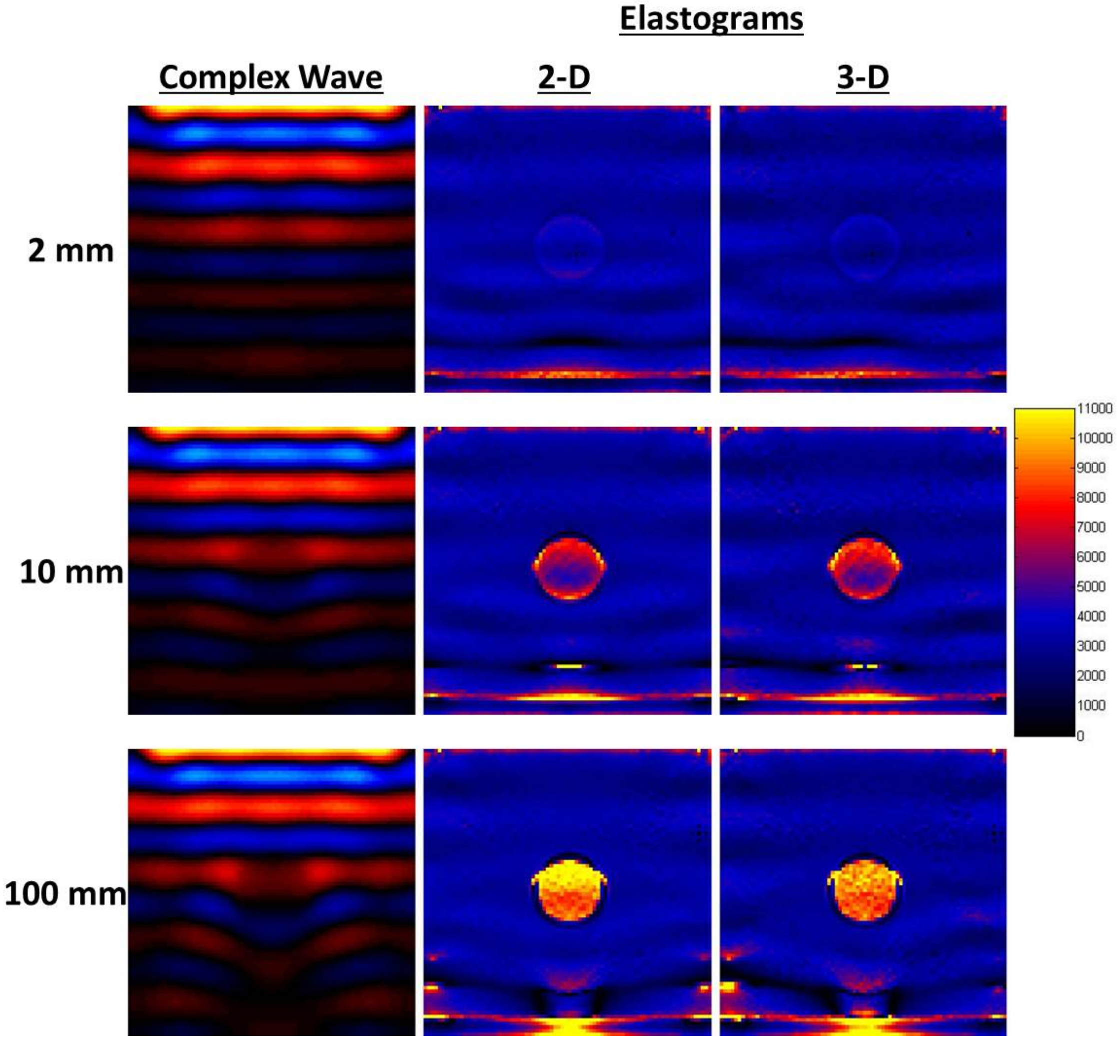

Figure 3.6: Examples of the complex wave images and corresponding elastograms from the out-of-plane insert geometry variations vibrated at 100 Hz and with a prescribed insert shear modulus of 9 kPa. Lengthening the insert caused increased measured values of the shear modulus. Reduced wave propagation can be seen in the region directly below the insert for the longer inserts with large artefacts in the elastograms in this region. There was no difference between the locations of the artefacts in the 2- and 3-D images.

the 30 mm diameter insert following 3-D inversion at 50 Hz there were errors of 4% and 17% for prescribed shear moduli of 4 and 9 kPa respectively). For both 2-D and 3-D the measurements remained relatively constant above a diameter of 10 mm (figure 3.8). As with the inserts in the out-of-plane geometries, there was typically little difference between the accuracy of the 70 and 100 Hz measurements (for the 30 mm diameter 9 kPa insert there were errors of 3% at both frequencies) though errors increased at 50 Hz (17%) (figure 3.9). Measurements in both the background and inserts were variable at all three frequencies

		4 kPa		9 kPa	
Frequency	Dimensions	Background	Insert	Background	Insert
50 Hz	2-D	134	58	188	450
	3-D	133	57	205	293
70 Hz	2-D	103	42	247	200
	3-D	475	47	179	215
100 Hz	2-D	210	97	227	222
	3-D	192	76	284	146

Table 3.2: Examples of the standard deviations for the out-of-plane insert geometry variations from the 100 mm length insert. Standard deviations in the measurements were of the same order of magnitude following both 2- and 3-D inversion in both the background and insert regions. For the purposes of this study, such differences were not considered large enough to represent image artefacts.

depending upon insert diameter. In general measurements at 70 Hz provided the greatest accuracy. Greater accuracy was again achieved in the inserts with the 3-D inversion in comparison to the 2-D inversion. There was little difference with respect to accuracy of the measurements from the 2- and 3-D inversions in the background region with artefacts in the same locations for both (figure 3.7). As with the out-of-plane measurements there were large variations in the standard deviations of the measurements in both regions, though again there was no apparent improvement seen using the 3-D inversion in comparison to the 2-D (table 3.3).

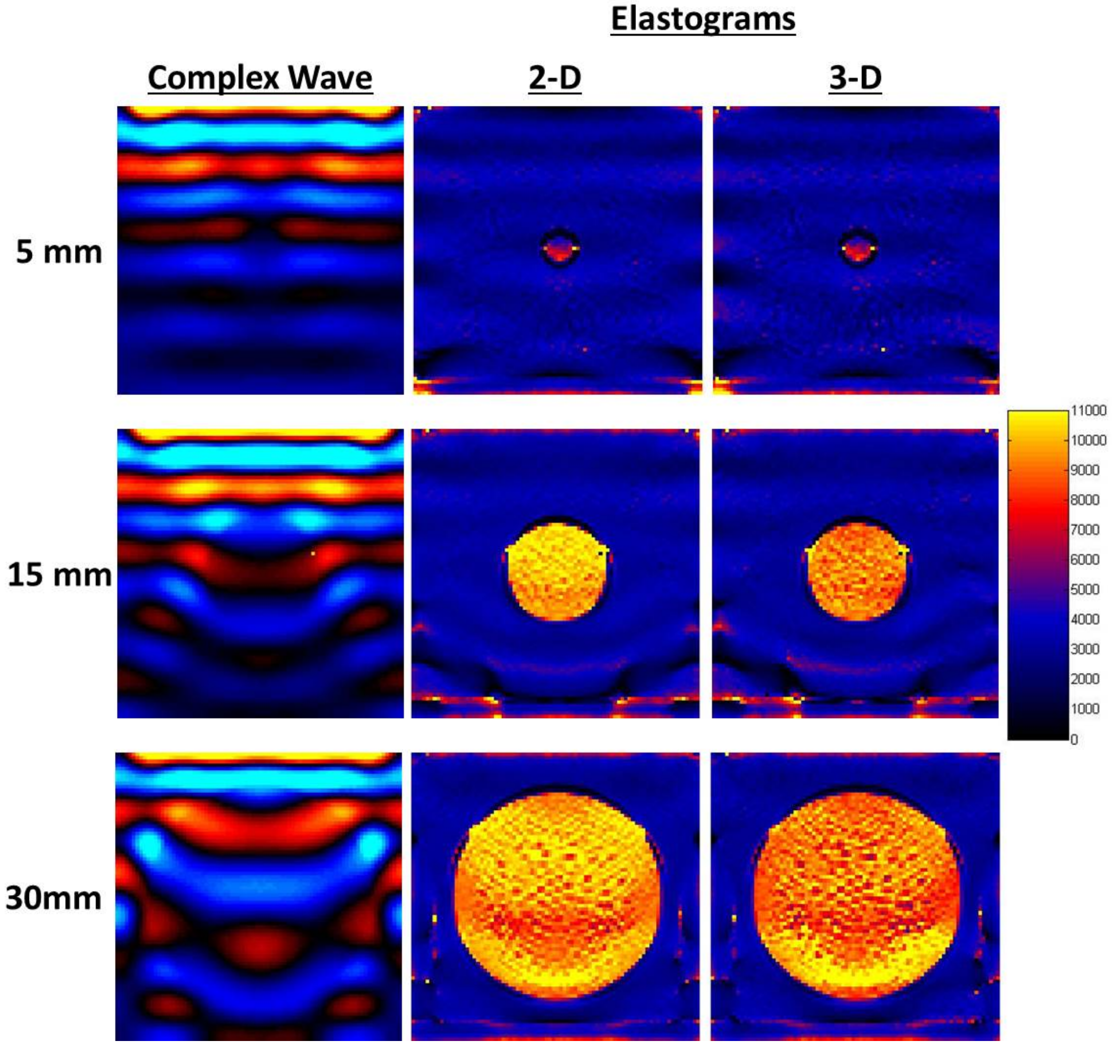

Figure 3.7: Examples of the complex wave images and corresponding elastograms from the in-plane insert geometry variations vibrated at 100 Hz and with a prescribed insert shear modulus of 9 kPa. Increasing the diameter of the insert caused increased measured values of the shear modulus.

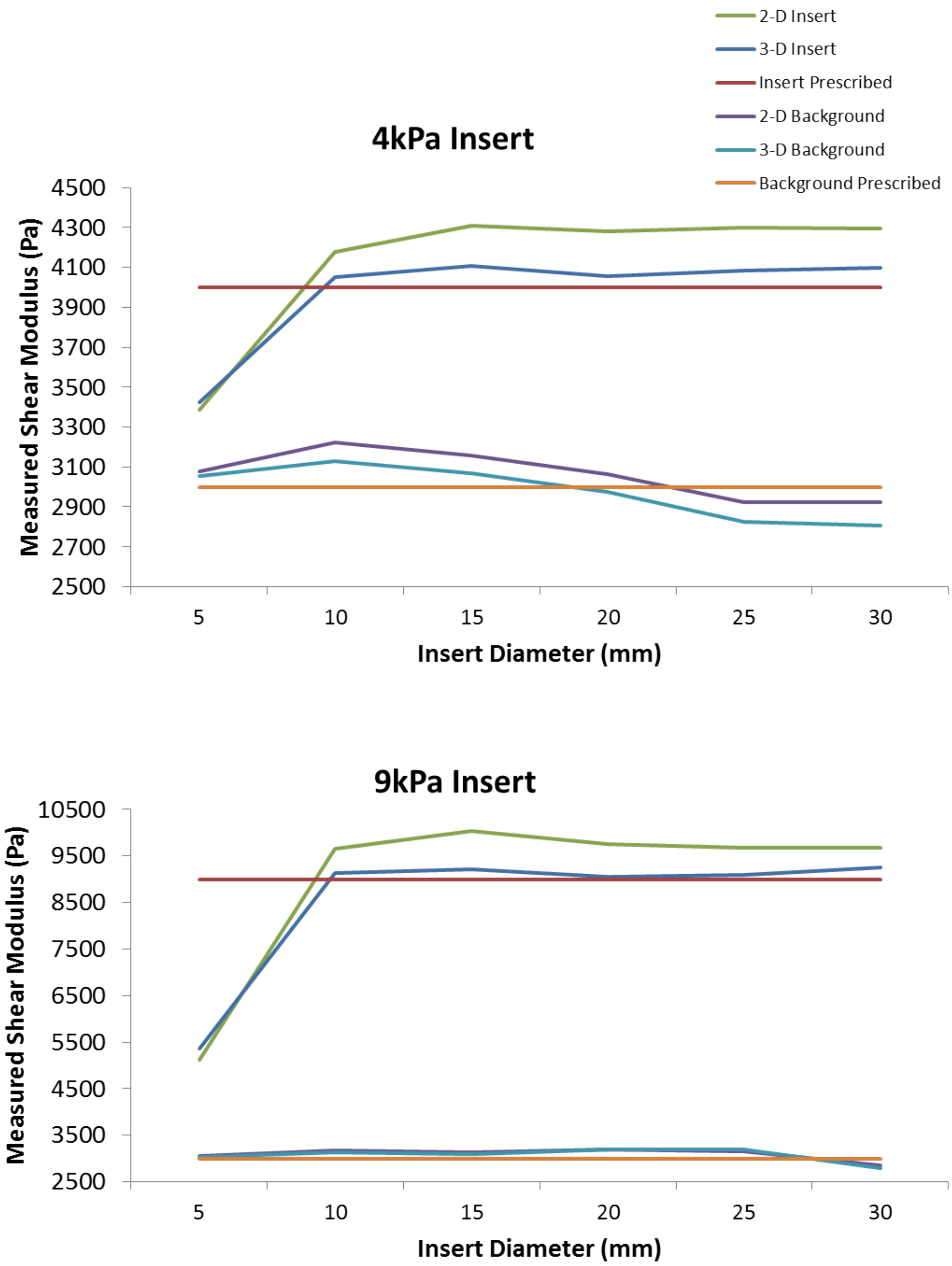

Figure 3.8: Graphs comparing the 2-D and 3-D shear modulus measurements from the background and inserts for the in-plane insert geometry variations for prescribed insert shear moduli of 4 and 9 kPa with 100 Hz vibrations. The 3-D measurements were more accurate in the inserts, yet there order of magnitude of the standard deviations was the same in each case.

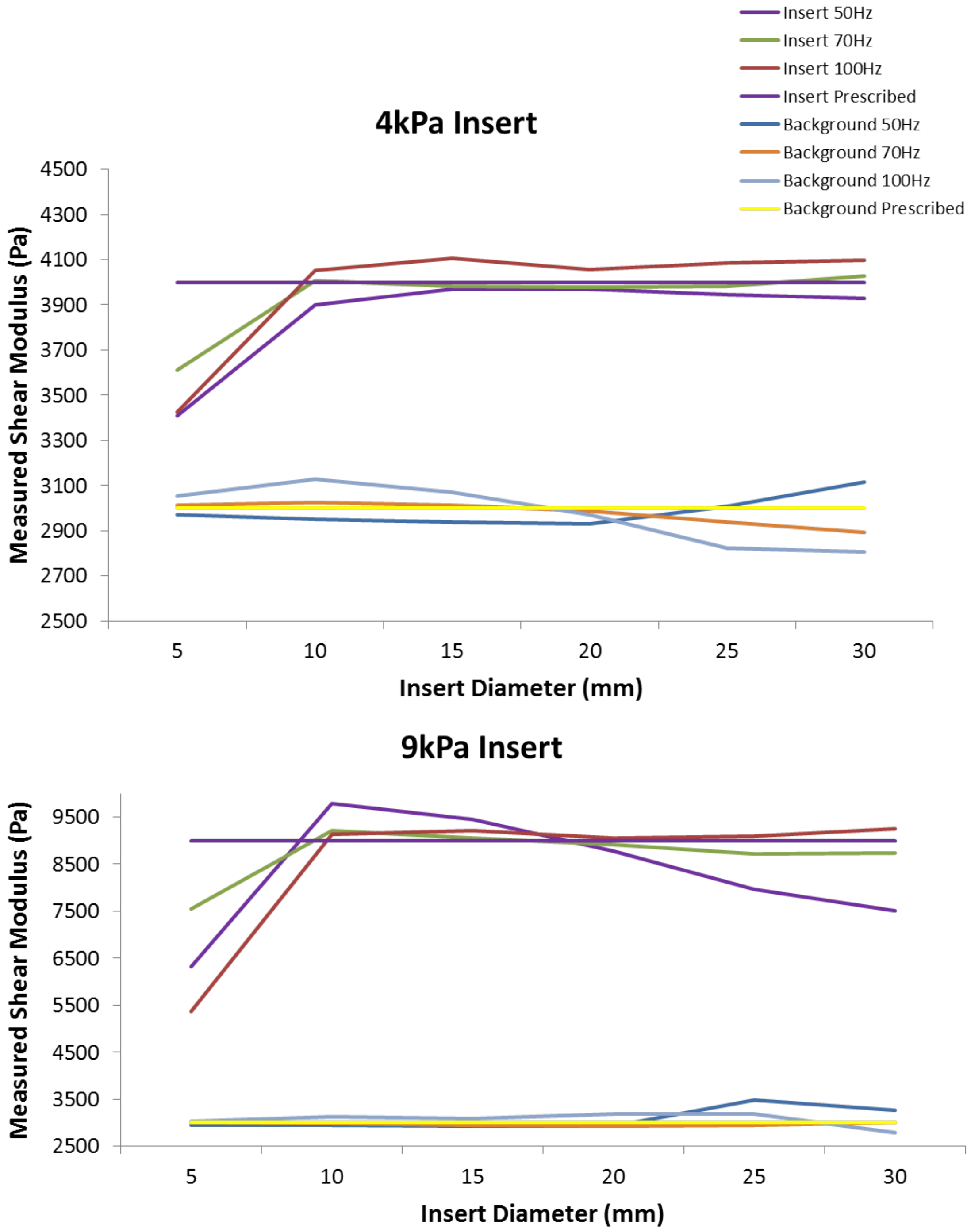

Figure 3.9: Graphs comparing shear modulus measurements following 3-D inversion at frequencies of 50, 70 and 100 Hz from the backgrounds and inserts for the out-of-plane insert geometry variations for prescribed insert shear moduli of 4 and 9 kPa. Poorest accuracy was achieved in the insert at 50 Hz. 70 Hz produced the most accurate measurements in the background whilst there was little difference in the accuracy of measurements at 50 and 100 Hz.

		4 kPa		9 kPa	
Frequency	Dimensions	Background	Insert	Background	Insert
50 Hz	2-D	142	75	517	854
	3-D	160	73	471	529
70 Hz	2-D	180	71	736	434
	3-D	205	96	1385	446
100 Hz	2-D	342	67	306	288
	3-D	383	80	273	433

Table 3.3: Examples of the standard deviations for the in-plane insert geometry variations from the 30 mm diameter insert. Again, standard deviations in the measurements were of the same order of magnitude following both 2- and 3-D inversion in both the background and insert regions. For the purposes of this study, such differences were not considered large enough to represent image artefacts.

DI .v. MDEV

In both the insert and the background MDEV failed to increase the accuracy of the measurements in comparison to the most accurate frequency for the out-of-plane geometries (figure 3.10). Standard deviations were dramatically lower in the background regions using MDEV in comparison to DI at all three frequencies, though values remained similar in the inserts (table 3.4). This was reflected by an increased uniformity in the background of the elastogram image (figure 3.11).

	4 kPa		9 kPa	
Frequency	Background	Insert	Background	Insert
50 Hz	133	57	205	293
70 Hz	475	47	179	215
100 Hz	383	80	273	433
MDEV	43	47	86	228

Table 3.4: Examples of the standard deviations for the out-of-plane insert geometry variations from the 100 mm length insert. Whilst the values following MDEV are similar to those following DI in the insert, they are dramatically lower in the background.

MDEV also failed to improve the accuracy of the measurements in the in-plane geometries (figure 3.12). Standard deviations were noticeably lower in the background and insert regions following MDEV inversion in comparison to DI of the three individual frequencies (table 3.5). This effect was most noticeable for higher prescribed shear insert shear moduli. Both the inserts and the background regions appeared to be more uniform in the MDEV elastogram than the frequencies inverted individually with DI (figure 3.13).

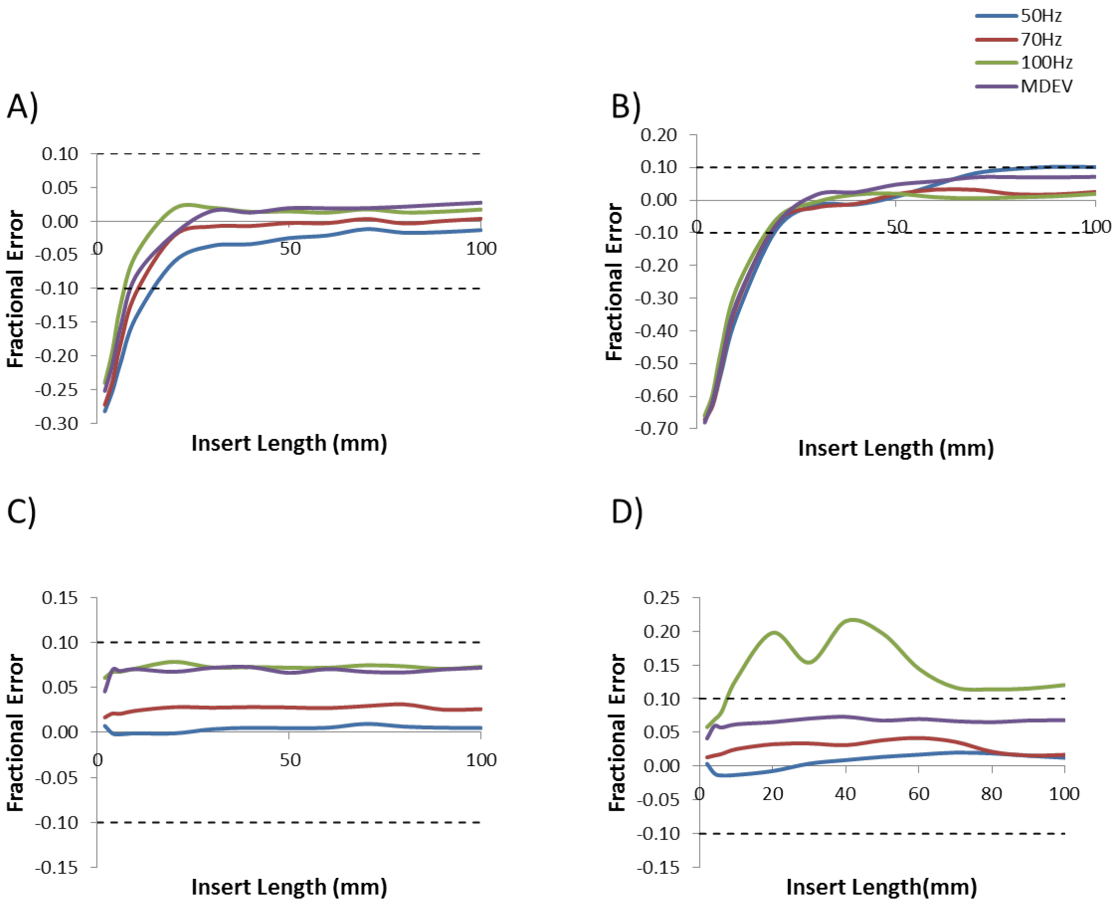

Figure 3.10: Data from the out-of-plane geometries. A) and B) are the fractional errors for the 4 and 9 kPa inserts respectively. These show the dependency of the measurements on insert length and prescribed shear modulus as well as frequency. C) and D) are the fractional errors for the backgrounds in these respective models. These show the independence of the measurements on both the size and prescribed shear modulus of the inserts and the variability of measurements from 100 Hz vibrations when the prescribed shear modulus is high. In both the background and the insert MDEV is unable to improve on the accuracy of the measurements. The black dashed lines represent fractional errors of ±0.1.

	4 kPa		9 kPa	
Frequency	Background	Insert	Background	Insert
50 Hz	160	73	471	529
70 Hz	205	96	1385	446
100 Hz	383	80	273	433
MDEV	41	62	166	177

Table 3.5: Examples of the standard deviations for the in-plane insert geometry variations from the 30 mm radius insert. The standard deviations are lower following MDEV than DI in both the background and the insert regions.

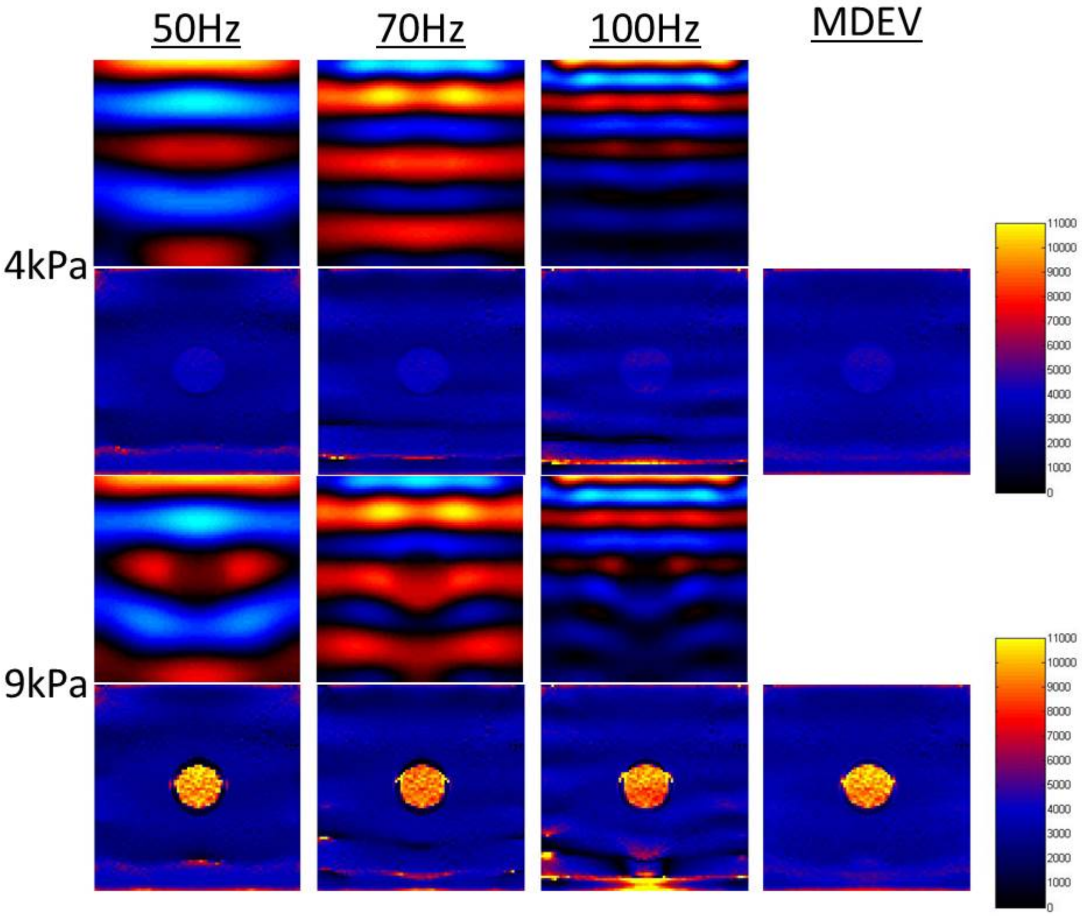

Figure 3.11: Examples of the complex wave images and elastograms for the out-of-plane insert geometries created using DI at three frequencies and MDEV for an insert length of 100 mm. Wave propagation can be seen to be reduced in the lower regions of the 100 Hz model leading to distortions in the elastogram in the background. The background region following inversion by MDEV is more uniform than all three frequencies and this is reflected by lower standard deviations.

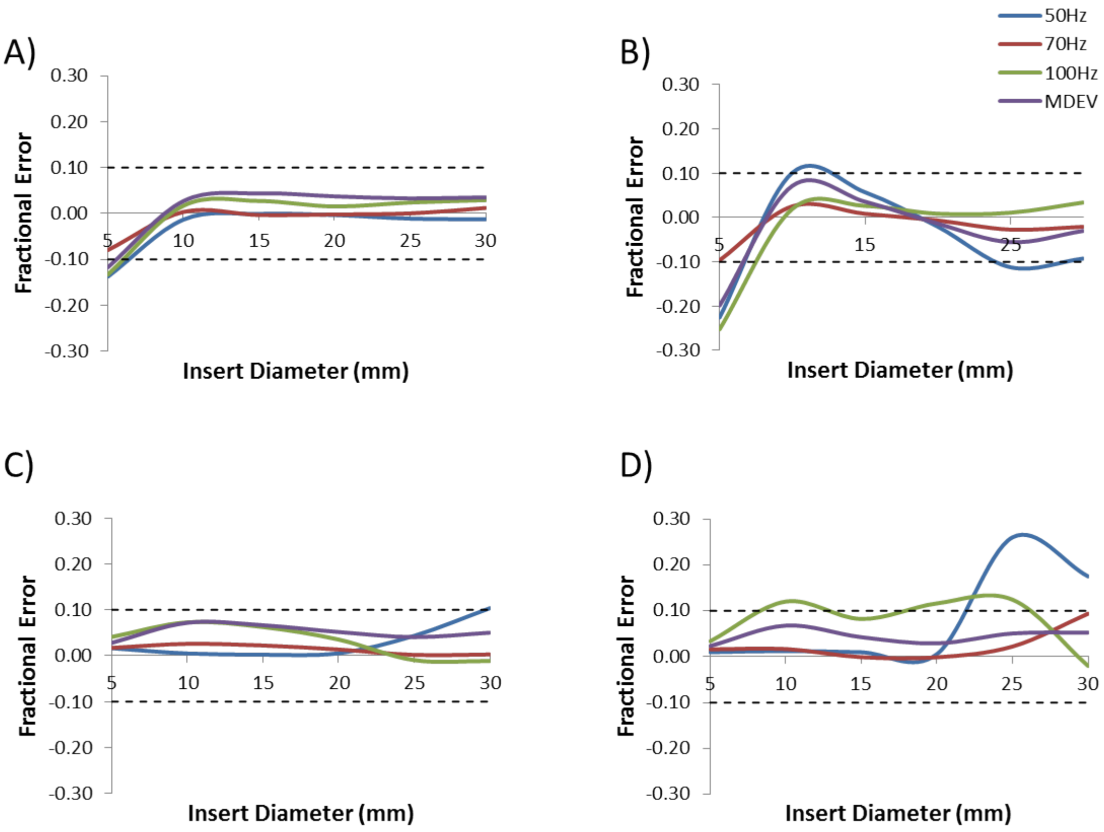

Figure 3.12: Data from the in-plane geometries. A) and B) are the fractional errors for the 4 and 9 kPa inserts respectively. These show the frequency, size and prescribed shear modulus dependence upon the accuracy of the measurements. C) and D) are the fractional errors for the backgrounds in these respective models. These show the frequency and prescribed shear modulus dependence on the accuracy of the measurements and the variabilty of the accuracy at various insert sizes. In both the background and the insert MDEV was unable to improve the accuracy of the measurements in comparison to DI of the three individual frequencies. The black dashed lines represent fractional errors of ±0.1.

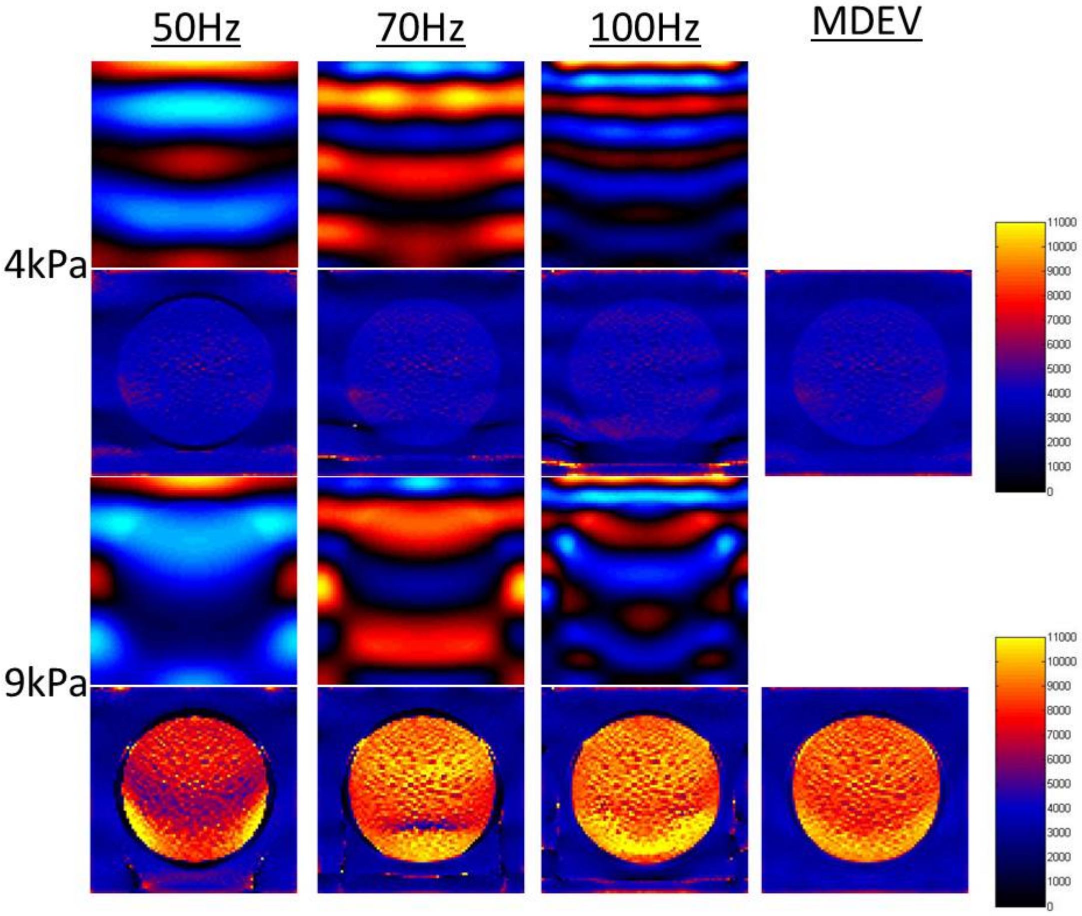

Figure 3.13: Examples of the complex wave images and elastograms for the in-plane insert geometries created using DI at three frequencies and MDEV for an insert radius of 30 mm. Again these show reduced wave propagation in the lower regions of the 100 Hz model and a more uniform background following inversion by MDEV.

3.3.2 Directional Filtering

2-D Filtering

For the out-of-plane geometry variations there was little difference between the measured insert values from the unfiltered data and the SPD filter in the inserts (the 100 mm length 9 kPa insert vibrated at 100 Hz were overestimated by 4 and 7% for the unfiltered and SPD filtered data respectively). In contrast there was a large reduction in the measured value following application of the cos filter (underestimated by 18%). This effect increased with increasing prescribed shear modulus. For the background region there was little difference between the unfiltered and cos filtered values for lower prescribed shear modulus, however for higher prescribed insert shear moduli and longer insert lengths the cos filtered values were typically larger (for the 100 mm length 9 kPa insert the unfiltered measurement was a 6% overestimate in comparison to an 18% overestimation for the cos filter). The background values for the all prescribed insert shear moduli were larger for the SPD filtered data than the unfiltered data (15% overestimation for the 100 mm 9kPa insert) (figure 3.14). The standard deviations in both regions were similar for both filters and the unfiltered data. There was a dramatic increase in the standard deviations of the background regions of the filtered data at high prescribed insert shear moduli (table 3.6). Visual inspection of the elastograms showed increased uniformity of the shear modulus in the upper regions, but large artefacts in the lower regions at higher prescribed insert shear moduli. In comparison to the unfiltered data, wave propagation appeared reduced in this region. Additionally wave propagation appeared closer to planarity in the filtered data. This was particularly true following application of the cos filter (figure 3.15).

	4 kPa		9 kPa	
	Background	Insert	Background	Insert
Unfiltered	210	97	227	222
SPD Filter	197	31	2668	194
Cos Filter	120	55	3700	267

Table 3.6: Examples of the standard deviations for the out-of-plane insert geometry variations from the 100 mm length insert for vibrations at 100 Hz. The values in the background were significantly higher for the filtered data at higher prescribed shear moduli.

With regards to the in-plane geometry variations there was little change in the insert measurements for low prescribed insert shear moduli with all filters. Whilst there was little

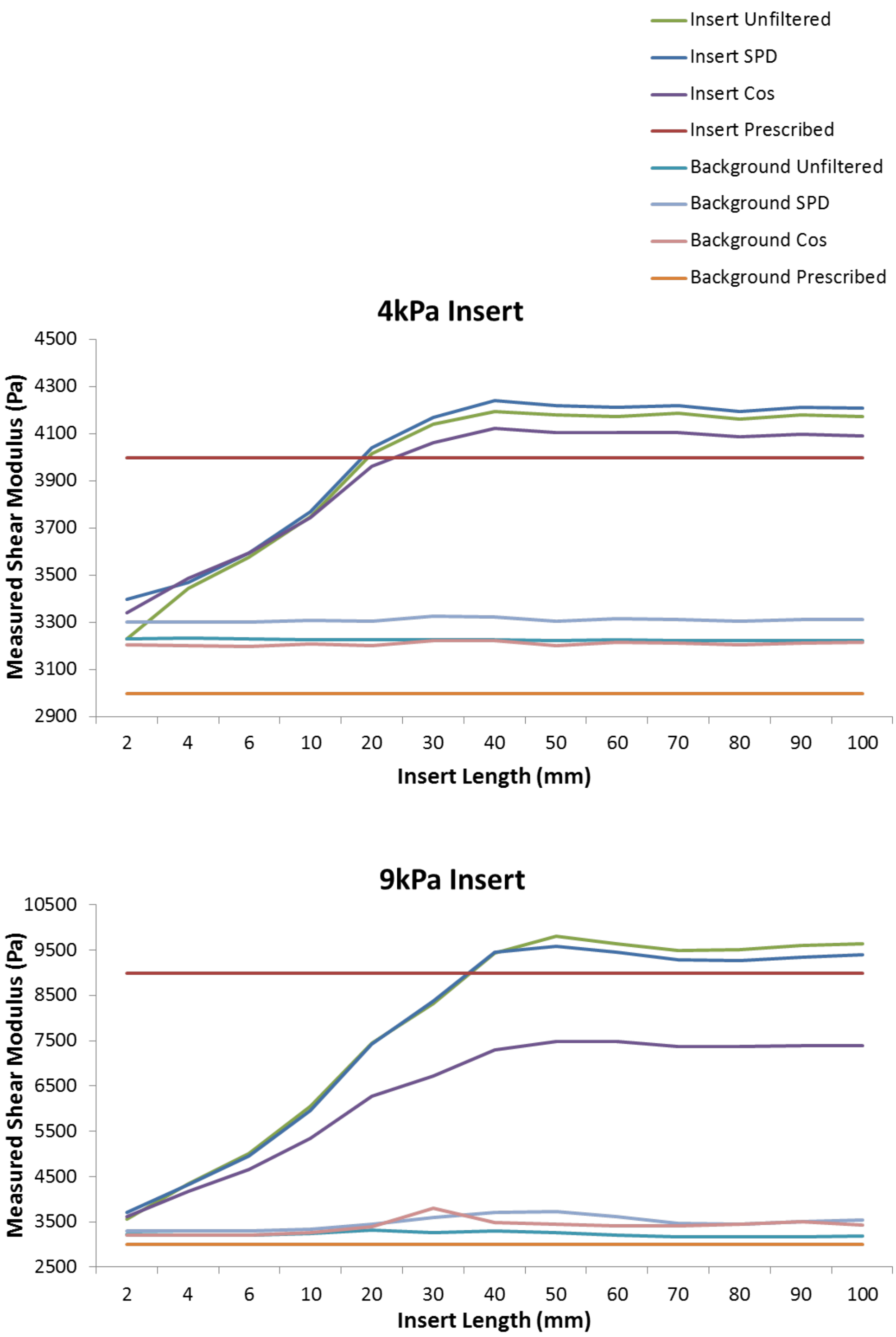

Figure 3.14: Graphs showing the measured shear modulus of unfiltered and directionally filtered 2-D data for the 10 mm radius insert vibrated at 100 Hz. The cos filter results in large reductions in the measured shear modulus value particularly for high prescribed insert shear moduli. Additionally application of both filters resulted in increased and variable measurements of the background shear modulus for high prescribed shear moduli.

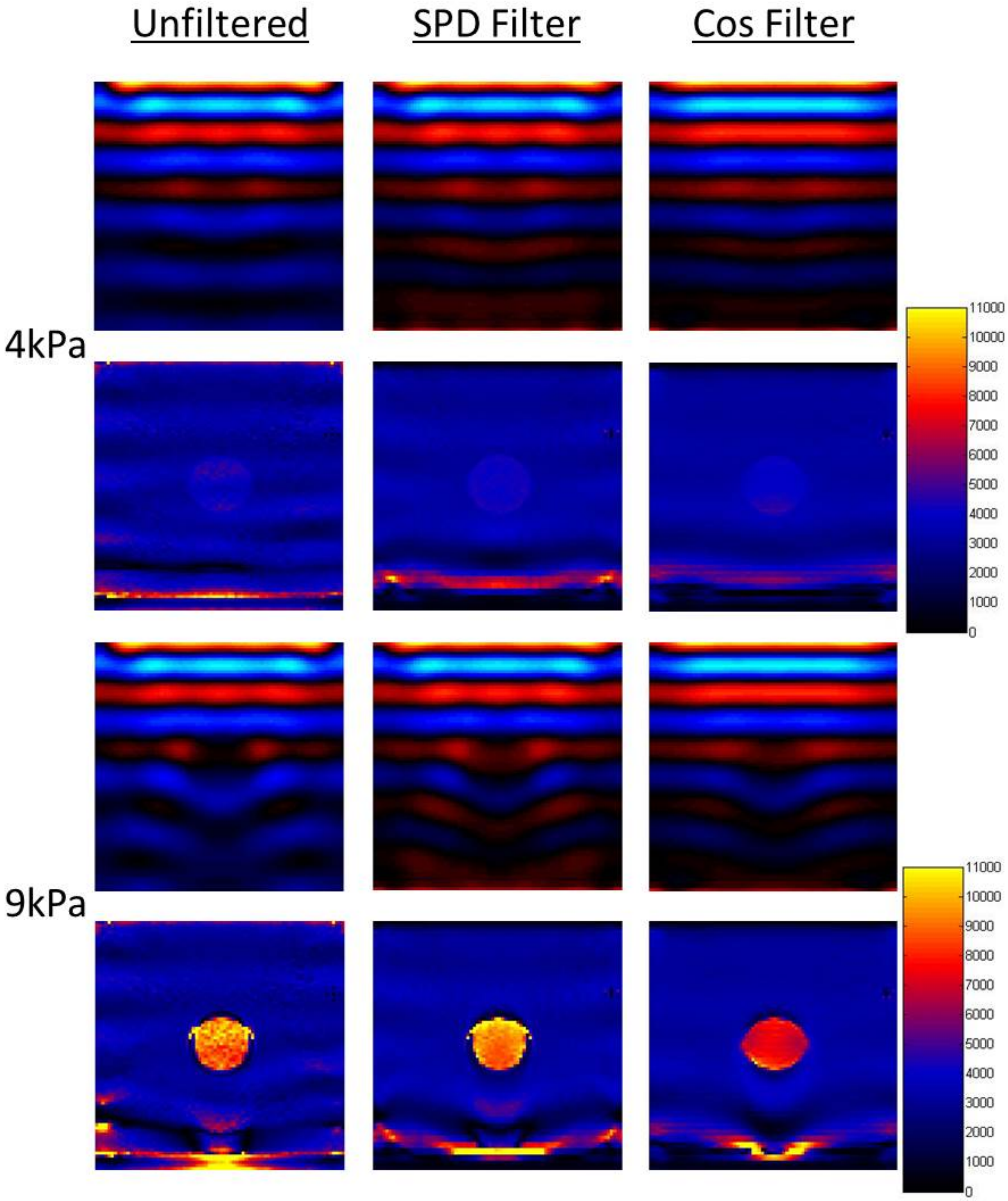

Figure 3.15: Examples of the complex wave images and elastograms following directional filtering for the 10 mm radius insert vibrated at 100 Hz. Whilst the upper regions of the background in the filtered datasets are smoother, artefacts remain in the lower regions of the background. Wave propagation noticeably appeared to better approximate planar propagation in the filtered data throughout the model whilst there was reduced wave propagation in the lower regions of the model.

difference between the unfiltered and SPD filtered data for high insert shear moduli, application of the cos filter again resulted in a large decrease in the measured value (for the 30 mm diameter 9 kPa insert at 100 Hz the cos filter underestimated by 4% in comparison to overestimations of 6 and 7% from SPD filtered and unfiltered data respectively). In the background regions both filters typically resulted in increased measurements for all prescribed shear moduli. Whilst the extent of this increase seemed dependent upon the insert diameter, this did not seem to be the case for the SPD filter (figure 3.16). Whilst there was little difference in the standard deviations in both the insert and the background regions for higher prescribed insert shear moduli, there was a large increase in the background shear modulus for lower prescribed shear moduli (table 3.7). The elastograms appeared smoother after application of the filters, with the cos filter again achieving the smoothest image in both the background and insert regions. Despite this there remained artefacts within the elastograms, particularly in the lower regions of the background. Again wave propagation appeared to more closely approximate planarity following application of the filters (figure 3.17).

	4 kPa		9 kPa	
	Background	Insert	Background	Insert
Unfiltered	342	67	306	288
SPD Filter	651	95	421	159
Cos Filter	1078	82	354	182

Table 3.7: Examples of the standard deviations for the in-plane insert geometry variations from the 100 mm length insert for vibrations at 100 Hz. The values in the background were significantly higher for the filtered data at lower prescribed shear moduli.

3-D Filtering

For the low prescribed insert shear moduli in the out-of-plane geometry variations there was little difference between the unfiltered data and SPD filtered data in the insert whilst there was a slight decrease in the measured value following application of the cos filter (for the 100 mm length 4 kPa insert at 100 Hz the measurement following cos filtering was underestimated by 2% compared to an overestimations of 1 and 2% for the unfiltered data and SPD filtered data). This contrasted with measurements in the background where there were increases in the measured values following application of the both filters (measurements for the 100 m length 9 kPa at 100 Hz measurements were overestimated by 4, 16

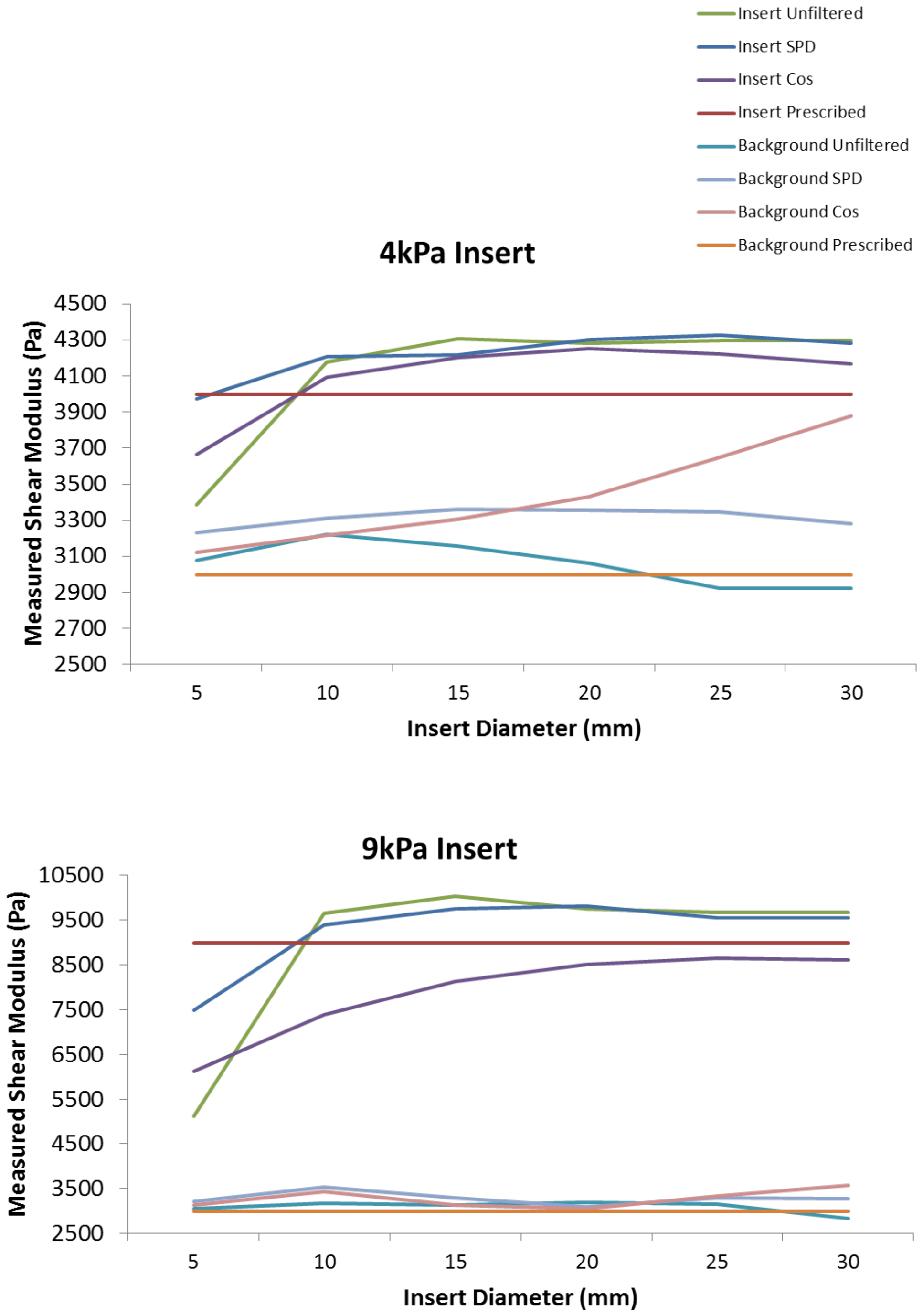

Figure 3.16: Graphs showing the measured shear modulus of unfiltered and directionally filtered 2-D data for the 100 mm length insert vibrated at 100 Hz. The cos filter results in large reductions in the measured shear modulus of the insert, particularly for high prescribed insert shear moduli. Application of the directional filters resulted in an increase in the measured shear modulus of the background. For the cos filter the measurements increased with diameter.

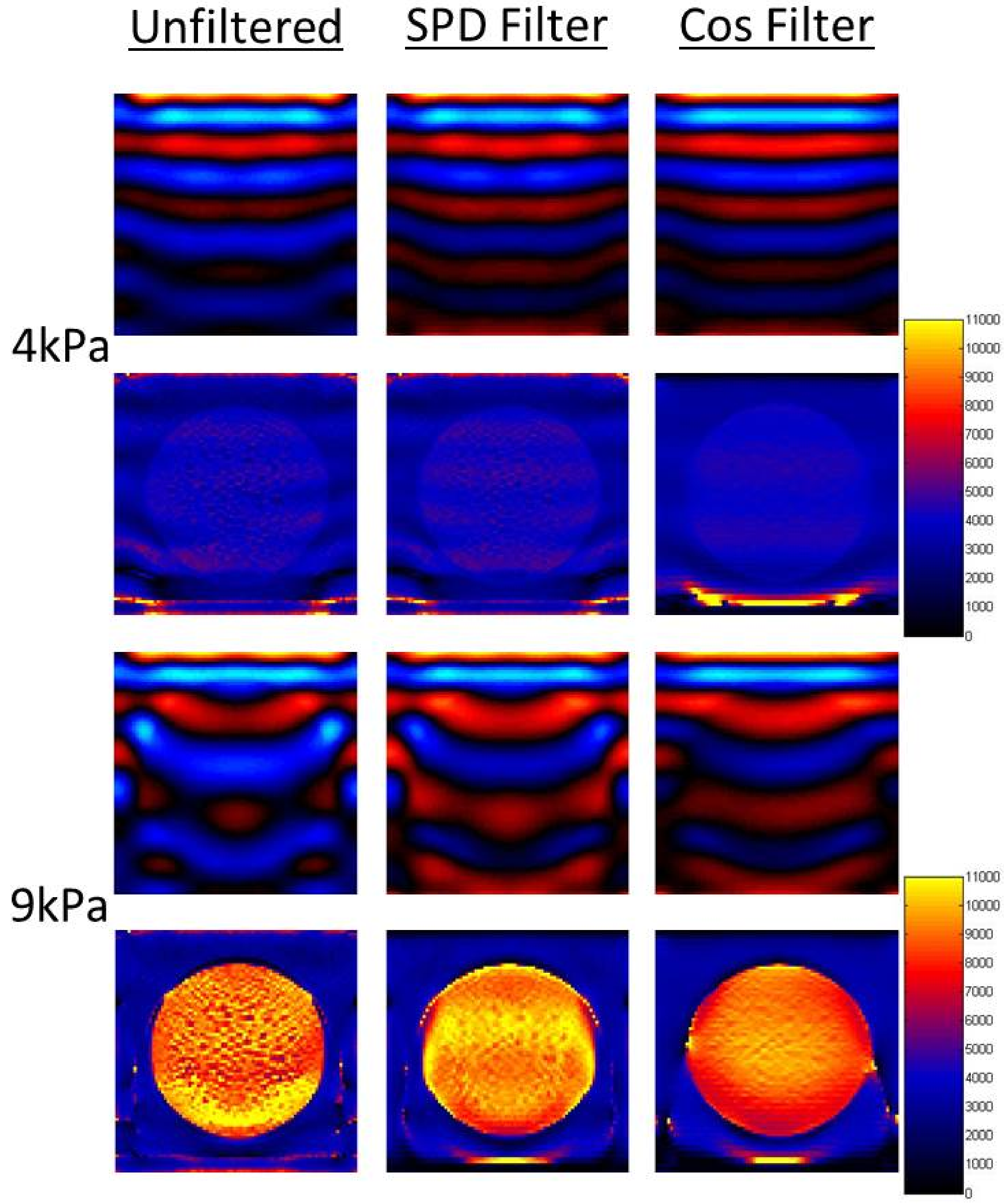

Figure 3.17: Examples of the complex wave images and elastograms following 2-D directional filtering for the 30 mm radius insert vibrated at 100 Hz. Whilst both the background and inserts in the filtered datasets appear smoother, artefacts remain in the lower regions of the background. As with the in-plane geometry variations wave propagation noticeably appeared to better approximate planar propagation in the filtered data throughout the model.

and 13% for the unfiltered, SPD filtered and cos filtered data respectively). For high shear moduli there was a decrease in the measured value for the insert following application of both filters, with this effect increased with the cos filter (underestimated by 4 and 24% for the SPD and cos filter respectively in comparison to an overestimation of 2% for the unfiltered data in the 100 mm length 9 kPa insert at 100 Hz). In the background there was an increase in the measured value and variability of the measured value with length following application of both directional filters (figure 3.18). Whilst the standard deviations for both filters and the unfiltered data were similar in the background and insert at low shear moduli and the insert at high shear moduli, there was a large increase in the standard deviations of the background at high insert shear moduli following application of both filters (table 3.8). Inspection of the elastograms showed that the upper regions of the background appeared smoother following filtering, whilst there remained artefacts towards the bottom (figure 3.19).

	4 kPa		9 kPa	
	Background	Insert	Background	Insert
Unfiltered	193	76	284	146
SPD Filter	183	37	3413	180
Cos Filter	93	58	3036	230

Table 3.8: Examples of the standard deviations for the out-of-plane insert geometry variations from the 100 mm length insert for vibrations at 100 Hz for the 3-D filtered data. The values in the background were significantly higher for the filtered data at higher prescribed shear moduli.

There was little difference in the accuracy of the insert measurements at low prescribed insert shear moduli for all filters for the in-plane geometry variations. Filtering increased the measured values in the background. With the cos filter this effect increased with insert diameter (for a 9 kPa insert at a frequency of 100 Hz the measured value was overestimated by 3% for a diameter of 5 mm in comparison to 17% for 30 mm). There was little difference between the insert measurements at high prescribed shear moduli in the unfiltered and SPD filtered data whilst application of the cos filter caused a large reduction in the measured value (for the 30 mm 9 kPa insert measurements were overestimated by 3 and 1% for the unfiltered and SPD filtered data in comparison to an underestimation of 8% for the cos filter). In the background there was again an increase in the measured value following application of both directional filters with this effect increasing with diameter for the cos filter (figure 3.20). Whilst there was a large reduction in the measured value of the 5 mm diameter when unfiltered, there was a dramatic increase in this value following application of the SPD filter. Vibrations at 100 Hz resulted in a relatively accurate measurement (an underestimation of 4% for the 9 kPa insert), however large overestimations were obtained at lower frequencies (67% at 50 Hz) (figure 3.21). There was little difference between the standard deviations for the unfiltered and filtered data (figure 3.9). Whilst filtering typically improved the smoothness of the elastograms, particularly with the cos filter, there remained artefacts in the lower regions of the model (figure 3.22).

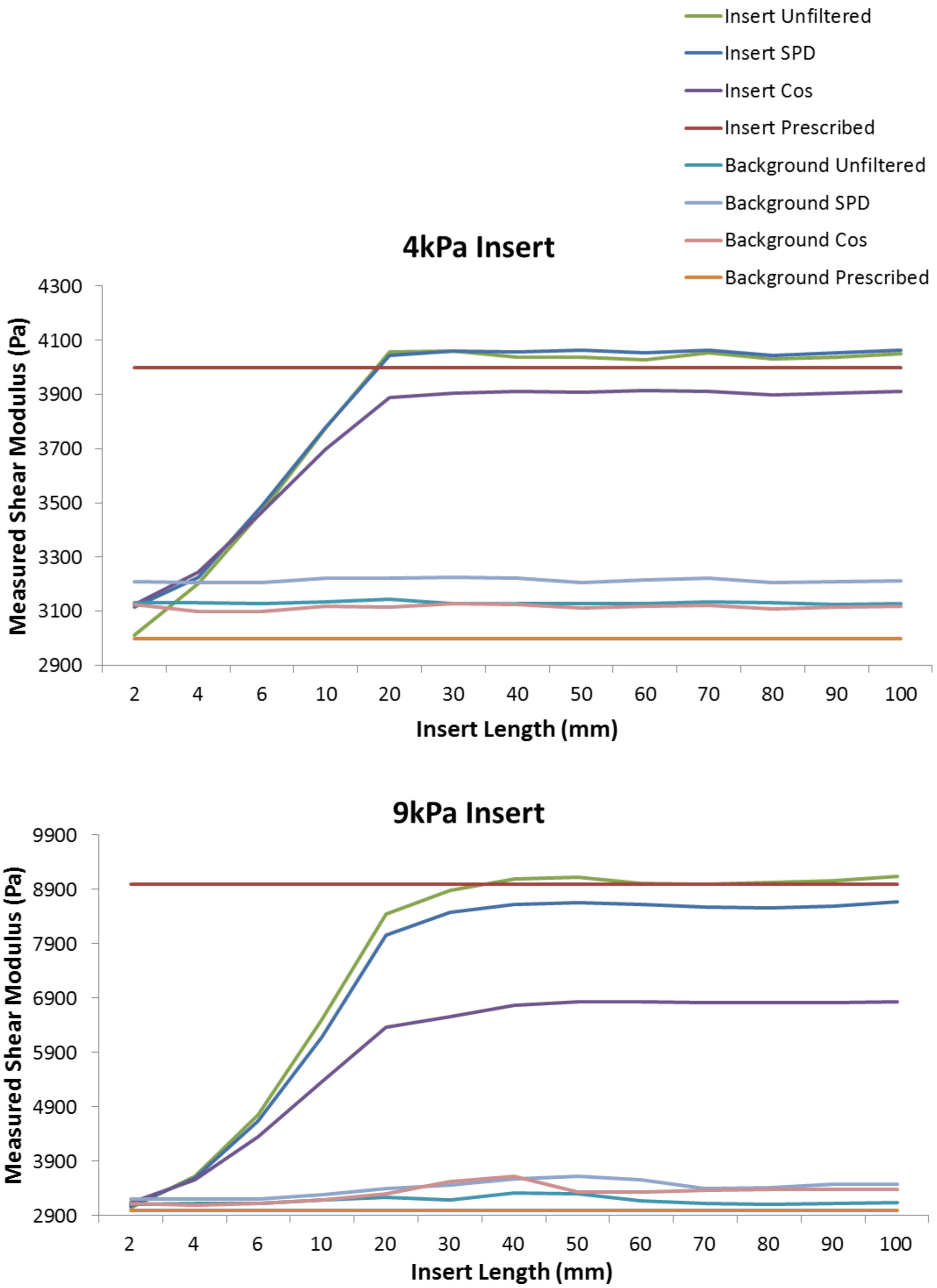

Figure 3.18: Graphs showing the measured shear modulus of unfiltered and directionally filtered 3-D data for the 10 mm radius insert vibrated at 100 Hz. The cos filter results in large reductions in the measured shear modulus of the insert, particularly for high prescribed insert shear moduli. Application of the directional filters resulted in an increase in the measured shear modulus of the background.

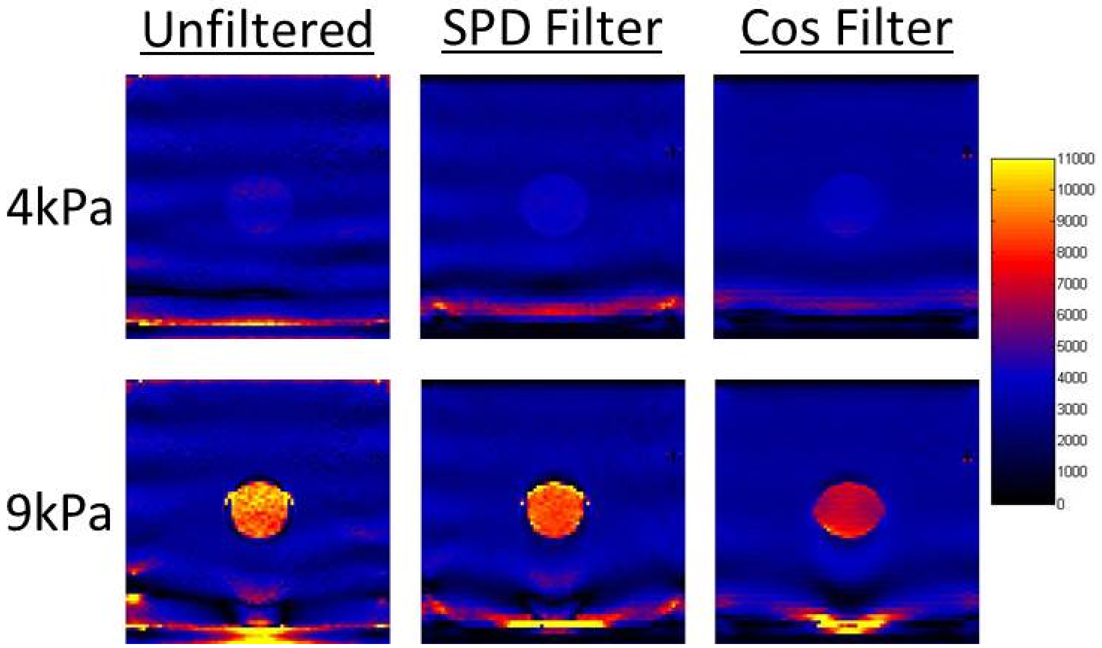

Figure 3.19: Examples of the elastograms following directional filtering for the 10 mm radius insert vibrated at 100 Hz. Whilst both the background and inserts in the filtered datasets appear smoother, artefacts remain in the lower regions of the background.

	4 kPa		9 kPa	
	Background	Insert	Background	Insert
Unfiltered	383	80	273	433
SPD Filter	561	83	440	181
Cos Filter	895	64	357	103

Table 3.9: Examples of the standard deviations for the out-of-plane insert geometry variations from the 10 mm radius insert for vibrations at 100 Hz for the 3-D filtered data. There was little difference in the standard deviations in all regions before and after filtering.

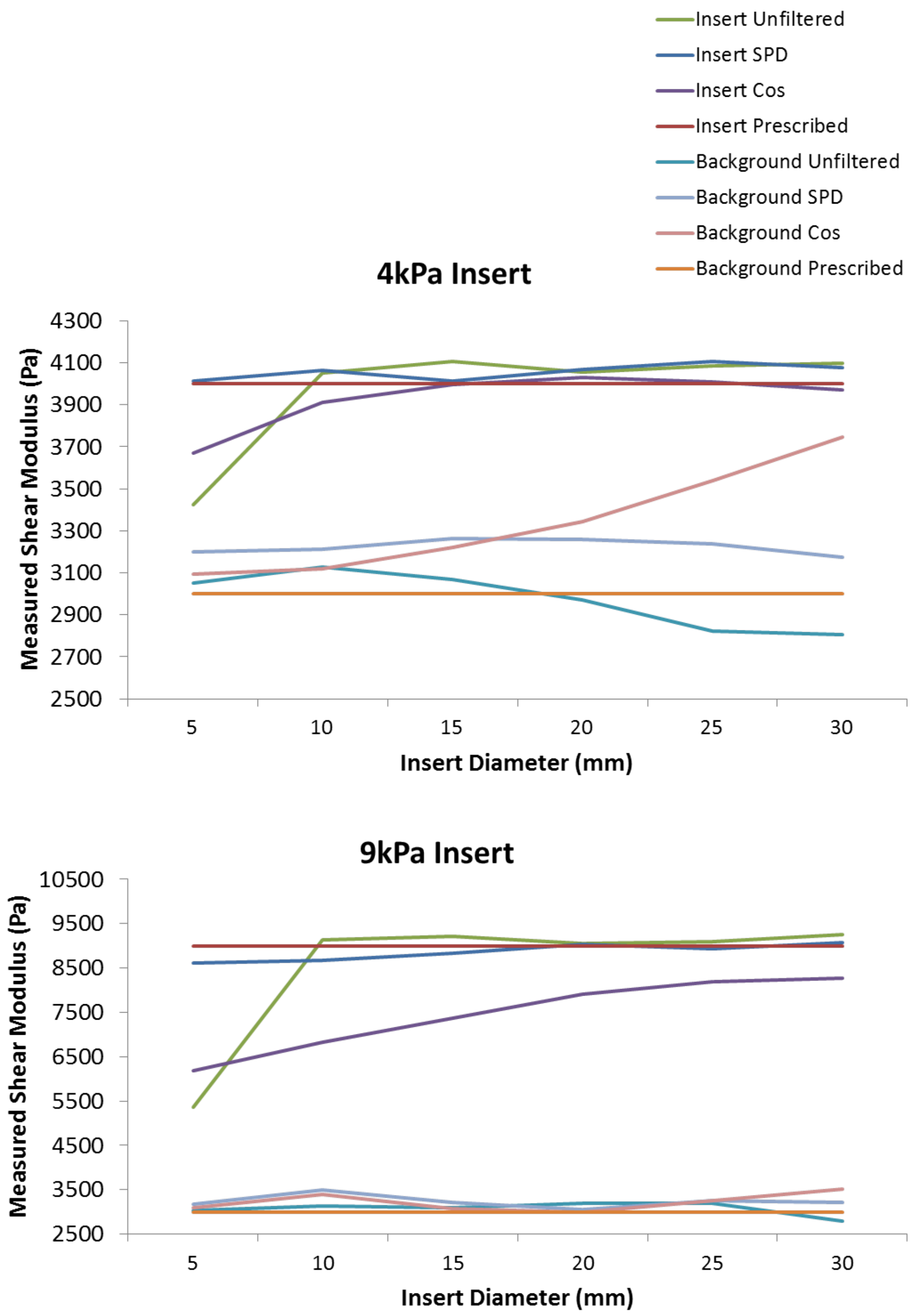

Figure 3.20: Graphs showing the measured shear modulus of unfiltered and directionally filtered 3-D data for the 100 mm length insert vibrated at 100 Hz. The cos filter results in large reductions in the measured shear modulus value, particularly for high prescribed insert shear moduli. Application of the directional filters resulted in an increase in the measured shear modulus of the background. The measured value for the insert was accurate following application of the SPD filter for all insert diameters.

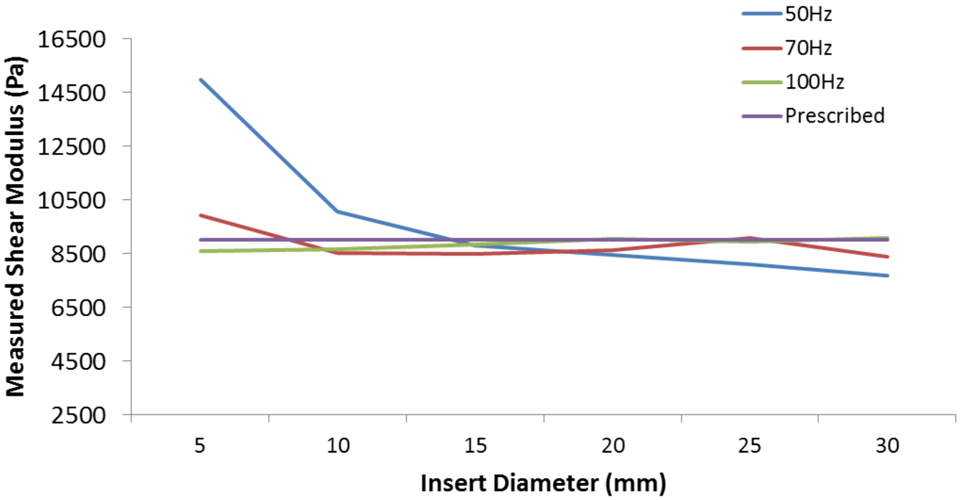

Figure 3.21: Graph showing the measured insert shear modulus at varying frequencies following application of the SPD filter for a prescribed shear modulus of 9 kPa. In contrast to the unfiltered data and the cos filtered data the measured value of the 5 mm length insert increases with decreasing frequency. Whilst this is an accurate measurement at 100 Hz it results in a large overestimation at 50 Hz.

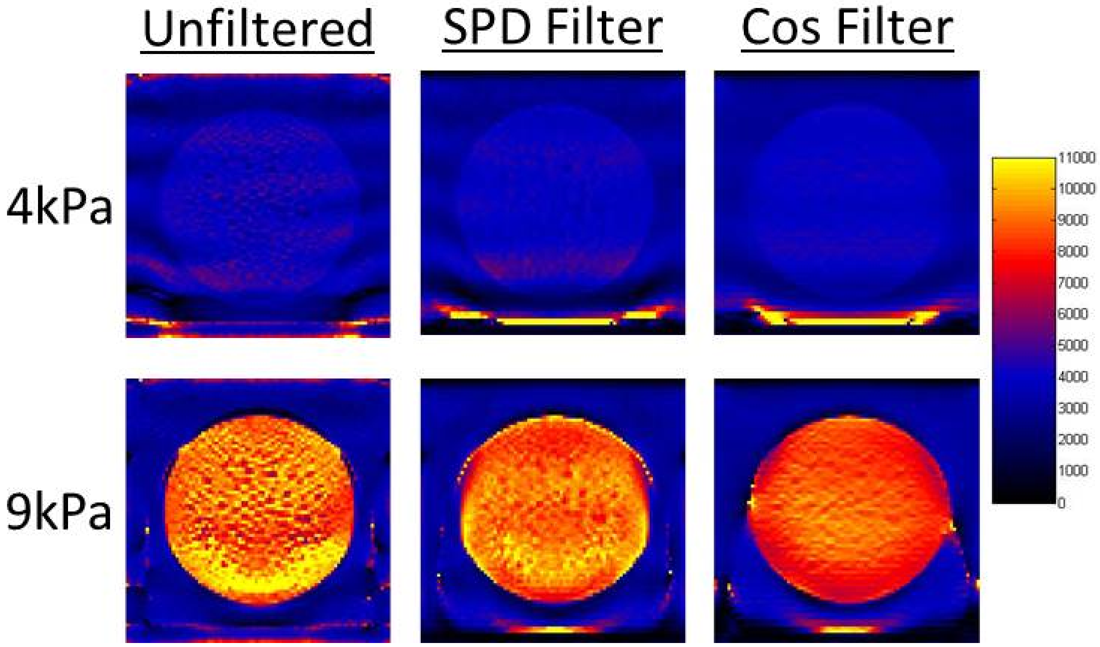

Figure 3.22: Examples of the elastograms following directional filtering for the 30 mm diameter insert vibrated at 100 Hz. The background and inserts generally appear smoother for the filtered data in both the inserts and the background, however there remain artefacts in the lower region of the background.

3.4 Discussion

Chapter 2 showed overestimations following 2-D inversion. This could in part be explained by the lack of information input to the 2-D inversion: it only utilises motion in one direction, therefore does not describe the full wave field. In contrast the 3-D inversion utilises information from all directions and thus offers a complete discretised description. It was therefore hypothesised that utilising the 3-D inversion algorithm would achieve more accurate results. The results of this chapter showed that this was the case, with the 3-D algorithm consistently producing more accurate results than the 2-D algorithm. Whilst underestimations were present following both 2-D and 3-D inversion for the smaller inserts, the out-of-plane length of the insert above which consistent measurements were made was shorter with the 3-D algorithm than it was with the 2-D algorithm (figure 3.4).

Despite the improvements made using the 3-D algorithm in comparison to the 2-D inversion, inaccuracies in the measurements still existed at lower frequencies for the larger inserts with respect to their geometry both in- and out-of-plane (figures 3.5 and 3.9). In all likelihood this was due to the same problem that restricts the 2-D inversion: the algorithm is still subject to the assumption that waves are propagating in a locally homogenous medium [83]. As in chapter 2 this potentially helps to explain why accuracy appears to decrease with frequency, since the ratio of the wavelength to the size of the region of measurement becomes greater.

The lack of a locally homogenous medium also helps to explain why the smaller inserts suffer from underestimations following both the 2- and 3-D inversions. Such underestimation would be expected for the out-of-plane 2 mm and 4 mm length inserts following 3-D inversion as the Laplacian operator used by this algorithm functions over a width of 5 pixels. Since the distance between each slice was 1 mm this implies that information from the wave in the background region where the material has a lower shear modulus was used in the calculation of the shear modulus of the insert. For insert lengths of 6 mm and above however, all the information used for the inversion came from the wave inside the insert yet underestimations still occurred. Inspection of the complex wave images in both the in- and out-of-plane geometry variations showed that wave propagation was less affected by the presence of a smaller insert than it was for a larger insert (figures 3.6 and 3.7). This again demonstrated that wave propagation was not simply dependent upon the material properties of the region under investigation, but also upon its size and shape. The direct inversion algorithm used in this thesis has no geometrical dependence and, like the LFE algorithm also used commonly throughout the literature, will therefore be unable to counter this issue without modification. In this regard, the forward inversion, utilising iterations of assigned material properties within an FE framework in order to match simulated data with real displacement data, makes no such assumptions and therefore potentially offers the best solution to this problem [148].

Although the 3-D algorithm improved upon the accuracy of the shear modulus measurements and reduced the length at which consistent measurements could be achieved, there was no visible improvement in the quality of the elastograms (figures 3.5 and 3.9). Additionally the standard deviations also remained comparable showing that the variability of the measurements was similar (tables 3.2 and 3.3). Since the artefacts following 2-D inversion are typically associated with reflections or a lack of wave propagation, it is not altogether surprising that these artefacts remain following 3-D inversion since the geometries are the same.

To this end MDEV inversion aims to counter these artefacts by utilising multiple frequencies. The underlying theory behind this approach is that the location of artefacts is typically frequency dependent so that when using MDEV, the effects of artefacts from each individual frequency will be limited by the other frequencies [197]. Inspection of the elastograms from the 3-D inversion here supported this conjecture, since the artefacts at 50, 70 and 100 Hz were all located in different positions. Indeed following MDEV inversion there was a clear improvement in the quality of the image, particularly in the background region (figures 3.11 and 3.13). Additionally the standard deviations in this region were reduced in comparison to all three frequencies analysed individually with DI, demonstrating reduced variability of the measured values due to the removal of these artefacts (tables 3.4 and 3.5).

Whilst the background image quality and standard deviations were improved by MDEV, this was not true for the smaller inserts. Artefacts remained in these regions whilst the standard deviations were also similar to those from the 3-D inversion. This suggests that the artefacts from the three frequencies overlap with one another such that MDEV inversion is unable to remove them. This was potentially because the effects of reflections are increased in these small inserts: a theory supported by the artefacts and standard deviations being reduced following MDEV inversion for the larger in-plane geometries.

The use of the MDEV inversion in the literature is limited, largely because it is a relatively recently developed technique. The publications utilising the algorithm have almost exclusively focused upon obtaining better resolution with reduced frequency based artefacts using *in vivo* subjects whilst little has been done to assess the accuracy of their measurements [165, 197, 198]. The work in this chapter showed that MDEV was unable to improve the accuracy of the inversion with respect to DI. Underestimations remained in smaller inserts both in- and out-of-plane, whilst for the larger inserts and the background the accuracy was typically somewhere in between the accuracy of the three frequencies when analysed individually using DI. This was not surprising since MDEV is essentially an extension of the DI, also using the Laplace operator, and therefore still subject to its assumptions. In situations where there are large artefacts at all frequencies that greatly affect the accuracy of DI in each case, it is possible that MDEV's ability to remove these artefacts could lead to an improvement in the accuracy of the measurement. In the relatively simple geometries utilised in this study however, the effects of these artefacts was small, as emphasised by the relatively good accuracy achieved through 3-D inversion. As such, whilst MDEV was unable to improve accuracy in the geometries used in this chapter, its ability in more complex geometries has not been investigated and warrants further research.

A second method aiming to reduce image artefacts tested in this chapter was directional filtering. Both of the filters tested here tended to result in a reduction in the measured value in the insert and an increase in the measured value in the background in both 2- and 3-D (figures 3.14, 3.16, 3.18 and 3.20). This suggests that the filters effectively smoothed wave propagation over the entire region to which it was applied. This was supported by the visual inspection of the complex waves, which appeared to more closely approximate planar wave propagation following filtering (figures 3.15 and 3.17). Of the two filters tested here, it appeared that this effect was more prominent for the cos filter where underestimations were particularly large.

Although application of the filters generally seemed to result in increased smoothness in the upper regions of the background in the elastograms, this was not typically the case in the lower regions. There remained large artefacts in these regions and the standard deviations tended to show increased variability in the measurements (tables 3.6, 3.7, 3.8 and 3.9). This suggests that the filter had the capability to remove the waves reflected off the top of the insert, but because these reflections were occurring, wave propagation through the insert into the lower regions of the model directly below the insert was reduced. For the unfiltered data wave propagation was still present in this region, but in all likelihood from waves reflected off the lower surface of the model, rather than from the incident wave itself. This implies that when the filters were applied, the primary source of wave propagation in this region was also removed, leading to the artefacts and high variability of the measurements seen here.

For the unfiltered data, and indeed MDEV, the relationship between accuracy of the measurements and the size of the insert was the same for size variations both in- and out-of-plane resulting in underestimations for the smaller inserts (figures 3.14, 3.16, 3.18 and 3.20). However this differed somewhat for the SPD filtered data (figure 3.21). Whilst the small out-of-plane inserts were underestimated at all frequencies, the small in-plane inserts were overestimated. Whilst in the context of this project, which is aiming to achieve accurate measurements of material properties within a region, this is not useful, it does suggest that the filter may have a use for identifying small regions of increased stiffness that would otherwise go undetected.

3.5 Conclusions

This chapter utilised the FEA technique developed in chapter 2 to further investigate the impact that size has upon measurements, the abilities of the 2- and 3-D inversion algorithms, the MDEV inversion algorithm and directional filtering. The 3-D algorithm was an improvement upon the 2-D algorithm although still suffered as a result of the assumptions used in its derivation. Although MDEV was unable to improve on the accuracy of the measurements, it was able to improve the quality of the images and would be worth investigating in more complex geometries. The directional filters meanwhile typically resulted in inaccurate measurements and suffered from their own artefacts which reduced image quality.

Chapter 4

Comparing Modelling with Reality

4.1 Introduction

The thesis to this point has focused upon the development of a modelling approach of MRE that allows testing and development of the post-processing software used by the technique and, as is the primary aim of this thesis, to investigate the potential for use of MRE in certain anatomical structures and disease states. A second methodology often utilised in imaging with the same purpose is an experimental approach involving the scanning of phantoms. This approach has been used extensively by modalities such as CT [199], ultrasound [200] and MRI [201] and involves the scanning of a test object that mimics the response of human tissue under that form of assessment. Phantoms are often created with certain properties known, such as the geometry or attenuation, so that the performance of the imaging device with respect to its ability to reclaim these properties can be assessed.

Phantoms have been used by a number of MRE studies to date. Most notably Weaver et al. (2001) [148] demonstrated good geometric reconstruction of their forward algorithm using an inclusion phantom developed in-house. Meanwhile, Kolipaka et al. (2009) [202] developed a spherical phantom that encased a balloon filled with water to simulate cardiac MRE, demonstrating linear correlation between the water pressure and the shear stiffness of the phantom as measured by MRE.

The aim of this chapter is to compare the results from FE simulations of MRE with a phantom scan and to discuss the advantages and disadvantages of each technique.

4.2 Methods

4.2.1 Phantom

The phantom used for this study was the CIRS elasticity QA model 049 phantom (*Computerized Imaging Reference Systems Inc., Norfolk, Virginia, USA*). The phantom is marketed primarily for use in ultrasound elastography but was also designed such that it is MR-compatible. The phantom is an 135 x 95 x 190 mm^3 cuboid containing eight spherical inserts. Four of the inserts are at a depth of 15 mm and are 10 mm in diameter whilst the other set, in a separate yz-plane, are at a depth of 35 mm and of 20 mm in diameter (figure 4.1). For the purposes of this study, only the larger inserts of the phantom have been investigated. The distance in the z-direction from the centre of one insert to another was 30 mm. The material properties were provided by the manufacturer as Young's moduli and were 8, 18, 48 and 80 kPa for the four inserts and 23 kPa for the background.

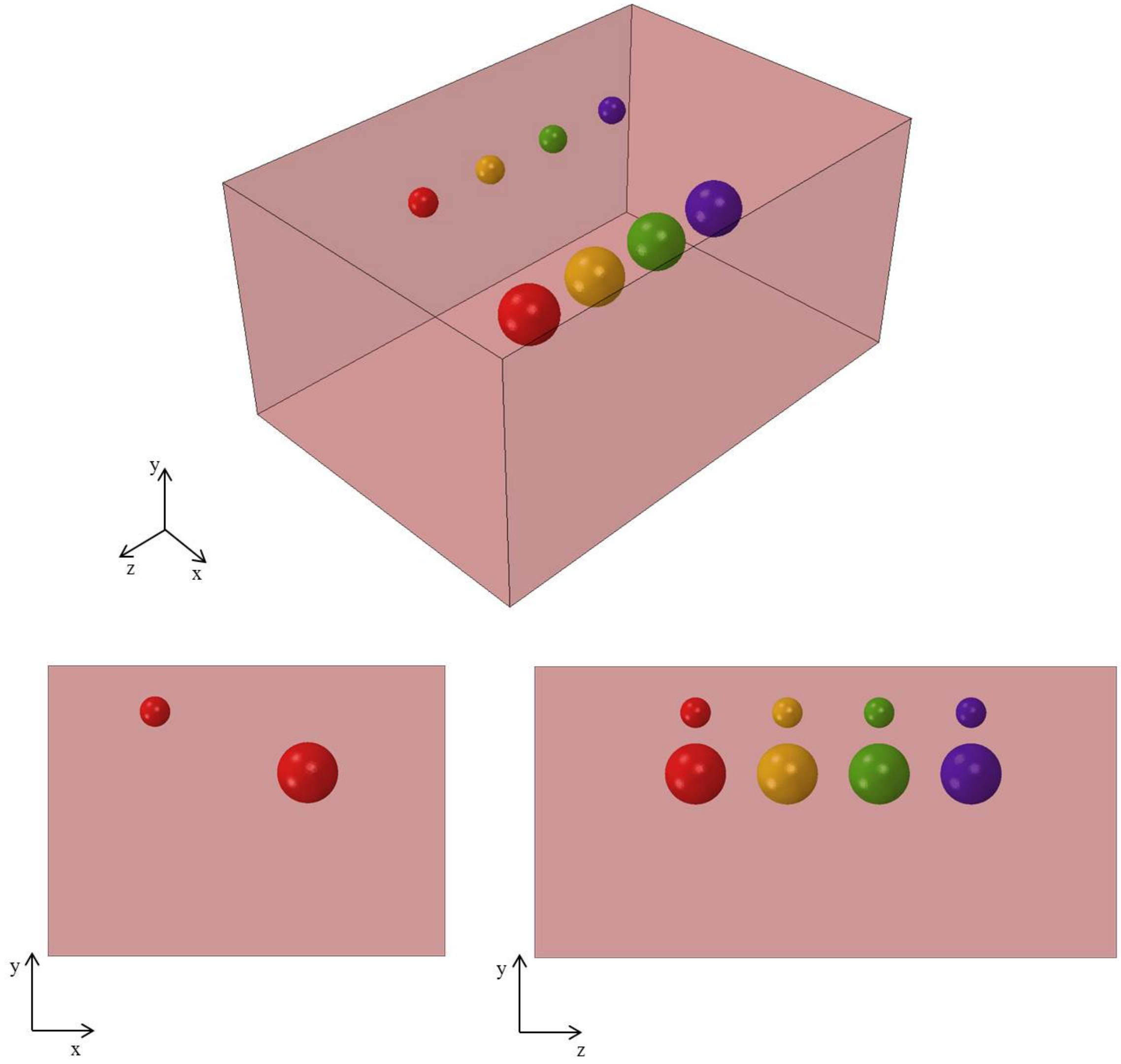

Figure 4.1: CAD illustration showing the design of the CIRS phantom used for this study.

4.2.2 MRI Scanning

Image Acquisition

MRI was performed using a Siemens 3 Tesla scanner (*Magnetom Verio: Siemens, Erlangen, Germany*). A single-shot spin-echo EPI sequence was used with TE 56 ms, TR 1600 ms, flip angle 90°, FOV 224 x 224 mm^2, acquisition matrix 112 x 112, pixel spacing 2 mm, slice thickness 2 mm, 5 slices and 8 MRE phase offsets. The sequence used had been optimised for use in the brain, where lower frequencies are typically applied because of the high degree of damping that exists here. As such vibrations in this study were induced at frequencies of 30, 35, 40, 45 and 50 Hz. Localiser scans were used to locate the spheres and the central slice was placed to cut through the centre of all four spheres in the yz-plane.

The phantom was placed in a head coil within the scanner with sandbags positioned around the edge to wedge the phantom in and reduce body motion during the scan. A transducer was placed on top of the box and attached to a loudspeaker outside the scanner using a carbon fibre rod (figure 4.2).

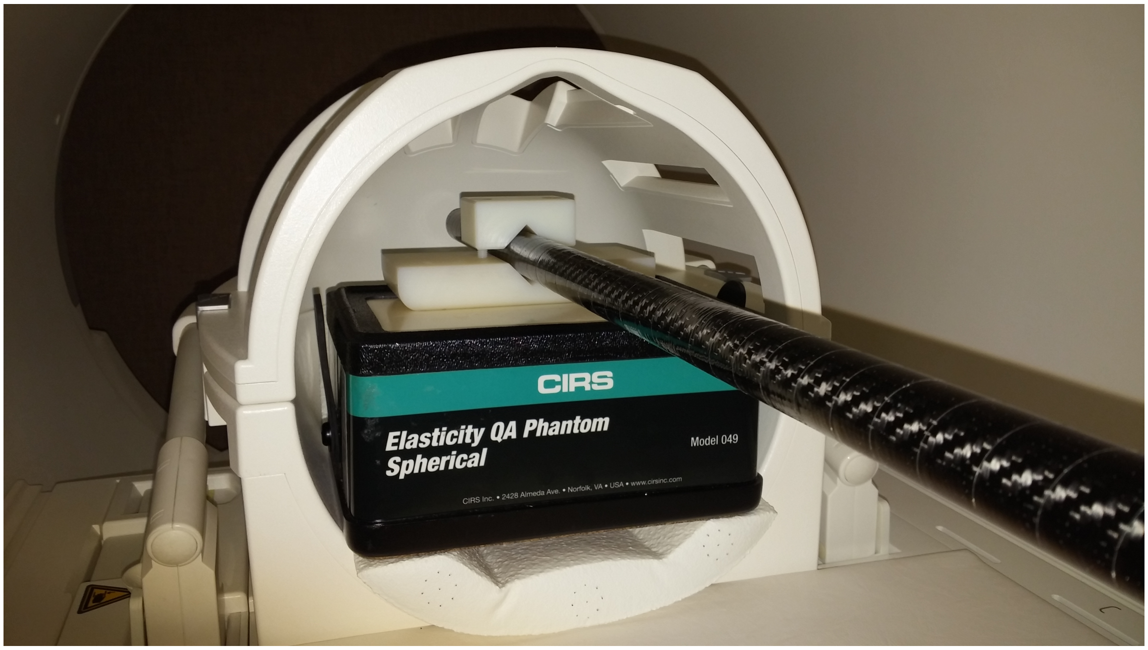

Figure 4.2: Setup for scanning the phantom. The carbon fibre rod transmitted waves from the loudspeaker.

Post-Processing

Data from scans requires more post-processing than modelling data due to the presence of phase wraps and increased noise. Unwrapping was performed using Laplacian-based estimate in the *PhaseTools* software package [158] in *ImageJ* (*U.S. National Institutes of Health, Bethesda. Maryland, USA*) (figure 4.3). Based on work by Barnhill et al. (*in submission*) low frequency noise was removed using a divergence-free wavelet Hodge decomposition [203], whilst high frequency noise was removed using complex dual-tree wavelet denoising [204].

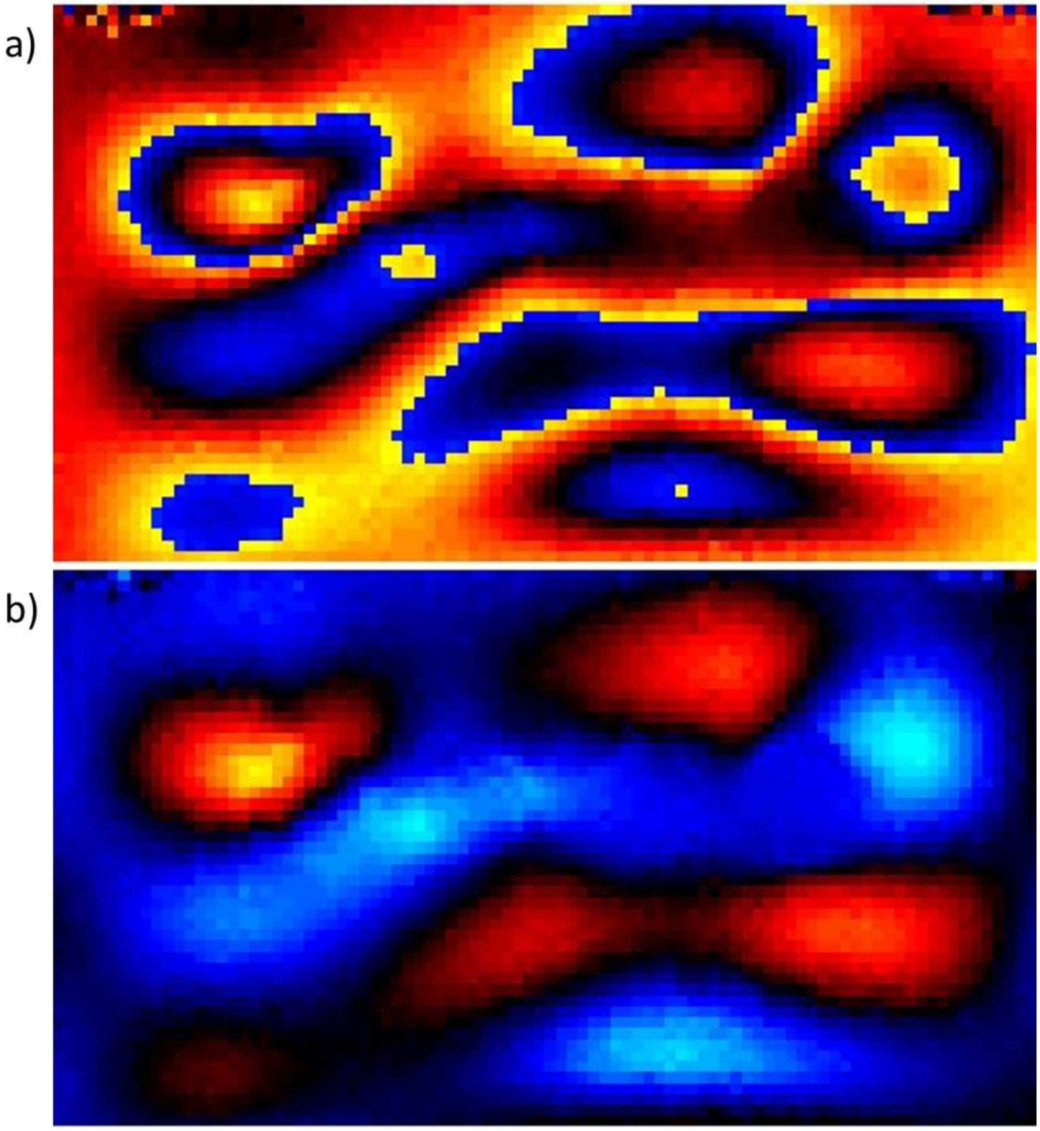

Figure 4.3: Phase image from the phantom vibrated at 50 Hz a) before and b) after the application of the unwrapping algorithm.

4.2.3 Modelling

Geometry

In order to decrease the simulation time, the size of the model was reduced to a size of 80 x 95 x 130 mm^3 focusing on the region containing the 20 mm diameter inserts alone (figure 4.4). The separate background and insert regions of the model were merged together as a single part.

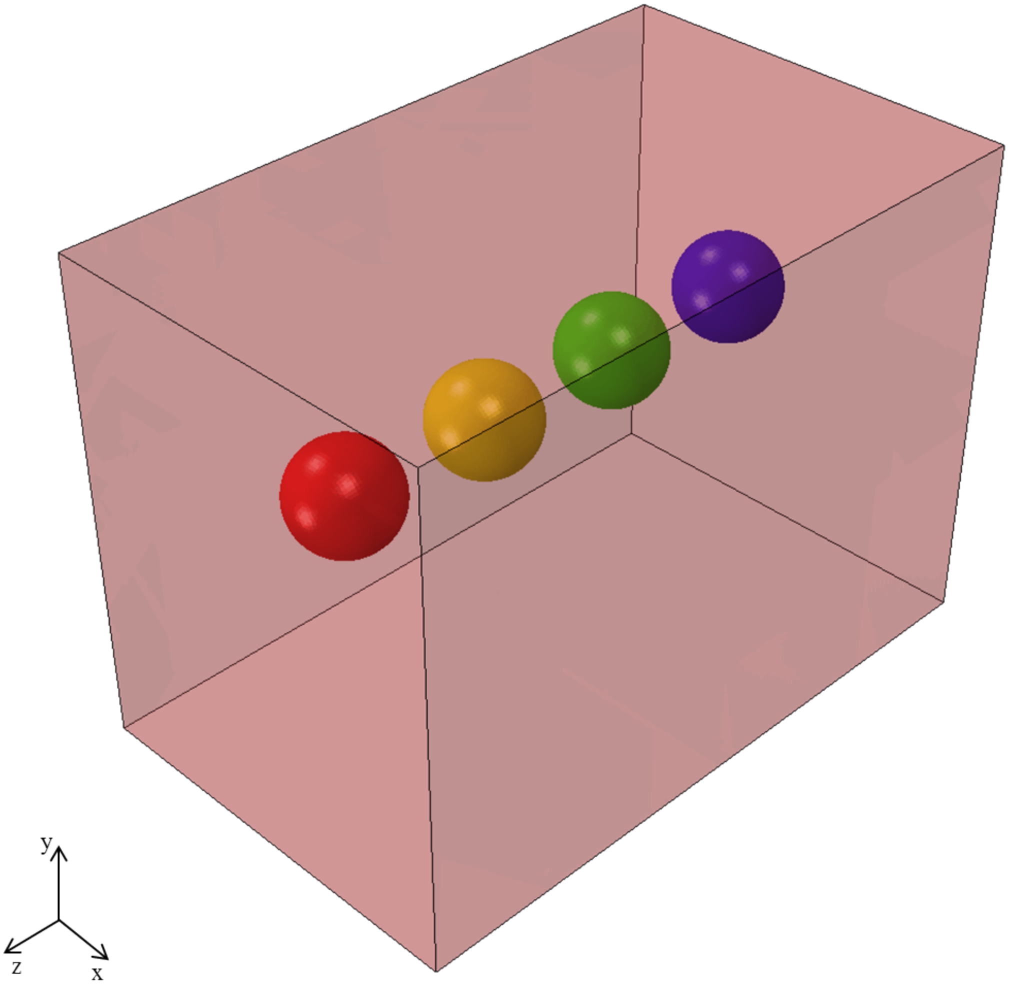

Figure 4.4: Geometry used for the modelling. This was reduced in size in comparison to the actual geometry so as to decrease the time the simulation would take.

Material Properties

The prescribed Young's moduli for the background and insert regions of the model were matched to the values provided by the manufacturer. The shear viscosity and density were not however provided in the documentation. It was assumed that the density of the tissue would correspond to human tissue and was therefore prescribed as 1047 $\text{kg}\cdot\text{m}^{-3}$. Viscoelastic properties were again prescribed in order to reduce the influence of reflections. Since the shear modulus of the background material was higher than those used in previous chapters, therefore meaning that attenuation would be reduced at an equivalent shear viscosity, the prescribed value in this chapter was higher at 3 Pa·s.

Modelling Setup

Load

The load was applied as a concentrated force to a set of nodes on the upper surface of the model in the x-direction with a force per node of 0.001 N. The size and position of this region constant for all simulations. The frequencies applied were matched with those from the scan.

Boundary Conditions

Symmetric boundary conditions in the z-direction were applied to all boundaries excluding that upon which the load was applied.

Mesh

The model was meshed using C3D10M elements. The element length along all edges in the model was defined as 1.25 mm and convergence studies were performed to ensure that this provided adequate accuracy.

Data Extraction

Data was extracted from 5 yz-planes in all three spatial directions. The points within each plane were 1 mm apart from one another and the spacing between each plane was 1 mm corresponding to a voxel size of 1 mm^3. The central plane was aligned with the centre of the spheres.

4.2.4 Inversion and Data Analysis

Both the scan data and the modelling data were inverted using DI at each individual frequency and using MDEV for all frequencies combined. For the modelling data masks were created for the background region and each insert, applied to the elastogram and then the mean within this region calculated (figure 4.5). Since the position of the spheres were less precisely known for the scan data, regions of interest were drawn manually in *ImageJ* based upon visual inspection of the elastograms and the mean value calculated within these regions.

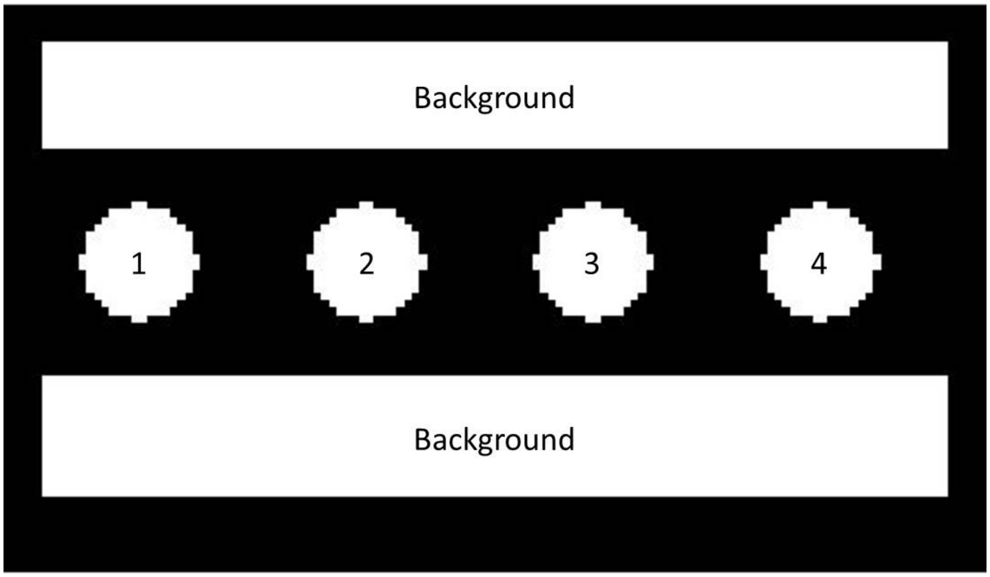

Figure 4.5: Combined image of the masks for the four inserts and the background region used on the modelling data.

4.3 Results

Visual inspection of the complex wave images showed that there was greater noise in the scan data than the simulated data, with waves also appearing to more closely approximate planar propagation in the simulated data (figure 4.6). Noise also appeared to increase in the elastograms for the scan data, although reflection artefacts were more visible in the elastograms from the simulated data (figures 4.7 and 4.8). MDEV had a greater influence on the quality of the elastogram from the FEA data, where reflection artefacts were greatly reduced, in comparison to the elastogram from the scan data, where noise remained high (figure 4.9).

Measurements of the background were underestimated by 19-27% for all frequencies from the scan data. From the simulated data however, the measurements increased with increasing frequency (at 30 Hz, the measurement was underestimated by 15%, whilst at 50 Hz it was overestimated by 20%). At lower frequencies, measurements of all inserts were larger from the simulated data than they were from the scan data. This was also true of the MDEV measurements. This effect was reduced at higher frequencies, with measured values from both datasets similar to one another at 50 Hz (figure 4.10).

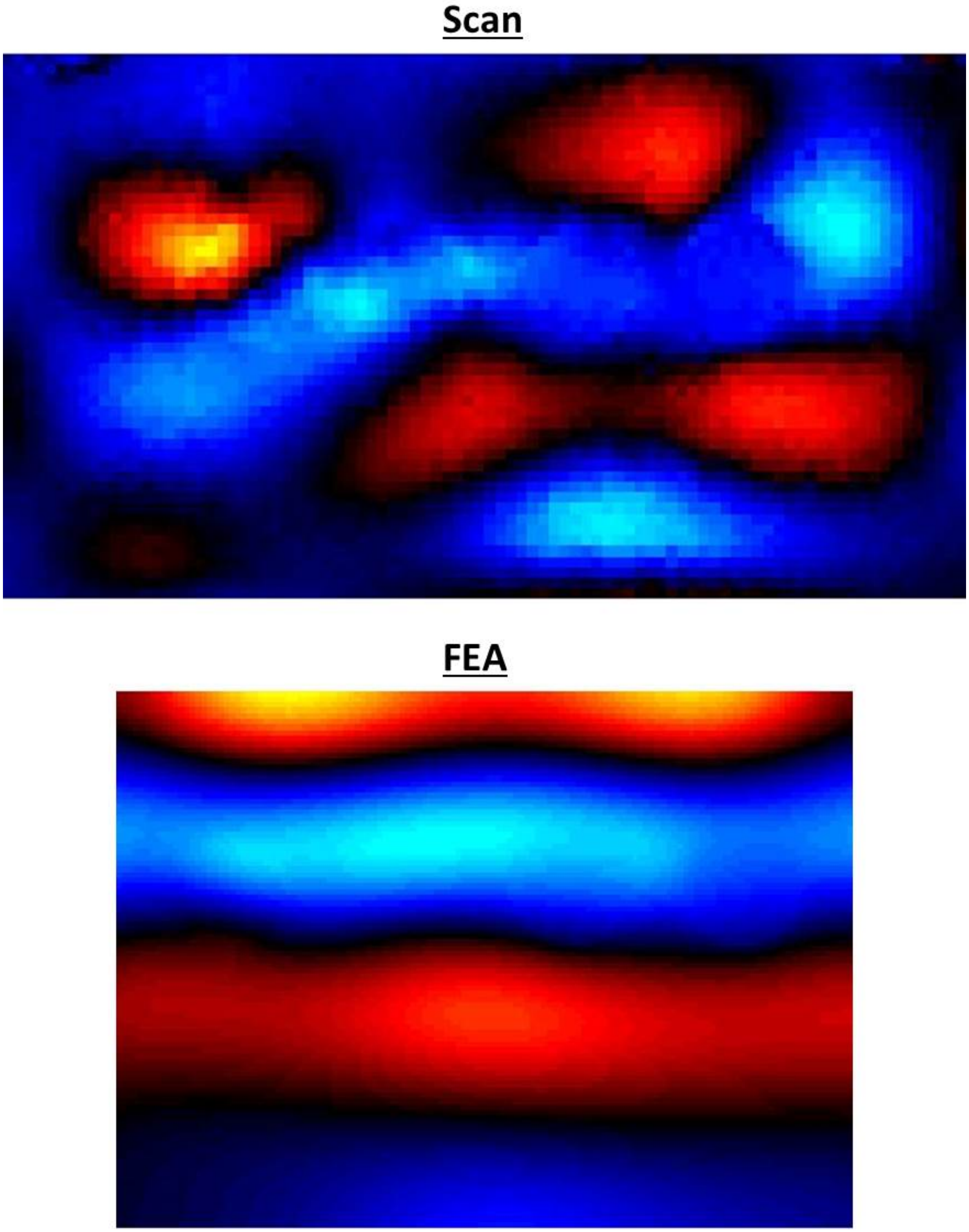

Figure 4.6: Visual inspection of the complex wave images showed that there was increased noise in the data from the scan and that the wave from the simulated data appeared to more closely appoximate planarity.

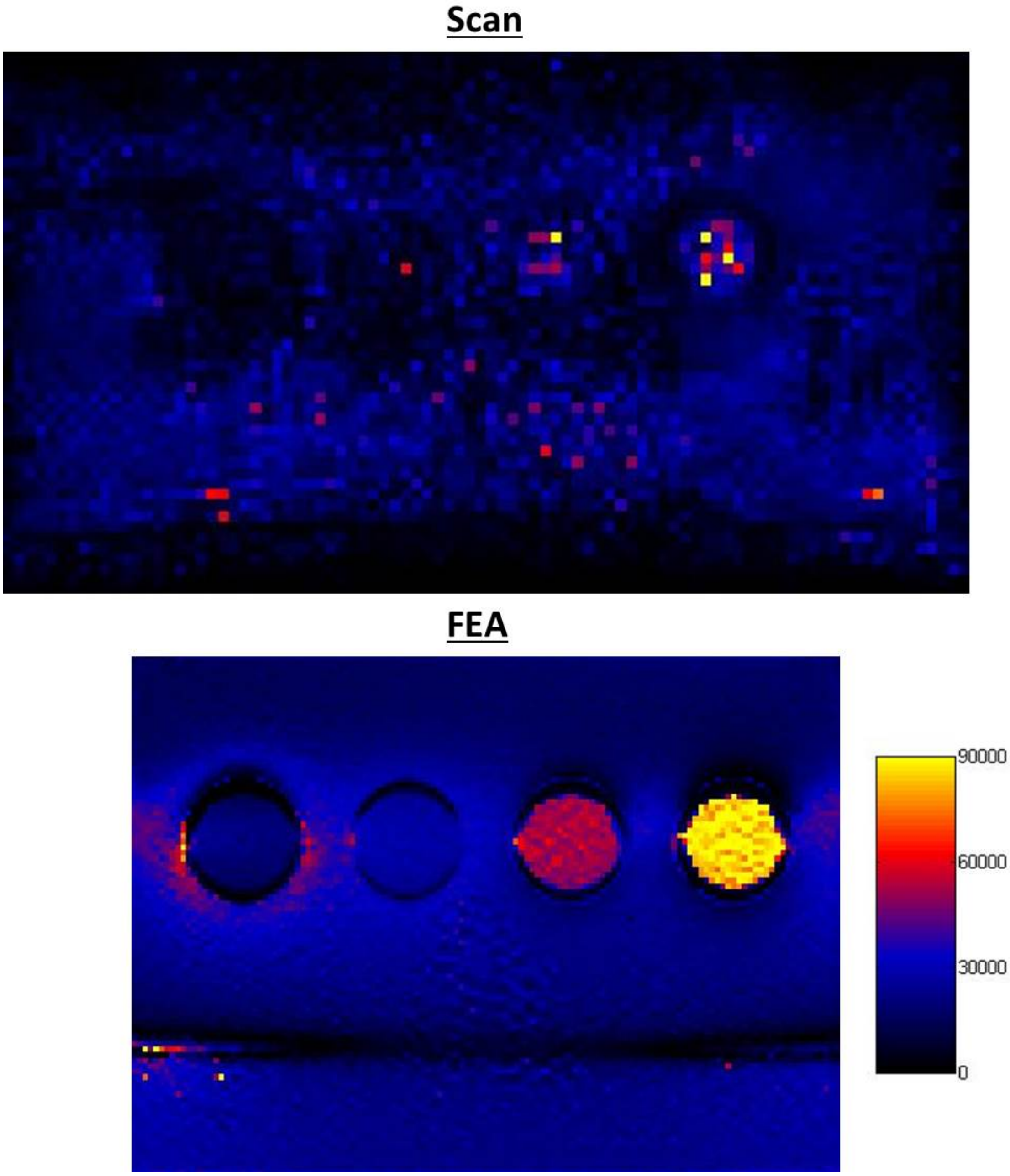

Figure 4.7: Elastograms from the scan and FEA datasets with vibrations applied at 30 Hz. There was greater noise in the elastogram from the scan than there was from the FEA where the presence of reflection artefacts was more noticeable. The inserts were better resolved in the FEA elastogram than the scan elastogram.

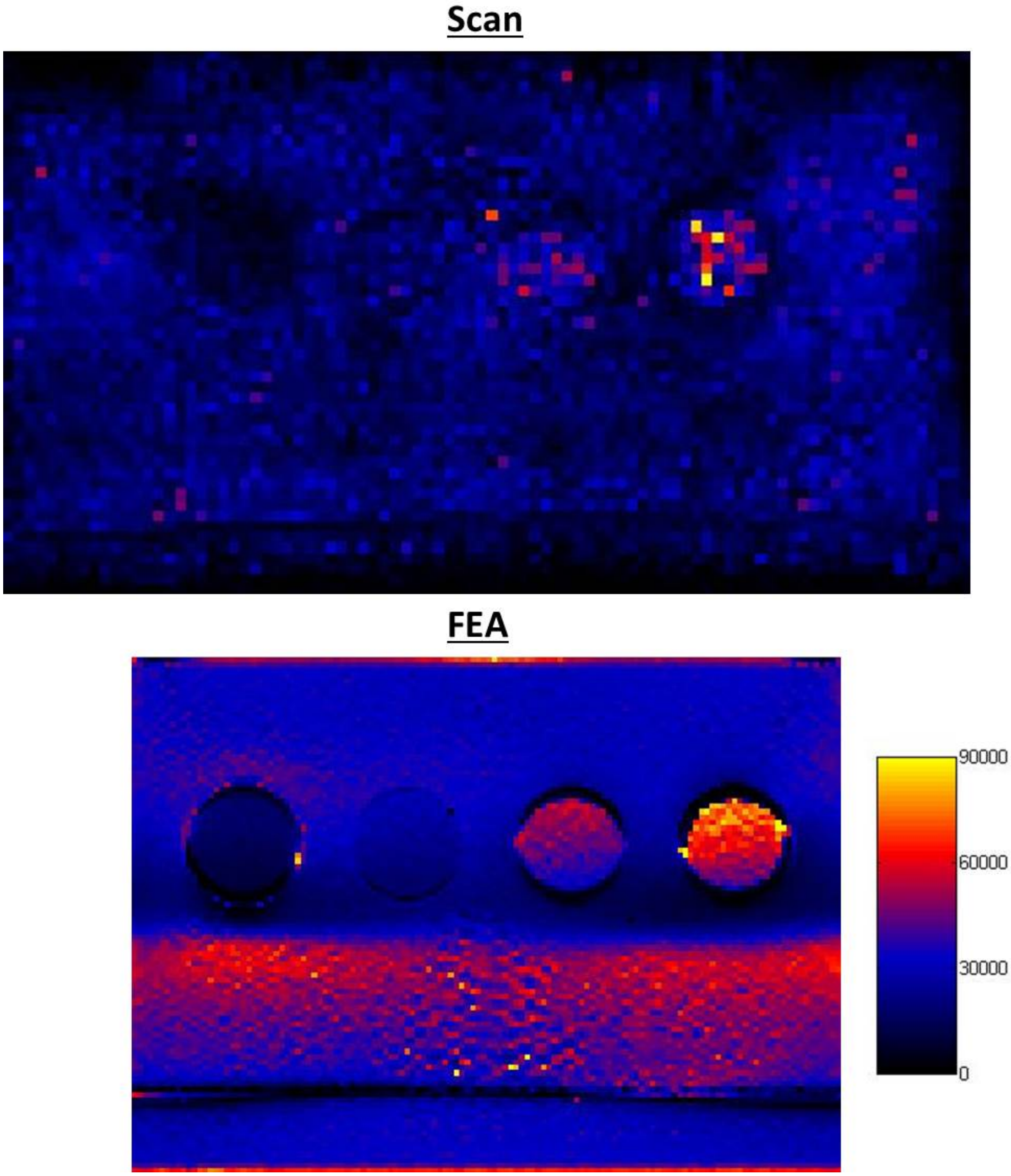

Figure 4.8: Elastograms from the scan and FEA datasets with vibrations applied at 50 Hz. As with 30 Hz, reflection artefacts were more noticeable in the FEA elastogram, whilst noise levels were higher in the elastogram from the scan.

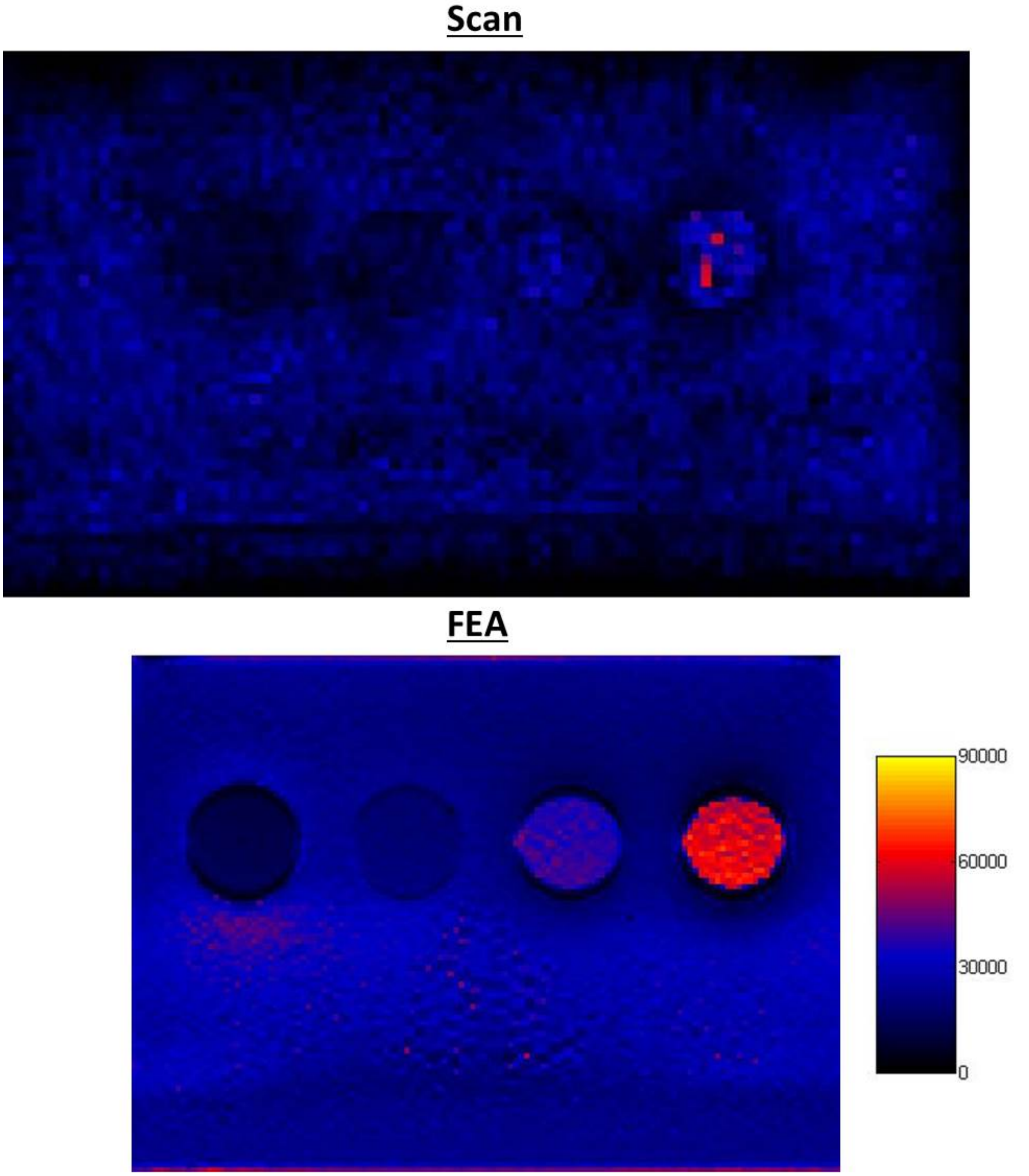

Figure 4.9: Elastograms from the scan and FEA datasets following MDEV inversion. The inversion seemed to have a greater influence in removing artefacts from the FEA datasets, with noise remaining relatively high in the elastogram from the scans.

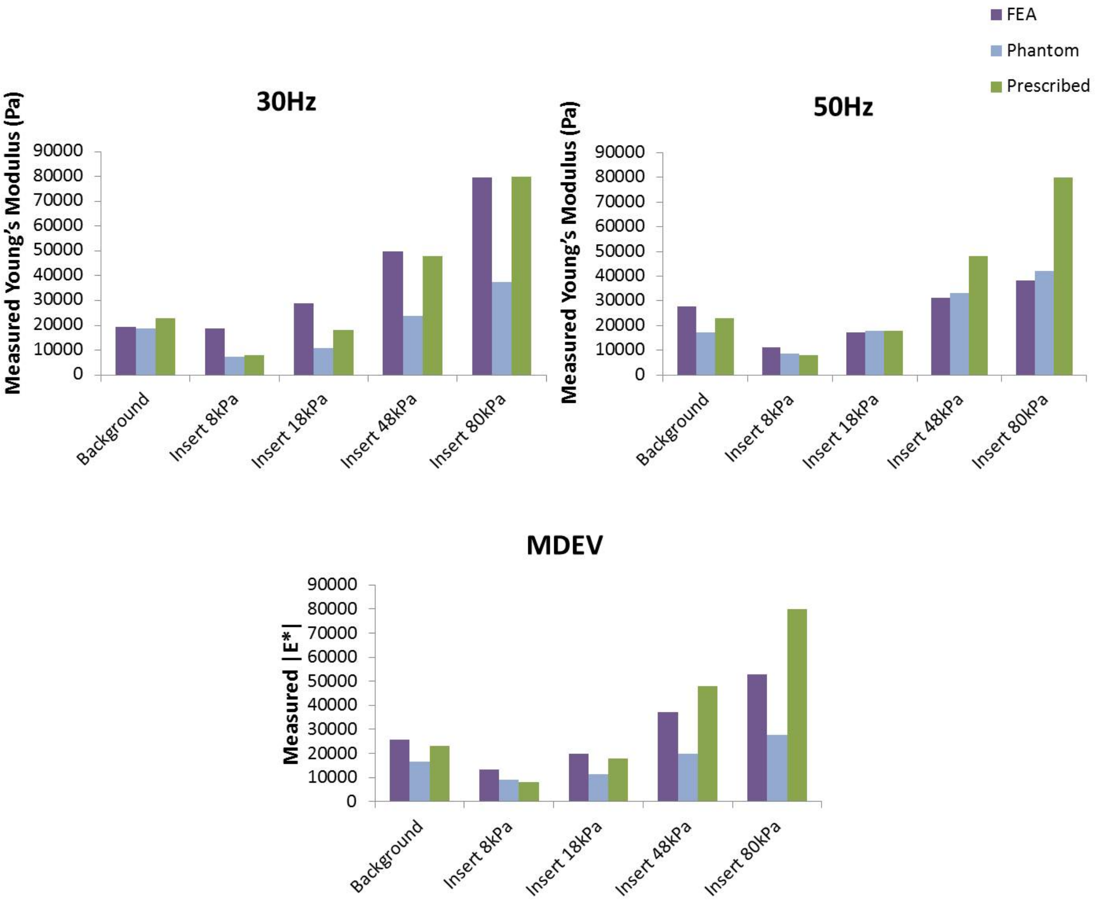

Figure 4.10: Graphs showing the measurements from the background and insert regions of the phantom from the scan and FEA datasets following DI at 30 and 50 Hz and MDEV inversion. For DI at 30 Hz and MDEV inversion the measurements were larger from the FEA datasets than they were from the scan, though this gap decreased with increasing frequency and the measurments at 50 Hz were similar to one another.

4.4 Discussion

Whilst viscoelastic properties are applied to the FEA model to reduce the effects of reflections, the lack of viscoelastic material property data provided by the manufacturer prevented these properties being matched to the phantom. Differences in the extent and effect of reflections between FEA and the scan were therefore to be expected. Furthermore a cited distinction between *in vivo* MRE and MRE of phantoms is the increased scattering resulting from the greater number of interfaces *in vivo* and heterogeneity of the tissue [193, 205]. It is likely that imperfections from the construction of the phantom and degradation of the material over time also result in a similar difference between phantoms and FEA, causing scattering throughout the medium to be greater in phantoms than FEA. This could potentially explain why reflection artefacts were more prominent *in silico* in this experiment and why wave propagation appeared less planar in the phantom (figures 4.7 and 4.8).

Aside from the presence of reflection artefacts, the quality of the elastograms from FEA was better than those from the scan with decreased noise and more clearly resolved inserts. This was in agreement with a previous study by Li et al. (2012) [152] which also compared data from FEA modelling with phantom scanning. The increased noise levels seen in the complex wave images helps explain these phenomena (figure 4.6), as well as the discrepancies between measurements at low frequencies, since both DI and MDEV use the Laplacian which is highly sensitive to noise [206]. This means any noise in the complex wave image is over-emphasised in the elastogram, which also leads to reduced contrast between different regions. Additionally, since noise is random, it is typically represented by high spatial frequencies in the frequency domain. When considering planar wave propagation, high spatial frequencies are associated with propagation through low shear moduli materials. This implies that the presence of noise in the complex wave image reduces the shear modulus measurements through inversion, an effect which increases with decreasing frequency of the induced MRE wave [156]. Since noise levels in the scan are greater than those in the FEA data, it would therefore be expected that the measurements at low frequencies would be larger from the scan than from FEA. Whilst filtering has been performed to remove such noise from the scan datasets, it is clear that noise removal remains a challenge in

MRE.

Chapters 2 and 3 of this thesis demonstrated several mechanisms by which inaccurate measurement of the shear moduli can occur. The existence of such mechanisms leads to an interesting scenario. For instance, consider the 48 kPa and 80 kPa inserts vibrated at lower frequencies, which are measured with relatively good accuracy from the modelling data (figure 4.10). Chapter 3 demonstrated that small inserts are often underestimated because they do not alter wave propagation sufficiently. Since the inserts in this study were relatively small, one would expect underestimations through this mechanism. Conversely, chapters 2 and 3 both demonstrated that when the wavelength of the induced wave is long in comparison to the size of the region of interest, overestimations often occur. For stiff inserts vibrated at low frequencies one would also expect this to be true, therefore through this mechanism overestimations would be expected. As such it is not inconceivable that both mechanisms effectively cancelled one another out to result in the accurate measurements seen here. This hypothesis is supported by the fact that increasing the frequency of vibrations reduced the measurements in these stiffer inserts, since this would result in a decrease of the expected wavelength in this region, thus meaning that the second of these mechanisms, which tends to result in overestimations, became less influential. It is also possible that a similar process happened in the scan data for the 8 kPa insert at low frequencies whereby noise, which typically results in underestimations, cancelled out the mechanism by which overestimations occur as a result of long wavelengths in a small region of interest to achieve an accurate measurement here.

Whilst the discussion to this point has focused on the difference between the results from the scan and FEA, there are also practical differences that should be considered when comparing the two techniques. A major advantage of FEA is its flexibility: geometries, material properties and boundary conditions can all easily be altered allowing extensive studies such as that performed in chapter 3 (although computational time does tend to limit the size of the models developed). In contrast, whilst phantoms can be constructed in a range of geometries, this process is often time consuming and it is much harder to accurately prescribe material properties.

As shown in this chapter, noise levels in FEA are relatively low in comparison to the phantom, and the data does not suffer from phase wraps. Clearly the MRE post-processing pipeline needs to incorporate software that can remove these phase wraps and noise before performing inversion. Whilst this thesis has focused on the capabilities of the inversion algorithm itself, both factors can easily be added into the FEA datasets to allow for development of noise removal and phase unwrapping software [178]. User addition of noise and phase wrapping allows a higher level of control over the extent to which they are present in the phase images than is achievable in scanning; a further advantage of FEA.

Although FEA provides an excellent foundation from which to test the post-processing software, it does not allow for testing of the MRE acquisition process itself. The MR sequence used for a scan is dependent on the type of information required and the part of the anatomy from which the data is to be collected. It is important to make sure that the data acquired from each new sequence is of adequate standard. To this end, phantoms provide an excellent tool with which to test the sequence; a process which is not possible with FEA.

4.5 Conclusions

This chapter aimed to compare results from FE simulations of MRE with a phantom scan. Differences between the two techniques were highlighted which decreased with increasing frequency. These differences were attributed to a failure to match prescribed viscoelastic material properties in the model to those of the actual phantom, due to lack of information provided by the manufacturers in this regard, and increased noise in the scan data. Whilst FEA provides an excellent platform upon which to perform extensive testing of post-processing software in a highly controlled environment, it is not able to test the capabilities of MR sequences used for data acquisition. As such both techniques should continue to play an important role in the development of the technique.

Chapter 5

Modelling Idealised AAAs

5.1 Introduction

The primary aim of this thesis was to investigate the potential of integrating MRE values into patient specific models of AAAs with a view to achieving a better predictor of whether the AAA would rupture or not. Chapter 2 described and investigated the parameters surrounding an FEA method that would replicate MRE *in silico*. One potential use was demonstrated in chapter 3, where the capabilities and limitations of different algorithms and filters were compared. A second potential use, and of particular relevance to this chapter, is to investigate directly the capabilities of the technique with respect to certain disease states.

There is currently little in the literature with this specific aim. Dao et al. (2014) [207] presented work which aimed to develop FEA of MRE in thigh skeletal muscle using 3-D geometries reconstructed from MRI datasets. Closer to the work in this thesis however, was the publication by Thomas-Seale et al. (2011) [182] which demonstrated that high-frequency MRE had potential in differentiating the size of a lipid pool within an atherosclerotic plaque utilising a steady-state FEA technique.

The work in this chapter aims to create 3-D axisymmetric idealised AAA geometries and utilise FEA to investigate the effectiveness of MRE at measuring the material properties of such geometries. One of the major concerns highlighted in chapter 3 was the geometrical dependence, both in- and out-of-plane, of MRE measurements. AAAs vary greatly in size therefore this chapter aims to investigate how this affected accuracy of measurements at a number of frequencies. Additionally the material properties themselves were shown to influence the accuracy of the measurements. As such this chapter also aims to investigate a range of shear moduli for the vessel wall and the thrombus in addition to the viscous properties of the thrombus. It was also hypothesised in chapter 3 that MDEV would be capable of achieving better results than direct inversion in more complex geometries and as such MDEV has again been compared against DI here.

5.2 Methods

5.2.1 Geometry

AAA geometries of diameter 50, 60 and 70 mm were created for this study. All AAAs were of length 90mm based on measurements from Hans et al. (2005) [53]. CAD was initially performed using *Autodesk Autocad Student Version 2015 (Autodesk, Inc., San Rafael, California, USA)*. For the thrombus a set of 2-D circles was created with a spacing of 5 mm between each circle in the z-direction. The centre of each circle was shifted in the x-direction such that the posterior point of each circle touched coincided with $z = 0$. The distribution of the radius about the central circle was Gaussian such that the geometry was symmetric in the xy- and xz-planes. Once the circles had been created they were lofted together to create a solid mould. This process was repeated in order to create the mould for the vessel wall. On this occasion however the radius of each circle was increased by 2 mm and translated by 2 mm in the negative z-direction such that a vessel wall of 2 mm could be created.

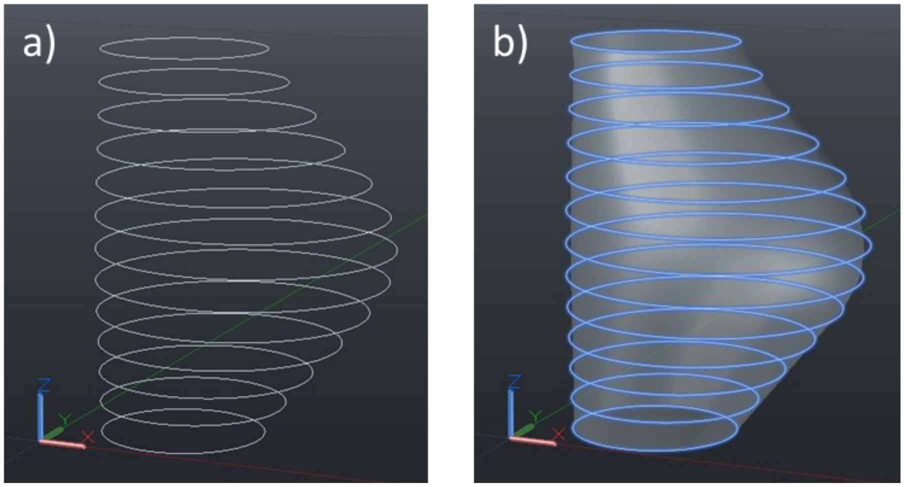

Figure 5.1: Circles are created at different heights with increasing radii towards the centre (a) and then lofted together to create a solid mould (b). Note: axes are switched when model is imported to Abaqus. Throughout this chapter the coordinate system as defined by Abaqus will be used rather than the coordinate system defined by Autodesk.

Following creation the vessel wall and thrombus moulds were exported as .iges files to *Abaqus/CAE* for further pre-processing with *Abaqus's* in-built CAD designer. Here a cylindrical lumen of radius 9 mm and cuboid boxes to encase the AAAs in were created. These varied in size depending upon the size of the AAA with the smallest distance from AAA to the edge of the box at the anterior being 20 mm and 10 mm on all other sides. Boolean operations were then performed to create the vessel wall and thrombus from the moulds. To reduce the size of the model and the simulation time 15 mm was cut from the top and bottom of the model reducing the AAA length to 60 mm. Finally the different sections of the model were tied together using constraints (figure 5.2).

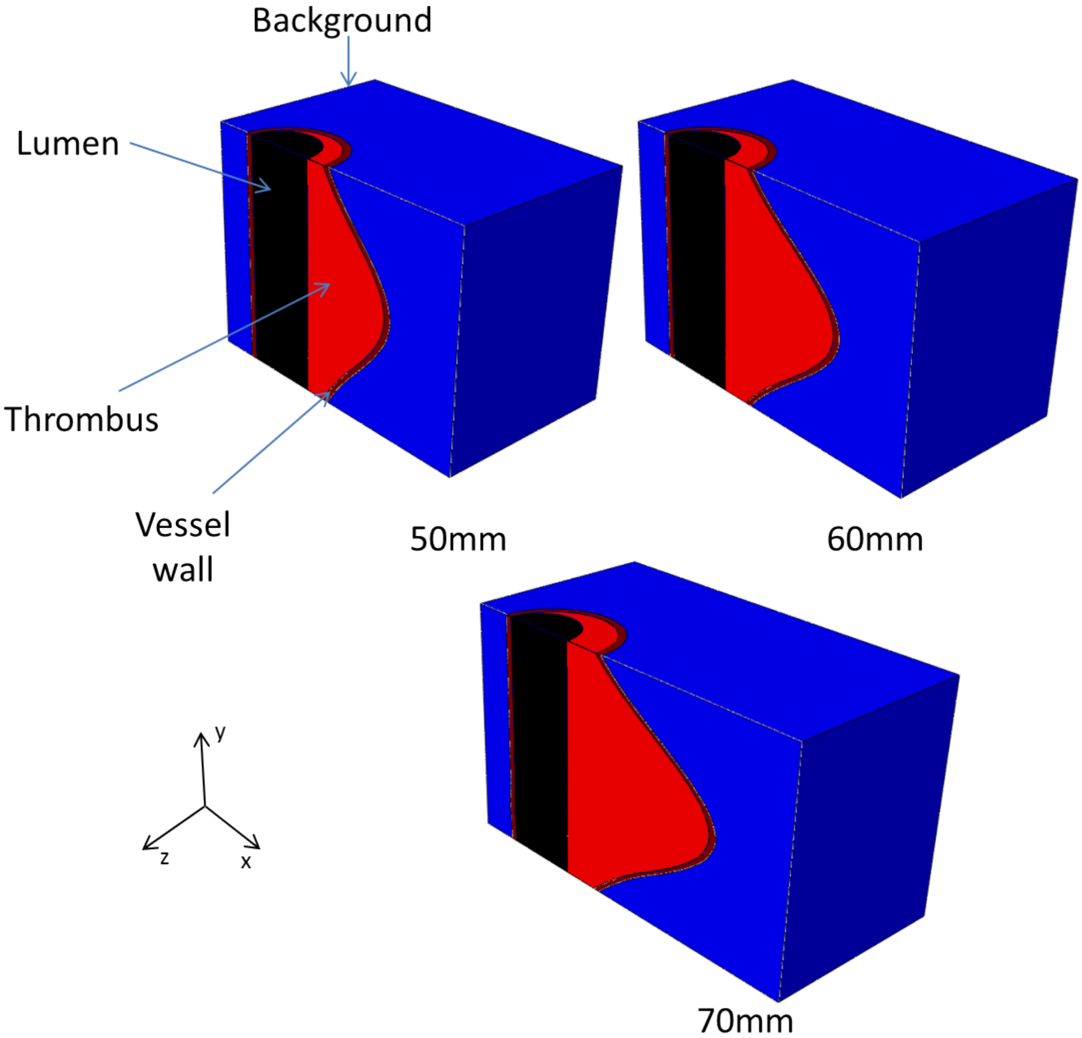

Figure 5.2: 50, 60 and 70 mm idealised AAA geometries consisting of a lumen, thrombus, vessel wall and background material.

5.2.2 Material Properties

The following section outlines the material properties utilised in the each part of the model and the reasons why these were chosen. The values used are outlined in table 3.1. Throughout the entire model the density was defined as 1047 kg·m^{-3} with all materials assumed incompressible with a Poisson's ratio of 0.49. The Kelvin-Voigt model was used to induce damping into the model and was defined as 1 Pa·s except where specified otherwise.

Vessel Wall

There have been several *in vivo* MRE studies looking to measure the properties of the vessel wall. The technique utilises the waveguide effect whereby longitudinal waves are induced via shear vibrations in the vessel wall. However, as acknowledged by Damughatla et al. (2013) [176], MRE does not provide an absolute measure of tissue elasticity since analysis has typically been performed in 2-D and wave propagation is not planar. More fundamentally, since wave propagation is longitudinal and not shear, the quoted stiffness is in fact the $E^{*}t$ product, dependent on t, the thickness of the vessel wall [174].

Woodrum et al. (2006) [172] utilised MRE to directly measure the stiffness of an *ex vivo* pig's aorta calculating a Young's modulus of approximately 0.9 MPa. A study by Martin et al. (2011) [208] using biaxial testing that compared human and porcine tissues showed that although human arteries were significantly stiffer than porcine aorta, the values were of the same order of magnitude 0.7 and 0.1 MPa respectively. Based on these values from the Woodrum and Martin studies, the shear modulus of the vessel wall was varied from 0.1-1 MPa.

Intraluminal Thrombus

To date there is nothing in the literature with regards to the shear modulus of the intraluminal thrombus in AAAs measured using MRE. There is large variability in the literature regarding the material properties of the thrombus using mechanical testing highlighted by Speelman et al. (2010) [209] whose review showed a range of values from 0.5 kPa to 180 kPa depending on the method of measurement used and the thrombus layer investigated, though most values are towards the lower end of this scale. Using shear ultrasound elastography, a technique similar in methodology to MRE, Schmitt et al. (2011) [210] investigated the shear modulus of blood clots at a variety of frequencies. Using the Kelvin-Voigt model the shear modulus was calculated as being 1 kPa. Based on this value and from the majority of values in the Speelman paper, the shear modulus of the thrombus was varied from 1-21 kPa.

Although the investigation of viscoelastic material models is outside the scope of this thesis, it was recognised that there is likely to be a large degree of variability of such properties in the ILT. The effects of variations in damping caused by such variability upon shear modulus measurements was therefore seen as worthy of investigation. As such the shear viscosity of the ILT was varied from 0.25-1.25 Pa·s.

Surrounding Material

Again there is nothing in the MRE literature regarding the shear modulus of the tissue surrounding the aorta. For the purposes of this study it was therefore assumed that the surrounding tissue was fatty soft tissue. Such tissue has been examined in heel pads [211] and breasts [212] and on both occasions has been characterised using MRE as having a shear modulus of approximately 8 kPa. Based on these papers the shear modulus of the surrounding tissue was defined as 8 kPa.

Lumen

To model the lumen accurately would require an FSI simulation outside the scope of this thesis. As such an alternative is sought. Thomas-Seale et al. (2011) [213] utilised an acoustic medium with a steady-state simulation in an investigation into atherosclerotic plaques. Models in that study were relatively small in comparison to those used here however, and as such the long computational time for a steady-state simulation was seen as impractical. Unfortunately the simulation time for a transient explicit analysis increases hugely if the wave amplitude in a region is a region of the model is very small. This was the case in the lumen when the material was defined as an acoustic medium with a small amount of demonstrating that individual models would take several weeks to run. This meant that realistic simulation of the lumen was not practical. Therefore to try and maintain a high level of damping within this region and to maintain reflections resulting from the change in medium, the shear modulus was defined as 100 Pa.

	Vessel Wall	Thrombus	Surrounding Tissue	Lumen
Shear Modulus	0.25-1.75 MPa	1-21 kPa	8 kPa	0.1 kPa
Shear Viscosity	1 Pa·s	0.25-1.25 Pa·s	1 Pa·s	1 Pa·s

Table 5.1: Table outlining the material properties prescribed for each section within the model.

5.2.3 Modelling Setup

Load

The load was applied as a concentrated force to a set of nodes on the anterior surface of the model in the z-direction with a force per node of 0.001 N. The size of this region was consistent throughout all of the models. Frequencies of 50, 70 and 100 Hz were applied to each model.

Boundary Conditions

Symmetric boundary conditions in the y-direction were applied to all surfaces apart from that upon which the load was applied.

Mesh

Models were meshed using C3D10M elements. The element length was defined as 2 mm along each edge within the model and convergence studies were performed on each geometry to demonstrate that this provided a high enough mesh density for accurate simulation.

5.2.4 Inversion

Inversion was performed using 2-D and 3-D DI and MDEV. For 3-D DI and MDEV this implied that data was extracted from 5 planes in all three spatial directions. Voxel sizes used in this study were 1 mm^3. Manually created masks were applied to the thrombus and surrounding tissue regions and the means and standard deviations of the measurements within these regions were calculated (figure 5.3).

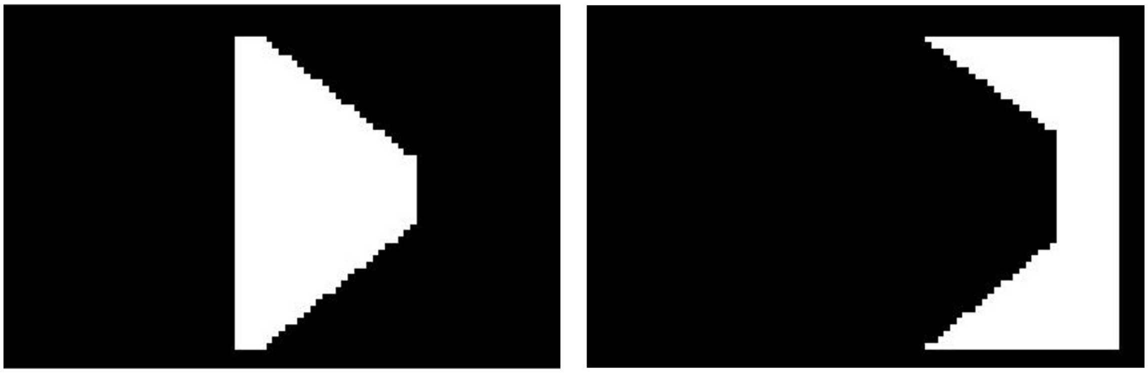

Figure 5.3: Examples of the masks used for the thrombus (left) and the surrounding tissue (right) for an AAA size of 60 mm. The elastogram is orientated such that the left hand side represents the posterior and the right hand side represents the anterior.

5.3 Results

5.3.1 Size

Following 2-D DI at 50 Hz there was large variability in the measurements made for different prescribed shear moduli values in both the thrombus and surrounding tissue region of the model for all three AAA sizes (figure 5.4) Following 3-D DI variability in the measurements remained in the surrounding tissue. At high prescribed shear modulus measurements made in the 60 and 70 mm AAAs suffered from large underestimations (34% and 47% for the 21 kPa thrombus respectively), contrasting with the 50 mm insert where large overestimations occurred (133% for a thrombus of 21 kPa).

At 70 Hz the variability in the background measurements over the range of prescribed thrombus shear modulus was reduced following 2-D inversion with measurements consistently underestimated by 12-19% (figure 5.5). However, there remained a large amount of variability in the thrombus measurements. After 3-D inversion the surrounding tissue measurements were underestimated by 9-17%. Thrombus values were overestimated for all three AAA sizes. The size of this overestimation was greatly increased for the 50 mm size AAA (145% for the 21 kPa prescribed thrombus) in comparison to the 60 and 70 mm AAAs (25% and 70% respectively).

Background measurements following 2-D inversion at 100 Hz were improved in accuracy in comparison to 70 Hz with errors in the range of 1-6% (figure 5.6). In the thrombus region there was little difference between errors for all three AAA sizes which were greatly reduced in comparison to 50 and 70 Hz (4, 0.6 and 16% errors for AAA sizes 50, 60 and 70 mm respectively for the 21 kPa prescribed thrombus shear modulus). Errors remained large for low prescribed thrombus shear moduli however (149%, 408% and 273% for the 50, 60 and 70 mm AAAs for a prescribed thrombus shear modulus of 1 kPa). Background measurements at 100 Hz following 3-D inversion also achieved a higher level of accuracy than at 50 and 70 Hz (0-15%). Thrombus measurements were also consistent for all AAA sizes and were much improved in terms of accuracy in comparison to measurements made at 50 and 70 Hz for higher prescribed thrombus shear modulus (10, 17 and 8% errors for the 50, 60 and 70 mm AAAs respectively for the 21 kPa prescribed thrombus shear modulus). As with the 2-D inversion however, errors remained large for the lower prescribed shear modulus (146%, 464% and 267% for the 50, 60 and 70 mm AAAs respectively for a prescribed thrombus shear modulus of 1 kPa). There was little difference between the errors in the 2-D and 3-D inversions at 100 Hz, but increasing the prescribed thrombus shear modulus always resulted in an increased thrombus measurement with the 3-D inversion in contrast to the 2-D inversion, where increasing the prescribed shear modulus from 13 kPa to 17 kPa resulted in a decrease in the measured value of the thrombus in the 60 mm thrombus.

MDEV inversion consistently underestimated the surrounding tissue by 10-20% though measurements were relatively consistent across all AAA sizes (figure 5.7). Whilst relatively good accuracy was achieved in the thrombus at higher prescribed thrombus shear moduli for the 60 and 70 mm AAAs (5 and 8% respectively for a prescribed value of 21 kPa), there were large overestimations for the 50 mm AAA (116%).

Inspection of the elastograms revealed artefacts in both the surrounding region and thrombus at all frequencies which were typically more pronounced in the 50 mm AAA (figure 5.8). The position of these artefacts was frequency dependent whilst the size of the artefact reduced with increasing frequency (figure 5.9). Artefacts still existed following MDEV inversion. The position of the largest artefact in the thrombus region matched the position of the artefact in the 50 Hz image. Whilst at lower frequencies standard deviations were typically higher following 2-D inversion than 3-D inversion, at 100 Hz the opposite was true (table 5.2). This effect was more noticeable with measurements from the thrombus.

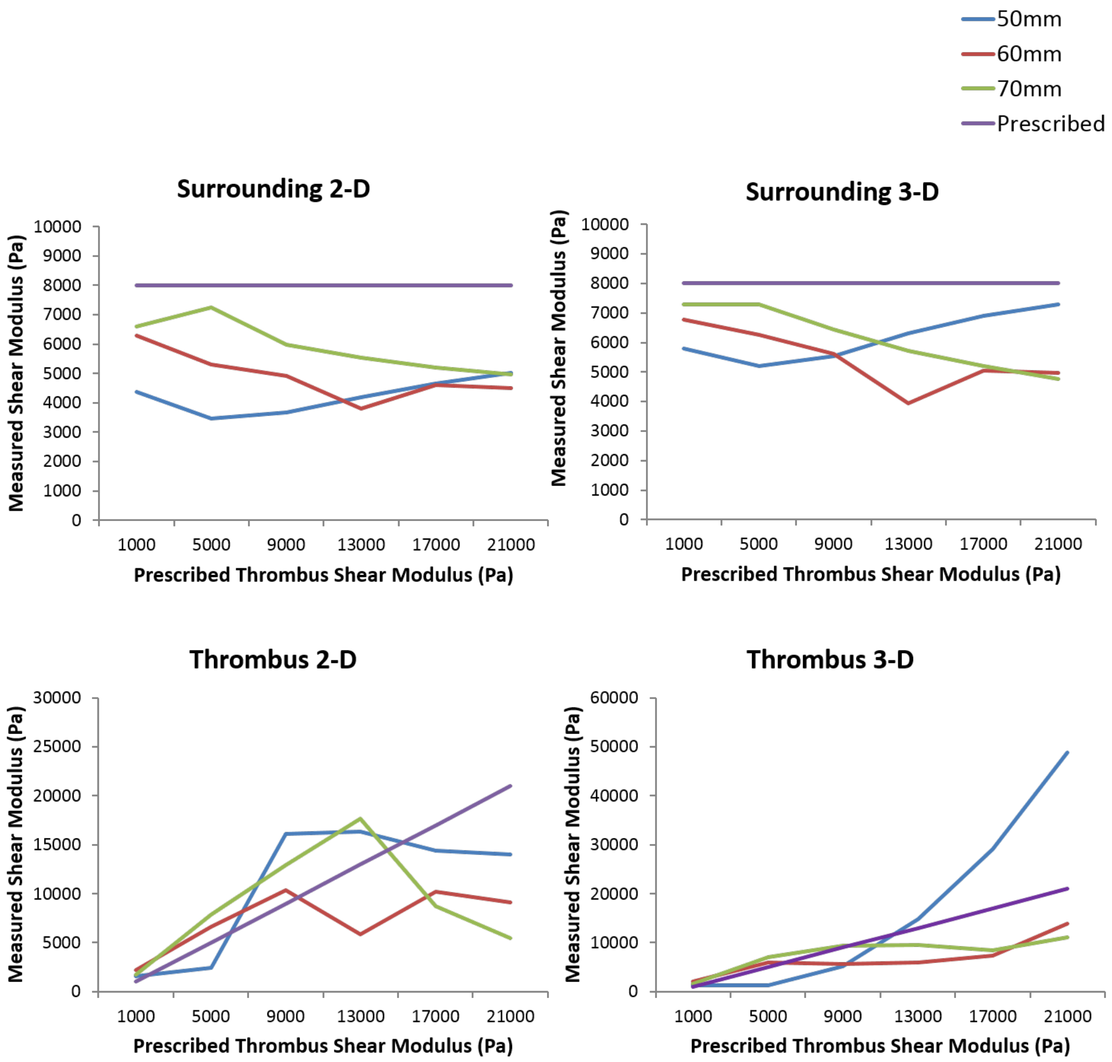

Figure 5.4: Graphs showing the measurements made in the surrounding tissue and thrombus following 2- and 3-D inversion of the 50 Hz waves. There was a large amount of variabilty in the surrounding tissue measurements for the different prescribed thrombus shear moduli. Accuracy in the measurements of the thrombus was poor following both inversions.

In both regions the standard deviation was lower following MDEV inversion than both the 2- and 3-D direct inversions.

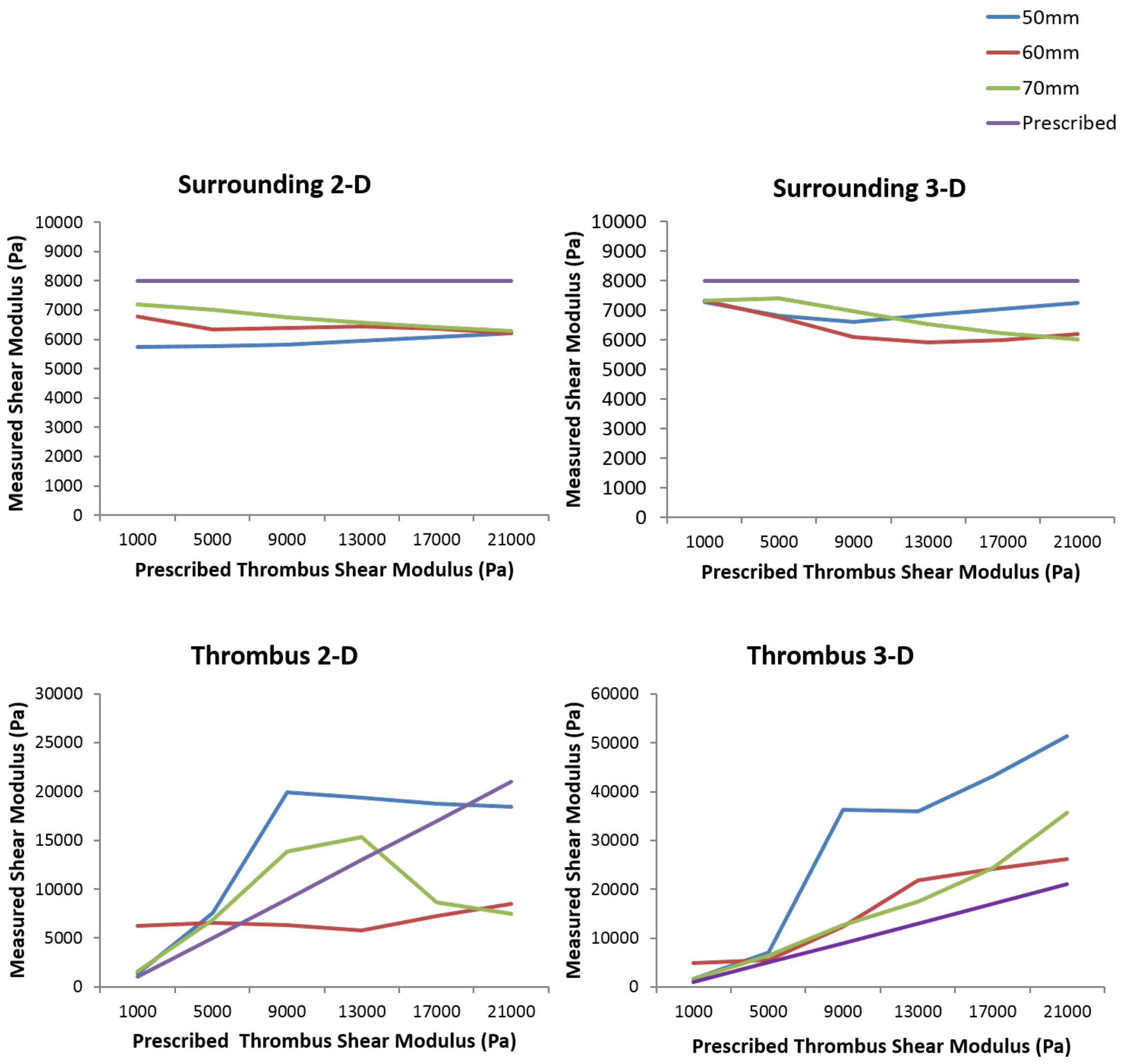

Figure 5.5: Graphs showing the measurements made in the surrounding tissue and thrombus following 2- and 3-D inversion of the 70 Hz waves. Variability in the surrounding tissue measurements for different prescribed thrombus values was decreased in comparison to 50 Hz. Measurements in the thrombus following 3-D inversion were overestimated with the size of the overestimation considerably larger for the 50 mm AAA.

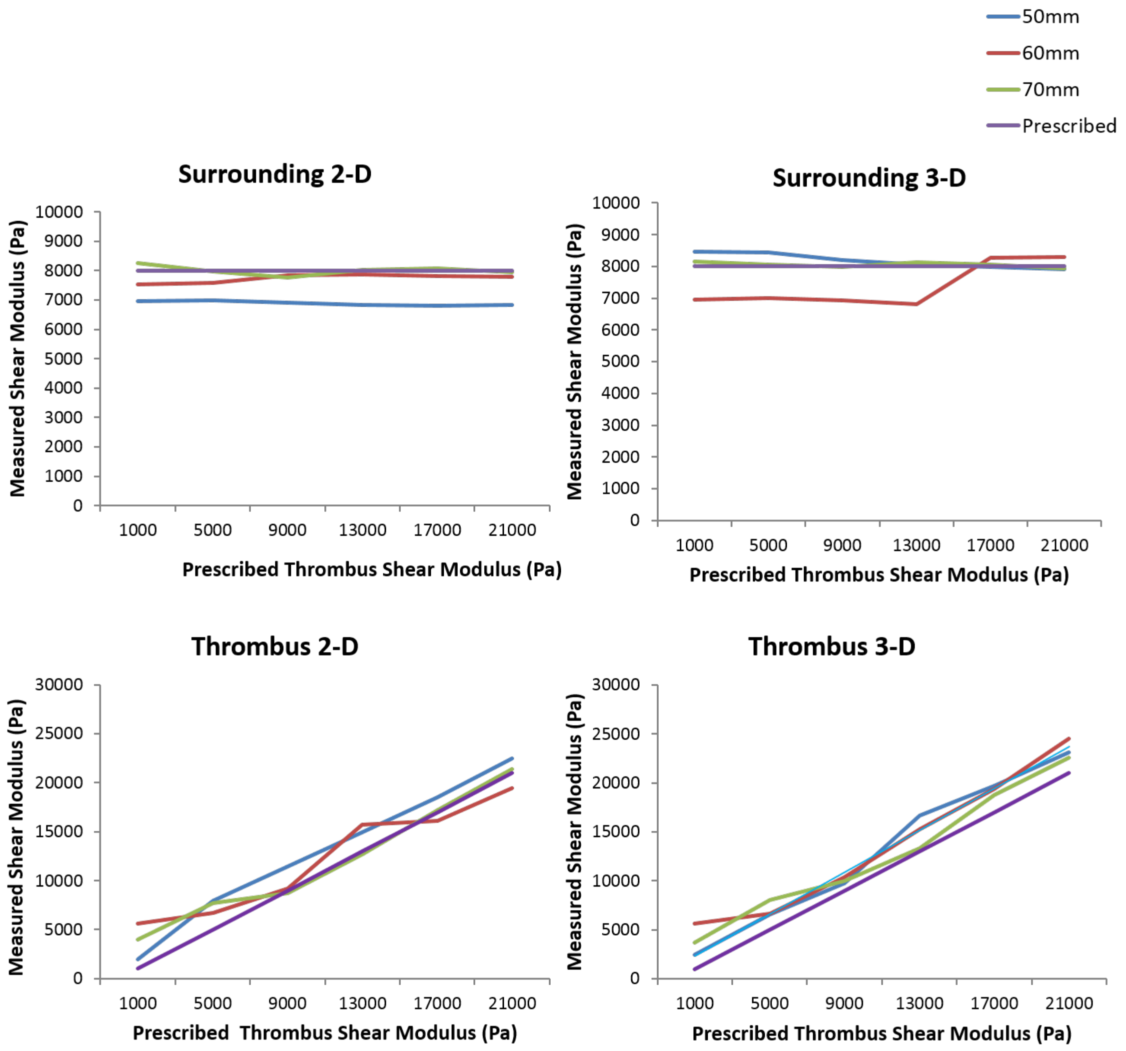

Figure 5.6: Graphs showing the measurements made in the surrounding tissue and thrombus following 2- and 3-D inversion of the 100 Hz waves. Consistency in the measurements in the surrounding tissue was good and accuracy of the measurements improved in this region in comparison to 70 Hz. Accuracy in the measurements within the thrombus was improved in comparison to 50 and 70 Hz, particularly for high prescribed shear modulus, though errors remained large at lower shear modulus. There was good consistency between the measurements made in all the three AAA sizes whilst there was little difference between the accuracy of the 2- and 3-D inversions.

		1 kPa		21 kPa	
		Surrounding	Thrombus	Surrounding	Thrombus
50 Hz	2-D	449	853	469	8566
	3-D	411	1295	674	4771
70 Hz	2-D	763	7094	493	13047
	3-D	626	4080	1177	5695
100 Hz	2-D	593	3913	602	1526
	3-D	737	5913	1014	5551
MDEV		408	457	335	1362

Table 5.2: Examples of the standard deviations from 60 mm AAA model. There was large variabiltiy in the standard deviations from both the 2- and 3-D DI algorithms. Although there was little difference in the surrounding tissue regions, at 50 and 70 Hz 3-D DI attained lower standard deviations than 2-D in the thrombus. This was however reversed at 100 Hz. MDEV consistently produced lower standard deviations than both 2- and 3-D DI in both regions.

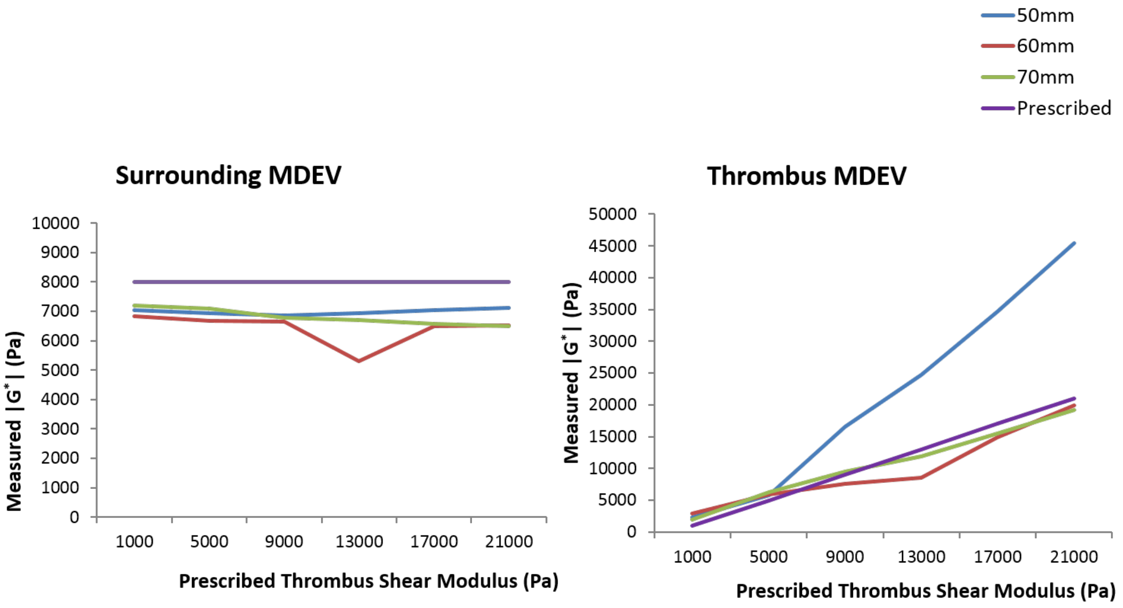

Figure 5.7: Graphs showing the $|G^*|$ values following MDEV inversion in the surrounding and thrombus regions of the model. For all AAA sizes MDEV consistently underestimated the shear modulus in the surrounding tissue. Whilst relatively good accuracy was achieved in the thrombus of the 60 and 70 mm AAAs, there were large overestimations for the 50 mm AAA.

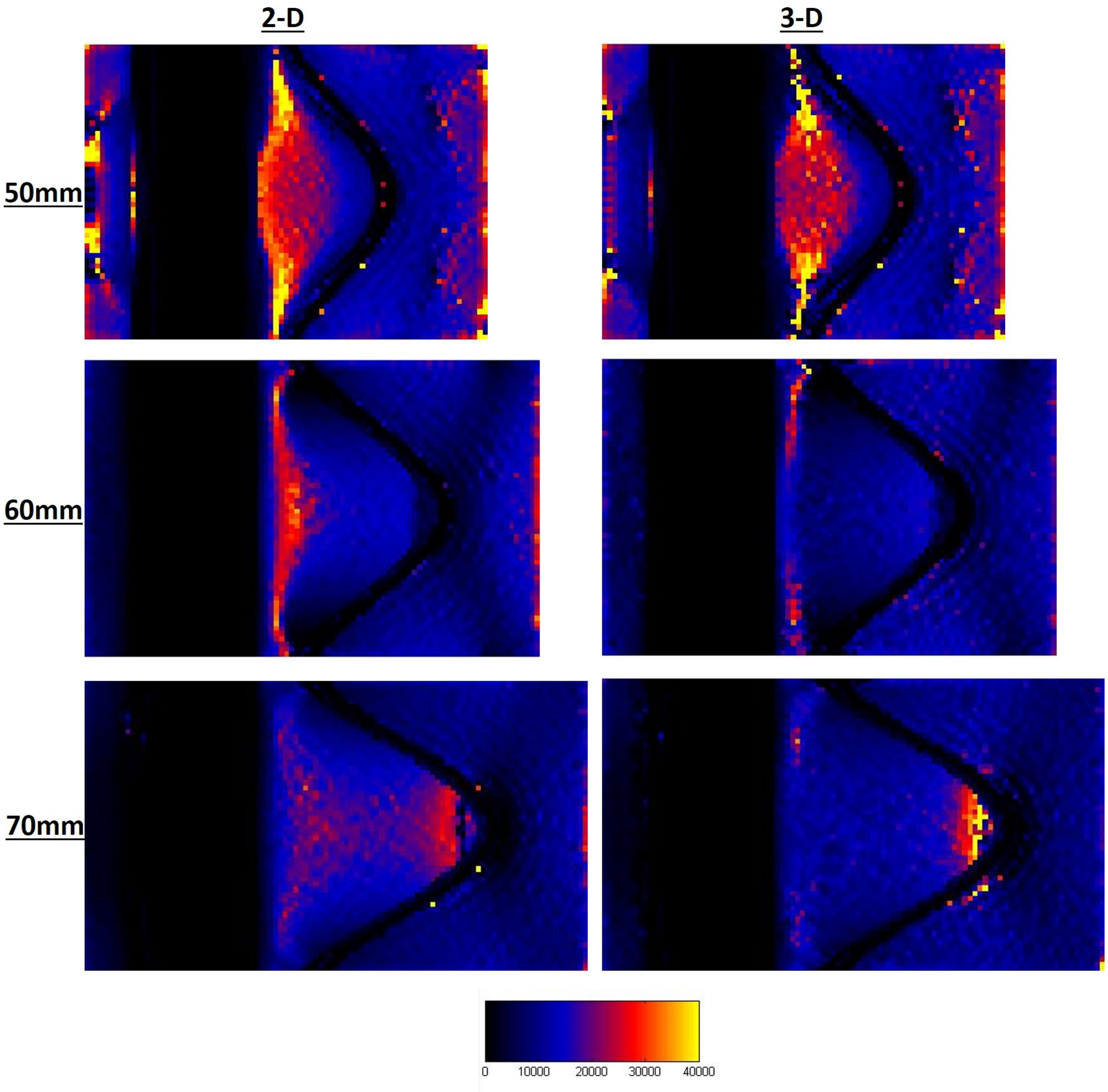

Figure 5.8: Examples of the elastograms from the three different size AAAs for a prescribed thrombus shear modulus of 9 kPa and with an induced frequency of 50 Hz. The artefact in the thrombus of the 50 mm AAA is more pronounced than those in the 60 and 70 mm AAAs.

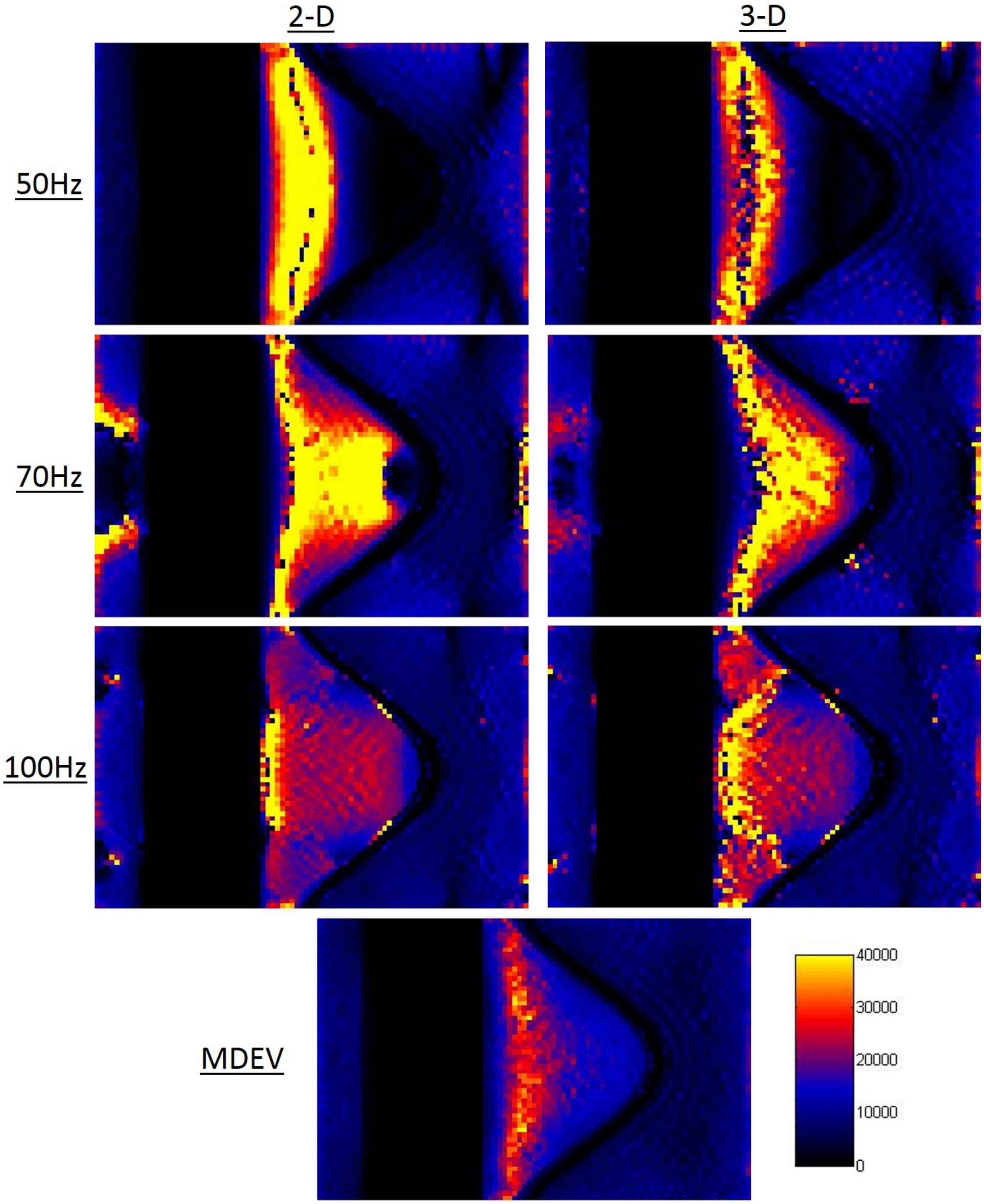

Figure 5.9: Elastograms from the 60 mm models following 2- and 3-D inversion and MDEV. The elastograms are subject to large artefacts, with the size and position of these artefacts reducing with frequency. Although reduced, artefacts were also present following MDEV inversion, with the position of the artefact corresponding to that following 50 Hz DI.

5.3.2 Vessel Wall Shear Modulus

At 50 and 70 Hz increasing the shear modulus of the vessel wall reduced the measurement in the surrounding region for both the 2- and 3-D inversions (figure 5.10), with this effect larger at 50 Hz (2-D inversion for a prescribed shear modulus of 1.1 MPa at 50 Hz resulted in an underestimation of 39% in comparison to 27% at 70 Hz). In contrast variations of the vessel wall shear modulus caused little difference in the surrounding tissue measurements at 100 Hz. For all three frequencies there was little difference between the measurements following 2- and 3-D inversion. There was a large reduction in the measurements of the thrombus with increasing vessel wall shear modulus at 50 Hz (a prescribed shear modulus of 0.1 MPa resulted in an overestimation of 18% in comparison to an underestimation of 35% for 1.1 MPa). This effect was increased following 3-D inversion (underestimation of 60% for a 1.1 MPa). At 70 Hz and 100 Hz increasing the shear modulus caused an increase in the measurements in the thrombus, though this effect was much smaller at 100 Hz than 70 Hz (overestimations of 21% in comparison to 80% for a prescribed shear modulus of 1.1 MPa). This effect was reduced with 3-D inversion compared to 2-D (at 100 Hz the error for 1.1 MPa following 2-D inversion was 36%).

Measurements of $|G^*|$ following MDEV inversion were underestimated in the surrounding tissue region with the size of the errors relatively consistent for all prescribed shear moduli (11-20%) (figure 5.11). Although thrombus measurements for prescribed shear moduli of 0.5 MPa and 0.7 MPa were notably reduced in comparison to the other prescribed values, all errors remained below 20%.

For both 2- and 3-D DI at all frequencies and MDEV, standard deviations were increased with prescribed shear moduli (table 5.3). This was complemented by the elastograms which showed a reduction in the presence of artefacts for lower prescribed shear moduli (figure 5.12).

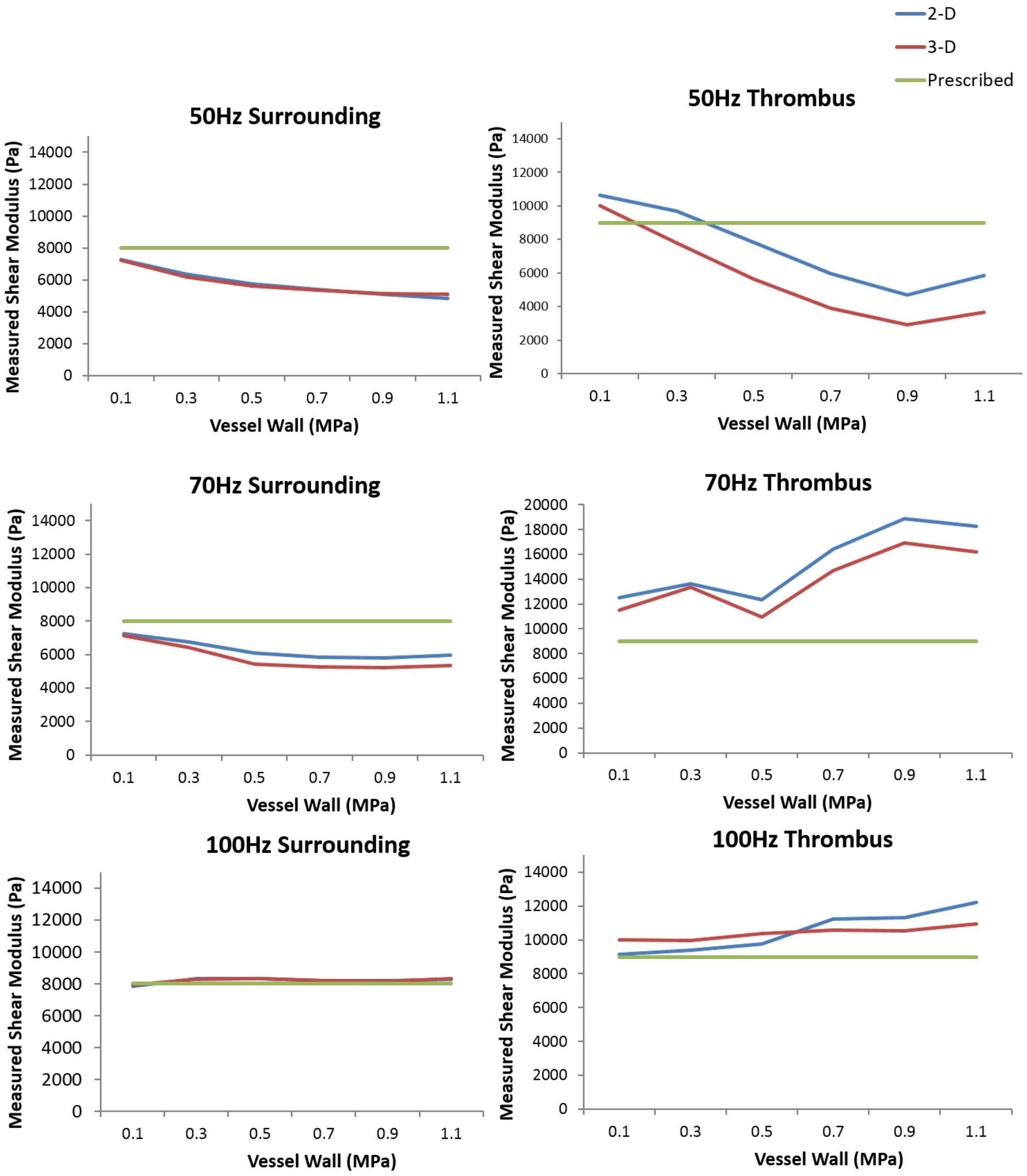

Figure 5.10: Graphs showing measured shear modulus of the surrounding regions and the thrombus for changes in the prescribed shear modulus of the vessel wall at frequencies of 50, 70 and 100 Hz. Changing the vessel wall shear modulus has a large effect at 50 and 70 Hz in both regions though this is greatly reduced at 100 Hz.

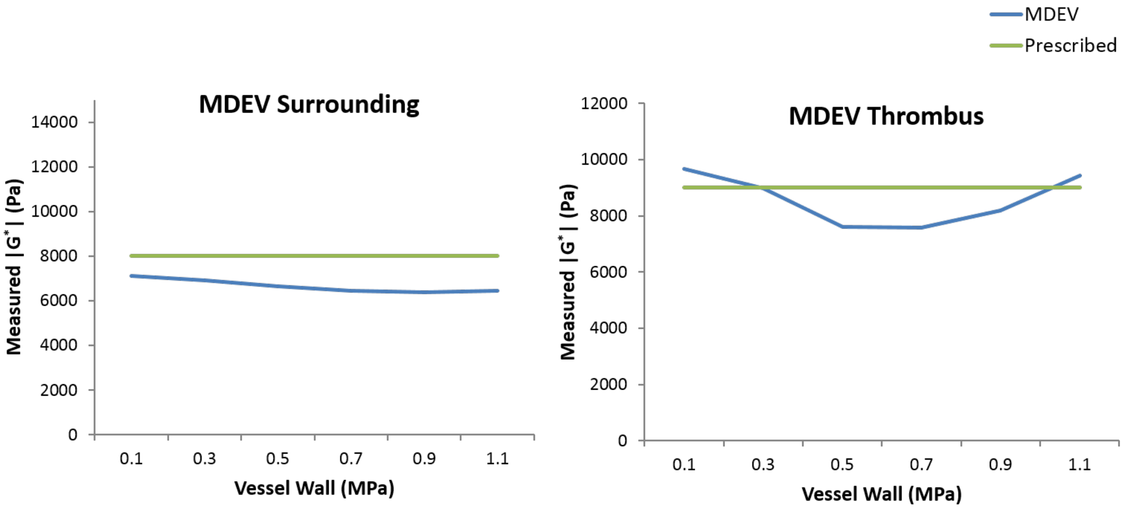

Figure 5.11: Graphs showing measured $|G^*|$ of the surrounding regions and the thrombus for changes in the prescribed shear modulus of the vessel wall following MDEV inversion. The surrounding tissue was underestimated for all prescribed values whilst relatively good accuracy was achieved in the thrombus.

		0.1 MPa		1.1 MPa	
		Surrounding	Thrombus	Surrounding	Thrombus
50 Hz	2-D	419	448	616	5663
	3-D	450	1019	623	4507
70 Hz	2-D	1119	1835	940	8243
	3-D	741	3673	591	6738
100 Hz	2-D	466	636	692	1938
	3-D	634	1597	1475	2578
MDEV		410	428	335	1362

Table 5.3: Examples of the standard deviations for variations in the prescribed shear modulus of the vessel wall. Whilst standard deviations of the surrounding region remained relatively similar for all prescribed shear moduli, there was a large increase in the standard deviations in the thrombus for increasing prescribed shear moduli for all inversion algorithms used.

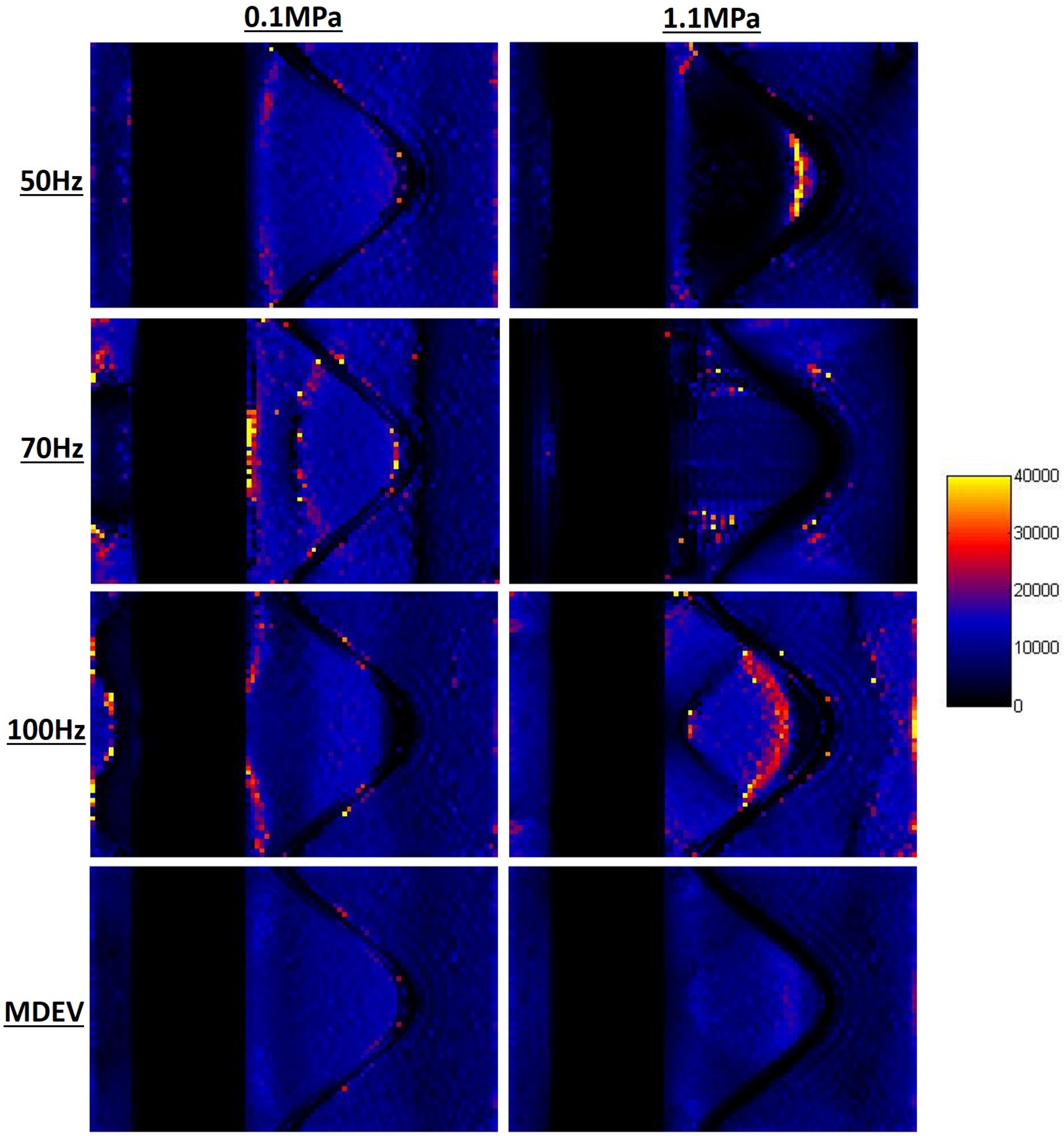

Figure 5.12: Examples of the elastograms following variations in the shear modulus of the vessel wall from 3-D inversion and MDEV. Artefacts were greatly reduced for lower prescribed shear moduli for all frequencies with DI and MDEV.

5.3.3 Thrombus Shear Viscosity

Varying the shear viscosity of the thrombus had no effect on measurements of the surrounding region at 50 Hz (all values were underestimated by 30% following 3-D inversion) and had negligible effect on measurements in the thrombus (underestimations in the background following 3-D inversion were all in the range 37-38%) for both 2- and 3-D inversion. This was also the case in the surrounding region at 70 (underestimated by 23-24%) and 100 Hz (overestimated by 4%). In the thrombus at 70 Hz overestimations increased with shear viscosity following both 2- (from 15% at 0.25 Pa·s to 26% at 1.5 Pa·s) and 3-D inversions. At 100 Hz meanwhile overestimations decreased with increasing shear viscosity following 2-D inversion (20% at 0.25 Pa·s to 5% at 1.5 Pa·s) but increased following 3-D inversion (9% at 0.25 Pa·s to 17% at 1.5 Pa·s) (figure 5.13). MDEV inversion also results in negligible changes to surrounding tissue measurements but a slight decrease in the underestimation of the thrombus (17% at 0.25 Pa·s to 14% at 1.5 Pa·s). There was little discernible change in the elastograms (figure 5.14) following DI at all frequencies and MDEV, whilst the standard deviations also remained unaffected.

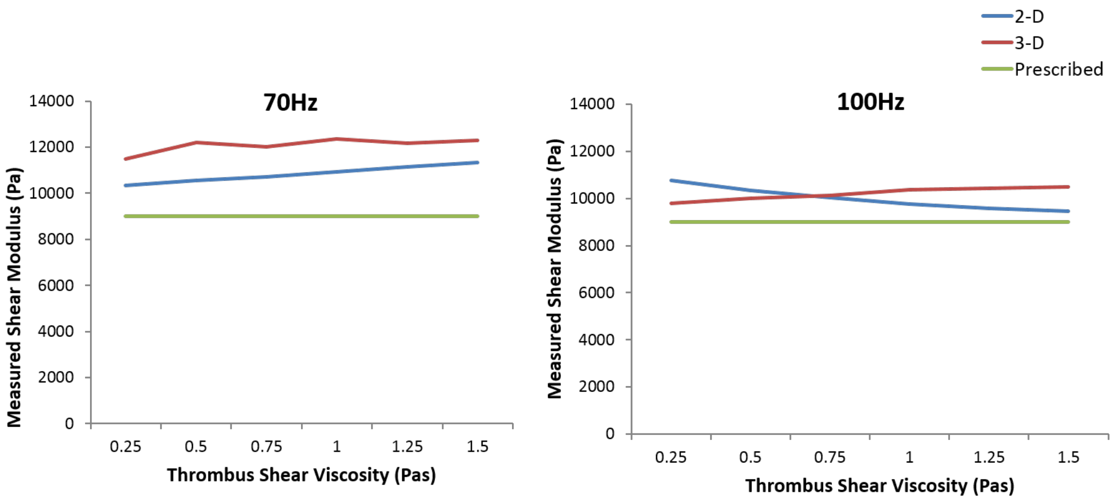

Figure 5.13: Examples of the graphs of measured thrombus shear modulus following variations in the shear viscosity of the thrombus from 2- and 3-D inversions at 70 and 100 Hz. The shear viscosity had a clear effect on the measurements made at both frequencies.

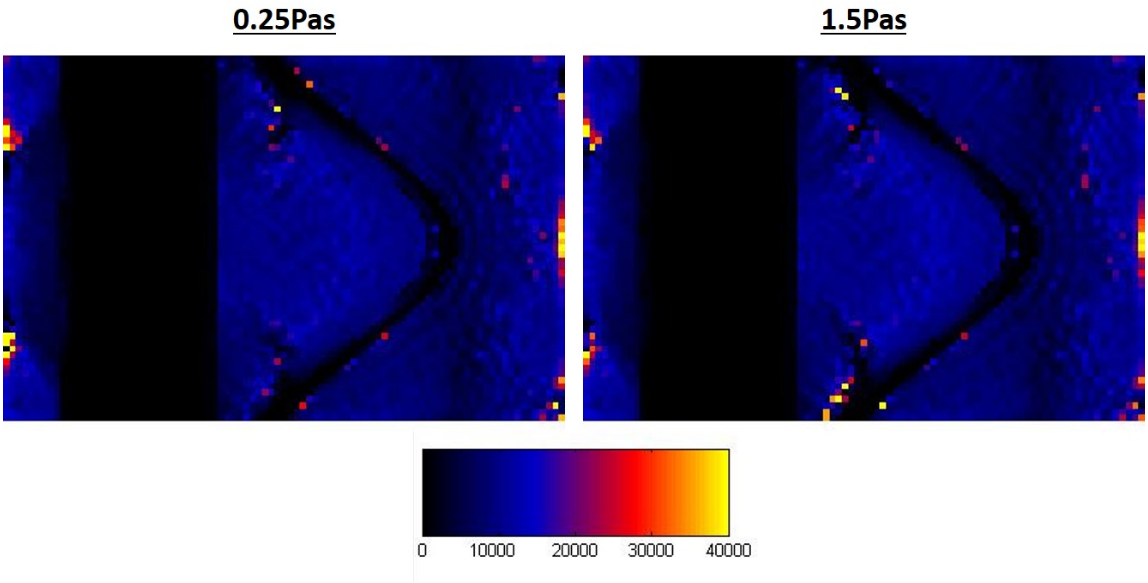

Figure 5.14: Examples of the elastograms from the 3-D inversions at 100 Hz for shear viscosities of 0.25 and 1.5 Pa·s. There was little noticeable difference between the elastograms for the different prescribed shear viscosities.

5.4 Discussion

The stress acting on the AAA wall is dependent on the material properties of both the wall and the thrombus [124]. This study however focused upon the ability to measure the material properties of the thrombus alone. There were three reasons as to why the ability to obtain measurements from the AAA wall was not investigated:

- Changes in material properties seemed to result in a shadowing effect around the boundaries following inversion. Since the AAA walls in the models used here were very thin they were almost totally obscured by the shadow in nearly all the elastograms. This made it very difficult to locate exactly where the wall was in the model and made it impractical to try and make measurements here.

- Whilst several studies have measured the material properties of the aortic wall using MRE, these have been based on the waveguide effect [174, 176, 177], whereby vibrations in the vessel wall induce a compressional wave into the blood [172]. Calculation of the shear modulus of the vessel wall in such circumstances utilises a modified version of the Moens-Korteweg equation which assumes wave propagation in a hollow cylinder. As such the equation is not appropriate to be used in AAA which have a vastly different geometry.

- DI and MDEV are both Laplacian based inversions. Computational calculation of the Laplacian involves either convolution of a 3x3 kernel, or as used in *Matlab* throughout this thesis, a gradient function, employed twice to obtain second spatial derivatives, which approximates derivatives through the central difference of 3 points (in each direction). In both cases the width of pixels used to calculate the Laplacian is wider than the vessel wall. As such any measurement of the shear modulus of the vessel wall would also have taken into account wave propagation outside of the region of interest. It is also additionally important to remember that the DI algorithm assumes propagation in an infinite homogenous medium [156]. Propagation over such a thin region clearly violates this assumption.

As demonstrated in chapter 3 there exists a clear relationship between errors in measurements, the size of the region under investigation and the frequency of the induced waves. In this study, at both 50 and 70 Hz measurements of the thrombus were dramatically higher in the 50 mm AAA than in the 60 and 70 mm AAAs (figures 5.4, 5.5 and 5.6) (though as shown in chapter 4, with the current standard of noise removal filters the extent of such overestimations may be reduced *in vivo* by the increased presence of noise). Meanwhile relatively good consistency in measurements across the different size AAAs was achieved at 100 Hz suggesting that, based upon size alone, a frequency above 70 Hz is required. This has important implications, since the majority of *in vivo* MRE experiments are performed at 70 Hz or lower [146] so as to achieve wave propagation at a sufficient depth. The ability to achieve adequate wave propagation at higher frequencies for measurement therefore poses a significant technical challenge.

Whilst measurements at 100 Hz were relatively consistent across the range of AAA sizes, sizeable inaccuracies remained present for the low prescribed shear moduli. This could potentially have been as a result of the increased damping that occurs at low shear moduli, or because the wavelength of waves at such a low shear modulus was long in comparison to the region of measurement. Increased damping would probably have more of an impact on accuracy for larger AAAs, whereas a long wavelength in comparison to the region of interest would have a greater impact for shorter AAAs. Whilst the geometries used in this chapter resulted in more complex wave propagation than seen in previous chapters, thus making visual determination of such factors more difficult, the fact that the largest error for a prescribed thrombus shear modulus of 1 kPa occurred for the middle sized 60 mm AAA suggested that the large errors at low shear moduli were a combination of both factors.

Response to changes in the shear modulus of the vessel wall also appeared to be frequency dependent with large errors for high shear moduli at both 50 and 70 Hz (figure 5.10). This effect was probably due to the increased contrast in material properties causing increased reflections. A study by Papazoglou et al. (2007) [193] demonstrated that wave reflections increased with frequency. This along with the data in this chapter suggests that although reduced in amplitude, reflections have a greater influence on the quality of elastograms and measurements at lower frequency. Whilst the influence of vessel wall shear modulus was reduced at 100 Hz, errors still increased by 10% across the range of prescribed values demonstrating a clear limitation of the use of MRE in measuring thrombus shear modulus.

Whilst increasing frequency improved the ability of the inversion to cope with changes in the size of the AAA and the shear modulus of the vessel wall, the opposite was true with regards to shear viscosity (figure 5.13). This was not surprising since, unlike the prescribed shear modulus, the shear viscosity is frequency dependent, leading to a greater reduction in wave propagation at higher frequencies. This demonstrates another limitation of using MRE to measure the shear modulus of the thrombus. More fundamentally, this continues to demonstrate weaknesses in DI with the loss component of the viscoelastic medium affecting measurement of the storage component.

Errors at all frequencies and in both regions where measurements were made in this chapter were often significantly larger than those seen in the previous chapters. This is likely to be because of a combination of the less simplistic geometries used in this study and a greater contrast between material properties from one region to another resulting in more complex wave propagation and larger reflections. This second point was supported by the presence of artefacts in the elastograms which seemed less prominent at higher frequencies where increased damping would decrease the effects of reflections (figure 5.9).

Chapter 3 hypothesised that MDEV may improve upon DI measurements in more complex geometries where frequency dependent artefacts are likely to play more of a role in inaccuracies than failure of the inversion algorithm to truly characterise the shear modulus from wave propagation. Artefacts in the elastograms throughout this chapter show strong frequency dependence (figure 5.9). Whilst the quality of the elastograms was improved by MDEV and standard deviations reduced in both measured regions (table 5.2), demonstrating reduced variability of the data, artefacts remained in the images and errors remained present in the measurements. This was most noticeable in the 50 mm AAA for high prescribed shear modulus in the thrombus. In these elastograms, the artefact following MDEV inversion, though reduced in prominence, occurred at the same location as those in the 50 Hz elastograms. Since MDEV essentially averages the contributions from multiple frequencies [197], this implies that whilst the effects of frequency dependent artefacts can be reduced, they can not necessarily be eliminated altogether if they are particularly large. A method of reducing the impact of such artefacts with MDEV would be to utilise more frequencies in the inversion. Whilst there is theoretically no limit on the number of frequencies used, in practice increasing the number of frequencies dramatically increases the overall scan time and is often therefore impractical.

In contrast to the results in chapter 3 there seemed to be little difference in the accuracy of the results from DI in 2- and 3-D at 100 Hz (figure 5.6). This potentially has important implications clinically with regards to the time of the scan. Acquisition for 2-D inversion requires data from a single slice and from only one motion-encoding direction, compared to 3-D inversion which requires at least 5 slices and 3 motion encoding directions. This implies that data collection from a single 3-D acquisition is at least 15 times as long as 2-D, meaning that whilst 2-D acquisition can be achieved in less than 10 s, a 3-D acquisition would take in excess of a minute. In scanning the abdomen, particularly when using a phase-contrast sequence, it is important to remove any unwanted sources of motion and as such the scan is typically breathe-hold and cardiac-gated [174]. This implies that 3-D datasets could not be obtained in a single acquisition, thus increasing the risk of patient motion during the scan causing image artefacts and reducing registration of phase images. The data here suggests that 2-D datasets would be adequate and therefore reduces these risks.

There were several limitations to this study. The first of these was in the definition of material properties. To date no MRE studies have investigated AAAs meaning that material properties were prescribed based upon measurements taken by other techniques. There was wide variability in the literature as to these properties, particularly in the thrombus [209]. Further *ex vivo* studies of these material properties with MRE would therefore prove useful in determining the range of values to prescribe for each material.

In addition to this, the lumen was prescribed as a viscoelastic material with a low shear modulus in order to run the simulations within a reasonable time frame. Although the lumen was removed from the analysis, as shown by the variations in the vessel wall shear modulus, measurements in a region of interest are not purely dependent on the material properties of that region, but on the material properties surrounding it as well. By prescribing a low shear modulus to reduce wave propagation within the lumen and by moving the region of interest away from the lumen, it was hoped that this effect would be limited, but it is likely to have still had some influence.

Another limitation is the potentially excessive presence of reflections within the model. The study by Papazoglou et al. (2007) [193] showed that the extent to which reflections occur is dependent on the properties of the interface between two mediums. It was demonstrated that reflections from welded interfaces were dramatically larger than those from non-welded interfaces. Throughout this thesis materials within the model have typically been tied together or initially defined as separate parts and then merged with one another. This is characteristic of welded conditions and is unlikely to be truly representative of *in vivo* tissue. The study by Papazoglou demonstrated that reflection artefacts increased with frequency, contrasting to the errors here, which seemed to decrease with increasing frequency. In this study viscoelastic properties were used to counter the effect of reflections, and these would have had more influence at higher frequency, hence the greater dependency of the shear modulus upon the shear viscosity at 100 Hz than at 50 Hz. For the 100 Hz vibrations overestimations were obtained at low shear moduli, and as previously described, this was assumed to be as a result of lack of wave propagation in the region of interest. For higher shear moduli however, the error was consistent. Were reflections having a large influence on the accuracy of the elastogram, then it would be expected that the error would increase with increasing prescribed shear moduli. This was not the case however, and combined with the frequency dependent nature of reflections shown in the Papazoglou study, suggests that the majority of the errors are in fact due to the geometry of the AAA rather than reflections. Such errors would likely be replicated *in vivo* where size is highly variable.

5.5 Conclusions

This chapter created idealised AAA models using CAD and used FEA to investigate the potential use of MRE to acquire shear modulus values for the thrombus. The results here demonstrated that low frequency measurements were more dependent on the AAA size and the shear modulus of the vessel wall than high frequency measurements. The opposite however was true when the shear viscosity of the thrombus was varied, which had a greater influence at higher frequency. Unlike the results demonstrated in chapter 3, there was no obvious improvement in the results following 3-D DI in comparison to 2-D DI, whilst MDEV suffered from large inaccuracies in smaller AAA.

Whilst this study began to identify some of the issues facing MRE of AAAs it should be recognised that *in vivo* scanning faces far more challenges than those investigated here. Most notable is the extent to which motion influences data quality with the anatomical region under investigation subject to motion from breathing, bowel movements and blood flow. Further development of FEA of MRE should aim to create more complex models that take these factors into account. Despite this, simplistic models such as those used in this chapter offer the potential to test the capabilities of the current post-processing software in idealised conditions, demonstrating its limitations and informing upon which parameters are fundamental requirements to achieve accurate results *in vivo*. Based on the models used in this chapter, MRE is not capable of achieving accurate measurements for PSM, with the primary concern being the large errors in the measurements of the smaller AAAs at the lower frequencies typically used *in vivo*.

Chapter 6

Scanning AAA Patients: A Pilot Study

6.1 Introduction

The thesis till this point has focused upon the development of a computational simulation of MRE. Whilst this allows testing of algorithms and other forms of post-processing software, the primary aim was to investigate the potential of using MRE to attain accurate material properties measurements of AAAs with a view that ultimately such values could be integrated into patient specific models to achieve more accurate prediction of rupture. Although the modelling allows investigation of the theoretical limitations of the technique, it does not allow exploration of the practical limitations.

To date there are no publications that have aimed to perform MRE scans upon AAA patients, though the challenges facing scanning this patient cohort are similar to those faced when scanning the healthy aorta. The largest of these challenges is how displacements from relatively low amplitude shear waves can be acquired from a region which is subject to such a large amount of motion from other sources such as blood flow, bowel movements and respiration.

This chapter outlines and discusses a pilot scanning study that ran in parallel to the modelling work. The aim of this was to identify whether wave propagation induced by mechanical excitation could be visualised in AAAs using an MRE sequence adapted with this purpose in mind.

6.2 Methods

6.2.1 Subjects

Aortic MRE was performed on four male AAA patients aged 60, 66, 72 and 88 with a mean body mass index (BMI) of 28.3. A reference scan was also performed on a male healthy volunteer aged 31 with a BMI of 21.6. Patients were recruited from a pre-existing patient group through their participation in the MA3RS trial, a clinical trial enlisting over 300 AAA and studying uptake of USPIO's in AAAs [214]. Ethical approval for the study was granted by the NHS research ethics committee and all patients and the volunteer consented to take part. Before scanning was performed a 20 mg$\cdot$ml^{-1} of hyoscine butylbromide (*Buscopan,* *Boehringer Ingelheim, Berkshire, United Kingdom*) was intravenously administered to the patients.

6.2.2 Image Acquisition

MRI was performed using the same Siemens 3 Tesla scanner that was used in chapter 4. A single-shot spin-echo EPI sequence was used with TE 30 ms, TR 257 ms, flip angle 90^o, FOV 214 x 214 mm^2, acquisition matrix 64 x 64, pixel spacing 3.34 mm, a single slice of thickness 8 mm and 8 MRE phase offsets. Displacement data was acquired in the read-out direction. ECG cardiac gating was performed using electrodes placed upon the index finger of the patient. The acquisition time was dependent upon the subject's heart rate but was typically less than 10 s. Subjects were asked to hold their breath for the duration of the scan.

Subjects were placed head first into the scanner in the supine position. Localiser scans were performed to ascertain the position of the aorta. Following this, members of the research entered the scan room and placed the rod and transducer upon the patients abdomen. The rod and transducer used were the same as those described in chapter 4. The rod was extended so that the actuator moved up the subjects abdomen and the subject was asked to confirm once the transducer came into contact with the bottom of their rib cage. The rod was then fixed in place here (figure 6.1). The scan on the healthy volunteer was performed with and without vibrations to confirm that any apparent wave propagation in the phase images was the result of induced vibrations and not blood flow.

6.2.3 Image Analysis

Phase images were unwrapped using the Laplacian-based estimate using the *PhaseTools* software package [145] in *ImageJ*. The images were then imported back to *Matlab* where a Fourier transform was performed in the temporal direction. The complex wave image for the second frequency bin relating to the induced frequency of vibrations was then inspected for signs of wave propagation.

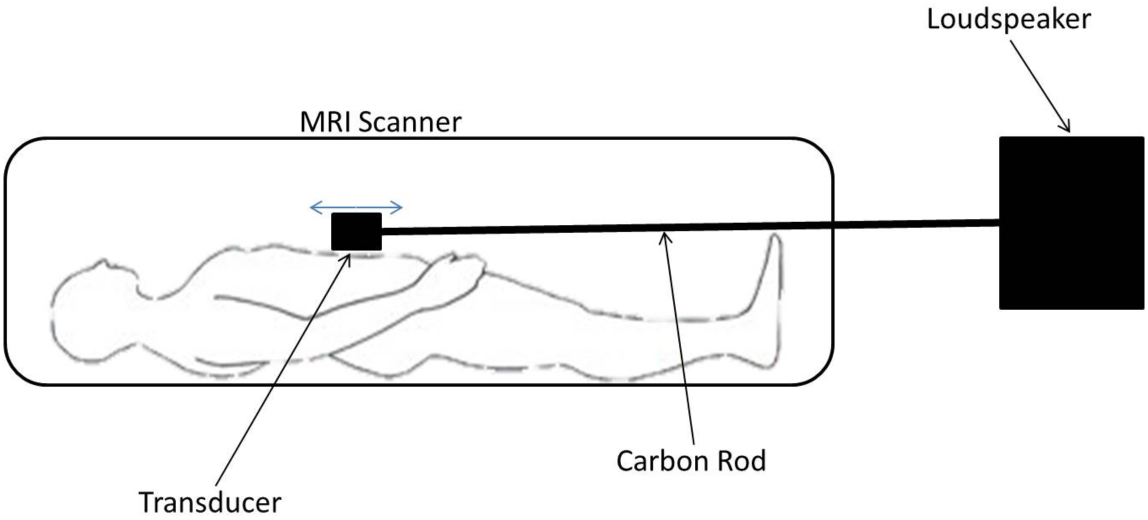

Figure 6.1: Schematic diagram showing the setup for an MRE scan of the aorta. The patient is placed in the MRI scanner with the transducer placed on their chest just below their ribcage.

6.3 Results

Identification of the geometry of the AAAs from the magnitude images was often difficult due to poor image quality and it was not possible to differentiate between the lumen, wall and thrombus in any of the scanned patients. Additionally ghosting artefacts were prominent in all of the magnitude images from the AAA scan. This contrasted with the images from the healthy volunteers where artefacts appeared less influential. Whilst distinction between the lumen and the vessel wall was not possible in the healthy volunteer, the geometry of the aorta was clearly visible (figure 6.2).

Visual inspection of the phase images from the AAA patients showed no clear wave propagation in the AAA or the surrounding region of tissue. This was supported by inspection of the complex wave images which were dominated by noise in all regions (figure 6.3). Similarly noise dominated the phase and complex wave images from the healthy volunteer when no vibrations were applied. In contrast following application of vibrations, wave propagation could be visualised in the phase images from the aorta of the healthy volunteer and also appeared to be present in the complex wave image. Creation of a mask around the aorta from the magnitude image and application to this complex wave image showed that this wave propagation co-localised to the lower region of the aorta (figure 6.4). The region of tissue anterior to the aorta was dominated by noise.

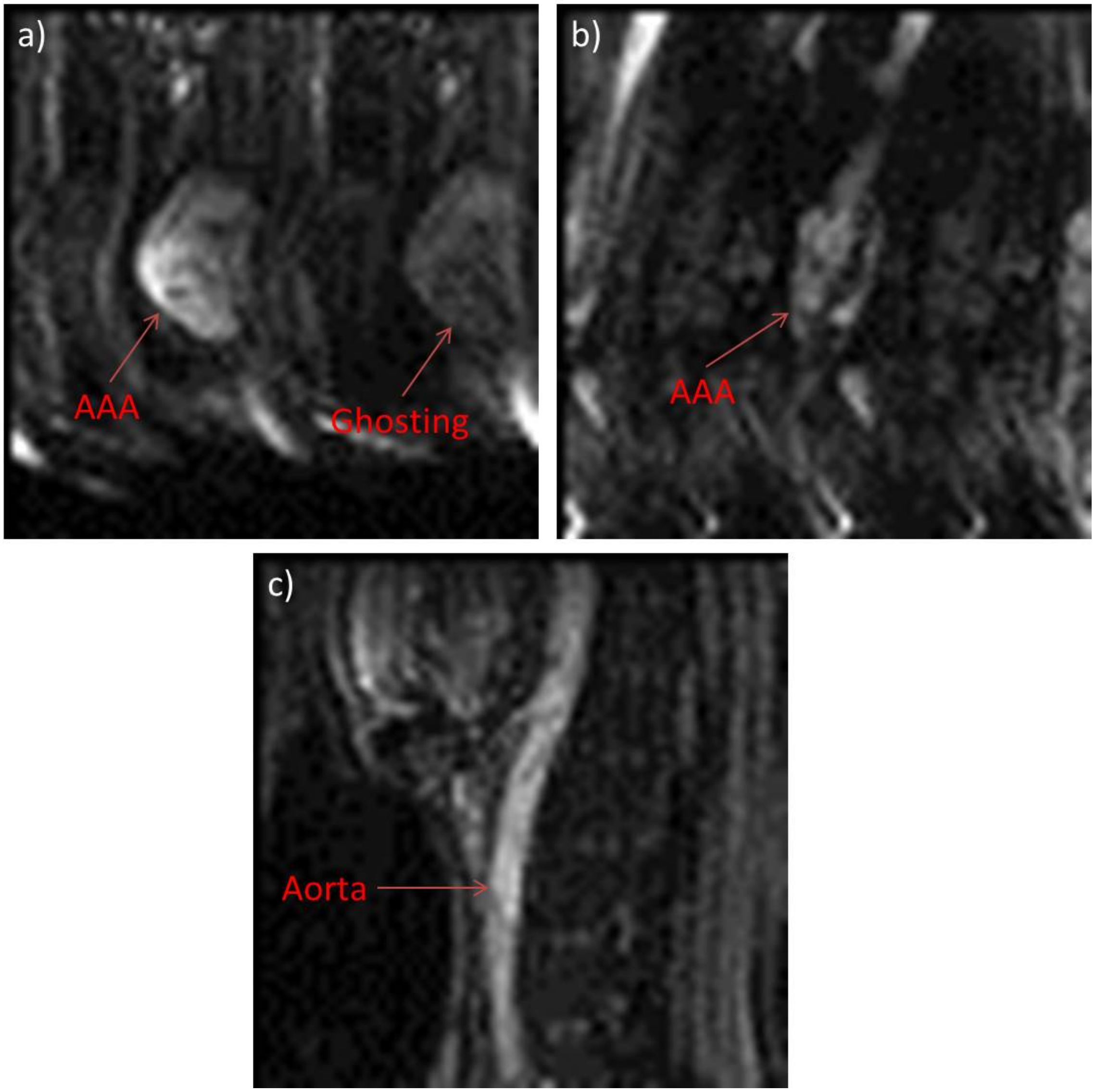

Figure 6.2: Examples of the magnitude images from a) and b) AAA patients and c) the healthy volunteer. There is a clear improvement in the image quality from the healthy volunteer in comparison to the AAA patients where ghosting artefacts are clearly visible.

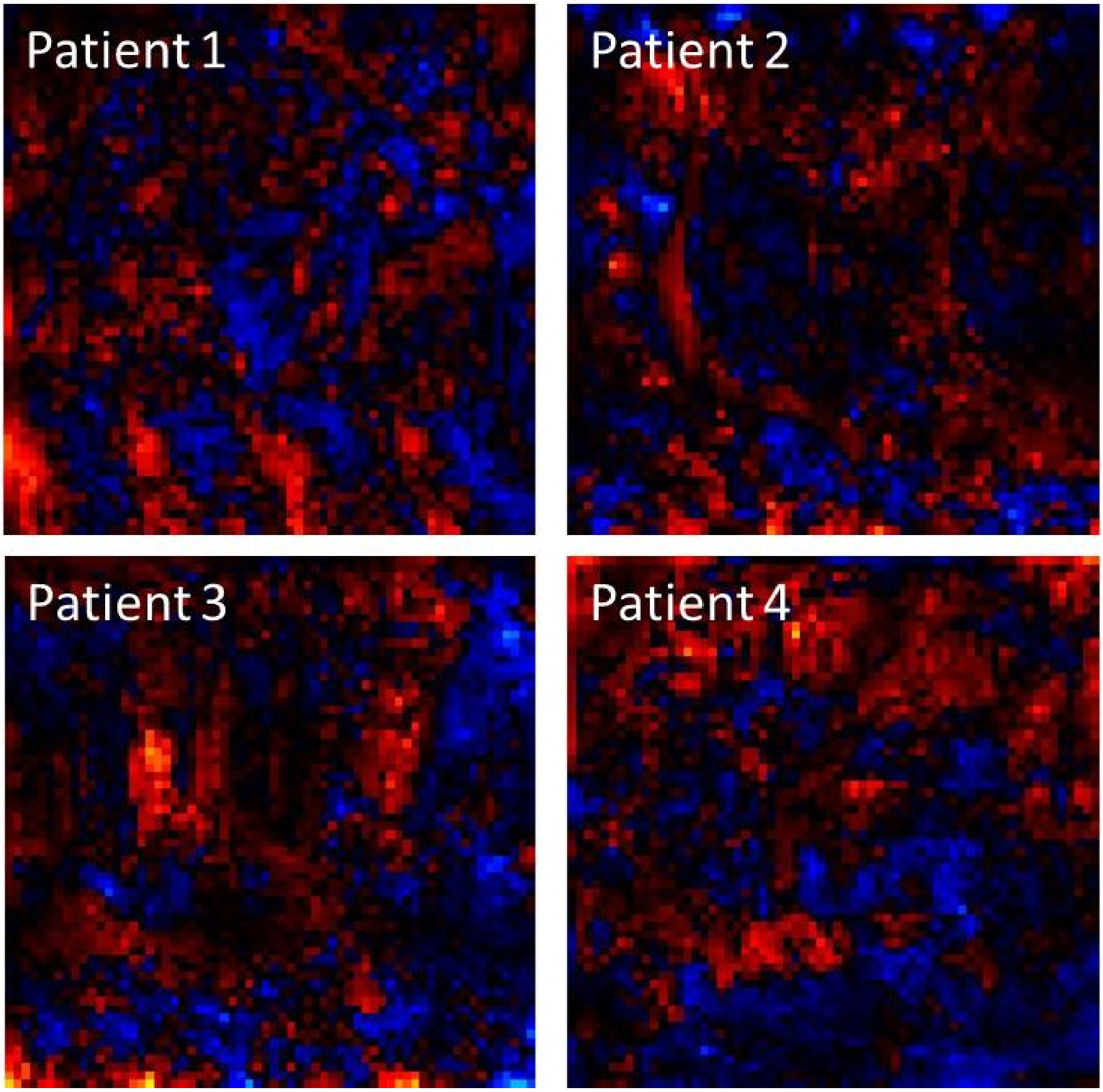

Figure 6.3: The complex wave images for all four AAA patients were dominated by noise with no signs of wave propagation.

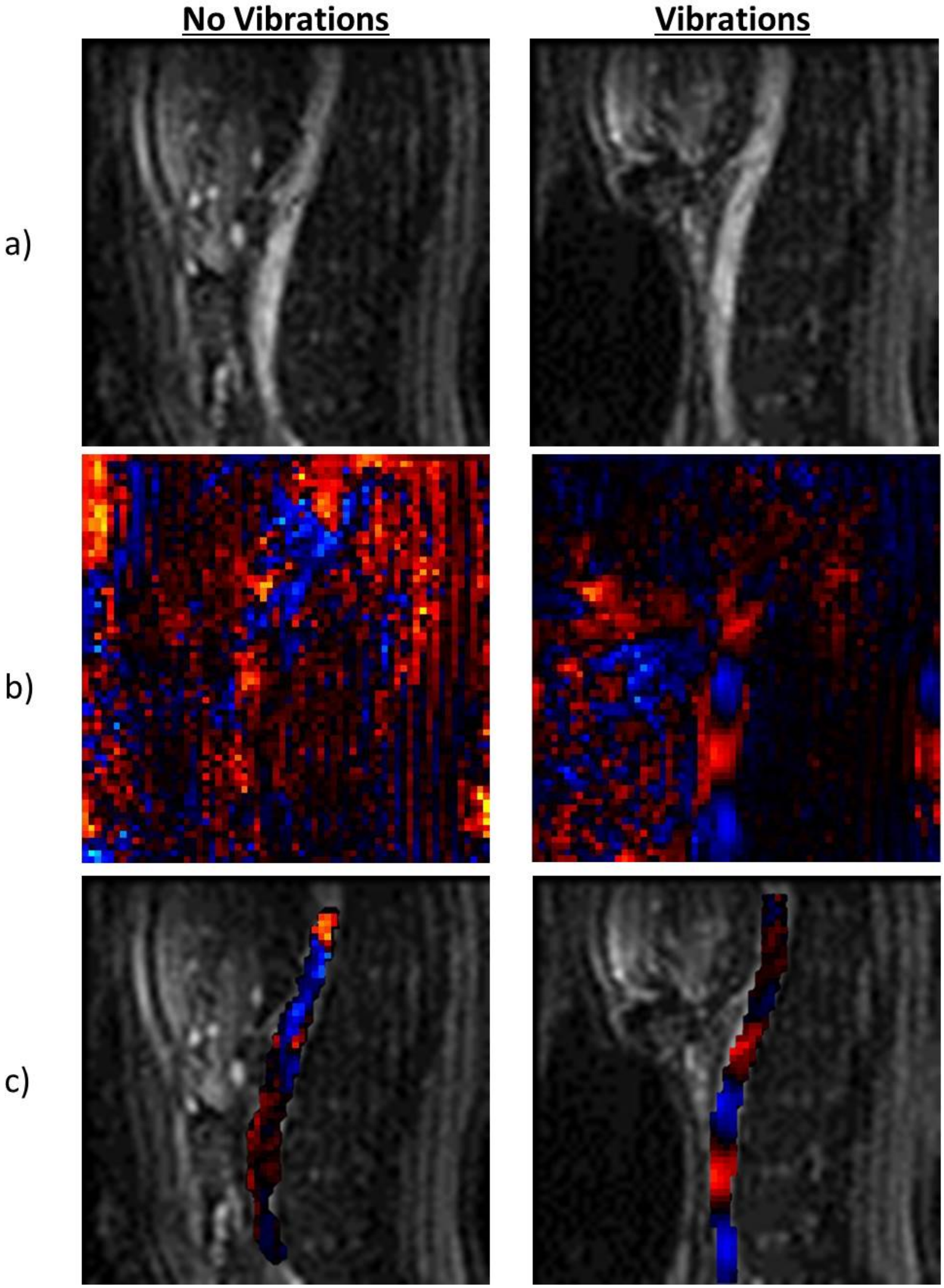

Figure 6.4: MRE scans of the aorta from the healthy volunteer with and without vibrations applied. a) Magnitude images. b) Complex wave images. Whilst the scan without vibrations was dominated by noise, propagation was apparent in the scan where vibrations were applied. c) Application of the aortic mask to the complex wave image confirmed that the region where wave propagation was present co-localised with the lower region of the aorta.

6.4 Discussion

The aorta provides a challenging environment in which to perform MRE primarily because of the large amount of motion from sources other than the induced shear waves that can influence the phase data. In an attempt to counteract such motion, Buscopan was administered to patients to reduce bowel movements before the scan (although ethical approval was not granted for its use in the healthy volunteer). Additionally scans were performed under breath-hold to reduce breathing artefacts and were prospectively gated such that data was acquired from the diastolic phase, where blood flow is greatly reduced in comparison to the systolic phase. These measures placed limits on the acquisition itself however, with short acquisition windows and repetition times. The effect of these limitations was clear in the magnitude images, which were of poor quality and appeared to suffer from a low signal-to-noise ratio (SNR) (figure 6.2). Although interpretation of phase images is more difficult, this would also have had a significant impact upon the quality of the data here too.

Propagation of waves induced into the aorta using MRE and the waveguide effect has been demonstrated by several groups previously [174–177]. In the scans performed here on the healthy volunteer the lack of apparent propagation in the aorta in the complex wave image when no vibrations were applied in comparison to when they were (figure 6.4), showed that motion captured by the MR sequence was due to the waves induced using MRE and not an artefact from blood flow.

Although wave propagation could clearly be visualised in the aorta, it could not be seen in the anterior tissue, where noise appeared dominant. Clearly in order for the wave to propagate in the aorta, it would have to propagate through the surrounding tissue. The lack of appearance of wave propagation in this region is in all likelihood due to the SNR being higher in blood than in the surrounding tissue. To this end blood has a relatively long T_2 relaxation time yielding a high SNR [215], and the bright appearance of the aorta in the magnitude image demonstrates that the signal from this region is strong. In contrast the structure of the region anterior to the aorta appears distorted (figure 6.4), possibly as a result of an artefact caused by the transducer being place near here. This could have also resulted in increased noise in the phase images at this location.

Whereas wave propagation was visualised in the aorta of the healthy volunteer, it was not in any of the AAA patients (figure 6.3). A probable explanation for this was a decrease in the signal from the propagating wave in the AAA patients in comparison to the healthy volunteer. In this regard it is likely that there was increased damping of the wave before it reached the AAA in the patients than the aorta of the volunteer due to the higher BMI of the patients in comparison. This would have led to a reduction in the signal from the AAA in comparison to the healthy aorta. Inspection of the magnitude images suggested that SNR in the MR images themselves were similar in both the patients and healthy volunteer, which would be expected since the setup was the same. There was however a noticeable reduction in the quality of the patient images in comparison to the volunteer due to the presence of ghosting artefacts, which would in all likelihood reduce the signal coming from the wave. Such ghosting artefacts are a common problem in EPI sequences, often caused by mis-timings between positive and negative readout gradients used to acquire successive lines in k-space [216], they can also be as a result of patient motion in the scanner [217]. Whilst the acquisition time was short, it remains conceivable that the patients struggled to remain still throughout the scan. Additionally, whilst ECG cardiac gating was used, blood flow in AAAs is typically turbulent [218]. This implies that blood is unlikely to be stationary in this region even through diastole. Since the phase offsets are synchronised to the frequency of the vibrations, such motion is not only liable to result in ghosting artefacts, but would also present as noise in the AAA.

Even assuming wave propagation had been observed in the AAAs, the poor quality of the magnitude images would present further challenges for inversion. Obtaining material property values for the AAA wall would be unfeasible for the reasons discussed in chapter 5, but also because the wall thickness is lower than the resolution of the scan. Additionally differentiation of the thrombus from the lumen was also not achievable in the magnitude images. Although it is possible that through the waveguide effect, wave propagation would be observable in both the thrombus and the lumen, the waves in the thrombus would be shear waves, whilst those in the lumen would be pressure waves [172]. This means that application of the inversion algorithm to both regions combined would be invalid, since the values calculated from DI assuming shear wave propagation and the values calculated from DI assuming the waveguide effect are not analogous to one another.

6.5 Conclusions

In agreement with the literature the work in this chapter demonstrated it was possible to induce waves into the healthy aorta using MRE. Replicating this technique in AAA patients proved more challenging however, and no such propagation was observed in any of the AAAs. Inspection of the magnitude images demonstrated that this was probably as a result of increased motion from other sources, such as turbulent blood flow in the AAA, resulting in higher noise. It was also seen as likely that the signal from the induced wave was reduced in the AAA because of the relatively high BMI of the patients in comparison to the volunteer.

Chapter 7

Conclusions and Future Work

7.1 Summary

AAA rupture is a potentially fatal event that continues to cause a large number of deaths in the elderly. Although the introduction of screening programmes and improvements in surgical procedures have improved mortality rates in recent years, the diameter criterion, a weak method of predicting AAA rupture upon which the decision to surgically intervene is based, is still used. A possible replacement for the diameter criterion is PSM, but the predictive power of this technique suffers as a result of a lack of patient specific information regarding material properties. To this end MRE, an MRI-based technique that allows non-invasive measurement of material properties *in vivo*, provides a possible solution. The aim of this thesis was to investigate the potential for using MRE in acquiring material property values from AAAs for integration into PSM.

To this end, a transient FE method of simulating MRE was developed and demonstrated in chapter 2. Models simulating planar wave propagation were created in 2- and 3-D, with measured shear modulus values from the MRE inversion algorithm and from manual measurements of the wavelength demonstrating good agreement with the prescribed values. Following this, insert models were created and the effects of varying modelling parameters investigated. Both element type and boundary conditions used in the model were shown to have an impact upon shear modulus measurements.

Whilst measurements from planar wave propagation in chapter 2 were in good agreement with prescribed values, when the wave propagation was not planar, overestimations were commonplace. It was hypothesised that this could have been because the chapter made use of the 2-D algorithm rather than the 3-D algorithm. This was investigated in more detail in chapter 3 alongside the MDEV inversion algorithm, which utilises information from multiple frequencies, and directional filtering, which aims to remove reflected waves to reduce artefacts in the image. Additionally the impact of insert geometry upon measurements was investigated, with the size of the insert both in- and out-of- the plane of image varied. The chapter showed that 3-D inversion improved measurements in comparison to 2-D inversion. Neither MDEV nor directional filtering improved the accuracy of the measurements, though MDEV's ability to remove artefacts and create a smoother elastogram offered hope. Geometry was shown to have a significant impact on the accuracy of the measurements, with small inserts both in- and out-of-plane underestimated.

Chapter 4 compared FEA of MRE to phantom scanning. To achieve this a commercially available phantom was acquired and scanned. It was then recreated for FEA using CAD from the parameters provided by the manufacturers. Whilst measurements acquired from the two techniques were different at low frequencies, these differences reduced with increasing frequency. This suggested that such differences were largely attributable to increased noise in the scanned datasets in comparison to FEA. The chapter helped to highlight the complex relationship that appears to exist between the accuracy of MRE measurements and the variety of parameters that it can be affected by such as noise, ROI geometry, frequency and shear modulus.

Chapter 5 utilised the developed FEA technique to investigate the ability to obtain accurate measurements of AAA thrombus using MRE. To achieve this idealised AAA geometries were created using CAD. AAA size, shear viscosity of the thrombus and shear modulus of the vessel wall were all shown to have an impact on the accuracy of the measurements, though the extent to which each of these factors influenced was dependent on the frequency. The chapter highlighted clear limitations with utilising MRE to make material property measurements in AAAs.

Chapter 6 outlined work that had run concurrently to the modelling and investigated the practicality of performing MRE upon AAA patients. Four AAA patients and the aorta of a healthy volunteer were scanned. Whilst wave propagation was visualised in the aorta of the healthy volunteer, no such propagation was seen in any of the AAA patients. The lack of any apparent propagation in the patients was attributed in part to a reduction the amplitude of the wave in AAAs in comparison to the aorta of the healthy volunteer, potentially due to the patients having a higher BMI than the volunteer, and to increased motion from sources other than the induced waves in the AAA scans, possibly coming from turbulent blood flow in the AAA. The chapter highlighted the difficulties of obtaining high quality data from AAA patients for inversion.

7.2 Conclusions

The aim of this thesis was to investigate the potential of using MRE for acquisition of material properties that could be incorporated into PSM of AAAs. To achieve this aim FEA of MRE was developed to test the post-processing software, whilst a small cohort of patients was scanned to test the capabilities of the current MRI setup. Both of these methods demonstrated that the current setup is not capable of making accurate measurements that could be incorporated into PSM: the scan setup was not able to visualise waves induced into the AAA, whilst the inversion algorithm was not capable of making accurate measurements from waves propagating in such geometries.

7.3 Future Work

The thesis used relatively simplistic models to test whether the inversion algorithm was capable of achieving accurate measurements. Future work should concentrate on increasing the complexity of the models so that they are more representative of real AAAs. This could potentially involve using patient geometries segmented from scan data, dividing the thrombus into layers and defining different material properties for each layer, and performing FSI simulations to incorporate blood flow in the AAAs.

Chapter 2 demonstrated the importance of boundary condition definition in modelling showing that they have a clear influence on wave propagation. This is likely to not just be significant in FEA but also *in vivo*, where boundaries and constraints between materials also exist. Further research is required to understand such conditions and how they can be better defined in FEA so that the models can be a more realistic representation.

The work throughout this thesis has repeatedly demonstrated the limitations of the DI algorithm. Perhaps the largest of these limitations was the variability of the measurements with regard to geometry. Whilst DI utilises local displacements caused by wave propagation, the evidence put forward in this thesis suggests that wave propagation itself is dependent upon global material properties. With this is mind, the author suggests that to achieve accurate material property measurements, focus should be placed upon finite element based forward inversion techniques such as that suggested by Van Houten et al.

(1999) [147], which are able to take into account displacements from a larger region.

Once accurate measurements have been demonstrated in a range of geometries, beginning with those models created throughout this thesis, development of the scanning technique should focus on increasing the SNR of the data. This would hopefully allow visualisation of wave propagation within the AAA.

Appendix I

Modelling MRE in Abaqus

This appendix aims to outline the steps involved in modelling MRE using *Abaqus* and the subsequent steps involved in processing the acquired data using *Matlab*. The process has been designed to be as replicable and efficient as possible and as such the *Matlab* and *Python* codes that are utilised have been included.

Step 1: Geometry Creation

Simplistic geometries can be created from the part module in *Abaqus/CAE*. More complex geometries require the use of more specialised CAD software. Such models in this thesis were constructed using *Autodesk AutoCAD*.

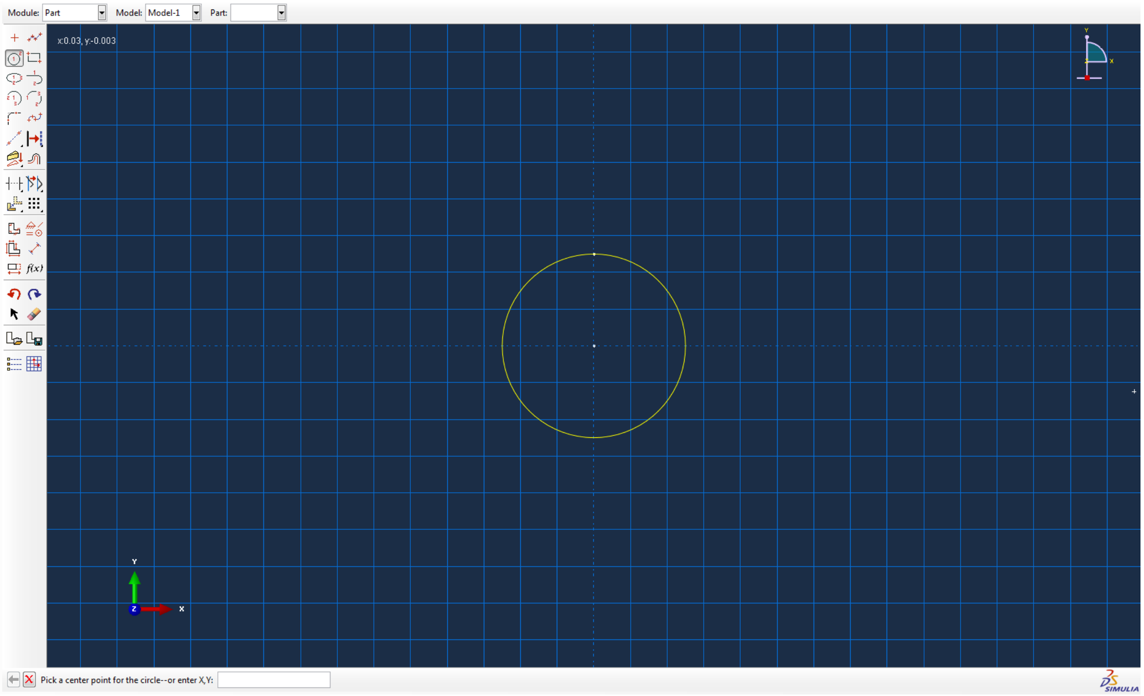
Module: Part Model: Model-1 Part:

x:0.03, y:-0.003

Pick a center point for the circle--or enter X,Y:

Figure I.1: CAD can be performed in Abaqus for simple geometries.

Step 2: Part instance

The parts created should then be instanced in the assembly module. Instances can be translated into the correct positions. In models with more than one part it is typical that parts will overlap. Where this applies the relevant geometries should be cut from one another creating a new part and corresponding instance. There are several methods by which the separate regions of the geometry can be made to interact with one another: an interaction or constraint can be defined between the two regions or the separate instances can be merged together in the assembly module. If the parts are merged it is important that the intersecting boundaries are retained so that different material properties can be applied to different regions.

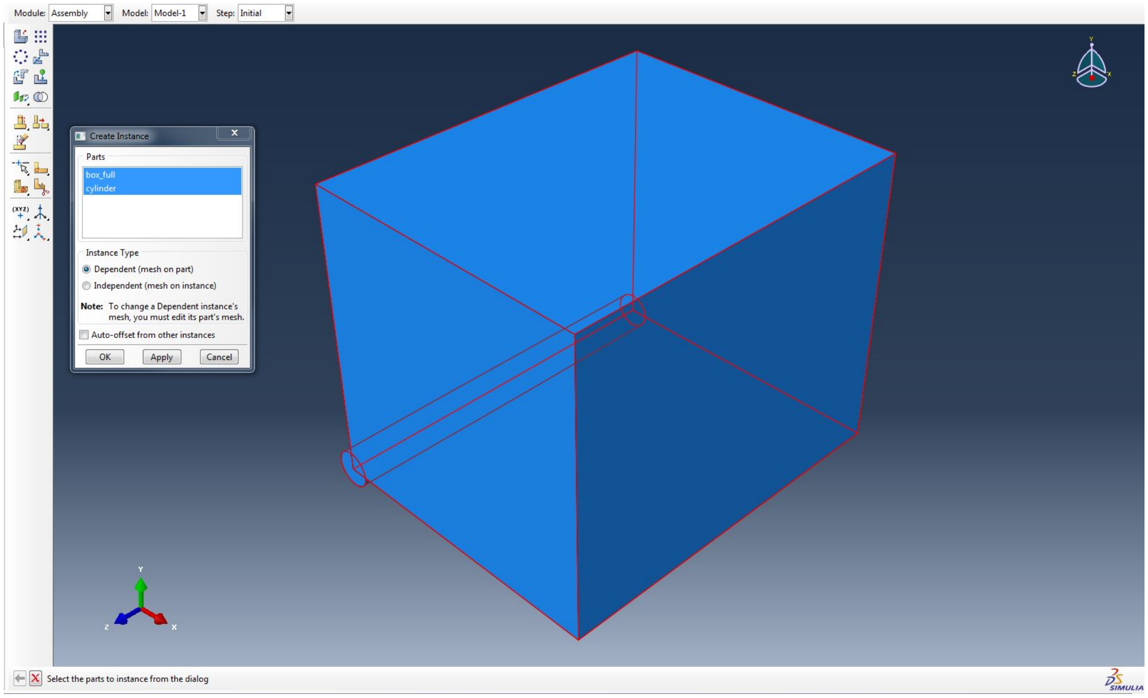
Module: Assembly
Model: Model-1
Step: Initial

Create Instance

Parts: box_full, cylinder

Instance Type
● Dependent (mesh on part)
○ Independent (mesh on instance)

Note: To change a Dependent instance's mesh, you must edit its part's mesh.

☐ Auto-offset from other instances

Select the parts to instance from the dialog

Figure I.2: In the assembly module parts can be instanced and then moved into their required position within the model.

Step 3: Material Property Defintion

Material property definitions are defined under the property module. In the "Edit Material" interface typically density (from the "General" dropdown), elastic and viscoelastic (from the "Mechanical" dropdown) are defined. The viscoelastic properties are defined in the time domain using frequency data read in from an external source. Sections are then created for each material and assigned to each part of the model.

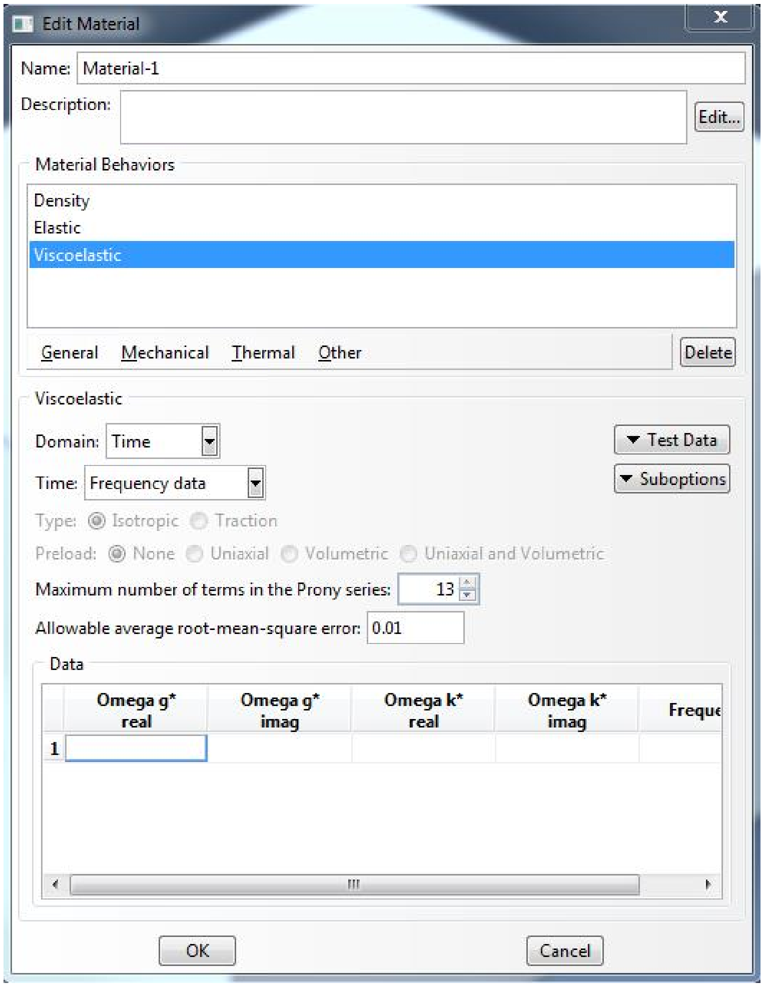

Name: Material-1

Description:

Material Behaviors

- Density
- Elastic
- Viscoelastic

Viscoelastic

Domain: Time

Time: Frequency data

Type: ● Isotropic ○ Traction

Preload: ● None ○ Uniaxial ○ Volumetric ○ Uniaxial and Volumetric

Maximum number of terms in the Prony series: 13

Allowable average root-mean-square error: 0.01

Data

	Omega g* real	Omega g* imag	Omega k* real	Omega k* imag	Freque
1					

Figure I.3: Density, elastic and viscoelastic properties should be defined for each section.

Step 4: Mesh Creation

Meshes are generated under the mesh module. “Seed Edges” used to define the size of the elements. The element type can be assigned using “Assign Mesh Controls” tab, whilst the “Assign Element Type” tab can be used to convert the geometric order of the elements from linear to quadratic (if quadratic elements are to be used the explicit library must be selected). The part can then be meshed. Where infinite elements are required a single row of elements should be defined as a separate section in the property module. Under the “Assign Mesh Controls” tab the “Sweep” technique should be selected with the sweep path set to point out of the model. In “element type” the acoustic elements in the acoustic library should be selected, giving an AC3D8R. This should be edited manually to CIN3D8 in the input file before the simulation is run.

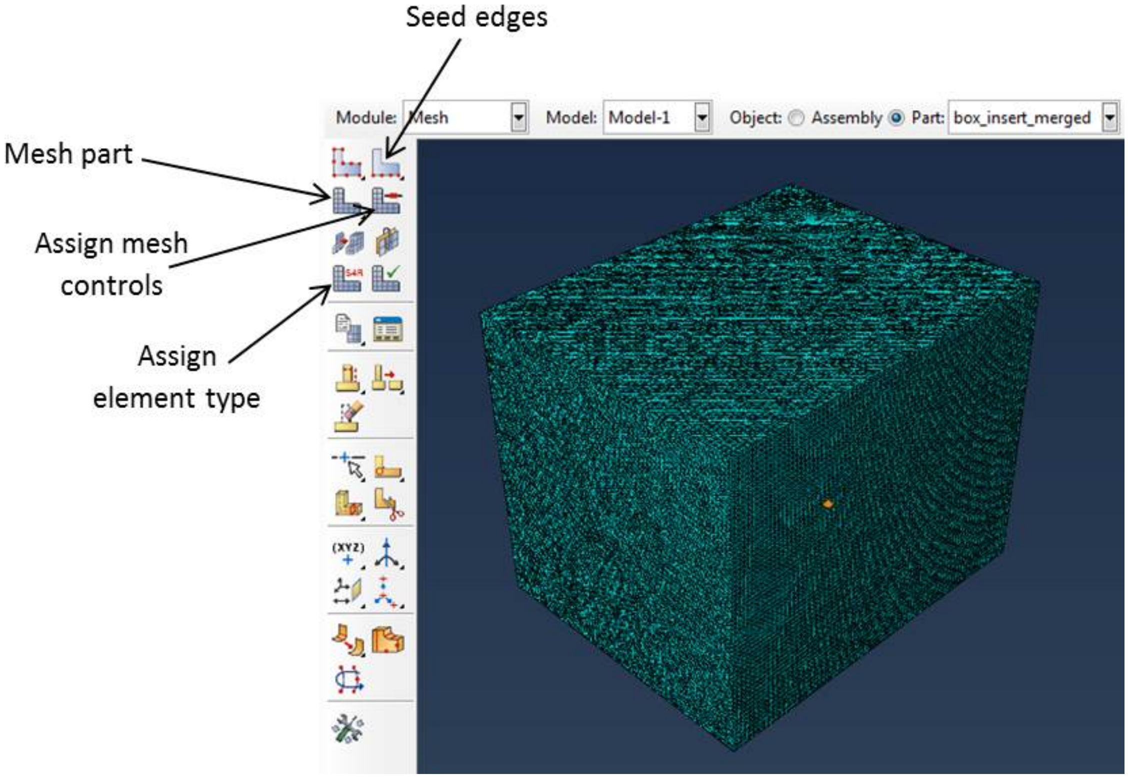

Figure I.4: The mesh module.

Step 5: Create Step

The step is created under the step module. Under the general procedure type the "Dynamic, Explicit" option is selected and the "Edit Step" interface will appear. The length of the time step should be altered to as minimal a value as possible whilst all other settings should be left the same.

Step 6: Field Output

The field output determines which variables are to be output and at what times. The frequency should be set to "From time points" and the "Create..." tab selected. This will allow manual entry of the times corresponding to each of the phase offsets. The only output variable that is required is "U, Translations and rotations".

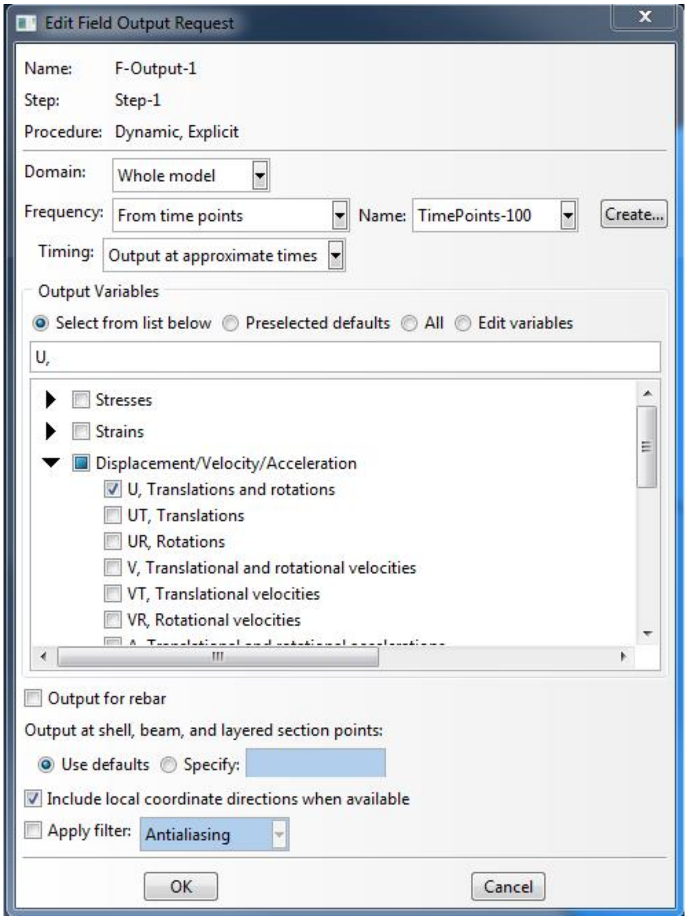

Edit Field Output Request

Name: F-Output-1
Step: Step-1
Procedure: Dynamic, Explicit

Domain: Whole model
Frequency: From time points
Name: TimePoints-100
Timing: Output at approximate times

Output Variables
● Select from list below ○ Preselected defaults ○ All ○ Edit variables

U,

- ☐ Stresses
- ☐ Strains
- ■ Displacement/Velocity/Acceleration
  - ☑ U, Translations and rotations
  - ☐ UT, Translations
  - ☐ UR, Rotations
  - ☐ V, Translational and rotational velocities
  - ☐ VT, Translational velocities
  - ☐ VR, Rotational velocities

☐ Output for rebar
Output at shell, beam, and layered section points:
● Use defaults ○ Specify:
☑ Include local coordinate directions when available
☐ Apply filter: Antialiasing

Figure I.5: Displacement should be output at a predefined set of time points.

Step 7: Load Application

Firstly the region over which the load is to be applied must be selected. This is done by selecting the “Sets” tab under the part module for the part to which the load is to be applied. The set should be created as a node set with the nodes over which the load is to be applied selected. For ease it is recommended that the entire surface upon which the load is to be applied is selected by angle before removal of nodes using the individual selection option. Once the load application region has been selected the frequency of the induced vibrations should be defined. This is achieved by selecting “Amplitude” under the load module with the type of load selected as “Periodic”. This allows definition of the angular frequency, starting time (= 0) and initial amplitude (= 0). The coefficients A and B should be set to 0 and 1 respectively. Finally the load should be defined as a concentrated force. When prompted to select points for the load the “Sets. . . ” tab should be selected and the previously defined set selected prompting the “Edit Load” interface to appear. CF1, CF2 and CF3 correspond to the vector components of the load, typically zero in two directions and non-zero in the other. The amplitude defined previously should also be selected from the drop down menu.

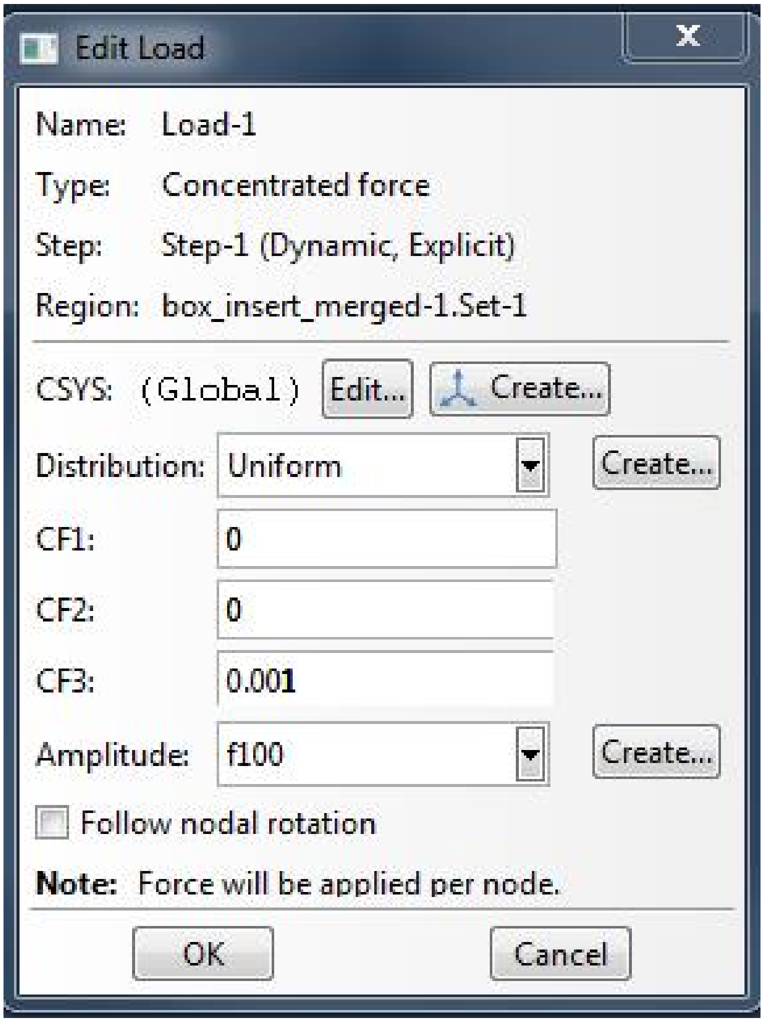
Edit Load

Name: Load-1

Type: Concentrated force

Step: Step-1 (Dynamic, Explicit)

Region: box_insert_merged-1.Set-1

CSYS: (Global)

Distribution: Uniform

CF1: 0

CF2: 0

CF3: 0.001

Amplitude: f100

☐ Follow nodal rotation

Note: Force will be applied per node.

Figure I.6: The load should be applied using a predefined amplitude relating to the frequency of the vibrations under investigation.

Step 8: Boundary Conditions

Boundary conditions are applied through the load module. On selection of the “BCs” tab the “Symmetry/Antisymmetry/Encastre” option should be selected for the type. Either encastred or symmetric boundary conditions are created by manually selecting the surfaces upon which they are being applied before the relevant option is selected in the “Edit Boundary Condition” interface.

Step 9: Running the Simulation

This is achieved through the job module. Selecting the “Create Job” tab will allow naming of the job. Once this has been performed the “Edit Job” interface will appear. Here the editing “Parallelization” tab will allow the simulation to be run over multiple core processors. This will tend to dramatically decrease the simulation time but also requires checking out more licenses. Single jobs can be run by right clicking on the job and selecting “Submit”. This process is not recommended for multiple job submission however, since it requires the user to manually set each job off to run. Instead the following protocol has been devised. Begin by ending the names of each of the jobs that are to be submitted with “_run” and create an input file for each job by right clicking on the job and selecting “Write Input”. Store all of the jobs in the same folder alongside an Abaqus license file. Using *Python/Idle* to run the following code and upon entering the directory in which the jobs are located this will allow *Abaqus/Explicit* to queue the jobs and run then back-to-back without any further user input:

```
import os
import io

## This line sets up the path to the folder with .inp files.
path = input('Location of .inp file directory: ')

## This line searches the above directory and creates a tuple of
   filenames which
## have the .inp extension.
target_files = [f for f in os.listdir(path) if f.endswith('.inp')]

## This line calculates how many .inp files there are and turns that
    value into an
## int for use in the for loop below.
```

```
a=int(len(target_files))

## Job submission code.
target_edited_files = [f for f in os.listdir(path) if f.endswith(’
   _run.inp’)]
b=int(len(target_files))
for i in range (0,b):
    new_jobfile=target_edited_files[i]
    new_jobname=new_jobfile.split(’.’)[0]
    jobcommand=’abaqus job=’+new_jobname+’ int cpus=16’
    os.system(jobcommand)
    print(target_edited_files[i]+’ has completed’)
```

Step 10: Extracting Data

The process of extracting data from *Abaqus* has been developed to deal efficiently with a large number of models that have the same basic geometries thus requiring the same set of paths. Furthermore the process has been developed to require minimal user input and to output data in a form compatible with the functions that import data into *Matlab* as outlined in Step 11. There are 4 stages in the data extraction process:

1. Creation of a coordinate system from which data should be output
2. Input of that coordinate system into *Abaqus*
3. Plotting and saving of XY-data in *Abaqus*
4. Output of *Abaqus* XY-data to an external report file (.rpt) that can be imported into *Matlab* for analysis.

Stage 1 of this process is separate from stages 2-4 since it is performed outside *Abaqus*. Whilst stages 2-4 have all been coded as separate scripts, all are performed in *Abaqus* therefore a single ‘base’ *Python* script has been created that collates these functions and runs them one after the other. For reasons described later a further *Python* code, termed here as the ‘upper level’, has been created that edits the base script and allows the operation to be performed through *Command Prompt* rather than the *Abaqus* interface. The code for each stage is outlined here in addition to the base and upper level codes. It should be noted that each code has been written to be compatible with the code in the levels above with variables often being carried through from one level to the next.

Stage 1: Creation of 'Paths'

Once the simulation has finished running the results are printed into the output database (.odb) file. In order to extract data a 'path' should be created; a set of coordinates at which data should be output. This is typically read into *Abaqus* in a 2-dimensional plane, with 3-dimensional data being extracted from five evenly spaced parallel planes. Path creation can be performed in *Matlab* using the following code:

```
function create_path_points_z_plane()
% define the pixel size
pixel_size = 0.001;

% define the x-coordinates where the path should begin and end.
x_start = 0;
x_final = 0.1;

% define the y-coordinates where the path should begin and end.
y_start = 0;
y_final = 0.1;

% define the z-plane from which data is to be extracted.
z_start = 0.05;

% calculate the number of pixels required in the x- and y-directions
x_dif = round(abs((x_start - x_final)/pixel_size));
y_dif = round(abs((y_start - y_final)/pixel_size));

n = 1;
```

```
% for loop to create the set of coordinates in the format require
    for Abaqus.
for i = 1:x_dif;

    for j = 1:y_dif
                b(n,1:3) = [(x_start + (i-1)*pixel_size) (y_start +
                    (j-1)*pixel_size) z_start];
                n = n + 1;
    end
end

% Write the coordinates to a .csv file that can be input into Abaqus
    .
csvwrite('path',b);
end
```

This code can be altered accordingly to adjust the pixel size, coordinates and plane required.

Stage 2: Inputting Paths into *Abaqus*

Since different geometries require a different set of paths a new *Python* script must be created for each. This can be easily achieved by firstly manually entering the paths into the *Abaqus* interface. Begin by selecting the ‘Paths’ icon in the results section. This will open the ‘Create Path’ window under which ‘Point list’ should be selected. Under the ‘Edit Point List Path’ menu that subsequently appears the .csv file previously created by Matlab should be read into the table by right-clicking on the first row of the table and selecting ‘Read from File…’. For the acquisition of 3-D data each of the five paths should be entered separately.

Once the paths have been manually input the *Python* code relating to that information can be easily created from the .rpy file associated with the *Abaqus* interface where each operation performed is recorded. The unnecessary code pertaining to the opening of the interface should be removed and the remaining code saved under the filename 'path_points_import.py' thus making it compatible with other scripts required later in the process. The Python code for this process takes the following form:

```
session.Path(name='Path-1', type=POINT_LIST, expression=((0.0, 0.0,
   0.003), (0.0, 0.001, 0.003), (0.0, 0.002, 0.003), (0.0, 0.003,
   0.003)))
session.Path(name='Path-2', type=POINT_LIST, expression=((0.0, 0.0,
   0.004), (0.0, 0.001, 0.004), (0.0, 0.002, 0.004), (0.0, 0.003,
   0.004)))
session.Path(name='Path-3', type=POINT_LIST, expression=((0.0, 0.0,
   0.005), (0.0, 0.001, 0.005), (0.0, 0.002, 0.005), (0.0, 0.003,
   0.005)))
session.Path(name='Path-4', type=POINT_LIST, expression=((0.0, 0.0,
   0.006), (0.0, 0.001, 0.006), (0.0, 0.002, 0.006), (0.0, 0.003,
   0.006)))
session.Path(name='Path-5', type=POINT_LIST, expression=((0.0, 0.0,
   0.007), (0.0, 0.001, 0.007), (0.0, 0.002, 0.007), (0.0, 0.003,
   0.007)))
```

The example shown here is for paths of 2 x 2 pixels. In reality the paths will be much larger than this and as such the required code several thousand lines long.

Stage 3: Plotting and Saving XY-Data in *Abaqus*

In the next stage *Abaqus* must plot and save the displacement data. This operation must be performed for each separate spatial direction at each time point and along each path. For 2-D analysis this implies that eight plots must be created (one direction, one path and eight time points) whilst for 3-D data 120 plots must be created (three directions, five paths and 8 time points). The code to perform this operation is as follows:

```
o1 = session.openOdb(
    name=odb_file_location)
```

```
session.viewports['Viewport: 1'].setValues(displayedObject=o1)
## creates for loops over the 5 paths used and the 8 timepoints that
    have been output at
for j in range(1,6):
    for i in range(1,9):
                ## displays the frame relating the the timepoint i
        session.viewports['Viewport: 1'].odbDisplay.setFrame(step=0,
            frame=i)
        ## states that the variable to be output is displacement and
            states the direction     session.viewports['Viewport
           :1'].odbDisplay.setPrimaryVariable(
        variableLabel='U', outputPosition=NODAL, refinement=(
           COMPONENT, 'U1'))
         ## creates and XY-plot and names it
                xyp = session.XYPlot('XYPlotX1-'+str(i)+'path-'+str(
                   j))
                chartName = xyp.charts.keys()[0]
                chart = xyp.charts[chartName]
                ## defines the path from which data should be output
                pth = session.paths['Path-'+str(j)]
        xy1 = xyPlot.XYDataFromPath(path=pth, includeIntersections=
           False,
        ## states that data should be output from the undeformed
           model and that the direction along the path of the
           coordinates is the y-direction
         shape=UNDEFORMED, labelType=TRUE_DISTANCE_Y)
                ## creates the XY plot
         c1 = session.Curve(xyData=xy1)
         chart.setValues(curvesToPlot=(c1, ), )
        session.viewports['Viewport:  1'].setValues(displayedObject=
           xyp)
         ## redefines the path for the data to be saves
         pth = session.paths['Path-'+str(j)]
        ## saves the XY-data under the defined name session.
           XYDataFromPath(name='x-path_'+str(j)+'_time_'+str(i),
           path=pth,
```

```
        includeIntersections=False, shape=UNDEFORMED, labelType=
           TRUE_DISTANCE_Y)
```

It should be noted that the code above if the extracting displacement data from the x-direction alone. In order to extract from the y- and z-directions the component input here as ‘U1’ should be changed to ‘U2’ and ‘U3’ respectively. Each code should be saved separately under the filenames ‘xy-data-x’, ‘xy-data-y’ and ‘xy-data-z’.

Stage 4: Outputting the data from *Abaqus*

The codes in stage 3 store the XY-data as objects whose names are dependent on the direction, path and time point from which they are output. This script simply outputs these to a directory predefined in the upper level. It is required that this directory contains three folders named ‘x-direction’, ‘y-direction’ and ‘z-direction’. The *Python* code for the x-direction is as follows:

```
for paths in range (1,6):
    x0 = session.xyDataObjects['x-path_'+paths+'_time_1']
    x1 = session.xyDataObjects['x-path_'+paths+'_time_2']
    x2 = session.xyDataObjects['x-path_'+paths+'_time_3']
    x3 = session.xyDataObjects['x-path_'+paths+'_time_4']
    x4 = session.xyDataObjects['x-path_'+paths+'_time_5']
    x5 = session.xyDataObjects['x-path_'+paths+'_time_6']
    x6 = session.xyDataObjects['x-path_'+paths+'_time_7']
    x7 = session.xyDataObjects['x-path_'+paths+'_time_8']
    session.writeXYReport(
fileName=output_file_location + 'x-direction/path-'+paths+'.rpt',
xyData=(x0, x1, x2, x3, x4, x5, x6, x7))
```

Stage 5: The Base and Upper Level Scripts

Theoretically the scripts in stages 2-4 can all be run independently in the Abaqus interface using the ‘Run Script’ option under the ‘file’ tab. This is inefficient since it involves user interaction at each stage. The base script was therefore created to remove as much of this interaction as possible also adding the potential of looping the operation over multiple .odb files. The scripts to plot and save XY-data for each direction were initially created to run one after another (in fact the direction was included in a ‘for’ loop of a single ‘xy-data’ script rather than the three files that exist in the current setup). It was however realised that the operations to output each direction are independent from one another, and that since this is the most time consuming stage of the process, efficiency could be dramatically increased by creating a separate thread for each direction and running these simultaneously (flow charts for these processes are demonstrated in figure I.7). Unfortunately support for threading in the *Python Development Environment* of *Abaqus* is poor. This led to the creation of the upper level, a script with two purposes. Firstly it edits a base Python data output file depending on the name of the .odb file and outputs three separate files for each spatial direction. Secondly it runs each of these scripts in parallel as threads. The code for the base file is:

```
Inserts
Mods

pde_file_locs
odb_file_locs
output_file_locs

# -*- coding: mbcs -*-
# Abaqus/Viewer Release 6.10-1 replay file
# Internal Version: 2010_04_29-14.17.36 102575
# Run by s1160274 on Sun Jan 11 15:12:49 2015
# from driverUtils import executeOnCaeGraphicsStartup
# executeOnCaeGraphicsStartup()
#: Executing "onCaeGraphicsStartup()" in the site directory ...
```

```
#: Warning: Warning: Permission was denied for "abaqus.rpy"; "abaqus
   .rpy.9" will be used for this session's replay file.

from abaqus import *
from abaqusConstants import *
session.Viewport(name='Viewport: 1', origin=(0.0, 0.0), width=98,
    height=209.866683959961)
session.viewports['Viewport: 1'].makeCurrent()
session.viewports['Viewport: 1'].maximize()
from viewerModules import *
from driverUtils import executeOnCaeStartup
executeOnCaeStartup()
o1 = session.openOdb(name=odb_file_location)

session.viewports['Viewport: 1'].setValues(displayedObject=o1)

o1 = session.openOdb(
    name=odb_file_location)
session.viewports['Viewport: 1'].setValues(displayedObject=o1)

execfile(
    pde_file_location+'/import_path_points.py',
    __main__.__dict__)

execfile(
    xy_data
    __main__.__dict__)

execfile(
    export_dat
    __main__.__dict__)

close
```

Meanwhile the code for the upper level is:

```
import threading
from threading import Thread
import os
import io

s = [ ]
l = [ ]

for ln in l:

    for sh in s:

        ## creates the text to be placed into the python
           scripts run through the abaqus pde
        ## if multiple values are used define the values as
           such [\'val1\',\'val2\']
        ## even if these variables do not exist within the
           filename, random values should be inserted
        ins = 'length = \''+str(ln)+'\''
        mod = 'shear = \''+str(sh)+'\''

        ## insert the locations of the pde and odb files and
            location to put the output files
        ## variables 'length' and 'shear' can be inserted in
            the odb and output strings to loop over these
           in the new files
        ## if loops are to be performed, strings should be
           inserted in the following format: ...\'+str(
           length)+\'
        pde='pde_file_location =
        odb='odb_file_location =
        output='output_file_location =

        ## other lines that need editing depending on the
           direction within the base code
```

```
xy_data_call=’pde_file_location+\’xy_data_’
export_output_call=’pde_file_location+\’
   export_output_’
close = ’session.odbs[pde_file_location].close(’


## creates an array pertaining to the different
   directions
vectors = [’x’,’y’,’z’]

## finds the base file from which the python files
   for the abaqus pde are created
target_files = [f for f in os.listdir() if f.
   startswith(’base’)]

a = int(len(target_files))

## for loop replacing the specified lines in the
   base file with the required lines for this
   output and
## saves the new file
for v in vectors:

        for i in range(0,a):

            bases=target_files[i]
            text_read=open(bases,’r’)
            output_file = ’data_output_’+str(v)+’_’+
               str(sh)+’_’+str(ln)+’.py’
            text_write=open(output_file,’w’)
            lines=text_read.read()
            if ’insert’ in lines:
                lines = lines.replace(’inserts’,ins)
            if ’mod’ in lines:
                lines = lines.replace(’mods’,mod)
            if ’pde_file_locs’ in lines:
```

```
                    lines = lines.replace('pde_file_locs
                        ',pde)
                if 'odb_file_locs' in lines:
                    lines = lines.replace('odb_file_locs
                        ',odb)
                if 'output_file_locs' in lines:
                    lines = lines.replace('
                        output_file_locs',output)
                if 'xy_data' in lines:
                    lines = lines.replace('xy_data',
                        xy_data_call+v+'\',')
                if 'export_dat' in lines:
                    lines = lines.replace('export_dat',
                        export_output_call+v+'\',')
                if 'close' in lines:
                    lines = lines.replace('close',close)
                text_write.write(lines)
                text_write.close()
                text_read.close()

## defines a function that opens a command window
   and inputs the command to run the data output
   file without
## the abaqus GUI in each direction
def func(vector):

        command = 'abaqus cae noGui=data_output_'+
            vector+'_'+sh+'_'+ln+'.py'
        os.system(command)

## creates threads to run three separate command
   windows simultaneously and output from each
   spatial direction
threads = []

for vec in vectors:
```

```
                    t=threading.Thread(target=func,args=(vec,))
                    threads.append(t)
                    t.start()
```

Step 11: Importing and Formatting Data in *Matlab*

The “Import Data” tab should be utilised to import the .rpt into *Matlab* with columns delimited by spaces and the data formatted in a matrix. Once the data have been imported they need to be formatted correctly. The columns of the imported data are the time points with rows of pixels stacked on top of one another. The first step is to remove any rows that are replicated as a result of lying on the boundary between two regions. The following *Matlab* code achieves this:

```
% find the size of the imported data
[m n] = size(data);

% creates a new matrix of zeros with an extra column
new = ones(m,n+1);

% puts the data into the final columns of the new matrix
new(:,2:end) = test;

% for loop to calculate the difference in position between one point and the next and returns this in a vector
for i = 1:m-1
    a = new(i+1,2) - new(i,2);
    vector(i+1)= a;
    vector = vector';
end

% creates a new matrix with the same size as the data plus on extra column
```

```
removed_rows = ones(m,n+1);

% places the vector for the difference in position in the first
   column of the new matrix and the rest of the data in the
   remaining columns
removed_rows(:,1) = vector;
removed_rows(:,2:end) = test;
removed_rows(1,1) = 1;

% removes rows where the first number in the column is equal to 0.
removed_rows(removed_rows(:,1)==0,:)=[];

% removes the first two columns corresponding to the pixel
   coordinate and distance between neighbouring coordinates
removed_rows = removed_rows(:,3:end);
```

Once the repeated rows have been removed the pixel rows within each time point, currently stacked on top of one another, must be separated and placed next to one another in order to form a displacement image. This allows creation of a third order tensor with two spatial dimensions and a temporal dimension:

```
% finds the size of the previously created removed_rows matrix
[m n] = size(removed_rows);

C = zeros(depth, length);

% for loop that separates the different time points into a vector.
   This is then placed into an image matrix for each time point.
for i = 1:n

   B = A(:,i);

   for j = 1:depth
```

```
            C(j,:) = B(1+length*(j-1):length+length*(j-1));

            waves(:,:,i) = C(:,:);
    end

end

end
```

The output of 3-D data from *Abaqus* is typically performed so that the displacement data from each spatial direction are stored in separate folders whilst an individual file is written within that folder for each path. When imported into *Matlab* this is stored as a fourth order tensor, with the first three orders corresponding to the spatial dimensions and the fourth order corresponding to the temporal dimension. The following *Matlab* function is used to import 3-D displacement data for one direction:

```
% finds the size of the previously created removed_rows matrix
function [w_direction cw_direction] = arrange_3d(length,depth)

% imports the wave in each path based upon the file names being
   named correctly in the directory
[path_1] = abaqus_to_wave('path-1.rpt',length,depth);
[path_2] = abaqus_to_wave('path-2.rpt',length,depth);
[path_3] = abaqus_to_wave('path-3.rpt',length,depth);
[path_4] = abaqus_to_wave('path-4.rpt',length,depth);
[path_5] = abaqus_to_wave('path-5.rpt',length,depth);

% stacks the images together to get 4th order tensors with three
   spatial and one temporal direction
for i = 1:8
w_direction(:,:,:,i) = cat(10,path_1(:,:,i),path_2(:,:,i),path_3
   (:,:,i),path_4(:,:,i),path_5(:,:,i));
end
```

```
% returns the 2nd complex wave image in three dimensions
cw = fft(w_direction,[],4);
cw_direction(:,:,:) = cw(:,:,:,2);
save('workspace','path_1','path_2','path_3','path_4','path_5')
```

Fourier Transfrom and Inversion of Data

Inversion is performed upon the complex wave image meaning that the waves must first be Fourier transformed. For the 3-dimensional data this is performed within the arrange_3d function. For the 2-dimensional data this is achieved simply with:

```
complex_wave = fft(waves,[ ],3);
```

Throughout this thesis inversion has been performed using the direct inversion of the Helmholtz equation. Whilst this is typically used in conjunction with noise removing filters there is little requirement for these with modelling data. As a result the code for the 3-dimensional direct inversion algorithm used here is:

```
function [G_3d] = inversion_3d(cwx,cwy,cwz,density,ang_freq,
   pixel_size)
%% where cwx, cwy and cwz are three dimensional objects
   representing the complex wave in each respective data.

% calculate pixel size in mm
dx = pixel_size/1000;
dy = pixel_size/1000;
dz = pixel_size/1000;

% calculate the first spatial derivatives
```

```
[gradx_x gradx_y gradx_z] = gradient(cwx,dx,dy,dz);
[grady_x grady_y grady_z] = gradient(cwy,dx,dy,dz);
[gradz_x gradz_y gradz_z] = gradient(cwz,dx,dy,dz);

% calculate the second spatial derivatives
[gradx_xx gradx_xy gradx_xz] = gradient(gradx_x,dx,dy,dz);
[gradx_yx gradx_yy gradx_yz] = gradient(gradx_y,dx,dy,dz);
[gradx_zx gradx_zy gradx_zz] = gradient(gradx_z,dx,dy,dz);

[grady_xx grady_xy grady_xz] = gradient(grady_x,dx,dy,dz);
[grady_yx grady_yy grady_yz] = gradient(grady_y,dx,dy,dz);
[grady_zx grady_zy grady_zz] = gradient(grady_z,dx,dy,dz);

[gradz_xx gradz_xy gradz_xz] = gradient(gradz_x,dx,dy,dz);
[gradz_yx gradz_yy gradz_yz] = gradient(gradz_y,dx,dy,dz);
[gradz_zx gradz_zy gradz_zz] = gradient(gradz_z,dx,dy,dz);

% utilise the second spatial derivatives to calculate the laplacian
   in each direction
laplac_x = gradx_xx + gradx_yy + gradx_zz;
laplac_y = grady_xx + grady_yy + grady_zz;
laplac_z = gradz_xx + gradz_yy + gradz_zz;

% prevent the algorithm from blowing up if the laplacian is equal to
    0
laplac = laplac_x + laplac_y + laplac_z;
laplac(laplac == 0) = NaN;

% 3-d direct inversion algorithm
G_3d = -density*ang_freq^2*((cwx + cwy + cwz)./(laplac));
```

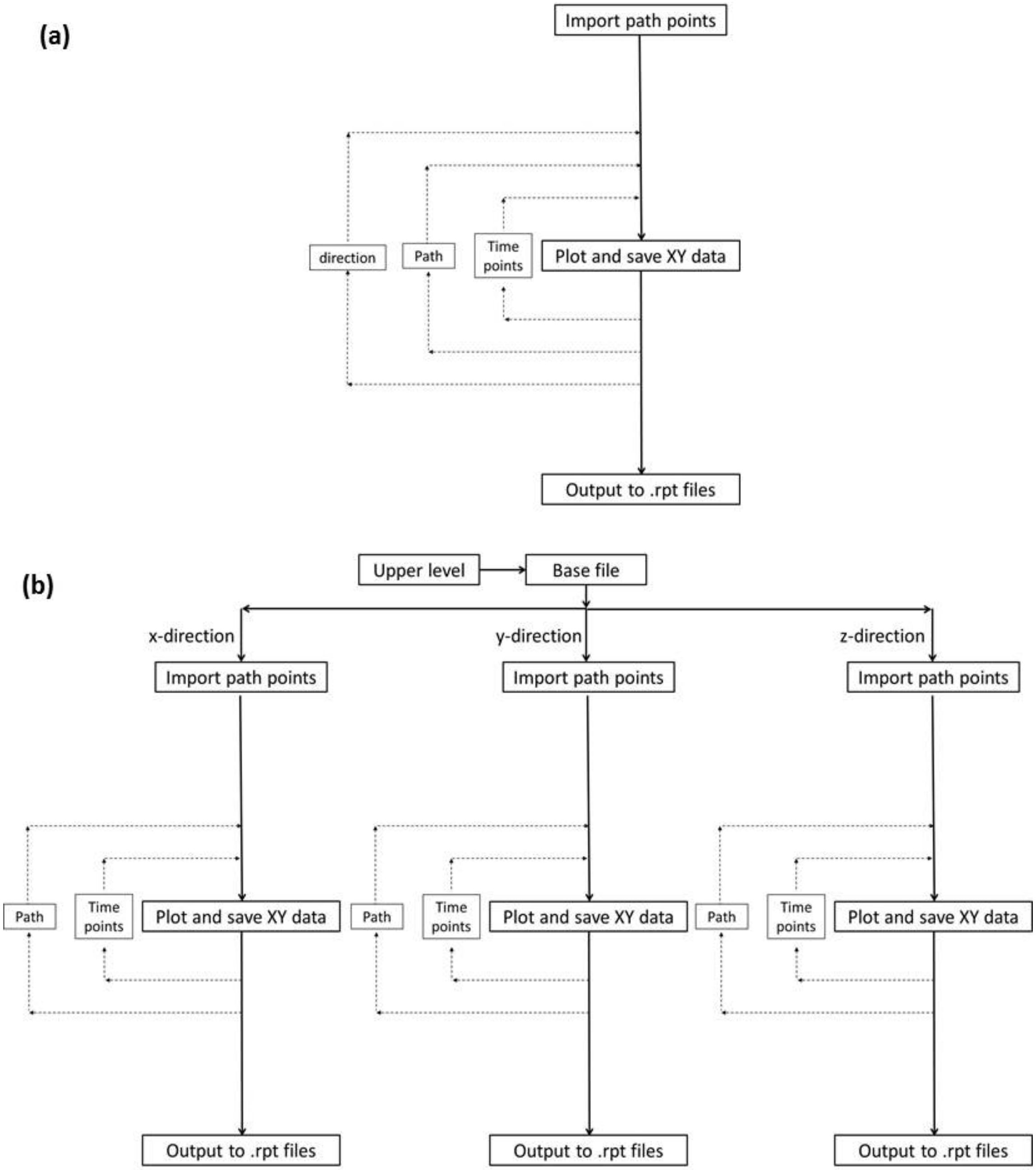

Figure I.7: Flow charts for the processes of outputting data from Abaqus. Originally a single program looped over the time points, path and direction (a). Efficiency was increased creating a separate thread for each direction (b).

Appendix II

Discretisation Errors in 1-D

Typically a mathematical operation is defined to operate upon a continuous function. In reality data are collected as measurements over a set of predefined intervals however and are therefore discrete. This implies that the operator must be approximated in order to make calculations on such data and there are associated discretisation errors as a result.

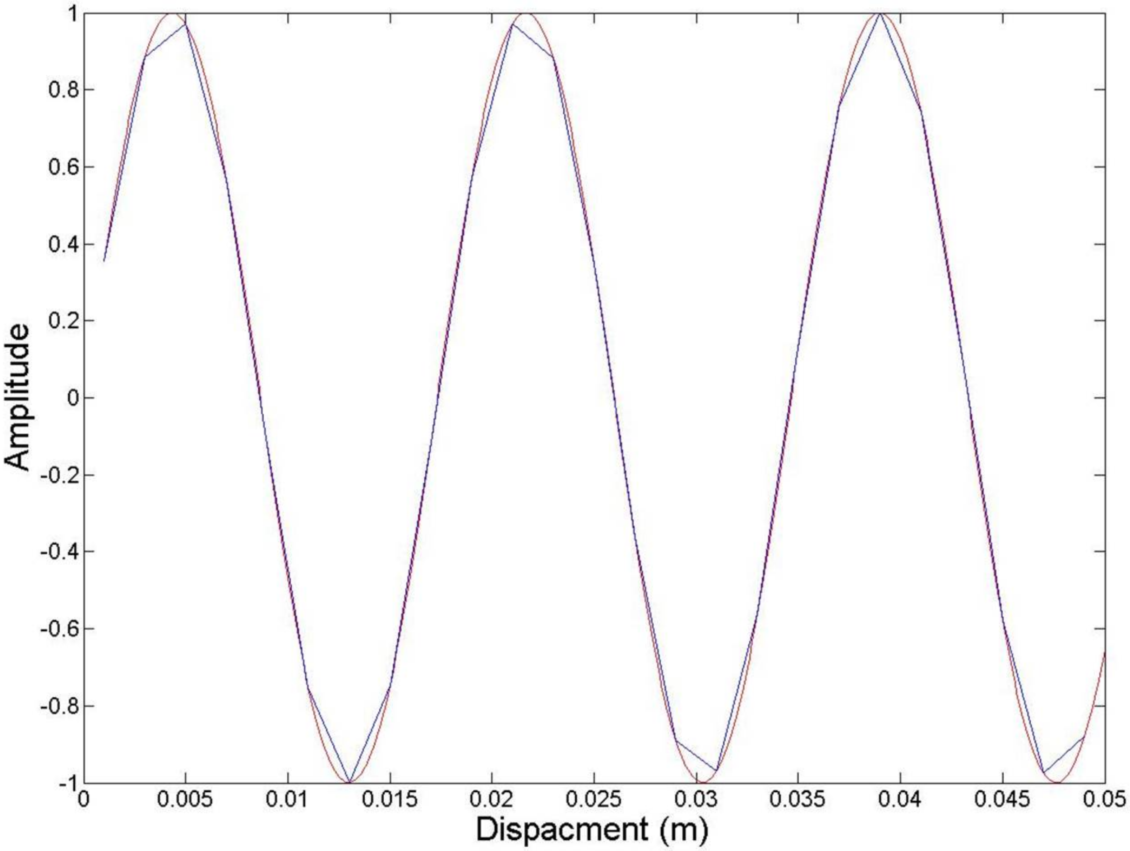

Figure II.1: Plot showing two sine waves with the same wavelength and amplitude. The blue wave is heavily discretised in comparison to the red wave.

In relation to this thesis, discretisation errors are associated with the Laplacian [156]. For a planar 2-D wave the size of this discretisation error can be estimated. To achieve this the x-axis is firstly aligned with the direction of wave propagation such that the velocity of the wave is given by:

$$|\mathbf{v}| = v_x \tag{II.1}$$

Since the wave is planar this implies that the first and second derivatives of the displacement in the y-direction are equal to 0. Resultantly the Laplacian becomes equivalent to the second derivative of the displacement in the x-direction. This implies that the second dimension of the planar wave can be discounted and characterisation of the discretisation error considered a 1-D problem.

In order to approximate the discretisation error, it should be recognised that the wavelength, λ, of a wave with frequency, f, travelling through a medium of known shear modulus, μ, and density, ρ is given by:

$$\lambda = \frac{1}{f}\left(\frac{\mu}{\rho}\right)^{1/2} \tag{II.2}$$

The spatial frequency, ν, of a wave is given by:

$$\nu = \frac{1}{\lambda} \tag{II.3}$$

This means that in the one spatial dimension the expected planar wave should take the form:

$$A(x) = A_0 \sin\left(2\pi f\left(\frac{\rho}{\mu}\right)^{1/2} x\right) \tag{II.4}$$

where A_0 is the amplitude (arbitrary in this instance) and x is the position along the x-axis. In *Matlab* x is defined discretely in concordance to the pixel size being used and as such an idealised but discretised 1-D wave can be created that matches the wavelength for the predefined frequency, shear moduli and density. Since the Laplacian in the inversion algorithm demonstrated in Appendix I is calculated by applying the gradient function in various spatial directions, a 1-D inversion can easily be applied to the sine wave created here. The mean shear modulus is typically distorted by applying this function to values towards the edge of the array since the operation acts over a width of 5 pixels. The median shear modulus is therefore chosen to represent the discretisation error. Increasing the frequency of vibrations increases the size of the discretisation error as does increasing the pixel size (figure II.2).

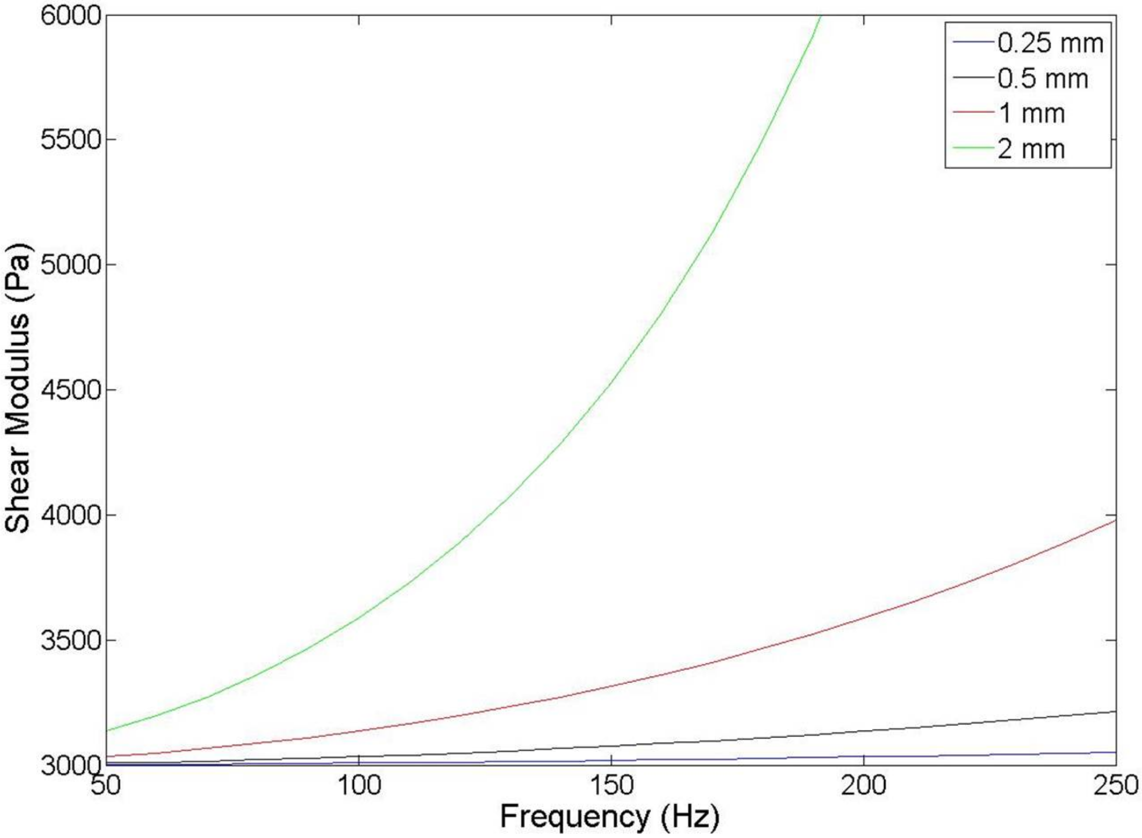

Figure II.2: Median shear moduli for four different pixel sizes across a range of frequencies. The input parameters for calculation of the sine wave were $\rho = 1000$ $kg{\cdot}m^{-3}$ *and* $\mu = 3000$ Pa*.*

Appendix III

Convergence Study

Convergence studies act as a crucial validation point for FEA. Typically accuracy of a simulation is dependent upon the number of elements that are used within the model, but increasing the number of elements also increases the computational time required for the simulation to solve. Fortunately the relationship between FEA accuracy and the number of elements is generally exponential meaning a finite number of elements and a finite simulation time are typically required to achieve a good approximation. In order to determine the number of elements required for a model, simulations are iteratively performed with an increasing mesh density. Normally displacements or stresses from the same region within each model are compared to one until convergence has judged to have been achieved.

Throughout this thesis convergence studies have been performed for each geometry and each element type used. Since the shear modulus calculated using the direct inversion algorithm is dependent upon displacement, this has been used as the parameter through which convergence is examined. This is also useful since the vibrational loads are applied via nodes on the surface and therefore are dependent on the size of the mesh used. Whilst the amplitude per node is altered to correct for this, there is likely to be a small difference between the loads applied for different mesh densities. Since the shear modulus is not directly dependent upon the amplitudes of the displacements but upon the wavelengths induced throughout the model, this helps to remove any differences in load application.

The example of the convergence study shown here is for the insert 1 model described in chapter 2 with C3D8R elements. All boundaries have been encastred whilst the shear moduli of the background and the insert are 3 and 9 kPa respectively. In the example shown edge lengths of 1, 1.25, 1.5, 1.75, 2, 2.25, 2.5, 2.75 and 3 mm have been used.

As can be seen convergence upon the mean has been achieved in both the background and the insert from element lengths of 2.75 mm downwards. The standard deviations were plotted alongside the mean and the elastograms were visually inspected to monitor for any discrepancies between the element sizes. Convergence has assumed to have been achieved if the percentage difference from one element size to the next is less than 5% in both the background and the insert.

Throughout this thesis simulations were typically performed with mesh densities much finer than deemed necessary by the convergence criteria outlined above. This was largely because simulation times for many of the models (particularly in chapter 2) were relatively short; often less than an hour. As such time constraints were not particularly significant throughout most of the thesis. This explains why the more complex geometries in chapter 5 were actually performed at a lower mesh density than the simpler geometries used earlier in the thesis: the computational time for these geometries was significantly longer and the size of the mesh was therefore a much more significant factor.

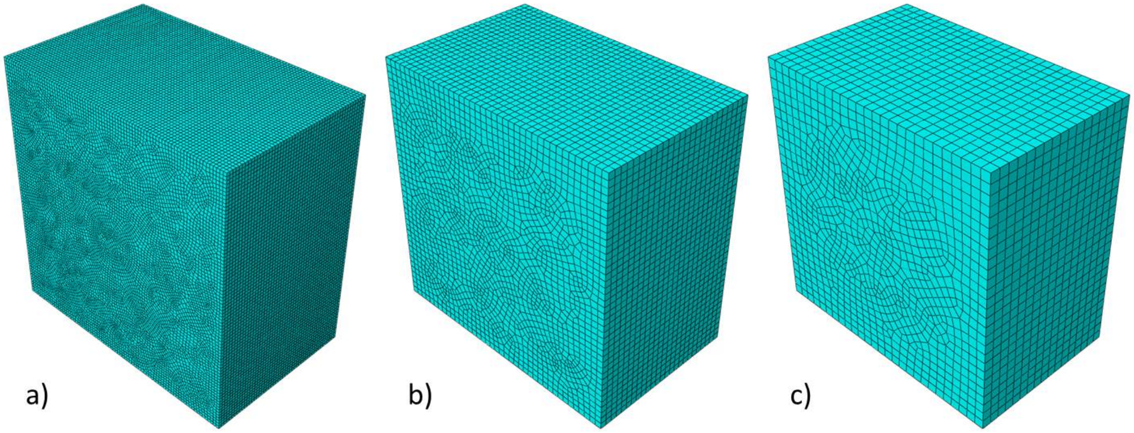

Figure III.1: Different mesh densities used in the convergence study described in this section. a) 1mm edge length, b) 2mm edge length and c) 3mm edge length.

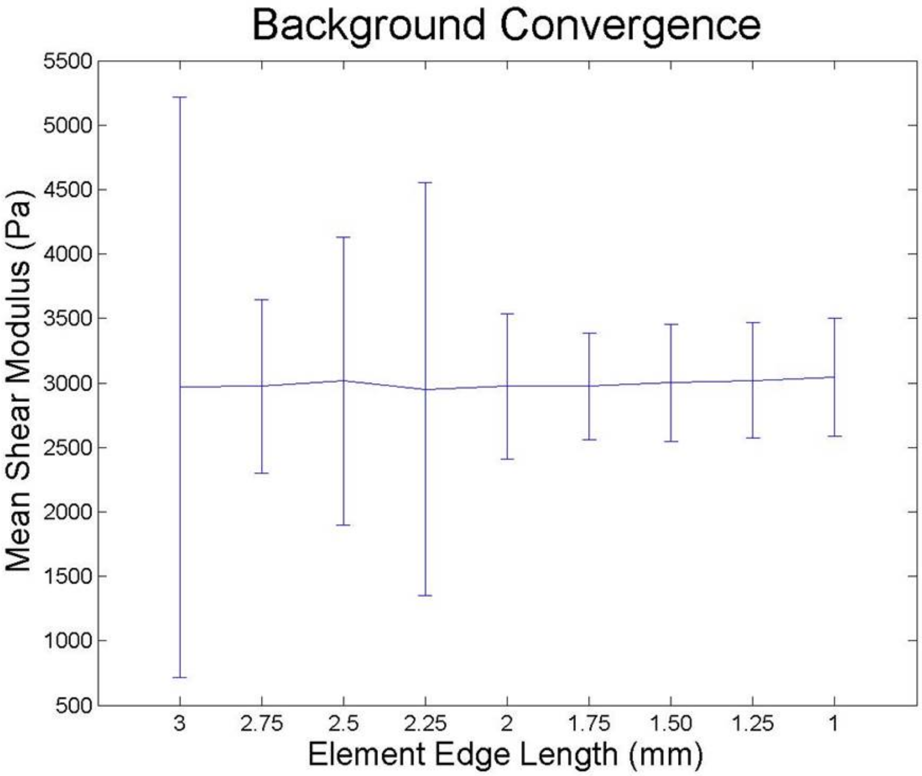

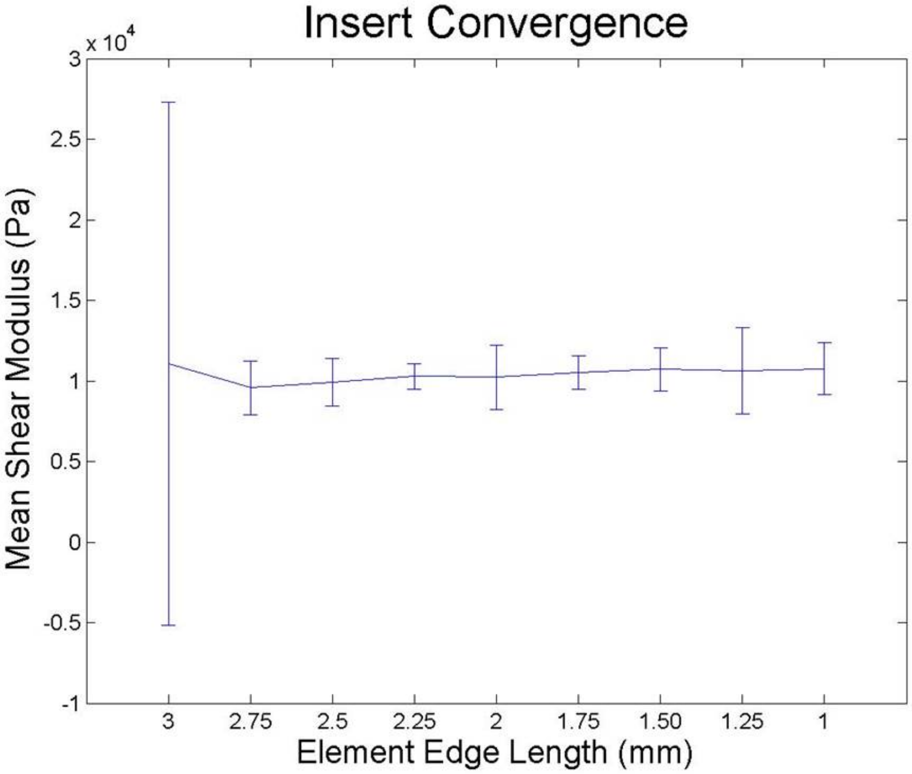

Figure III.2: Graphs showing convergence of the means of the shear modulus in the background and the insert with the error bars showing the standard deviations of the values within the region of interest.

Appendix IV

MDEV Inversion

Like direct inversion, MDEV also utilises the Helmholtz equation but includes a summation over the frequencies to calculate the frequency independent variable, $|G^*|$ [194]:

$$|G^*| = \rho \frac{\sum_{m=1}^{3} \sum_{n=1}^{N} \omega_n |u_m^*(\omega_n)|}{\sum_{m=1}^{3} \sum_{n=1}^{N} \nabla^2 |u_m^*(\omega_n)|} \tag{IV.1}$$

for N frequencies and 3 directions. G^* represents a complex number consisting of G', the storage moduli, and G'', the loss moduli, such that $G^* = G' + iG''$. This implies that:

$$|G^*| = \left((G')^2 + (G'')^2\right)^{1/2} \tag{IV.2}$$

Since $|G^*|$ calculated using MDEV is a single value dependent upon multiple frequencies, whilst G calculated using the direct inversion is dependent on a single frequency alone, the two values are not directly comparable to one another.

In order to perform the inversion the data must be converted into the right format. As outlined in Appendix I the complex wave images are imported into *Matlab* and stored as 3-D objects for each direction. These must be imported for each frequency independently and then stacked as 4-D objects:

```
cw_x = cat(4,cwx_freq1,cwx_freq2,cwx_freq3);
cw_y = cat(4,cwy_freq1,cwy_freq2,cwy_freq3);
cw_z = cat(4,cwz_freq1,cwz_freq2,cwz_freq3);
```

Inversion to calculate $|G^*|$ can then be performed:

```
function [G] = MDEV_G(cw_x,cw_y,cw_z,dx,dy,dz,freq,density)

[m n o p] = size(cw_x);

% calculate pixel size in mm
dx = pixel_size/1000;
dy = pixel_size/1000;
dz = pixel_size/1000;
```

```
% split the complex waves into separate components for each frequency and
% calculate the numerator and denominators for each independent frequency
% in equation 8 of Guo et al.(2013)

for i = 1:p

%     calculate the laplacians for each direction
    cwx(:,:,:) = cw_x(:,:,:,i);
    [gradx_x gradx_y gradx_z] = gradient(cwx,dx,dy,dz);

    [gradx_xx,~,~] = gradient(gradx_x,dx,dy,dz);
    [~,gradx_yy,~] = gradient(gradx_y,dx,dy,dz);
    [~,~, gradx_zz] = gradient(gradx_z,dx,dy,dz);

    lx = gradx_xx + gradx_yy + gradx_zz;

    cwy(:,:,:) = cw_y(:,:,:,i);
    [gradx_x gradx_y gradx_z] = gradient(cwy,dx,dy,dz);

    [gradx_xx,~,~] = gradient(gradx_x,dx,dy,dz);
    [~,gradx_yy,~] = gradient(gradx_y,dx,dy,dz);
    [~,~, gradx_zz] = gradient(gradx_z,dx,dy,dz);

    ly = gradx_xx + gradx_yy + gradx_zz;

    cwz(:,:,:) = cw_z(:,:,:,i);
    [gradx_x gradx_y gradx_z] = gradient(cwz,dx,dy,dz);

    [gradx_xx,~,~] = gradient(gradx_x,dx,dy,dz);
    [~,gradx_yy,~] = gradient(gradx_y,dx,dy,dz);
    [~,~, gradx_zz] = gradient(gradx_z,dx,dy,dz);

    lz = gradx_xx + gradx_yy + gradx_zz;
```

```
%     calculate the numerators for eqn. 8 for each direction
    numx = abs(cwx);
    numy = abs(cwy);
    numz = abs(cwz);

%     calculate the denominators for eqn. 8 for each direction
    denx = (abs(lx));
    deny = (abs(ly));
    denz = (abs(lz));

%     add the contribution from each direction together
    numall = numx + numy + numz;
    denall = denx + deny + denz;

%     create object containing all the frequencies
    num(:,:,:,i) = ((2*pi*freq(i)).^2)*numall(:,:,:);
    den(:,:,:,i) = denall(:,:,:);

end

% sum the frequencies together
numfreq = sum(num,4);
denfreq = sum(den,4);

% calculate the absolute value of the complex shear modulus
G = 1000*(numfreq./denfreq);
```

Appendix V

Directional Filtering

Reflections are well established as a source of noise in MRE as a result of destructive interference of the reflected wave with the induced wave. To this end a paper by Manduca et al. (2003) [195] introduced several methods of filtering these reflected waves out and thus removing the interference caused by these reflections. This appendix discusses how these filters work and includes the *Matlab* code that was developed in this thesis to implement them.

Spatio-Temporal Directional Filtering

Assuming that the contributions to the wave are in the vertical plane, then the 3rd order tensor used to represent displacement at each point through time, can be sliced into a set of 2nd order tensors with one temporal and one spatial dimension (in the direction of assumed propagation of the wave). The displacement at any point in this array is the sum of the displacement due to the induced wave, and the displacement due to its subsequent reflection from the boundary wall opposite to that at which the load is induced [196]:

$$u(y,t) = u_{incident}(y,t) + u_{reflected}(y,t) \tag{V.1}$$

Performing a 2-D Fourier transform upon this expression gives:

$$u(\omega,k) = \sum_{x=-\infty}^{\infty} \sum_{t=-\infty}^{\infty} U_{incident}(x,t)e^{-i(\omega t-kx)} + U_{reflected}(x,t)e^{-i(\omega t-kx)} \tag{V.2}$$

where ω is the temporal frequency and k is the spatial frequency whilst U represents the amplitudes of the waves. The phase velocity of a wave is given by $c = \omega/k$. This implies that when ω and k are both greater than or both less than zero, then the phase velocity is positive, thus the wave is incident. Conversely where one is negative and the other positive, the phase velocity is negative and the wave has been reflected. As a result applying a mask over the regions of the ω, k plot where $\omega > 0,\ k < 0$ and $\omega < 0,\ k > 0$ removes the reflected waves (figure V.1). An inverse Fourier transformation back to the time domain therefore allows reconstruction of the wave images and subsequent calculation of the elastogram without interference from reflected waves.

This principle can theoretically be further extended to remove contributions to the displacement in directions both perpendicular and opposite to the direction of propagation of the wave by slicing the 3rd order tensor in each of these planes. As such applying a filter in 3 directions, two perpendicular to the direction of propagation of the wave and one opposite, removes contributions in all direction with the exception of the direction of interest.

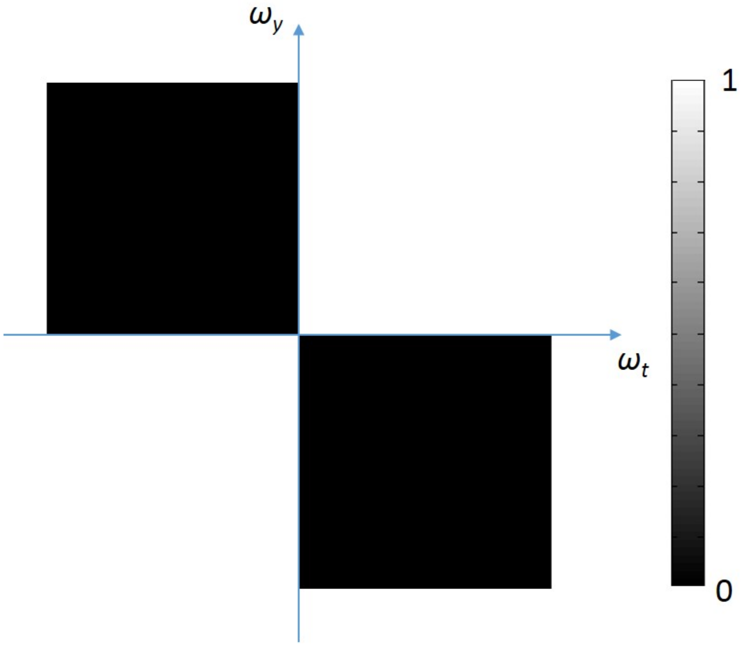

Figure V.1: The mask placed on the Fourier domain for the spatio-temporal directional filter.

The *Matlab* code used for this directional filter is:

```
%% cw_d - the Fourier transform of the directionally filtered wave
   images
%% wd - the directionally filtered wave images
%% w - the input wave image
function [cw_d wd] = directional_filter_down(w)

% find the size of w
[m n o] = size(w);

% create the mask to be applied to the spatio-temporal frequency
   domain
[x y] = meshgrid((m-1)/2:-1:-(m-1)/2,-(n-1)/2:1:(n-1)/2);
```

```
right = ones(m,n);
right(x(:,:) < 0) = 0;

top = ones(m,n);
top(y(:,:) < 0) = 0;

top_right = top.*right;

left = ones(m,n);
left(x(:,:) > 0) = 0;

bottom = ones(m,n);
bottom(y(:,:) > 0) = 0;

bottom_left = bottom.*left;

mask = top_right + bottom_left;

% create an array, z, of size matching w
wd = zeros(size(w));

% separates the matrix into n mxo matrices to perform the Fourier
   transform, applies the mask to the frequency domain and then
   inverse Fourier transforms to the time domain to obtain the
   directionally filtered wave images
for j = 1:n

    x(:,:) = w(:,j,:);
    f = fft2(x);
    f = fftshift(f);
    F = f.*mask;
    F = ifftshift(F);
    y = ifft2(F);
    wd(:,j,:) = y;
    wd = real(wd);
```

```
    clear f F y

end

% perform Fourier transform in the temporal direction to obtain the
   complex wave image
cw_d = fft(wd,[],3);

end
```

Cos-Squared Dependent Filter

The cos-squared dependent filter applies a mask to the frequency domain of the spatial wave images. The cos-squared filter aims to mask out negative frequencies in one direction so as to remove reflections. This is achieved through a $\cos^2$ term. Additionally the frequencies in the direction perpendicular to the transmitted waves are limited by the inclusion of a $\tan^{-1}$ term:

$$f(x,y) = \cos^2\left(\tan^{-1}\left(\frac{x}{y}\right)\right) \tag{V.3}$$

The resultant mask is shown in figure V.2 and an example of directionally filtered data using this filter is shown in figure V.3.

The *Matlab* code used for this directional filter is:

```
%% cw_d - the Fourier transform of the directionally filtered wave
   images
%% wd - the directionally filtered wave images
%% w - the input wave image
[cw_d wd] = cos_squared_filter_down(w)

% determine the size of the input tensor
[m n o] = size(w);
```

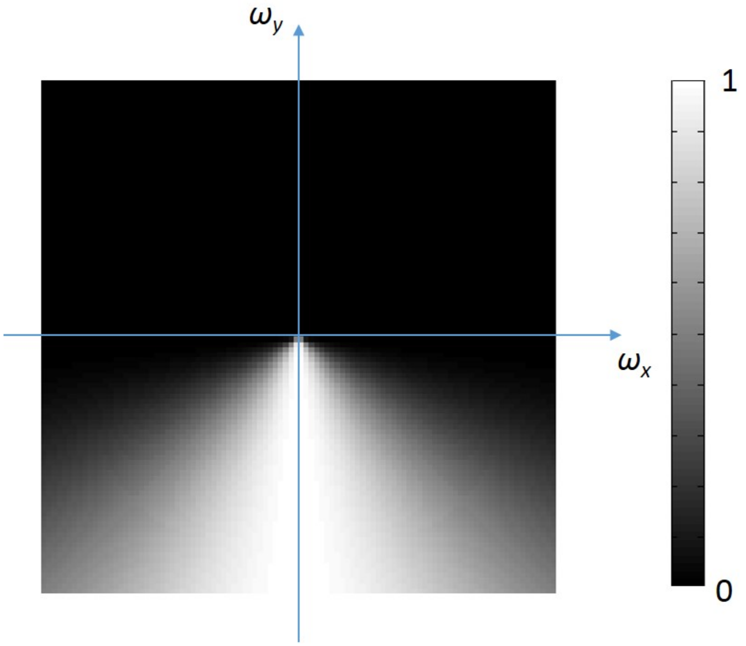

Figure V.2: The mask is placed on the 2-d Fourier domain of the spatial wave images.

```
% create the mask to be applied to the spatial frequency domain
[x y] = meshgrid((m-1)/2:-1:-(m-1)/2,-(n-1)/2:1:(n-1)/2);

h = ones(m,n);

h(y(:,:) < 0 ) = 0;

f(:,:) = (sin(atan(y./x))).^2;

cos_mask = f.*h;

% for loop that applies the filter to the fourier domain of the
    spatial
% image at each time point
for i=1:o

    x_spatial(:,:) = w(:,:,i);

    f_spatial = fftshift(fft2(x_spatial));
```

```
    f_spatial_masked = f_spatial.*cos_mask;

    x_spatial_filtered = ifft2(ifftshift(f_spatial_masked));

% remove NaN values
    real_x_spatial_filtered = real(x_spatial_filtered);

    imag_x_spatial_filtered = imag(x_spatial_filtered);

    real_x_spatial_filtered(isnan(real_x_spatial_filtered) == 0);
    imag_x_spatial_filtered(isnan(imag_x_spatial_filtered) == 0);

    new_x_spatial_filtered = real_x_spatial_filtered + i*
       imag_x_spatial_filtered;

    wd(:,:,i) = x_spatial_filtered;

end
%%

cw_d = fft(wd,[],3);
```

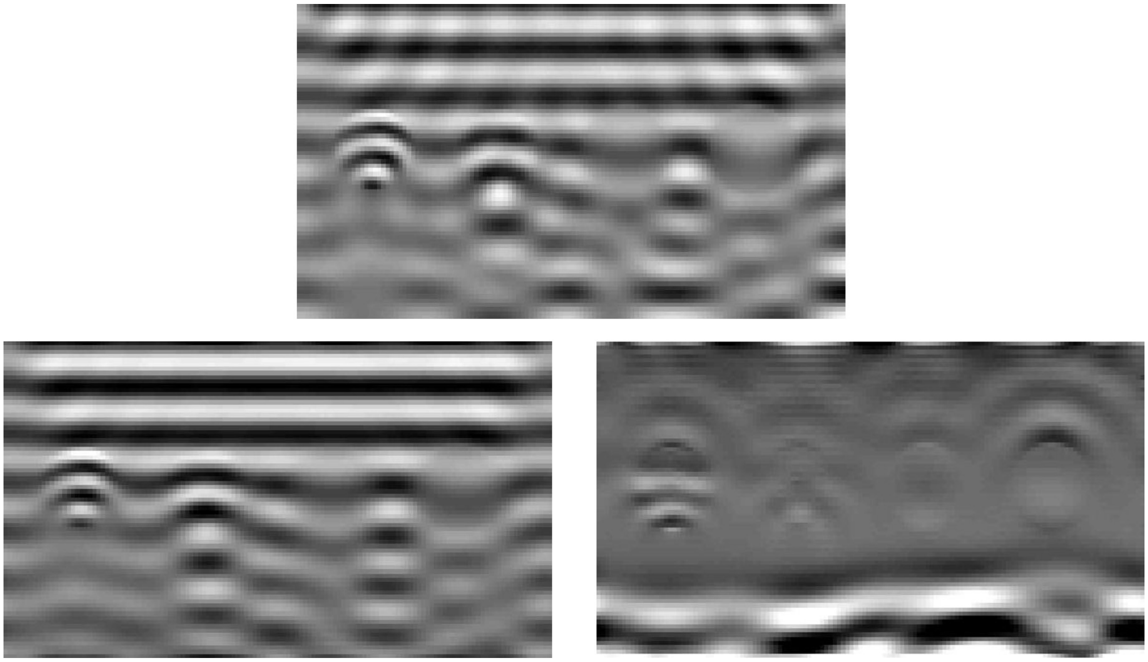

Figure V.3: Example of filtered data using the cos-squared dependent filter upon FEA modelled data. The geometry is that outlined in chapter 4. The top image is the unfiltered complex wave image. The bottom left is the complex wave image which has been filtered to remove waves travelling upwards, whilst the image in the bottom right is the complex wave image which has been filtered to remove waves travelling in the downwards direction. The waves reflected from both the top and bottom of the inserts are clear here as are the waves reflected of the bottom of the model.

Conference Proceedings

Hollis L, Thomas-Seale L, Kennedy P, Pankaj P, Roberts N, Hoskins PR. Computational Simulations of Magnetic Resonance Elastography to Investigate the Dependency of Directionally Filtered Stiffness Data on the Number of Measurements Obtained. *CIVIS Annual Scientific Meeting.* (Sept 2013, Edinburgh). Poster.

Hollis L, Thomas-Seale L, Conlisk N, Roberts N, Pankaj P, Hoskins PR. Development of Magnetic Resonance Elastography to Acquire Material Properties of Abdominal Aortic Aneurysms. *Scottish Cardiovascular Forum.* (February 2014, Aberdeen). Oral presentation.

Hollis L, Thomas-Seale L, Conlisk N, Roberts N, Pankaj P, Hoskins PR. Development of Magnetic Resonance Elastography to Improve Patient Specific Modelling of Abdominal Aortic Aneurysms. *BHF 4-year Cardiovascular Science Annual Meeting.* (April 2014, Manchester). Oral presentation.

Hollis L, Thomas-Seale L, Conlisk N, Roberts N, Pankaj P, Hoskins PR. Development of a Computational Simulation of Magnetic Resonance Elastography for Idealised Abdominal Aortic Aneurysms. *World Congress of Biomechanics.* (July 2014, Boston). Poster.

Hollis L, Thomas-Seale L, Conlisk N, Kennedy P, Barnhill E, Roberts N, Pankaj P, Hoskins PR. Comparison of Transient and Steady-State Simulations of Magnetic Resonance Elastography. *2nd National Conference on Patient Specific Modelling.* (May 2014, Edinburgh). Oral presentation.

Hollis L, Thomas-Seale L, Conlisk N, Barnhill E, Kennedy P, Pankaj P, Roberts N, Hoskins PR. Development of a Transient Simulation of Magnetic Resonance Elastography. *Annual Meeting of the British Chapter of ISMRM.* (September 2014, Edinburgh). Poster.

Hollis L, Roberts N, Pankaj P, PR Hoskins. Computational Modelling to Investigate the Potential Use of MR Elastography in Abdominal Aortic Aneurysms. *Joint BHF Centres of Research Excellence Imaging Symposium.*(June 2015, London.) Poster.

Hollis L, Conlisk N, Roberts N, Pankaj P, Hoskins PR. Comparison of 2-D and 3-D Direct Inversion Algorithms in MR Elastography for Different Geometrical Structures. *Congress of the International Society of Biomechanics.* (July 2015, Glasgow). Oral presentation.

Hollis L, Thomas-Seale L, Conlisk N, Roberts N, Pankaj P, Hoskins PR. The Impact of Loading and Boundary Conditions in Finite Element Analysis of MR Elastography. *Congress of the International Sociey of Biomechanics.* (July 2015, Glasgow). Oral presentation.

Hollis L, Conlisk N, Roberts N, Pankaj P, Hoskins PR. Computational Simulations of MR Elastography in Idealized Abdominal Aortic Aneurysm. *International Symposium on Computer Methods in Biomechanics and Biomechanical Engineering.* (September 2015, Montréal). Oral Presentation.

Publications

Hollis L, Thomas-Seale L, Conlisk N, Roberts N, Pankaj P, Hoskins PR. Investigation of Modelling Parameters for Finite Element Analysis of MR Elastography. *Computational Biomechanics for Medicine: Imaging, Modelling and Computing.* Springer-NY. *2016.*

Hollis L, Barnhill E, Conlisk N, Thomas-Seale L, Roberts N, Pankaj P, Hoskins PR. Finite Element Analysis to Compare the Accuracy of the Direct and MDEV Inversion Algorithms in MR Elastography. *IAENG International Journal of Computer Science. 2016.*

References

[1] N Townsend, J Williams, P Bhatnagar, K Wickramasinghe, and M Rayner. Cardiovascular Disease Statistics 2014. Technical report, British Heart Foundation, University of Oxford, 2014.

[2] JJ Earnshaw. Doubts and dilemmas over abdominal aortic aneurysm. *Brit J Surg*, 98(5):607–8, may 2011.

[3] JC McGregor, JG Pollock, and HC Anton. The value of ultrasonography in the diagnosis of abdominal aortic aneurysm. *Scot Med J*, 20(3):133–7, may 1975.

[4] B Sonesson, T Länne, F Hansen, and T Sandgren. Infrarenal aortic diameter in the healthy person. *Eur J Vascular Surg*, 8(1):89–95, jan 1994.

[5] GR Upchurch and TA Schaub. Abdominal aortic aneurysm. *Am Fam Physician*, 73(7):1198–204, apr 2006.

[6] TE Rasmussen and JW Hallett. Inflammatory Aortic Aneurysms A Clinical Review with New Perspectives. *Ann Surg*, 225(2):155–64, 1997.

[7] JS Lindholt and P Norman. Screening for abdominal aortic aneurysm reduces overall mortality in men. A meta-analysis of the mid- and long-term effects of screening for abdominal aortic aneurysms. *Eur J Vasc Endovasc*, 36(2):167–71, aug 2008.

[8] HA Fink, FA Lederle, CS Roth, CA Bowles, DB Nelson, and BA Haas. The accuracy of physical examination to detect abdominal aortic aneurysm. *Arch Intern Med*, 160, 2000.

[9] AD Jacob, PL Barkley, KC Broadbent, and TTT Huynh. Abdominal Aortic Aneurysm Screening. *Semin Roentgenol*, 50(2):118–126, apr 2015.

[10] K Singh, KH Bønaa, BK Jacobsen, L Bjørk, and S Solberg. Prevalence of and risk factors for abdominal aortic aneurysms in a population-based study: The Tromsø Study. *Am J Epidemiol*, 154(3):236–44, aug 2001.

[11] RAP Scott and NM Wilson. Influence of screening on the incidence of ruptured abdominal aortic aneurysm: 5 year results of a randomized controlled study. *Brit J Surg*, 82:1066–1070, 1995.

[12] HA Ashton, MJ Buxton, NE Day, LG Kim, TM Marteau, SG Thompson, NM Walker, and RAP Scott. The Multicentre Aneurysm Screening Study (MASS) into the effect of abdominal aortic aneurysm screening on mortality in men: a randomised controlled trial. *Lancet*, 360:1531–1539, 2002.

[13] PE Norman, K Jamrozik, MM Lawrence-Brown, MTQ Le, CA Spencer, RJ Tuohy, RW Parsons, and JA Dickinson. Population based randomised controlled trial on impact of screening on mortality from abdominal aortic aneurysm. *Brit Med J*, 329(7477):1259, nov 2004.

[14] JS Lindholt, S Juul, H Fasting, and EW Henneberg. Screening for abdominal aortic aneurysms: single centre randomised controlled trial. *Brit Med J*, 330(7494):750, apr 2005.

[15] AM Conway, AH Malkawi, RJ Hinchliffe, PJ Holt, S Murray, MM Thompson, and IM Loftus. First-year results of a national abdominal aortic aneurysm screening programme in a single centre. *Brit J Surg*, 99(1):73–7, jan 2012.

[16] R Søgaard, J Laustsen, and JS Lindholt. Cost effectiveness of abdominal aortic aneurysm screening and rescreening in men in a modern context: evaluation of a hypothetical cohort using a decision analytical model. *Brit Med J*, 345:4276, jan 2012.

[17] J Collin, J Walton, L Araujo, and D Lindsell. Oxford screening programme for abdominal aortic aneurysm in men aged 65 to 74 years. *Lancet*, 2(8611):613–615, 1988.

[18] AJ Lee, FG Fowkes, MN Carson, GC Leng, and PL Allan. Smoking, atherosclerosis and risk of abdominal aortic aneurysm. *Eur Heart J*, 18(4):671–6, apr 1997.

[19] STR MacSweeney, M Ellis, PC Worrell, RM Greenhalgh, and JT Powell. Smoking and growth rate of small abdominal aortic aneurysms. *Lancet*, 344(8923):651–2, 1994.

[20] AR Brady, SG Thompson, FGR Fowkes, RM Greenhalgh, and JT Powell. Abdominal aortic aneurysm expansion: risk factors and time intervals for surveillance. *Circulation*, 110(1):16–21, jul 2004.

[21] KA Vardulaki, NM Walker, NE Day, SW Duffy, HA Ashton, and RA Scott. Quantifying the risks of hypertension, age, sex and smoking in patients with abdominal aortic aneurysm. *Brit J Surg*, 87(2):195–200, feb 2000.

[22] TB Wilmink, CR Quick, and NE Day. The association between cigarette smoking and abdominal aortic aneurysms. *J Vasc Surg*, 30(6):1099–105, dec 1999.

[23] ALB Jacob-Ferreira, ACT Palei, SB Cau, H Moreno, MLL Martinez, TC Izidoro-Toledo, RF Gerlach, and JE Tanus-Santos. Evidence for the involvement of matrix metalloproteinases in the cardiovascular effects produced by nicotine. *Eur J Pharmacol*, 627(1-3):216–22, feb 2010.

[24] ZZ Li and QY Dai. Pathogenesis of Abdominal Aortic Aneurysms: Role of Nicotine and Nicotinic Acetylcholine Receptors. *Mediat Inflamm*, 2012:1–8, jan 2012.

[25] HJC Pleumeekers, AW Hoes, E Van Der Does, H Van Urk, A Hofman, PTVM De Jong, and DE Grobbee. Aneurysms of the Abdominal Aorta in Older Adults The Rotterdam Study. *Am J Epidemiol*, 142(12):1291–9, 1995.

[26] RA Scott, HA Ashton, and DN Kay. Abdominal aortic aneurysm in 4237 screened patients: prevalence, development and management over 6 years. *Brit J Surg*, 78(9):1122–5, sep 1991.

[27] HG Alcorn, SK Woldson, K Sutton-Tyrell, LH Kuller, and D O'Leary. Risk factors for abdominal aortic aneurysms in older adults enrolled in the cardiovascular health study. *Arterioscl Throm Vas*, 16(8):963–970, 1996.

[28] JE Estes. Abdominal aortic aneurysm: a study of one hundred and two cases. *Circulation*, 2(2):258–264, aug 1950.

[29] J Hager, T Länne, P Carlsson, and F Lundgren. Lower prevalence than expected when screening 70-year-old men for abdominal aortic aneurysm. *Eur J Vasc Endovasc Surg*, 46(4):453–9, oct 2013.

[30] D Robinson, B Mees, H Verhagen, and J Chuen. Aortic aneurysms - screening, surveillance and survival. *Austral Fam Physician*, 42(6):364–369, 2013.

[31] DJ Katz, JC Stanley, and GB Zelenock. Gender differences in abdominal aortic aneurysm prevalence, treatment, and outcome. *J Vasc Surg*, 25(3):561–8, mar 1997.

[32] NL Harthun. Current issues in the treatment of women with abdominal aortic aneurysm. *Gend Med*, 5(1):36–43, 2008.

[33] The United Kingdom Small Aneurysm Trial. Long-term outcomes of immediate repair compared with surveillance of small abdominal aortic aneurysms. *New Engl J Med*, 346(19):1445–52, may 2002.

[34] RC Lo, RP Bensley, AD Hamdan, M Wyers, JE Adams, and ML Schermerhorn. Gender differences in abdominal aortic aneurysm presentation, repair, and mortality in the Vascular Study Group of New England. *J Vasc Surg*, 57(5):1261–8, 1268.e1–5, may 2013.

[35] JT McPhee, JS Hill, and MH Eslami. The impact of gender on presentation, therapy, and mortality of abdominal aortic aneurysm in the United States, 2001-2004. *J Vasc Surg*, 45(5):891–9, may 2007.

[36] M Mehta, WJ Byrne, H Robinson, SP Roddy, PSK Paty, PB Kreienberg, P Feustel, and RC Darling. Women derive less benefit from elective endovascular aneurysm repair than men. *J Vasc Surg*, 55(4):906–13, apr 2012.

[37] L Mureebe, N Egorova, JF McKinsey, and KC Kent. Gender trends in the repair of ruptured abdominal aortic aneurysms and outcomes. *J Vasc Surg*, 51(4 Suppl):9S–13S, apr 2010.

[38] K Johansen and T Koepsell. Familial tendency for abdominal aortic aneurysms. *JAMA-J Am Med Assoc*, 256(14):1934–6, 1986.

[39] H Kuivaniemi, H Shibamura, C Arthur, R Berguer, CW Cole, T Juvonen, RA Kline, R Limet, G Mackean, O Norrgård, G Pals, JT Powell, P Rainio, N Sakalihasan, C van Vlijmen-van Keulen, A Verloes, and G Tromp. Familial abdominal aortic aneurysms: collection of 233 multiplex families. *J Vasc Surg*, 37(2):340–5, feb 2003.

[40] RM Sandford, MJ Bown, NJ London, and RD Sayers. The genetic basis of abdominal aortic aneurysms: a review. *Eur J Vasc Endovasc Surg*, 33(4):381–90, apr 2007.

[41] IM Nordon, RJ Hinchliffe, IM Loftus, and MM Thompson. Pathophysiology and epidemiology of abdominal aortic aneurysms. *Nat Rev Cardiol*, 8(2):92–102, feb 2011.

[42] DJ Barker. The fetal origins of coronary heart disease. *Brit Med J*, 422:78–82, jul 1997.

[43] JT Powell. Familial clustering of abdominal aortic aneurysm–smoke signals, but no culprit genes. *Brit J Surg*, 90(10):1173–4, oct 2003.

[44] DA Vorp. Potential influence of intraluminal thrombus on abdominal aortic aneurysm as assessed by a new non-invasive method. *Cardiovasc Surg*, 4(6):732–739, dec 1996.

[45] TC Gasser, RW Ogden, and GA Holzapfel. Hyperelastic modelling of arterial layers with distributed collagen fibre orientations. *J Roy Soc Interface*, 3(6):15–35, feb 2006.

[46] N Sakalihasan, R Limet, and OD Defawe. Abdominal aortic aneurysm. *Lancet*, 365(9470):1577–89, 2005.

[47] LE Niklason. Functional arteries grown in vitro. *Science*, 284(5413):489–493, apr 1999.

[48] AE Koch and GK Haines. Human abdominal aortic aneurysms. Immunophenotypic analysis suggesting an immune-mediated response. *Am J Pathol*, 137(5):1199–1213, 1990.

[49] J Golledge and PE Norman. Atherosclerosis and abdominal aortic aneurysm: cause, response, or common risk factors? *Arterioscl Throm Vas*, 30(6):1075–7, jun 2010.

[50] F Helderman, IJ Manoch, M Breeuwer, U Kose, O Schouten, MRM van Sambeek, D Poldermans, PTM Pattynama, W Wisselink, AFW van der Steen, and R Krams. A numerical model to predict abdominal aortic aneurysm expansion based on local wall stress and stiffness. *Med Biol Eng Comput*, 46(11):1121–7, nov 2008.

[51] ML McCormick, D Gavrila, and NL Weintraub. Role of oxidative stress in the pathogenesis of abdominal aortic aneurysms. *Arterioscl Throm Vas*, 27(3):461–9, mar 2007.

[52] DC Guo, CL Papke, R He, and DM Milewicz. Pathogenesis of thoracic and abdominal aortic aneurysms. *Ann NY Acad Sci*, 1085:339–52, nov 2006.

[53] SS Hans, O Jareunpoon, M Balasubramaniam, and GB Zelenock. Size and location of thrombus in intact and ruptured abdominal aortic aneurysms. *J Vasc Surg*, 41(4):584–8, apr 2005.

[54] AV Salsac, SR Sparks, and JC Lasheras. Hemodynamic changes occurring during the progressive enlargement of abdominal aortic aneurysms. *Ann Vasc Surg*, 18(1):14–21, jan 2004.

[55] J Biasetti, F Hussain, and TC Gasser. Blood flow and coherent vortices in the normal and aneurysmatic aortas: a fluid dynamical approach to intra-luminal thrombus formation. *J Roy Soc Interface*, 8(63):1449–61, oct 2011.

[56] JS Wilson, L Virag, P Di Achille, I Karsaj, and JD Humphrey. Biochemomechanics of intraluminal thrombus in abdominal aortic aneurysms. *J Biomed Eng*, 135(2):021011, feb 2013.

[57] TJ Corbett, BJ Doyle, A Callanan, MT Walsh, and TM McGloughlin. Engineering silicone rubbers for in vitro studies: creating AAA models and ILT analogues with physiological properties. *J Biomed Eng*, 132(1):1–25, 2010.

[58] DHJ Wang, MS Makaroun, MW Webster, and DA Vorp. Mechanical properties and microstructure of intraluminal thrombus from abdominal aortic aneurysm. *J Biomed Eng*, 123(6):536, jun 2001.

[59] M Folkesson, A Silveira, P Eriksson, and J Swedenborg. Protease activity in the multi-layered intra-luminal thrombus of abdominal aortic aneurysms. *Atherosclerosis*, 218(2):294–9, oct 2011.

[60] PN Watton, NA Hill, and M Heil. A mathematical model for the growth of the abdominal aortic aneurysm. *Biomech Model Mechan*, 3(2):98–113, nov 2004.

[61] PN Watton and NA Hill. Evolving mechanical properties of a model of abdominal aortic aneurysm. *Biomech Model Mechan*, 8(1):25–42, 2009.

[62] JD Humphrey and GA Holzapfel. Mechanics, mechanobiology, and modeling of human abdominal aorta and aneurysms. *J Biomech*, 45(5):805–814, mar 2012.

[63] C Dubost, M Allary, and N Oeconomos. Resection of an aneurysm of the abdominal aorta: reestablishment of the continuity by a preserved human arterial graft, with result after five months. *Arch Surg*, (1):2–5, 1952.

[64] JC Parodi, JC Palmaz, and HD Barone. Transfemoral intraluminal graft implantation for abdominal aortic aneurysms. *Ann Vasc Surg*, 5(6):491–499, oct 1991.

[65] A Dua, SR Kuy, CJ Lee, GR Upchurch, and SS Desai. Epidemiology of aortic aneurysm repair in the United States from 2000 to 2010. *J Vasc Surg*, 59(6):1512–7, jun 2014.

[66] JE Tarride, G Blackhouse, G De Rose, T Novick, JM Bowen, R Hopkins, D O'Reilly, and R Goeree. Cost-effectiveness analysis of elective endovascular repair compared with open surgical repair of abdominal aortic aneurysms for patients at a high surgical risk: A 1-year patient-level analysis conducted in Ontario, Canada. *J Vasc Surg*, 48(4):779–87, oct 2008.

[67] SB White and SW Stavropoulos. Management of endoleaks following endovascular aneurysm repair. *Semin Intervent Rad*, 26(1):33–8, mar 2009.

[68] LJ Leurs, J Kievit, PC Dagnelie, PJ Nelemans, and J Buth. Influence of infrarenal neck length on outcome of endovascular abdominal aortic aneurysm repair. *J Endovasc Ther*, 13(5):640–8, oct 2006.

[69] RM Greenhalgh and LC Brown. Endovascular versus open repair of abdominal aortic aneurysm. *New Engl J Med*, 362:1863–1871, 2010.

[70] R Paravastu, SCV Jayarajasingam, R Cottam, SJ Palfreyman, JA Michaels, and SM Thomas. Endovascular repair of abdominal aortic aneurysm. In Steven M Thomas, editor, *Cochrane Database Syst Rev*, number 1. John Wiley & Sons, Ltd, Chichester, UK, jan 2014.

[71] L Mureebe, N Egorova, JK Giacovelli, A Gelijns, KC Kent, and JF McKinsey. National trends in the repair of ruptured abdominal aortic aneurysms. *J Vasc Surg*, 48(5):1101–7, nov 2008.

[72] R Moore, M Nutley, CS Cina, M Motamedi, P Faris, and W Abuznadah. Improved survival after introduction of an emergency endovascular therapy protocol for ruptured abdominal aortic aneurysms. *J Vasc Surg*, 45(3):443–50, mar 2007.

[73] AD Dueck, DS Kucey, KW Johnston, D Alter, and A Laupacis. Survival after ruptured abdominal aortic aneurysm: effect of patient, surgeon, and hospital factors. *J Vasc Surg*, 39(6):1253–60, jun 2004.

[74] B Sonesson, T Sandgren, and T Länne. Abdominal aortic aneurysm wall mechanics and their relation to risk of rupture. *Eur J Vasc Endovasc Surg*, 18(6):487–493, dec 1999.

[75] The U.K. small aneurysm trial: Design, methods and progress. *Eur J Vasc Endovasc Surg*, 9(1):42–48, jan 1995.

[76] RC Darling, CR Messina, DC Brewster, and LW Ottinger. Autopsy study of unoperated abdominal aortic aneurysms. The case for early resection. *Circulation*, 56(3 Suppl):161–4, sep 1977.

[77] J Stenbaek, B Kalin, and J Swedenborg. Growth of thrombus may be a better predictor of rupture than diameter in patients with abdominal aortic aneurysms. *Eur J Vasc Endovasc Surg*, 20(5):466–9, nov 2000.

[78] KA Vardulaki, TC Prevost, NM Walker, NE Day, AB Wilmink, CR Quick, HA Ashton, and RA Scott. Growth rates and risk of rupture of abdominal aortic aneurysms. *Brit J Surg*, 85(12):1674–1680, 1998.

[79] DC Brewster, JL Cronenwett, JW Hallett, KW Johnston, WC Krupski, and JS Matsumura. Guidelines for the treatment of abdominal aortic aneurysms. Report of a subcommittee of the Joint Council of the American Association for Vascular Surgery and Society for Vascular Surgery. *J Vasc Surg*, 37(5):1106–17, may 2003.

[80] JMJ Richards, SI Semple, TJ MacGillivray, C Gray, JP Langrish, M Williams, M Dweck, W Wallace, G McKillop, RT Chalmers, OJ Garden, and DE Newby.

Abdominal aortic aneurysm growth predicted by uptake of ultrasmall superparamagnetic particles of iron oxide: a pilot study. *Circ Cardiovasc Imaging*, 4(3):274–81, may 2011.

[81] S Svensjö, M Björck, and A Wanhainen. Update on screening for abdominal aortic aneurysm: A topical review. *Eur J Vasc Endovasc Surg*, 48(6):659–667, 2014.

[82] PA Kelly. *An Introduction to Solid Mechanics.* University of Auckland, 2013.

[83] TE Oliphant, A Manduca, RL Ehman, and JF Greenleaf. Complex-valued stiffness reconstruction for magnetic resonance elastography by algebraic inversion of the differential equation. *Magnet Reson Med*, 45(2):299–310, feb 2001.

[84] DA McDonald. *Blood Flow in Arteries.* Taylor and Francis Group, London, 6th editio edition, 1974.

[85] HA Barnes, JF Hutton, and K Walters. *An introduction to rheology.* 1989.

[86] D Roylance. *Engineering viscoelasticity: course notes.* Springer US, Boston, MA, 2014.

[87] J Vincent. *Structural Biomaterials.* Princeton University Press, 3rd edition, 2012.

[88] D Klatt, U Hamhaber, P Asbach, J Braun, and I Sack. Noninvasive assessment of the rheological behavior of human organs using multifrequency MR elastography: a study of brain and liver viscoelasticity. *Phys Med Biol*, 52(24):7281–94, dec 2007.

[89] V Thomée. From finite differences to finite elements. *J Comput Appl Math*, 128(1-2):1–54, mar 2001.

[90] Dassault Systèmes Simulia Corp. ABAQUS Documentation. 2011.

[91] TJR Hughes, KS Pister, and RL Taylor. Implicit-explicit finite elements in nonlinear transient analysis. *Comput Method Appl M*, 17(18):159–182, 1979.

[92] KJ Bathe. *Finite Element Procedures.* Prentice Hall, New Jersey, 1996.

[93] SR Wu and W Qiu. Nonlinear transient dynamic analysis by explicit finite element with iterative consistent mass matrix. *Commun Numer Meth En*, 25(3):201–217, mar 2009.

[94] CV Nielsen, W Zhang, LM Alves, N Bay, and PAF Martins. *Modeling of Thermo-Electro-Mechanical Manufacturing Processes*. SpringerBriefs in Applied Sciences and Technology. Springer London, London, 2013.

[95] A Sirbu and L Farkas. Programming the transient explicit finite analysis with matlab. *UPB Sci Bull*, 75, 2013.

[96] Lenaerts and G van Lenthe. Multi-level patient-specific modelling of the proximal femur. A promising tool to quantify the effect of osteoporosis treatment. *Philos T Roy Soc A*, 367:2079–93, 2009.

[97] JH Keyak. Improved prediction of proximal femoral fracture load using nonlinear finite element models. *Med Eng Phys*, 23:165–173, 2001.

[98] HJ Kim, IE Vignon-Clementel, JS Coogan, CA Figueroa, KE Jansen, and CA Taylor. Patient-specific modeling of blood flow and pressure in human coronary arteries. *Ann Biomed Eng*, 38(10):3195–3209, 2010.

[99] R Werner, J Ehrhardt, R Schmidt, and H Handels. Patient-specific finite element modeling of respiratory lung motion using 4D CT image data. *Med Phys*, 36(5):1500–11, 2009.

[100] http://www.vph-institute.org/. 2015.

[101] BJ Doyle, P Coyle, EG Kavanagh, PA Grace, and TM Mcgloughlin. A finite element analysis rupture index (FEARI) assessment of electively repaired and symptomatic/ruptured abdominal aortic aneurysms. In *Proceedings of the World Congress of Biomechanics 2010*, volume 31, pages 883–886, 2010.

[102] DA Vorp and JP Vande Geest. Biomechanical determinants of abdominal aortic aneurysm rupture. *Arterioscl Throm Vas*, 25(8):1558–66, aug 2005.

[103] M Breeuwer, U Götte, R Hoogeveen, BJBM Wolters, S de Putter, HVD Bosch, J Buth, JM Rouet, and F Laffargue. Assessment of the rupture risk of abdominal aortic aneurysms by patient-specific hemodynamic modeling—initial results. *Int J Comput Assist Radiol Surg*, 1268:1090–1095, jun 2004.

[104] AK Venkatasubramaniam, MJ Fagan, T Mehta, KJ Mylankal, B Ray, G Kuhan, IC Chetter, and PT McCollum. A comparative study of aortic wall stress using

finite element analysis for ruptured and non-ruptured abdominal aortic aneurysms. *Eur J Vasc Endovasc Surg*, 28(2):168–76, aug 2004.

[105] ML Raghavan, DA Vorp, MP Federle, MS Makaroun, and MW Webster. Wall stress distribution on three-dimensionally reconstructed models of human abdominal aortic aneurysm. *J Vasc Surg*, 31(4):760–9, apr 2000.

[106] MF Fillinger, SP Marra, ML Raghavan, and FE Kennedy. Prediction of rupture risk in abdominal aortic aneurysm during observation: wall stress versus diameter. *J Vasc Surg*, 37(4):724–32, apr 2003.

[107] ATM Phillips. The femur as a musculo-skeletal construct: A free boundary condition modelling approach. *Med Eng Phys*, 31:673–680, 2009.

[108] MD Gasbarro, K Shimada, and ES Di Martino. Explicit finite element method for in-vivo mechanics of abdominal aortic aneurysm. *Eur J Comput Mech*, 16:337–363, 2007.

[109] MW Gee, C Reeps, HH Eckstein, and WA Wall. Prestressing in finite deformation abdominal aortic aneurysm simulation. *J Biomech*, 42:1732–1739, 2009.

[110] JH Leung, AR Wright, N Cheshire, J Crane, SA Thom, AD Hughes, and Y Xu. Fluid structure interaction of patient specific abdominal aortic aneurysms: a comparison with solid stress models. *Biomed Eng*, 5:33, 2006.

[111] K H Fraser, M-X Li, W T Lee, W J Easson, and P R Hoskins. Fluid-structure interaction in axially symmetric models of abdominal aortic aneurysms. *Proceedings of the Institution of Mechanical Engineers. Part H, Journal of engineering in medicine*, 223:195–209, 2009.

[112] CL Siegel, RH Cohan, M Korobkin, MB Alpern, DL Courneya, and RA Leder. Abdominal aortic aneurysm morphology: CT features in patients with ruptured and nonruptured aneurysms. *Am J Roentgenol*, 163(5):1123–1129, 1994.

[113] SP Marra, CP Daghlian, MF Fillinger, and FE Kennedy. Elemental composition, morphology and mechanical properties of calcified deposits obtained from abdominal aortic aneurysms. *Acta Biomater*, 2(5):515–20, sep 2006.

[114] L Speelman, A Bohra, EH Bosboom, GWH Schurink, FN van de Vosse, MS Makaorun, and DA Vorp. Effects of wall calcifications in patient-specific wall stress analyses of abdominal aortic aneurysms. *J Biomech Eng*, 129(1):105–9, feb 2007.

[115] A Maier, MW Gee, C Reeps, HH Eckstein, and WA Wall. Impact of calcifications on patient-specific wall stress analysis of abdominal aortic aneurysms. *Biomech Model Mechan*, 9(5):511–21, oct 2010.

[116] F Inzoli, F Boschetti, M Zappa, T Longo, and R Fumero. Biomechanical factors in abdominal aortic aneurysm rupture. *Eur J Vasc Endovasc*, 7(6):667–74, nov 1993.

[117] BJ Doyle, A Callanan, and TM McGloughlin. A comparison of modelling techniques for computing wall stress in abdominal aortic aneurysms. *Biomed Eng*, 6:38, jan 2007.

[118] AR Sparks, PL Johnson, and MC Meyer. Imaging of abdominal aortic aneurysms. *Am Fam Physician*, 65(8):1565–70, apr 2002.

[119] GG Hartnell. Imaging of aortic aneurysms and dissection: CT and MRI. *J Thorac Imag*, 16(1):35–46, jan 2001.

[120] ML Raghavan, J Kratzberg, EM Castro de Tolosa, MM Hanaoka, P Walker, and ES da Silva. Regional distribution of wall thickness and failure properties of human abdominal aortic aneurysm. *J Biomech*, 39(16):3010–6, jan 2006.

[121] G Martufi, ES Di Martino, CH Amon, SC Muluk, and EA Finol. Three-dimensional geometrical characterization of abdominal aortic aneurysms: image-based wall thickness distribution. *J Biomech Eng*, 131(June 2009):061015, 2009.

[122] TC Gasser, G Martufi, M Auer, M Folkesson, and J Swedenborg. Micromechanical characterization of intra-luminal thrombus tissue from abdominal aortic aneurysms. *Ann Biomed Eng*, 38(2):371–9, feb 2010.

[123] D Bluestein, K Dumont, M De Beule, J Ricotta, P Impellizzeri, B Verhegghe, and P Verdonck. Intraluminal thrombus and risk of rupture in patient specific abdominal aortic aneurysm – FSI modelling. *Comput Method Biomech*, 12(1):73–81, feb 2009.

[124] DA Vorp. Biomechanics of abdominal aortic aneurysm. *J Biomech*, 40(9):1887–1902, jan 2007.

[125] DA Vorp, PC Lee, DH Wang, MS Makaroun, EM Nemoto, S Ogawa, and MW Webster. Association of intraluminal thrombus in abdominal aortic aneurysm with local hypoxia and wall weakening. *J Vasc Surg*, 34(2):291–9, aug 2001.

[126] M Kazi, J Thyberg, P Religa, J Roy, P Eriksson, U Hedin, and J Swedenborg. Influence of intraluminal thrombus on structural and cellular composition of abdominal aortic aneurysm wall. *J Vasc Surg*, 38(6):1283–1292, dec 2003.

[127] S. Polzer, TC Gasser, J Swedenborg, and J Bursa. The impact of intraluminal thrombus failure on the mechanical stress in the wall of abdominal aortic aneurysms. *Eur J Vasc Endovasc Surg*, 41(4):467–473, 2011.

[128] ML Raghavan and DA Vorp. Toward a biomechanical tool to evaluate rupture potential of abdominal aortic aneurysm: Identification of a finite strain constitutive model and evaluation of its applicability. *J Biomech*, 33:475–482, 2000.

[129] David H.J. Wang, Michel S. Makaroun, Marshall W. Webster, and David A. Vorp. Effect of intraluminal thrombus on wall stress in patient-specific models of abdominal aortic aneurysm. *Journal of vascular surgery: official publication, the Society for Vascular Surgery [and] International Society for Cardiovascular Surgery, North American Chapter*, 36(3):598–604, sep 2002.

[130] David A. Vorp, M. L. Raghaven, Satish C. Muluk, Michel S. Makaroun, David L. Steed, Ron Shapiro, and Marshall W. Webster. Wall Strength and Stiffness of Aneurysmal and Nonaneurysmal Abdominal Aorta. *Annals of the New York Academy of Sciences*, 800(1 The Abdominal):274–276, nov 1996.

[131] WR Mower, WJ Quiñones, and SS Gambhir. Effect of intraluminal thrombus on abdominal aortic aneurysm wall stress. *J Vasc Surg*, 26(4):602–8, oct 1997.

[132] BJ Doyle, AN Callanan, PA Grace, and EG Kavanagh. On the influence of patient-specific material properties in computational simulations: A case study of a large ruptured abdominal aortic aneurysm. *Int J Numer Method Biomed Eng*, 29(October 2012):150–164, 2012.

[133] JP Vande Geest, DHJ Wang, SR Wisniewski, MS Makaroun, and DA Vorp. Towards a noninvasive method for determination of patient-specific wall strength distribution in abdominal aortic aneurysms. *Ann Biomed Eng*, 34(7):1098–1106, 2006.

[134] A Maier, MW Gee, C Reeps, J Pongratz, HH Eckstein, and WA Wall. A comparison of diameter, wall stress, and rupture potential index for abdominal aortic aneurysm rupture risk prediction. *Ann Biomed Eng*, 38(10):3124–3134, 2010.

[135] PC Lauterbur. Image formation by induced local interaction: examples employing nuclear magnetic resonance. *Nature*, 242(March 16):190–191, 1973.

[136] FW Smith, JM Hutchison, JR Mallard, G Johnson, TW Redpath, RD Selbie, A Reid, and CC Smith. Oesophageal carcinoma demonstrated by whole-body nuclear magnetic resonance imaging. *Brit Med J*, 282(February):510–512, 1981.

[137] DW McRobbie, EA Moore, MJ Graves, and MR Prince. *MRI from Picture to Proton*. Wiley-Blackwell, 4th editio edition, 2002.

[138] C Ozturk, JA Derbyshire, and ER McVeigh. Estimating Motion From MRI Data. *P IEEE*, 9(10):1627–1648, oct 2003.

[139] D Moratal, A Vallés-Luch, L Martí-Bonmatí, and M Brummer. k-Space tutorial: an MRI educational tool for a better understanding of k-space. *Biomed Imag Interv J*, 4(1):e15, jan 2008.

[140] R Muthupillai, DJ Lomas, PJ Rossman, JF Greenleaf, A Manduca, and RL Ehman. Magnetic resonance elastography by direct visualization of propagating acoustic strain waves. *Science*, 269(5232):1854–7, sep 1995.

[141] R Muthupillai, PJ Rossman, DJ Lomas, JF Greenleaf, SJ Riederer, and RL Ehman. Magnetic resonance imaging of transverse acoustic strain waves. *Magnet Reson Med*, 36:266–274, 1996.

[142] PR Moran. A flow velocity zeugmatographic interlace for NMR imaging in humans. *Magn Reson Imaging*, 1982.

[143] M Doyley and J Weaver. Magnetic Resonance Elastrography: Experimental Validation and Performance Optimazation. In *Alternative Breast Imaging: Four Model Based Approaches*. Springer Science and Business Media, 2005.

[144] H Wang, JB Weaver, II Perreard, MM Doyley, and KD Paulsen. A three-dimensional quality-guided phase unwrapping method for MR elastography. *Phys Med Biol*, 56(13):3935–52, jul 2011.

[145] E Barnhill, P Kennedy, CL Johnson, M Mada, and N Roberts. Real-time 4D phase unwrapping applied to magnetic resonance elastography. *Magnet Reson Med*, 73(6):2321–31, 2014.

[146] YK Mariappan, KJ Glaser, and RL Ehman. Magnetic resonance elastography: a review. *Clin Anat*, 23(5):497–511, 2010.

[147] EE Van Houten, KD Paulsen, MI Miga, FE Kennedy, and JB Weaver. An overlapping subzone technique for MR-based elastic property reconstruction. *Magnet Reson Med*, 42(4):779–86, oct 1999.

[148] JB Weaver, EEW Van Houten, MI Miga, FE Kennedy, and KD Paulsen. Magnetic resonance elastography using 3D gradient echo measurements of steady-state motion. *Med Phys*, 28(8):1620, 2001.

[149] H Knutsson, CF Westin, and G Granlund. Local multiscale frequency and bandwidth estimation. In *Proceedings of 1st International Conference on Image Processing*, volume 1, pages 36–40. IEEE Comput. Soc. Press, 1994.

[150] A Manduca, R Muthupillai, PJ Rossman, JF Greenleaf, and RL Ehman. Local wavelength estimation for magnetic resonance elastography. In *Proceedings of 3rd IEEE International Conference on Image Processing*, volume 3, pages 527–530. IEEE, 1996.

[151] DA Woodrum, J Herrmann, A Lerman, AJ Romano, LO Lerman, and RL Ehman. Phase-contrast MRI-based elastography technique detects early hypertensive changes in ex vivo porcine aortic wall. *J Magn Reson Im*, 29(3):583–7, mar 2009.

[152] BN Li, CK Chui, SH Ong, T Numano, T Washio, K Homma, S Chang, S Venkatesh, and E Kobayashi. Modeling shear modulus distribution in magnetic resonance elastography with piecewise constant level sets. *Magn Reson Imaging*, 30(3):390–401, apr 2012.

[153] A Manduca, TE Oliphant, MA Dresner, JL Mahowald, SA Kruse, E Amromin, JP Felmlee, JF Greenleaf, and RL Ehman. Magnetic resonance elastography: non-invasive mapping of tissue elasticity. *Med Image Anal*, 5(4):237–54, dec 2001.

[154] B Banerjee, TF Walsh, W Aquino, and M Bonnet. Large scale parameter estimation problems in frequency-domain elastodynamics using an error in constitutive equation functional. *Comput Method Biomech*, 253:60–72, 2013.

[155] F Kallel and M Bertrand. Tissue elasticity reconstruction using linear perturbation method. *IEEE T Med Imaging*, 15(3):299–313, 1996.

[156] S Papazoglou, U Hamhaber, J Braun, and I Sack. Algebraic Helmholtz inversion in planar magnetic resonance elastography. *Phys Med Biol*, 53(12):3147–58, jun 2008.

[157] Stacie I Ringleb, Qingshan Chen, David S Lake, Armando Manduca, Richard L Ehman, and Kai-Nan An. Quantitative shear wave magnetic resonance elastography: comparison to a dynamic shear material test. *Magnetic resonance in medicine : official journal of the Society of Magnetic Resonance in Medicine / Society of Magnetic Resonance in Medicine*, 53(5):1197–201, may 2005.

[158] E Barnhill, P Kennedy, S Hammer, EJR van Beek, C Brown, and NR Roberts. Statistical mapping of the effect of knee extension on thigh muscle viscoelastic properties using magnetic resonance elastography. *Physiol Meas*, 34(12):1675–98, dec 2013.

[159] OI Kwon, C Park, HS Nam, EJ Woo, JK Seo, KJ Glaser, A Manduca, and RL Ehman. Shear modulus decomposition algorithm in magnetic resonance elastography. *IEEE T Med Imaging*, 28(10):1526–33, oct 2009.

[160] MC Murphy, J Huston, ClR Jack, KJ Glaser, A Manduca, JP Felmlee, and RL Ehman. Decreased brain stiffness in Alzheimer's disease determined by magnetic resonance elastography. *J Magn Reson Im*, 34:494–498, 2011.

[161] J Wuerfel, F Paul, B Beierbach, U Hamhaber, D Klatt, S Papazoglou, F Zipp, P Martus, J Braun, and I Sack. MR-elastography reveals degradation of tissue integrity in multiple sclerosis. *Neuroimage*, 49(3):2520–2525, 2010.

[162] SA Kruse, GH Rose, KJ Glaser, A Manduca, JP Felmlee, CR Jack, and Richard L. Ehman. Magnetic resonance elastography of the brain. *Neuroimage*, 39:231–237,

2008.

[163] EE Drakonaki, GM Allen, and DJ Wilson. Ultrasound elastography for musculoskeletal applications. *Brit J Radiol*, 85(November):1435–1445, 2012.

[164] CL Johnson, JL Holtrop, MDJ McGarry, JB Weaver, KD Paulsen, JG Georgiadis, and BP Sutton. 3D multislab, multishot acquisition for fast, whole-brain MR elastography with high signal-to-noise efficiency. *Magnet Reson Med*, 485(December 2013):477–485, dec 2013.

[165] J Guo, S Hirsch, A Fehlner, S Papazoglou, M Scheel, J Braun, and I Sack. Towards an elastographic atlas of brain anatomy. *PloS One*, 8(8):e71807, jan 2013.

[166] O Rouvière, M Yin, MA Dresner, PJ Rossman, LJ Burgart, JL Fidler, and RL Ehman. MR elastography of the liver: preliminary results. *Radiology*, 240(2):440–448, 2006.

[167] JA Talwalkar, M Yin, JL Fidler, SO Sanderson, PS Kamath, and RL Ehman. Magnetic resonance imaging of hepatic fibrosis: Emerging clinical applications. *Hepatology*, 47:332–342, 2008.

[168] L Huwart, C Sempoux, E Vicaut, N Salameh, L Annet, E Danse, F Peeters, LC ter Beek, J Rahier, R Sinkus, Y Horsmans, and BE Van Beers. Magnetic resonance elastography for the noninvasive staging of liver fibrosis. *Gastroenterology*, 135(1):32–40, jul 2008.

[169] J Rump, D Klatt, J Braun, C Warmuth, and I Sack. Fractional encoding of harmonic motions in MR elastography. *Magnet Reson Med*, 57(2):388–95, feb 2007.

[170] A Kolipaka, KP McGee, A Manduca, AJ Romano, KJ Glaser, PA Araoz, and RL Ehman. Magnetic resonance elastography: Inversions in bounded media. *Magnet Reson Med*, 62(6):1533–42, dec 2009.

[171] A Kolipaka, PA Araoz, KP McGee, A Manduca, and RL Ehman. Magnetic resonance elastography as a method for the assessment of effective myocardial stiffness throughout the cardiac cycle. *Magnet Reson Med*, 64(3):862–70, sep 2010.

[172] DA Woodrum, AJ Romano, A Lerman, UH Pandya, D Brosh, PJ Rossman, LO Lerman, and RL Ehman. Vascular wall elasticity measurement by magnetic resonance imaging. *Magnet Reson Med*, 56(3):593–600, sep 2006.

[173] L Xu, J Chen, M Yin, KJ Glaser, Q Chen, DA Woodrum, and RL Ehman. Assessment of stiffness changes in the ex vivo porcine aortic wall using magnetic resonance elastography. *Magn Reson Imaging*, 30(1):122–7, jan 2012.

[174] A Kolipaka, D Woodrum, PA Araoz, and RL Ehman. MR elastography of the in vivo abdominal aorta: a feasibility study for comparing aortic stiffness between hypertensives and normotensives. *J Magn Reson Im*, 35(3):582–6, mar 2012.

[175] L Xu, J Chen, KJ Glaser, M Yin, PJ Rossman, and RL Ehman. MR elastography of the human abdominal aorta: a preliminary study. *J Magn Reson Im*, 38(6):1549–53, jan 2013.

[176] AR Damughatla, B Raterman, T Sharkey-Toppen, N Jin, OP Simonetti, RD White, and A Kolipaka. Quantification of aortic stiffness using MR elastography and its comparison to MRI-based pulse wave velocity. *J Magn Reson Im*, 41(1):44–51, nov 2015.

[177] WE Kenyhercz, B Raterman, VSP Illapani, J Dowell, X Mo, RD White, and A Kolipaka. Quantification of aortic stiffness using magnetic resonance elastography: Measurement reproducibility, pulse wave velocity comparison, changes over cardiac cycle, and relationship with age. *Magnet Reson Med*, 00(November 2014):n/a–n/a, 2015.

[178] G Nir, RS Sahebjavaher, R Sinkus, and SE Salcudean. A framework for optimization-based design of motion encoding in magnetic resonance elastography. *Magnet Reson Med*, 73(4):1514–25, may 2014.

[179] YK Mariappan, KJ Glaser, RD Hubmayr, A Manduca, RL Ehman, and KP McGee. MR elastography of human lung parenchyma: technical development, theoretical modeling and in vivo validation. *J Magn Reson Im*, 33(6):1351–61, jun 2011.

[180] Q Chen, SI Ringleb, A Manduca, RL Ehman, and KN An. A finite element model for analyzing shear wave propagation observed in magnetic resonance elastography. *J Biomech*, 38(11):2198–203, nov 2005.

[181] GE Leclerc, F Charleux, MC Ho Ba Tho, and SF Bensamoun. Identification process based on shear wave propagation within a phantom using finite element modelling and magnetic resonance elastography. *Comput Method Biomech*, (September 2014):37–41, aug 2013.

[182] LEJ Thomas-Seale, P Pankaj, NR Roberts, and PR Hoskins. Computational Modelling of Magnetic Resonance Elastography Shear Wave Behaviour through Atherosclerotic Plaque with Disease Development. In *Proceedings of the World Congress on Engineering*, volume 3, pages 6–9, 2011.

[183] SF Bensamoun, SI Ringleb, L Littrell, Q Chen, M Brennan, RL Ehman, and Kai-nan An. Determination of thigh muscle stiffness using magnetic resonance elastography. *J Magn Reson Im*, 23(2):242–7, mar 2006.

[184] H Ghasemzadeh and AA Abounouri. Compressional and shear wave intrinsic attenuation and velocity in partially saturated soils. *Soil Dyn Earthq Eng*, 51:1–8, 2013.

[185] Z Li, B Gu, X Ma, and G Liang. Separating P- and S-waves in prestack elastic seismograms using the equivalent form of elastic wave equation. *J Appl Geophys*, 114:210–223, 2015.

[186] R Sun, J Chow, and KJ Chen. Phase correction in separating P- and S-waves in elastic data. *Geophysics*, 66(5):1515–1518, 2001.

[187] R Sun, GA McMechan, and HH Chuang. Amplitude balancing in separating P- and S-waves in 2D and 3D elastic seismic data. *Geophysics*, 76(3):S103–S113, 2011.

[188] BMW Lee. Velocity Ratio and its Application to Predicting Velocities U . S . Department of the Interior. *U.S. Geological Survey Bulletin*, 2197, 2003.

[189] U. Tinivella and F. Accaino. Compressional velocity structure and Poisson's ratio in marine sediments with gas hydrate and free gas by inversion of reflected and refracted seismic data (South Shetland Islands, Antarctica). *Mar Geol*, 164(1-2):13–27, 2000.

[190] ZP Bazant. Spurious reflection of elastic waves in nonuniform finite element grids. *Comput Method Appl M*, 16:91–100, 1978.

[191] E Wang, T Nelson, and R Rauch. Back to elements-tetrahedra vs. hexahedra. In *Proceedings of the 2004 International ANSYS Conference*, Munich, Germany, 2004.

[192] X Bourdin and X Trosseille. Comparison of Tetrahedral and Hexahedral Meshes for Organ Finite Element Modeling: An Application to Kidney Impact. In *20th Century Enhanced Safety of Vehicles Conference: Innovations for Safety: Apllications and Challenges*, Lyon, France, 2007.

[193] S Papazoglou, U Hamhaber, J Braun, and I Sack. Horizontal shear wave scattering from a nonwelded interface observed by magnetic resonance elastography. *Phys Med Biol*, 52(3):675–84, feb 2007.

[194] Sebastian Papazoglou, Sebastian Hirsch, Jürgen Braun, and Ingolf Sack. Multifrequency inversion in magnetic resonance elastography. *Phys Med Biol*, 57(8):2329–46, apr 2012.

[195] A Manduca, DS Lake, SA Kruse, and RL Ehman. Spatio-temporal directional filtering for improved inversion of MR elastography images. *Med Image Anal*, 7(4):465–73, dec 2003.

[196] T Deffieux, JL Gennisson, J Bercoff, and M Tanter. On the effects of reflected waves in transient shear wave elastography. *IEEE T Ultrason Ferr*, 58(10):2032–5, oct 2011.

[197] J Braun, J Guo, R Lützkendorf, J Stadler, S Papazoglou, S Hirsch, I Sack, and J Bernarding. High-resolution mechanical imaging of the human brain by three-dimensional multifrequency magnetic resonance elastography at 7T. *Neuroimage*, 90:308–314, 2014.

[198] S Hirsch, J Guo, R Reiter, S Papazoglou, T Kroencke, J Braun, and I Sack. MR Elastography of the Liver and the Spleen Using a Piezoelectric Driver, Single-Shot Wave-Field Acquisition, and Multifrequency Dual Parameter Reconstruction. *Magnet Reson Med*, 71(1):267–277, 2014.

[199] JP Ko, H Rusinek, EL Jacobs, JS Babb, M Betke, G McGuinness, and DP Naidich. Small pulmonary nodules: volume measurement at chest CT–phantom study. *Radiology*, 228(3):864–870, 2003.

[200] X Yang, L Hollis, F Adams, F Khan, and PR Hoskins. A fast method to estimate the wall shear stress waveform in arteries. *Ultrasound*, 21(1):23–28, feb 2013.

[201] DK Jones, MA Horsfield, and A Simmons. Optimal strategies for measuring diffusion in anisotropic systems by magnetic resonance imaging. *Magnet Reson Med*, 42(3):515–525, 1999.

[202] A Kolipaka, KP McGee, PA Araoz, KJ Glaser, A Manduca, AJ Romano, and RL Ehman. MR elastography as a method for the assessment of myocardial stiffness: comparison with an established pressure-volume model in a left ventricular model of the heart. *Magnet Reson Med*, 62(1):135–40, jul 2009.

[203] PY Chen and IW Selesnick. Translation-invariant shrinkage/thresholding of group sparse signals. *Signal Process*, 94(1):476–489, 2014.

[204] IW Selesnick, RG Baraniuk, and NC Kingsbury. The dual-tree complex wavelet transform. *IEEE Signal Proc Mag*, 22(6):123–151, nov 2005.

[205] S Papazoglou, J Braun, D Klatt, and I Sack. Shear wave diffusion observed by magnetic resonance elastography. In *New Developments in the Visualisation and Processing of Tensor Fields*, pages 157–168. 2012.

[206] LJ van Vliet, IT Young, and GL Beckers. A nonlinear laplace operator as edge detector in noisy images. *Comput Vision Graph*, 45(2):167–195, 1989.

[207] TT Dao, P Pouletaut, F Charleux, MHB Tho, and S Bensamoun. Analysis of shear wave propagation derived from MR elastography in 3D thigh skeletal muscle using subject specific finite element model. In *Conference Proceedings of IEEE Eng Med Biol Soc*, pages 4026–9, 2014.

[208] C Martin, T Pham, and W Sun. Significant differences in the material properties between aged human and porcine aortic tissues. *Eur J Cardio-Thorac*, 40(1):28–34, 2011.

[209] L Speelman, GWH Schurink, EMH Bosboom, J Buth, M Breeuwer, FN van de Vosse, and MH Jacobs. The mechanical role of thrombus on the growth rate of an abdominal aortic aneurysm. *J Vasc Surg*, 51(1):19–26, jan 2010.

[210] C Schmitt, A Hadj Henni, and G Cloutier. Characterization of blood clot viscoelasticity by dynamic ultrasound elastography and modeling of the rheological behavior. *J Biomech*, 44(4):622–9, feb 2011.

[211] JB Weaver, M Doyley, Y Cheung, F Kennedy, EL Madsen, EEW Van Houten, and K Paulsen. Imaging the shear modulus of the heel fat pads. *Clin Biomech*, 20(3):312–9, mar 2005.

[212] EEW Van Houten, MM Doyley, FE Kennedy, JB Weaver, and KD Paulsen. Initial in vivo experience with steady-state subzone-based MR elastography of the human breast. *J Magn Reson Im*, 17(1):72–85, jan 2003.

[213] LEJ Thomas-Seale, D Klatt, P Pankaj, N Roberts, I Sack, and P Hoskins. A simulation of the magnetic resonance elastography steady state wave response through idealised atherosclerotic plaques. *IAENG Int J Comput Sci*, 38(4):2636–39, 2011.

[214] OMB McBride, C Berry, P Burns, RTA Chalmers, B Doyle, R Forsythe, OJ Garden, K Goodman, C Graham, PR Hoskins, R Holdsworth, TJ MacGillivray, G McKillop, G Murray, K Oatey, JMJ Robson, G Roditi, S Semple, W Stuart, EJR van Beek, A Vesey, and DE Newby. MRI using ultrasmall superparamagnetic particles of iron oxide in patients under surveillance for abdominal aortic aneurysms to predict rupture or surgical repair: MRI for abdominal aortic aneurysms to predict rupture or surgery - the MA3RS study. *Brit Med J*, 2(1), 2015.

[215] GJ Stanisz, EE Odrobina, J Pun, M Escaravage, SJ Graham, MJ Bronskill, and RM Henkelman. T1, T2 relaxation and magnetization transfer in tissue at 3T. *Magnet Reson Med*, 54(3):507–512, 2005.

[216] SB Reeder, E Atalar, BD Bolster, and ER McVeigh. Quantification and reduction of ghosting artifacts in interleaved echo-planar imaging. *Magnet Reson Med*, 38(3):429–439, sep 1997.

[217] D Le Bihan, C Poupon, A Amadon, and F Lethimonnier. Artifacts and pitfalls in diffusion MRI. *J Magn Reson Im*, 24(3):478–488, 2006.

[218] EA Finol and CH Amon. Blood Flow in Abdominal Aortic Aneurysms: Pulsatile Flow Hemodynamics. *J Biomech Eng*, 123(5):474, 2001.